Computational Investigations of Fundamental Plasma Processes in Semiconductor Industrial Applications

by

Chenhui Qu

A dissertation submitted in partial fulfillment
of the requirements for the degree of
Doctor of Philosophy
(Electrical and Computer Engineering)
in the University of Michigan
2020

Doctoral Committee:

Professor Mark J. Kushner, Chair
Professor John Foster
Professor Yogesh B. Gianchandani
Professor Brian Gilchrist
Associate Professor Eric Johnsen

Chenhui Qu

chenqu@umich.edu

ORCID iD: 0000-0002-8300-9398

Dedication

This dissertation is dedicated to my mother, Lingyu Wang, and my father, Meng Qu.

Acknowledgments

It was six years ago that I first joined University of Michigan. Looking back and I see an intriguing and exhilarating journey that still brings excitement to me. It is something I will treasure throughout my whole life. Doing research work can be fulfilling at some time but difficult at others. I am extremely lucky to have so many mentors and friends to share my joy and guide me through the hard times. I cannot imagine the past years without their helps.

Firstly, I want to thank my advisor Prof. Mark J. Kushner. I am so honored to be his student and am extremely thankful for all the guidance he offered. He showed me how exciting plasma science is and how a professional scientist should do to perform high-quality research work. He unconditionally shared his valuable experiences, from the proficient coding habit to the efficient communicating tactics with fellow researchers. The lessons I learned from him will indisputably benefit me life-long.

Secondly, I would like to thank my thesis committee members, Prof. John Foster, Associate Prof. Eric Johnsen, Prof. Brian Gilchrist, and Prof. Yogesh B. Gianchandani, for their warmly help and advices on my research. I would like to thank my project collaborators: Sang Ki Nam, (Samsung Electronics); Prof. Steven C. Shannon, Joel Brandon, Kristopher Ford, and Carl Smith (North Carolina State University); David Coumou (MKS Instrument); Prof. Vincent M. Donnelly, Priyanka Arora, Tianyu Ma, and Tyler List (University of Houston); Assitant Professor Abbas Semnani (University of Toledo); Pulkit Agarwal, Yukinori Sakiyama, and Adrien LaVoie (Lam Research Corp.). I want to thank them for their invaluable inputs, and

iii

extreme patience when they offer their helps. They have broadened my view on plasma science and showed me ways to look at it from various aspects. I would also like to thank my friends at Lam Research Corporation: Saravanapriyan Sriraman, Rohini Mishra, Juline Shoeb, Rajesh Dorai, Kapil Sawlani, Alex Paterson, John Holland, and Harmeet Singh. They showed me the cutting-edge technology of plasma application in the semiconductor industry and helped me having a good time during my internship there.

Thirdly, I would love to thank the sponsors, the US Department of Energy Office of Fusion Energy Science, National Science Foundation, Lam Research Corporation, and Samsung Electronics for providing the financial support to the projects for my graduate study. It is their supports make everything possible. Their generous help is very much appreciated.

I want to also thank all the group members: Prof. Hae June Lee, Yiting Zhang, Peng Tian, Seth Norberg, Wei Tian, Chad Huard, Michael Logue, Soheila Mohades, Guy Parsey, Aram Markosyan, Juliusz Kruszelnicki, Steven Lanham, Amanda Lietz, Shuo Huang, Xifeng Wang, Jordyn Polito, Mackenzie Meyer, Kseniia Konina, and Florian Krueger. I've spent most of my time with them in the past years. They are the friendliest and are always there to offer their help. Discussing with them is indeed a happy experience and an extremely efficient way to learn. I would also like to give my special thanks to Julia Falkovitch-Khain, who has been taken care of all the administrative issues I had in the past years. She made my life much easier so that I can focus on my research work whole-heartedly.

Finally, I would like to thank my family. I would love to thank my parents for raising me and supporting me chasing my dream. Nothing would be possible without them. Also, I would like to thank my girlfriend Yan Zhuang for standing by me and encouraging me to be a better self.

Table of Contents

List of Figures

xiv

List of Tables

List of Acronyms

0-d	0-dimensional
2-d	2-dimensional
3-d	3-dimensional
ALE	Atomic Layer Etching
ALD	Atomic Layer Deposition
AR	Aspect Ratio
CCP	Capacitively Coupled Plasma
CD	Critical Dimension
CW	Continuous Wave
DBD	Dielectric Barrier Discharge
dc	direct current
DC	Duty Cycle
DF-CCP	Dual-frequency Capacitively Coupled Plasma
eMCS	electron Monte Carlo Simulation
EED	Electron Energy Distribution
EETM	Electron Energy Transport Module
EMM	Electromagnetic Module
FKPM	Fluid Kinetics Poisson Module
GPC	Growth Per Cycle
HAR	High Aspect Ratio
HPEM	Hybrid Plasma Equipment Model
IAD	Ion Angular Distribution
ICP	Inductively Coupled Plasma
IEAD	Ion Energy and Angular Distribution
IED	Ion Energy Distribution
IMN	Impedance Matching Network
LTP	Low Temperature Plasma
MCFPM	Monte Carlo Feature Profile Model
MD	Molecular Dynamic
MF-CCP	Multi-frequency Capacitively Coupled Plasma
NEAD	Neutral Energy and Angular Distribution
ODE	Ordinary Differential Equation
OES	Optical Emission Spectroscopy

PCMCM	Plasma Chemistry Monte Carlo Module
PDE	Partial Differential Equation
PRF	Pulse Repetition Frequency
PSI	Plasma Surface Interaction
RF	Radiofrequency
SF-CCP	Single-frequency Capacitively Coupled Plasma
S-G	Scharfetter-Gummel
SKM	Surface Kinetics Module
SOR	Successive-over-Relaxation
SSBM	Surface Site Balance Model
SVR	Surface-to-Volume Ratio
TF-CCP	Tri-frequency Capacitively Coupled Plasma
UV	Ultraviolet

Abstract

The continuous downsizing of the critical dimensions (CDs) of semiconductor devices poses challenges to plasma-involved semiconductor fabrication processes. As the CD decreases to sub-ten nanometers (e.g., 6 nm-width fin field-effect transistor [FinFET]), control of plasma properties to provide atomic scale precision becomes necessary. Meanwhile, to ensure high yield, semiconductor fabrication is often deployed on a large scale, on 300 mm wafers. Therefore, it is essential to have a uniform plasma distribution across the reactor for consistent yields.

In this thesis, reactor and feature scale modeling was performed. The research work involves developing computational modules and applying acceleration mechanisms in two simulation platforms: the Hybrid Plasma Equipment Model (HPEM), for reactor scale modeling, and the Monte Carlo Feature Profile Model (MCFPM), for feature scale simulations. Frequency tuning and impedance matching with an impedance matching network (IMN) were implemented in the HPEM to study the electrical dynamics during pulsed-plasma operation. Surface reaction mechanisms of SiO_2 plasma-enhanced atomic layer deposition (PE-ALD) using bis-tertiary-butyl-amino-silane (BTBAS) as the precursor were developed.

In an inductively coupled plasma (ICP) reactor, the power deposition into the plasma is always less than the output from the power source. The power that is not directed into the plasma is lost in the transmission line, reflected at the coil-plasma interface due to the impedance mismatch, or dissipated by the materials in the plasma reactor. The power reflection is

minimized by implementing an IMN between the power source and the coil. By tuning the circuit components used in the IMN, the impedance of the pre-plasma circuit (including coils, IMNs, and power source) is brought close to the impedance of the plasma, thus reducing the power reflection. However, in practice, the components in an IMN have fixed values because tuning the IMN is a mechanical process that takes several miliseconds to even seconds. Frequency tuning is another mechanism for impedance matching, which takes advantage of the high tuning rate with solid state electronics. This technique can be used with an IMN if the plasma has a rapidly changing impedance (e.g., pulsed plasma). The function of analytically calculating the circuit components in IMN to minimize power reflection in an ICP reactor was implemented in the HPEM. An algorithm of frequency tuning in an ICP was also added to enable impedance matching by adjusting RF frequency when the IMN is fixed.

SiO_2 films are widely used in semiconductor devices, and PE-ALD is a preferred method for deposition when a low process temperature is needed. The PE-ALD of SiO_2 has two major steps: precursor dosing and plasma exposure. During precursor dosing, a silicon precursor such as BTBAS is used to treat the target surface and forms a monolayer of Si-H compounds. Subsequently, in the plasma exposure step, the target surface is treated with an oxygen plasma and is oxidized. The reaction is self-limiting for both steps, and a monolayer of SiO_2 is deposited in one cycle. However, in experiments, the growth-per-cycle (GPC) is often less than one monolayer, which partly is caused by steric hindrance. Incomplete reactions during precursor dosing leave alkyl ligand remains on the target surface, which block neighboring sites, and slows the deposition. The impacts of the operating conditions and steric hindrance on SiO_2 films during PE-ALD were studied.

Chapter 1: Introduction

1.1 Low Temperature Plasmas in Semiconductor Processing

Since the mid-1980's, the use of low-temperature plasmas (LTPs) has become an essential part of the semiconductor industry. In fact, developments in manipulating LTPs have become a driving force for increasing transistor density in computer microchips that keeps pushing the technology to follow Moore's law [6,7]. Different types of plasmas are often categorized as a function of electron density and electron temperature, as shown in Fig 1.1 [4]. In this thesis, the focus is on a greater understanding of low-temperature plasmas and their application in the semiconductor industry.

Plasma is commonly referred to as the fourth state of matter. It is an electrically quasi-neutral gas consisting of charged and neutral particles with collective behaviors [1]. Generally speaking, as temperatures increase from absolute zero a substance experiences phase changes from solid, to liquid, to gas. Beyond the gas phase, if additional energy is provided, the matter transforms into the plasma state. It is recognized that the majority of the matter in the visible universe is plasma. For example, both the ionosphere of the earth and the photosphere of the sun are plasmas. Because plasma provides highly reactive particles, and its behavior is subject to the surrounding external electrical field (E-field), it is widely used for industrial applications. The most recognizable examples of these are plasmas in visual display panels and in fluorescent lighting. Both of these utilize ultraviolet (UV) light produced in a plasma [2,3]. From

fluorescent lighting to the surface of the sun, plasma parameters cover a vast range of possible uses.

There is no strict definition of low-temperature plasmas (LTPs). However, for plasma processing applications, an LTP often refers to a non-thermal-equilibrium, weakly-ionized plasma with an electron temperature (T_e) between several to 10s eV [5]. The electron density (n_e) of an LTP is often at 10^8 - 10^{13} cm^{-3}, and the pressure is from a few mTorr up to atmospheric pressure (100s Torr). The properties of an LTP depend on many factors, including but are not limited to the input power, pressure, and the geometry of the reactor. Therefore, many control knobs can be manipulated to characterize an LTP for specific applications, which is typically not the case for other manufacturing approaches.

The wide range of chemical and electrical properties of an LTP exceed the boundary of normal manufacturing. For example, using LTP enables high aspect ratio (HAR) etching in microchip manufacturing within nanometer-scale critical dimensions (CD) due to the emphasis on physical etching [8]. Before the use of plasmas, wet chemical etching was the mainstream etching technique. However, wet etching is isotropic, and therefore is not suitable for HAR processing. Applying LTP also enables the deposition of dielectric material with nanometer-scale precision in low temperature (< 300 ˚C) applications [9]. Access to the reactive particles in the LTP moderates otherwise thermally expensive reactions therefore allowing deposition to be performed on temperature-sensitive devices. Examples such as those mentioned above demonstrate that LTPs become indispensable components in semiconductor fabrication. As the technology node hits sub-10 nm, and the design of semiconductor devices shifts from 2-dimensional (2D) to 3-dimensional (3D), it is critical to have precise control over the

2

manufacturing processes. Producing highly uniform plasmas, with abundant desired reactants and maximum power efficiency, continues to be the goal of industrial related LTP research.

This dissertation focuses on two topics: to survey the possible methods for improving plasma uniformity and stability; and to investigate the impact of operating conditions on a PE-ALD of SiO_2. Both topics are studied using computational tools. A brief overview of the fundamentals of LTP and plasma sources is presented in Section 1.2. PE-ALD of SiO_2 is briefly explained in Section 1.3 and the modeling of reactor-scale plasma phenomena and feature-scale deposition processes is described in Section 1.4 and 1.5.

1.2 Plasma Sources

To sustain a plasma, an external supply is required to provide the power to ionize and excite the neutral particles. The resulting ions and excited state species are essential components in plasma and are often desired for surface treatment or etching.

LTPs are made up of bulk and sheath regions and make up a quasi-neutral dynamic system with a delicate charge balance in the sheath-bulk plasma interface. The sheath is a thin high-electrical field region above all the surfaces exposed to the plasma. A diagram of the plasma sheath is shown in Fig. 1.2 [10]. In an LTP, $T_e \gg T_i$ and the mass of an electron (m_e) is much less than the mass of an ion (m_i). Therefore, the thermal velocity of the electron is much faster than that of heavy ions. When a surface is presented in a plasma, electrons are lost at a much faster rate than neighboring ions due to their high velocity. Because the plasma is a quasi-neutral system, the loss of electrons to the surface results in a positively charged region almost exclusively containing only cations and neutrals. This charge provides a plasma potential that leads to the formation of an electrical field (E-field) from the plasma bulk to the surface. This

potential repels the electron flux (Γ_e) and accelerates cation fluxes (Γ_i) toward the surface. This high E-field region with $n_i > n_e$ is commonly referred to as the sheath region. If the surface is not grounded, it is referred to as an electrically floating surface. A floating surface can be charged by fast-moving electrons, and this also results in a surface-pointing E-field and the development of the sheath. The sheath formation on a powered electrode is more complicated and will be discussed in detail later.

Most of the plasma chemical reactions occur in the bulk plasma. Charged particles and excited state species are created through ionization and excitation, and they are lost through recombination reactions and diffusion to the wall. Electron impact reactions are the most common types of reactions in an LTP. Electrons accelerated by the E-field gain energy and collide with neutral particles, and this transitions the particle to an excited state. If the electron energy is high enough, ionization occurs. The energy of a species is often plotted on a potential energy curve. For example, the potential energy curve of O_2 is shown in Fig. 1.3 [11]. When external energy is applied to the ground state oxygen molecule, it can be pumped to another potential curve and this represents the shifting of its energy states and the occurrence of a reaction. If two potential curves cross, a shift of states may occur. Most of the reactions in LTPs are energy-dependent, meaning the reaction rate varies with the energy of the reactant electrons. This energy-dependence is addressed by using cross section (σ) in the expression of the reaction rate coefficient. A cross section is an energy-dependent parameter of the unit of area and is specific for each species. The electron impact cross sections for oxygen are shown in Fig. 1.4 [12]. Inelastic collisions such as ionization and excitation have threshold energy requirements, while the momentum transfer reaction (elastic collision) is available across all energy regimes. An averaged reaction rate constant (k) is:

$$k = \int_0^\infty \sigma(\varepsilon)\left(\frac{2\varepsilon}{m}\right)^{1/2} f(\varepsilon)d\varepsilon, \tag{1.1}$$

where $f(\varepsilon)$ is the electron energy distribution function (EEDF).

Note that plasma is a dynamic system defined by the group behavior of electrons and ions. One of the most important features of a plasma is its plasma frequency. The electrons and ions are constantly oscillating due to the self-restoring force caused by the perturbation of local charge equilibrium. The electrons and ions oscillate at different frequencies ω_{pe} and ω_{pi}:

$$\omega_{p(e,i)} = \sqrt{\frac{q^2 n_0}{\varepsilon_0 m_{(e,i)}}}, \tag{1.2}$$

where q is the elementary charge, n_0 is the plasma density, and $m_{e,i}$ are the electron and ion masses, respectively. Because the electron mass is much smaller than the ion mass, the electron plasma frequency is always much larger than the plasma ion frequency, $\omega_{pe} \gg \omega_{pi}$. Therefore, in most scenarios, it is safe to consider only the electron plasma frequency and treat ions as stationary particles. The oscillation of the charge species creates a local non-equilibrium of charge density. In an LTP, the scale over which the charge-equilibrium can be violated is the Debye Length (λ_D):

$$\lambda_D = \sqrt{\frac{\varepsilon_0 T_e}{q^2 n_e}}, \tag{1.3}$$

where T_e is the electron temperature. Remember that within the sheath, the plasma is not charge-neutral ($n_i > n_e$). The thickness of the sheath is often several λ_D.

1.2.1 Inductively Coupled Plasma Source

Inductively coupled plasma (ICP) sources are widely deployed in the semiconductor industry. A commonly used ICP has the "stovetop coil" configuration shown in Fig. 1.5 [13]. In this case, radiofrequency (RF) power is fed through the planar coil. The oscillating E-field

generates a time-varying magnetic field in the reactor which then creates an E-field that oscillates in the azimuthal direction. This E-field accelerates electrons back and forth and transmits the power from the coil to the plasma. The plasma potential is often low in an ICP (10s V). This low potential results in a thin sheath and low ion energy onto the surface, thus causing less sputtering and contamination in the plasma. Because the targeted feature size can be 10s or sub-10 nm scale, reducing contamination is critical. Usually, separately controlled power sources are applied to the substrate in an ICP reactor to control the ion energy and angular distributions (IEADs) onto the wafer. Therefore, an almost independent control of the plasma density and IEADs is made possible with the use of ICP.

In an industrial application, the frequency of the RF power is typically at 13.56 MHz, and the pressure is 10s mTorr. The momentum transfer collision frequency (v_m) is less than or close to the driving frequency of the coil. Under these conditions, the skin depth of the electromagnetic field (EM-field) into the plasma can be approximated by

$$\delta = \left(\frac{m_e}{q^2 \mu_0 n_e} \right)^{1/2} \tag{1.4}$$

where δ represents the skin depth, and μ_0 is the vacuum permeability. The power is mainly transferred to the plasma within the range of this skin-depth. Power transition is largely carried out through collisionless heating due to the low pressure. In a typical ICP, $\delta \approx$ 1-2 cm.

To optimize the power delivery to the plasma, an impedance matching network (IMN) is often implemented between the power source and the coil [14,15]. An IMN is a circuit that contains only inductors and capacitors, so there is no net power consumption. By tuning the circuit components used in the IMN, the input impedance of the IMN is matched to the output impedance of the power source, which usually is 50 Ω. Using IMN ensures high power delivery

efficiency by reducing the power reflection. The electric field reflection coefficient (Γ_R) is calculated as

$$\Gamma_R = \frac{Z_L - Z_0}{Z_L + Z_0},$$ (1.5)

where Z_L is the impedance of the load, including the impedances of IMN, plasma, and the electrical termination components; Z_0 is the 50 Ω impedance of the power source. The power deposition into the plasma is then equaled $P_{tot}(1-|\Gamma_R|^2)$, where P_{tot} is the power output from the power source.

Pulsed power is often used to gain better control of the reactive species fluxes to the substrate. The pulse repetition frequency (PRF) is often between 1-20 kHz, and the duty cycle (the fraction of the power-on time in the whole period) is 10s of percent. Using pulsed power enables higher plasma density while maintaining a moderate average power. Also, unique plasma chemistry is enabled during the power-off period [16-18]. Even better control of the reactive particles fluxes to the wafer can be achieved when combining the pulsed ICP power with a separately controlled powered substrate [19, 20].

A commonly observed behavior in a pulsed plasma is that T_e often spikes over the quasi-steady state value at the leading edge of pulse-on, as shown in Fig. 1.6 [21]. This phenomenon is caused by low n_e during the pulse-off. Without power input, electrons are rapidly lost to the chamber wall and through recombination and attachment reactions. Therefore, at the end of the pulse-off, n_e can be as low as 10^8 cm^{-3}. Consequently, 10s to 100s of Watts of power are distributed in a small number of electrons in the early pulse, which efficiently heat the electrons and causes the spike of T_e. With high T_e, the ionization reaction rate increases, leading to a boost of n_e, and sequentially causes the drop of T_e to the quasi-steady state value. Because the spike of

T_e depends on the low n_e during pulse-off, it is more significant when the PRF is low and when the plasma is sustained in gases with high electron affinity, such as Cl_2 [22, 23].

Another unique dynamic of a pulsed ICP is the E-H mode transition during power ramps when n_e changes abruptly. The ICP operates in H-mode when the plasma density is high. In H-mode, the skin depth (δ) of the electromagnetic wave is smaller than the dimension of the reactor. The power is mainly transferred to the plasma through the azimuthal E-field. However, $\delta \propto 1/n_e$. When n_e is low, such as at the beginning of the pulse-on, δ can be longer than the dimension of the reactor, meaning power cannot be effectively transferred to the plasma through the azimuthal E-field. However, because the coils are high-voltage metals, according to Poisson's equation, they produce E-field in the axial direction. This E-field propagates into the plasma and accelerate electrons accordingly. The power coupled to the plasma through this method is the capacitively coupled power. When the power is mainly coupled through capacitive coupling, the plasma operates in the E-mode.

The E-mode occurs when δ extends further into the plasma, and n_e is low, which is most often the condition at the end of the pulse-off. Therefore, in a pulsed plasma, it is often observed that during the power ramp-up, a plasma begins in E-mode. As n_e increases, the plasma experiences an E-H transition and switches to H-mode dominant. The E-H transition has been observed in various studies, and often shows hysteresis behavior [24-27]. The E-to-H and H-to-E transition can occur at different powers. The pressure, dimension of the reactor, and even the power loss in the transmission line, are all believed to affect the E-H transition, which explains the uniqueness of the phenomenon from case to case [28, 29]. An ionization instability and the modulation of the electron density (n_e) are often the outcomes of an E-H transition [30]. Because E-H transition results from the re-ignition of the plasma, one approach to avoid it is to use a

high-low pulsed power scheme [31]. With a low power input during the low-power period, a minimum plasma density is maintained to ensure the plasma always operates in the H-mode. Another method to minimize the effect of E-H transition is to apply a Faraday shield between the planar coil and the dielectric window, which minimizes capacitive power coupling to the plasma [32].

1.2.2 Capacitively Coupled Plasma Source

Another widely used plasma source is the capacitively coupled plasma (CCP). A conceptual diagram and an experimental CCP reactor are shown in Fig. 1.7 [33]. Comparing with an ICP reactor, the CCP reactor typically is shorter in the axial direction. The smaller dimension allows it to operate under higher pressures. In the semiconductor industry, a CCP reactor is often used in the deposition process when the pressure is up to several Torr.

Unlike an ICP, in a CCP reactor, the power is fed into the plasma through the plate electrodes. As the voltage on the electrode varies at radio frequency, so does the E-field created adjacent to the electrode. The oscillating E-field creates an oscillating sheath that heats electrons and sustains the plasma. This electron heating mechanism with a time-varying sheath is called stochastic heating. In a CCP, the plasma potential is often high due to its capacitive power coupling. This high plasma potential creates a high time-averaged E-field pointing from the plasma bulk to the electrode, which accelerates ions to an energy up to 100s eV. These energetic ions bombard the electrode, leading to the emission of electrons. This process is referred to as a secondary electron emission. However, the secondary electron emission is not uniquely caused by ions. A hot neutral species, that is, a neutral particle with high energy that can be created by charge exchange reactions, can also cause secondary electron emissions. Even so, the ion-induced secondary electron emission usually dominates in a CCP. The probability of the secondary electron emission depends on the energy, mass, states of the heavy particles impacting

9

on the surface, and the material of the electrode. Note that the secondary electron emission is not a simple kinetic energy transfer process.

If a CCP is primarily sustained by the hot electrons from a secondary electron emission, that is, the secondary electrons cause most of the ionization and excitation reactions, the plasma is regarded as in γ-mode. Otherwise, if the plasma is sustained by the bulk electrons heated by stochastic heating, the plasma is in α-mode. The difference between these two modes has been extensively studied [34-37]. A transition from α- to γ-mode CCP with an increasing applied voltage in a Neon discharge is depicted in Fig. 1.8 [34]. Unlike ICP switching between E- and H-mode in a single process, a CCP mostly does not experience a γ- and α-mode transition. The reason partly is that whether the plasma operates in γ- or α-mode highly depends on the local operating conditions, such as pressure and radio frequency, which are commonly constant in a process.

The sheath plays a critical role in the generation of a CCP. Another important parameter closely related to sheath properties is the self-generated DC-bias voltage. This DC-bias voltage is the key parameter to affect the plasma properties that are most important for a semiconductor fabrication process, such as IEADs. Brief descriptions of the sheath on a powered electrode and the generation of the DC-bias are provided as follows.

As mentioned at the beginning of Chapter 1.2, electrons are much easier lost to a surface than ions in an LTP because of electron temperature is much larger than ion temperature ($T_e \gg T_i$). The thin electron-barren layer formed next to the surface with high E-field generates the plasma potential (V_P). This layer is effectively a sheath. A sheath also forms on a powered electrode, but the mechanism is more complicated. Since it is connected to the power source the potential of the electrode is oscillating at the radio frequency, which is often several to 10s MHz.

Therefore, when the potential of the electrode is in the positive half, it attracts nearby electrons and causes the sheath to collapse. When the potential of the electrode is in the negative half, it repels electrons and leads to the sheath expansion. As a result, the sheath in a CCP is constantly oscillating. These sheath dynamics are so important that stochastic heating is one of the main electron heating mechanisms in a CCP.

In a CCP reactor, a blocking capacitor is often connected to the electrode to dominate over the effects of any stray impedance. Upon this capacitor, a DC-bias is generated. The DC-bias is produced due to the geometrical asymmetry, that the surface area of the grounded surface (A_{ground}) is inequal to the surface area of the power surface (A_{power}). This asymmetry results in current inconsistency in the reactor as the current magnitude will be larger on the surface with larger area. Therefore, a DC-bias is built up on the blocking capacitor to maintain the current consistency. In most LTP reactors, $A_{ground} > A_{power}$, which produces a negative DC-bias ($-V_{bias}$) on the powered electrode. With this DC-bias, the superpositioned voltage on the electrode is shifted by the amount $-V_{bias}$, and the time when the RF potential on the electrode exceeds the floating plasma potential is shortened, as shown in Fig. 1.9. When a DC-bias is generated on the substrate, it is one of the most important parameters that affect the ion energy because ions only react to low-frequency or continuous wave (CW) voltages due to their heavy masses.

One of the shortcomings of the CCP is that most plasma properties are heavily coupled. For example, in an ICP, the plasma density and the ion energy to the wafer can be independently controlled. This disassociation is caused by the negligible heating of electrons by the thin sheath above the substrate. In a CCP, varying the operating conditions often result in the changes of many plasma parameters. In some cases, increasing the power leads to the increase of plasma density, but also causes high ion fluxes to the substrate. In the deposition process, a high plasma

density is desired because it leads to high deposition rates. However, high ion flux can lead to damage of the deposited film and should be avoided. Such a dilemma is common when using a conventional single-frequency CCP (SF-CCP). One approach to decoupling the plasma parameters is to use a dual- or multi-frequency CCP [38-44]. As mentioned above, in a CCP, power can be transferred predominantly to the plasma electrons through stochastic heating. If so, the electron power transfer efficiency is proportional to the radio frequency. Therefore, input power with a high-frequency (10s MHz) affects the heating of electrons more than at low-frequency (several MHz). At the same time, heavy particles, such as most ions, can barely follow the fast-changing E-field but will respond well to a low-frequency signal. Therefore, theoretically, by applying dual-frequency power, the plasma density and ion fluxes and the IEAD can be independently controlled to some degree. Ideally, high-frequency power is used to control the plasma density while low-frequency power is used to control the IEAD to the wafer. Even so, some level of coupling still occurs. Secondary electron emission, which are proportional to the ion energy and flux, affects the electron density if the plasma and operate in γ-mode. In these cases, the low-frequency affects the plasma density by influencing ion fluxes, even though two frequencies are applied [45]. Following this process, multi-frequency power sources are implemented to have more control options in a CCP-involved process [46, 47].

1.3 Plasma Enhanced Atomic Layer Deposition of Silicon Dioxide

Some sort of dielectric material is one of the most prevalent materials in semiconductor fabrication. As the complexity of semiconductor devices escalates, the requirements on the dielectric material deposition become more stringent including high conformality, a low level of contamination, high deposition rates, and low wet etch rates (WER) of the film [48, 49]. Atomic layer deposition (ALD) technology for the deposition of many dielectric layers has improved in

the past decades [50-54]. A schematic of the ALD process is shown in Fig. 1.10 [50]. An ALD process often involves two steps, and each step deposits a portion of the desired material on the target surface. Typically, a monolayer of the chemical compound is deposited at the end of each cycle. This ALD process is called the AB binary reaction sequence. A successful ALD strictly depends on the successful self-limiting of surface reactions on each step. That is to say, deposition saturates once the surface is covered with one layer of the target material and self-limitedly prevents any build-up, ensuring nanometer scale control and is the key factor in ALD.

Plasma enhanced atomic layer deposition (PE-ALD) has become more important in the past few years and particularly involves the use of LTP. In fact, one of the most significant advantages of the PE-ALD is its low deposition temperature requirement. The ions in the LTP can activate the surface by transferring kinetic energy to the surface particles during the bombardment. Also, the reactive species in LTP often have a lower energy threshold for their surface reactions. Therefore, less thermal energy is needed in a PE-ALD process. The deposition temperature can be decreased from 100s to 100 or even 10s˚C for some processes [55-57]. Another advantage is that this decrease of deposition temperature broadens the choices of material available for semiconductor fabrication. Materials that break down under high temperature become usable if PE-ALD replaces thermal depositions.

Silicon dioxide (SiO_2) is a material frequently used in semiconductor devices. SiO_2 film deposition is common and requires precise control as the size of the feature decreases. In a SiO_2 PE-ALD process, the target surface is first dosed with the silicon precursor and then is exposed to oxidant-containing plasma. Depending on the choice of silicon precursor, and the plasma operating conditions, the plasma exposure time can vary from 100s ms to 10 s [58-60]. The rule of thumb is that the plasma exposure time is long enough for the oxidant to oxidize the surface,

13

but not so long as to induce significant ion bombardment that damages the film. The variable requirements of SiO$_2$ film quality, and various plasma operating conditions cause this order of magnitudes difference of plasma exposure time for particular applications. Note that oxygen plasma is mainly used as the oxidant agent in most SiO$_2$ PE-ALD processes.

One's choice of silicon precursor is another critical factor that affects the PE-ALD process. Irrespective of the popularity of using silane as the precursor for silicon-based material deposition, it is rarely used in an ALD process due to its low adsorption probability [61]. As an alternative, alkyl- or amine-ligand containing silane precursors are commonly used [62-64]. The asymmetrical structures of these species often lead to lower bonding energy between the silicon core and the ligands, thus increases their adsorption probability. One shortcoming of these organic silicon precursors is that if adsorption is incomplete, and the large ligand groups remain on the surface, other sites on the surface can be physically blocked by these ligands [65]. This results in decreases in the growth per cycle (GPC).

1.4 Modeling of Low Temperature Plasmas

Computational investigation is a critical approach to studying the physics of LTPs. It provides insights into LTPs without the need to conduct experiments. Modeling work is more cost-efficient compared with the experiments, and broader parameters of study can be performed. Therefore, computational modeling of LTP is often performed as the first step of reactor design.

There are three kinds of LTPs models: kinetic, hybrid, and fluid [66]. The main differences between these models are the scale and the equations they are built on. Generally speaking, the fluid model is the most time-efficient, and the kinetic model is the most accurate. A hybrid model is a combination of the fluid and kinetic model, thus can lean towards either high efficiency or high fidelity, based on the chosen setup. There is no definitive superior model.

The choice of the model being used should depend on the particular problem that is being addressed.

The fluid model uses macroscopic properties such as densities, mean velocities, and mean energies to describe LTPs. A fluid model is based on the Boltzmann equation. Nearly all of the governing equations of a fluid model, the continuity, momentum, and energy equations, can be derived from the Boltzmann equation. Then the effect of the electromagnetic field on the plasma is gained by coupling these equations with Maxwell's equation. Because the fluid model is governed by the fluid equations, the number of variables (densities, energies, and velocities) being tracked is a function of the number of species included in the model, which is often 50 or more. As described, a fluid model is computationally light and is proven useful when conducting a quick study on the LTPs. However, information such as electron energy distribution functions (EEDFs) is missing in a fluid model, which may introduce inaccuracy in the results.

In a kinetic model pseudoparticles that are the computational units used to represent groups of particles of various species. The kinetic model is based on first-principles equations, such as the Newton-Lorentz and Maxwell's equations. Because of this, the kinetic model often provides highly accurate results [67,68]. However, because the time consumed in executing a kinetic model scales with the number of pseudoparticles used, a kinetic model is often computationally expensive. In most scenarios, only the electrons and ions can be tracked using pseudoparticles, while the neutral species are treated as background gas to save computational time. Another method for accelerating a kinetic model is to apply a high-speed computational unit, such as a graphic processing unit (GPU), for modeling. In any case, it is advantageous to

use the kinetic model when studying plasma with non-Maxwellian EEDFs, statistical properties such as the EEDFs are captured.

The hybrid model is the combination of the fluid and kinetic models. It combines sections that solve the plasma properties in the macroscopic scale as in a fluid approach as well as sections tracking the plasma properties using pseudoparticles as in a kinetic model [69]. A full fluid model provides the quickest result when studying the quasi-steady state of an LTP, however, if EEDFs are the subject of interest, electrons can be treated using the Monte Carlo approach, while ion properties are solved using fluid equations. If ion energy and angular distributions (IEADs) are the key factors that need to be logged, ions can be treated as pseudoparticles. The hybrid model provides high flexibility between accuracy and efficiency and can be customized to a specific task.

Because in a hybrid model both the macro- and micro-scale physics are tracked, it is difficult to choose the proper time step [70]. The time step requirements can vary by orders of magnitude. Microscale physics, such as the oscillation of the E-field at radio frequency occurs at a time scale smaller than 1 ns. On the other hand, to capture some phenomena that occur at the reactor scale (e.g., gas flow), several seconds are needed. This issue is often addressed in a hybrid model by dividing the calculation into different modules. Each module has its own time step for resolving the natural behavior of the corresponding physics, with parameters updated and transferred between the modules in a time-slicing fashion. That is, the parameters are updated hierarchically until the system reaches the quasi-steady state.

1.5 Feature Profile Modeling

The frontline of material processing using LTPs is the plasma-material interface. LTPs provide reactive particles to modify both the chemical (e.g., surface components) and physical

(e.g., topology) properties of the surface material. The products of the surface reactions are released into the plasma, causing modification of the plasma properties. The interaction between LTPs and the material is called a plasma surface interaction (PSI). Modeling the PSI offers physics insight, and provides valuable information for the subsequent process optimization.

There are three major approaches to the PSI modeling: ab initio modeling, molecular dynamic (MD) modeling, and kinetic Monte Carlo (KMC) modeling [71]. The ab initio model is based on quantum mechanics, and uses the densities functional theory (DFT) to calculate the particle potentials. Therefore, this model generally provides the result with the highest accuracy [72]. However, it is challenging to apply the ab initio model on the entire feature with a scale of 1,000s nanometers. The ab initio model is mainly used to study the particle surface reaction without considering the topology of the surface. The bulk surface material defined in an ab initio model often contains up to 100s atoms.

In a molecular dynamic model, unlike the ab initio model, the potentials of the particles are not solved from the time-independent Schrödinger's equation, but is part of the input. The solution of an MD model therefore depends on the choice of this potential. However, errors can be induced if the potential is chosen improperly. Even so, the MD model is computationally much lighter than the ab initio model due to its use of this semi-empirical potential function. Therefore, the MD model is frequently used to explore the atomic scale reaction mechanisms of a PSI [73, 74]. Despite the fact that an MD model is computationally lighter than an ab initio model, it still is almost impossible to apply the MD model to a large simulation domain that covers the whole structure at, say, 100s nanometer scale.

To have the entire target structure covered in a simulation, kinetic Monte Carlo models are often developed. The prerequisite for using a KMC model is the inclusion of experimental

data or the simulation results from ab initio or MD models. The KMC model takes those surface reaction rates as a known parameter while focusing on the topological development of the feature. Three methods can be used to represent the surface in a KMC model: the string method, level set method, and the cell-based method [75]. The string method uses the straight-line connected nodes (segments) to represent the surface. The movement of the surface is captured by moving segments along with the nodes. Because the slope of the segments remains constant during the simulation, the string method is most suitable for modeling an isotropic procedure such as wet chemical etching. In the level set method, the surface is given an initial profile. This profile is updated by applying a time- and space-dependent force on it. This force is then calculated based on the local conditions on each node. If compared with the string method, the level set method can much more easily capture the anisotropic properties of a process. But updating the driving force is computationally intensive, which is a difficult trade off to make for many applications that require high efficiency.

A cell-based method defines each mesh cell as associated material and the gas phase particles are also tracked. Any surface reactions are addressed as Monte Carlo collisions when gas phase particles hit the solid material. The cell-based method directly tracks the feature profile and the topological evolvement. By choosing the proper cell size, the computational time can be effectively reduced. However, this is proportional to the number of Monte Carlo particles involved. If many particles are tracked, the cell-based method can also be computationally heavy.

1.6 Summary

To continue to pursue Moore's law, the semiconductor industry is now targeting sub-10 nm scale manufacturing techniques. Plasma-involved processes continue to play an important

role in fulfilling this task, requiring a highly uniform and stable plasma. Applying a multi-frequency power source and modifying the power profile are two widely used techniques for achieving these goals. Properties of a triple-frequency capacitively coupled plasma and an inductively coupled plasma sustained in low-high pulsed power are discussed in this dissertation. Triple-frequency power offers more control options to modify plasma properties, while a low-high pulsed power mitigates the abrupt changes of plasma properties during power transitions.

To enable a fabrication process to benefit from these unique power formats, it is essential to have optimal power delivery to the plasma. The majority of the power delivered to such systems is at radio frequencies, delivered to the plasma reactor by a transmission line. One needs to minimize the power reflection by the reactor so that the power delivered to the plasma has the desired profile. Since the power delivery efficiency is a function of the impedances of the load represented by the reactor, impedance matching circuitry is often used. Using pulsed power, the impedance of the reactor changes significantly, making matching difficult. Set-point matching uses a fixed impedance matching network (IMN) between the power supply and the plasma reactor with the goal of having a matched load at some point during the pulsed cycle. Frequency tuning employs a power supply with having a variable frequency for dynamic impedance matching. The effects of both impedance matching techniques on pulsed ICPs are discussed in this dissertation.

Finally, the ultimate goal for a plasma processing in semiconductor fabrication is to manufacture nm-scale features. In this regard, the use of plasma enhanced atomic layer deposition (PE-ALD) for SiO_2 films is discussed. The impact of macroscopic parameters such as input power and pressure in the reactor on the film deposition are discussed.

To summarize, in this dissertation, both reactor and feature scale simulation results are studied to investigate the effects of operating conditions on an LTP, the proper IMNs setup in a pulsed plasma, and the possible optimization methods of a SiO_2 PE-ALD process.

In Chapter 2, the algorithms used for the models applied in this dissertation are described. A 2-dimensional model, the Hybrid Plasma Equipment Model (HPEM), is used for the reactor scale plasma simulation and the basic structure of the HPEM is discussed. The calculation of the IMNs with consideration of power reflection is also described. A 3-dimensional model, the Monte Carlo Feature Profile Model (MCFPM), was used in the investigation of PE-ALD of SiO_2 films and a description of this model is also provided in Chapter 2.

In Chapter 3, the transient plasma properties of an ICP driven by high-low pulsed power are discussed. The plasma is sustained in an Ar/Cl_2 gas mixture, and the pressure is 10s mTorr. The use of Cl_2 enables unique chemistry during the low-power period due to its high electron affinity. The high electron attachment rate to Cl_2 leads to low electron density (n_e) in the late low-power period. This low n_e causes a spike in the electron temperature (T_e) shortly after low-high power transition due to the transitional boost of energy per particle. This overshoot of T_e ends promptly as n_e increases and approaches the quasi-steady state. However, plasma transit states differ from various positions. For example, spikes of T_e disappear 10 cm away from the power source, near the wafer. But the response time of the plasma to the power transition is then longer due to transport delay. Elongating the power ramp and applying higher "low power" can stabilize the plasma near the wafer at the cost of having less low-power chemistry.

In Chapter 4, the power transition from a power source to the plasma is discussed with an impedance matching network (IMN) included. The plasma is an ICP sustained with Ar/Cl_2 gas mixture at a pressure of 10s mTorr using pulsed power. At the beginning of the pulse, when the

plasma density is low, the power is mainly capacitively coupled to the plasma, and the plasma is in E-mode. As the n_e increases with the power, plasma switches from E- to H-mode, meaning the power is predominantly inductively coupled to the plasma and no abrupt change of n_e is captured during the mode transition in this work. The IMN used in this work is a set-point matching circuit. That is, the IMN is fixed during the pulsing period. Picking the match point appears to have a significant impact on power delivery. For example, matching the early pulse suppresses the E-mode but causes consistent power reflection through the pulse-on. On the contrary, matching the late pulse increases the averaged power delivery efficiency but emphasizes E-mode in the early pulse.

In Chapter 5, results from a computational investigation regarding power transition with impedance matching network (IMN) and frequency tuning are discussed. This investigation is conducted on a pure Ar plasma sustained in a 5 kHz pulsed power. The reactor used is the ICP reactor ICAROS, designed in North Carolina State University, Dr. Shannon's group. The values of the circuit components used in the IMN are first analytically calculated to match the impedance of the load to the impedance of the power supply. The IMN is then fixed according to this result to match the impedance at certain point in a pulse referred to as match point. The use of only the IMN for impedance match is referred to as set-point matching. A real-time impedance matching technique, frequency tuning, is applied along with set-point matching to further optimize the impedance matching through the entire pulse and provides optimal power transition. Impedance matching in early pulse is found vital for the plasma ignition, which is difficult if there is severe impedance mismatch in the early stage of a pulse. Frequency tuning becomes necessary when plasma operates away from the match point for long periods of time.

In Chapter 6, the results of a computational investigation on a triple-frequency CCP (TF-

CCP) sustained in Ar/CF$_4$/O$_2$ gas mixture are discussed. The pressure being 10s mTorr, and the gap length between the electrode is 2-5 cm. Three power sources are connected to two electrodes: 80 MHz 500 W on the top electrode, and 10 MHz and 5 MHz power on the bottom electrode with 400 W on each frequency. All the power sources are controlled independently. The 80 MHz power has been found to predominantly control the plasma density. Increasing the power from 80 MHz power source is much more effective in raising the n_e than increasing power on low frequencies. A more lifted high-energy tail of the electron energy distribution function (EEDF) can be observed near the top electrode than near the substrate, even though the power is lower from the 80 MHz power source compared with the total power from the low frequencies. Increasing high frequency signifies the stochastic heating, and this weakens the local electrostatic effect on the edge of the wafer, and improves the plasma uniformity.

In Chapter 7, results are discussed from an integrated investigation from both reactor- and feature-scale simulations on SiO$_2$ atomic layer deposition. The deposition is performed in a CCP reactor and the process consists of two steps: precursor dosing, and plasma exposure. An Ar/O$_2$ plasma is used during the plasma exposure to oxidizing the precursors adsorbed on the surface during precursor dosing. The pressure in the reactor is several Torr in both steps. And the power of 100s W is used to generate the oxygen plasma. Varying pressure has been found to be more effective in affecting SiO$_2$ film properties than varying power. High pressure creates a collisional sheath, therefore reducing ion bombardment damage on the film. When depositing in a trench or a via structure, conduction limit hinders the oxidation in the bottom of the feature, causing slow film growth rate and high vacancy concentration. Because compared to the other unstable oxidants (e.g., excited state O$_2$ and O$_3$), O is less subjected to conduction limit. Therefore, it predominantly determines the oxidation process in the bottom of a high AR feature.

In Chapter 8, a summary of the discussed research work is given. Some interesting future work is suggested.

1.7 Figures
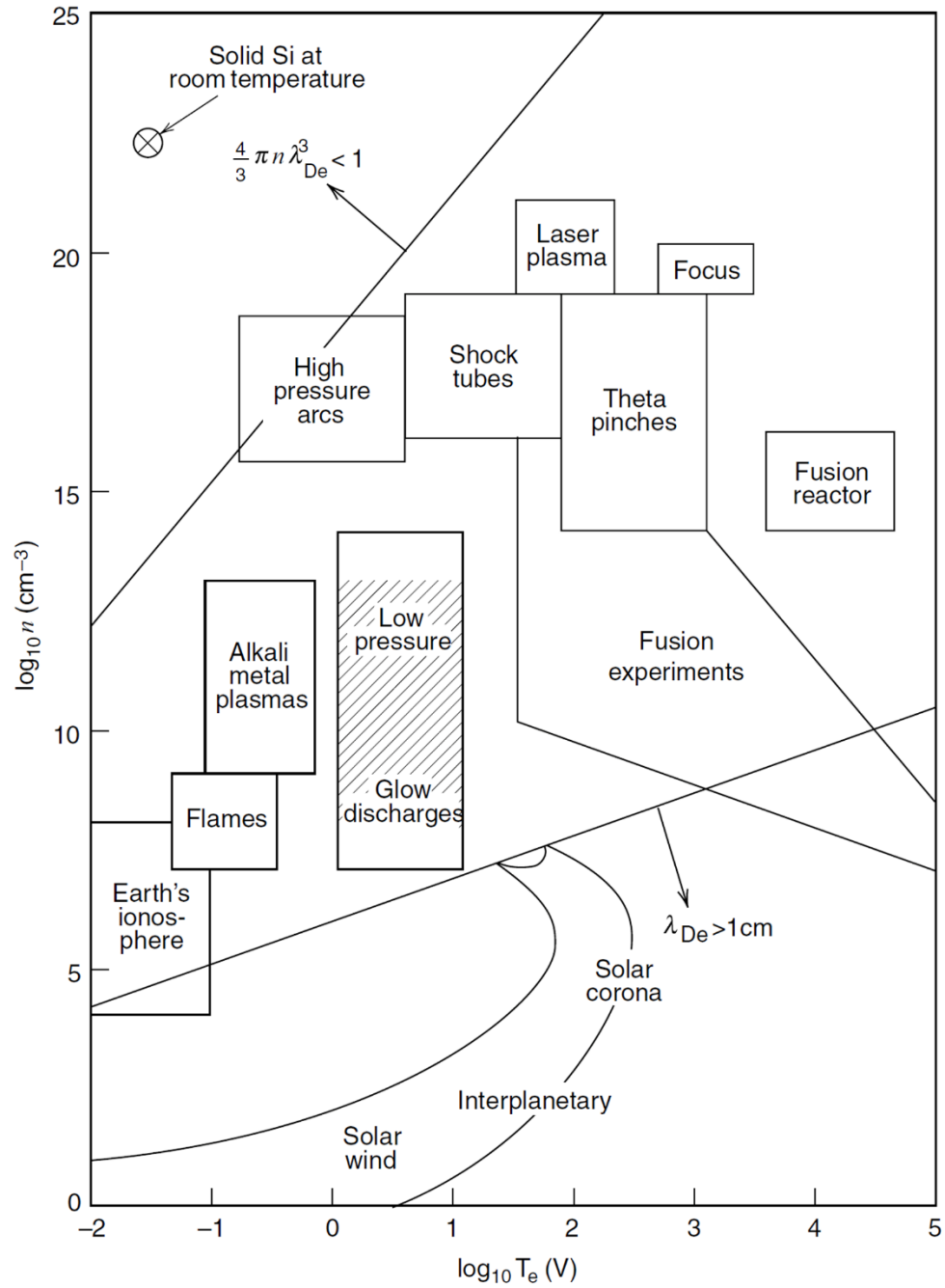
Fig. 1.1 Plasma categorized by electron density (n_e) and electron temperature (T_e). The low-temperature plasma is shadowed. Reproduced from Ref. [4].
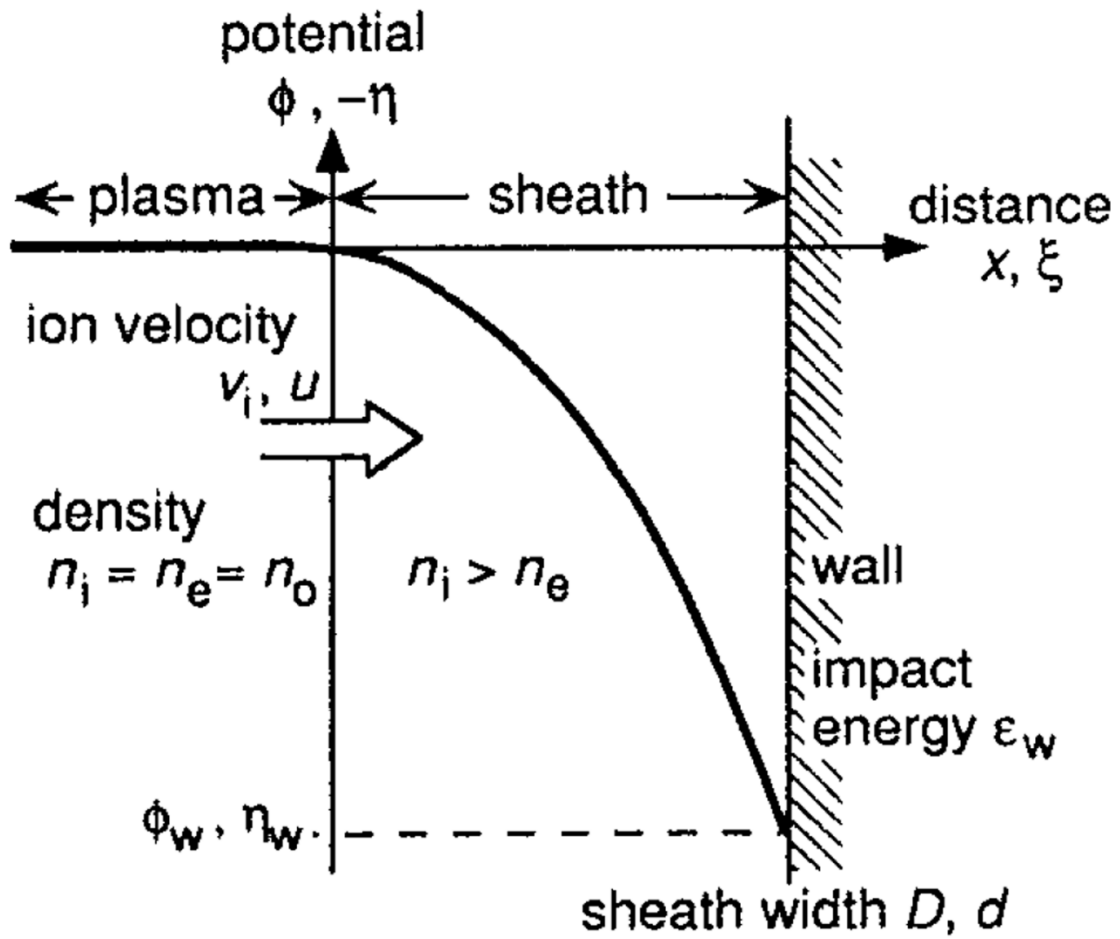
Fig. 1.2 Diagram of the sheath with potential Φ_W. Ion density (n_i) is higher than electron density (n_e) in the sheath due to the high electron temperature (T_e) and small electron mass (m_e). v_i is ion velocity on the sheath boundary. Reproduced from Ref. [10].
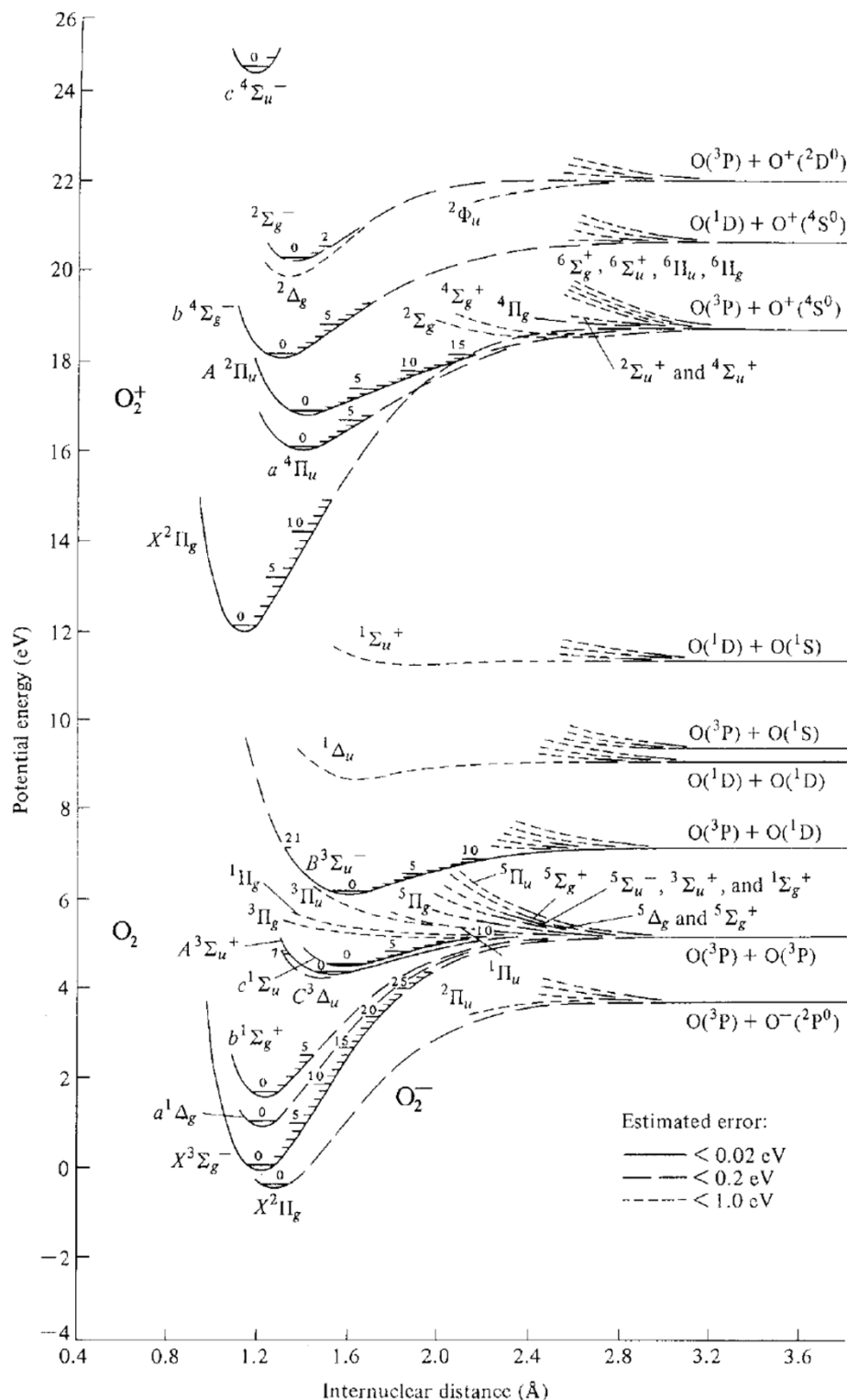
Fig. 1.3 Potential energy curves of oxygen molecule and ions. Reproduced from Ref. [11].
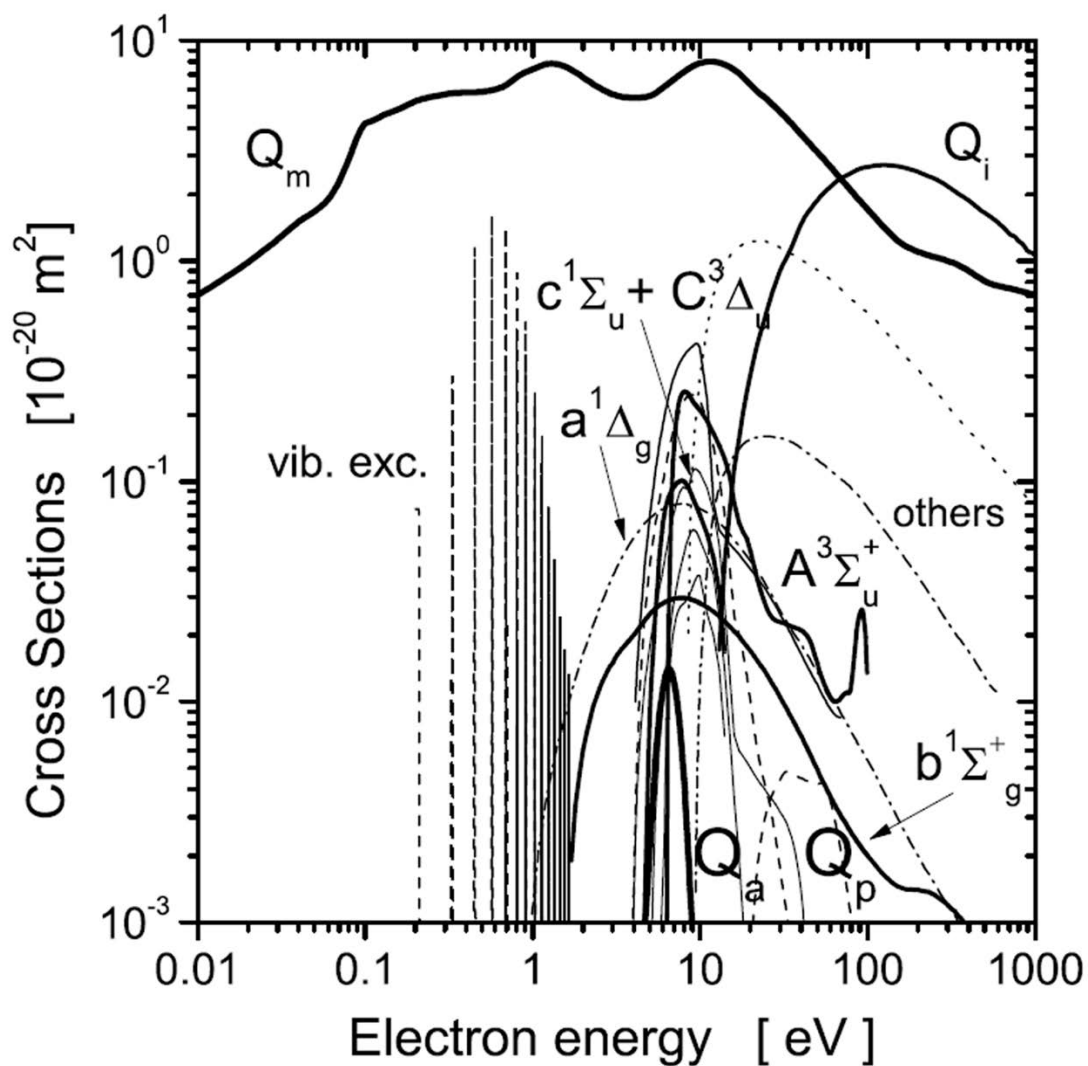
Fig. 1.4 Electron impact O_2 cross section. Q_m is momentum transfer, Q_a is attachment, Q_p is ion-pair formation, and Q_i is ionization. vib. exc. represents vibrational excitation states. Reproduced from Ref. [12].
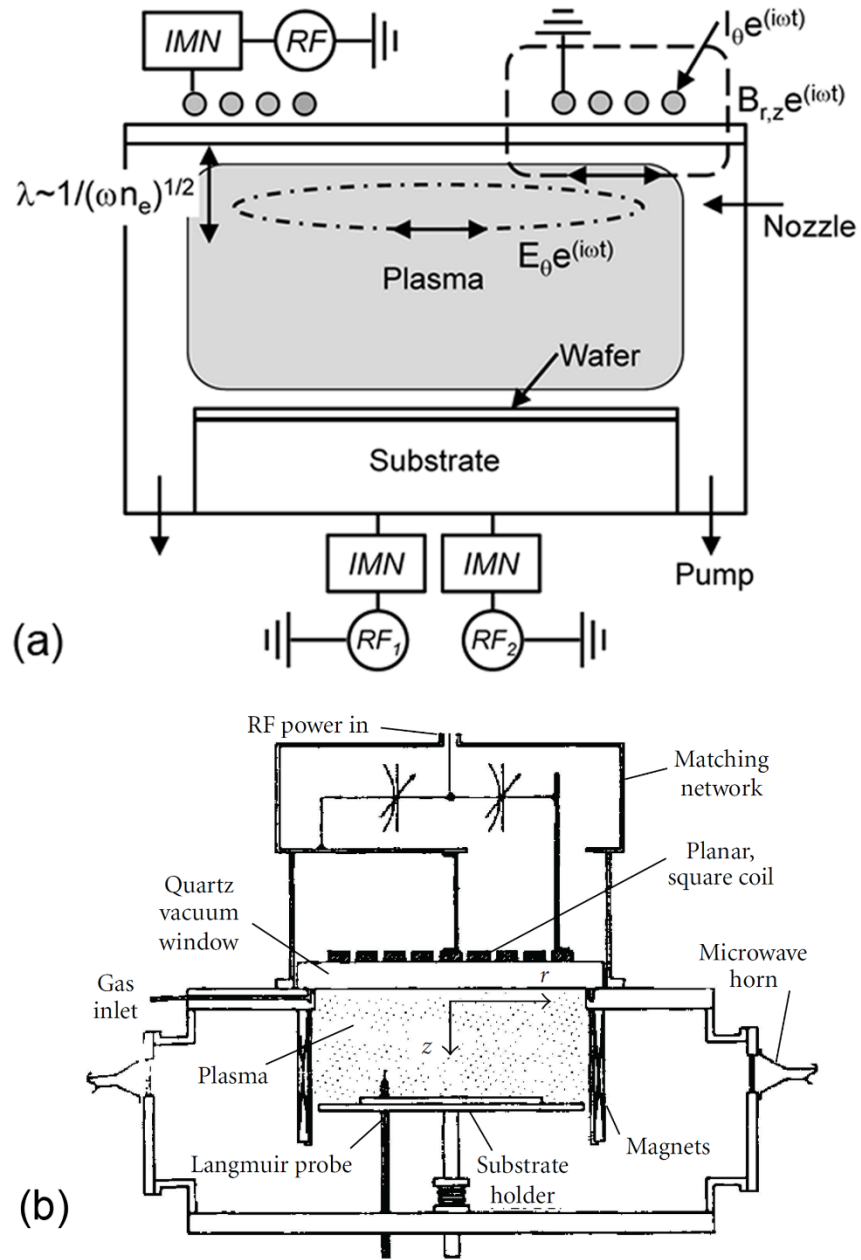
Fig. 1.5 a) An ICP reactor setup with planar coil configuration and b) one of the early ICP reactor designed at IBM. Reproduced from Ref. [13].
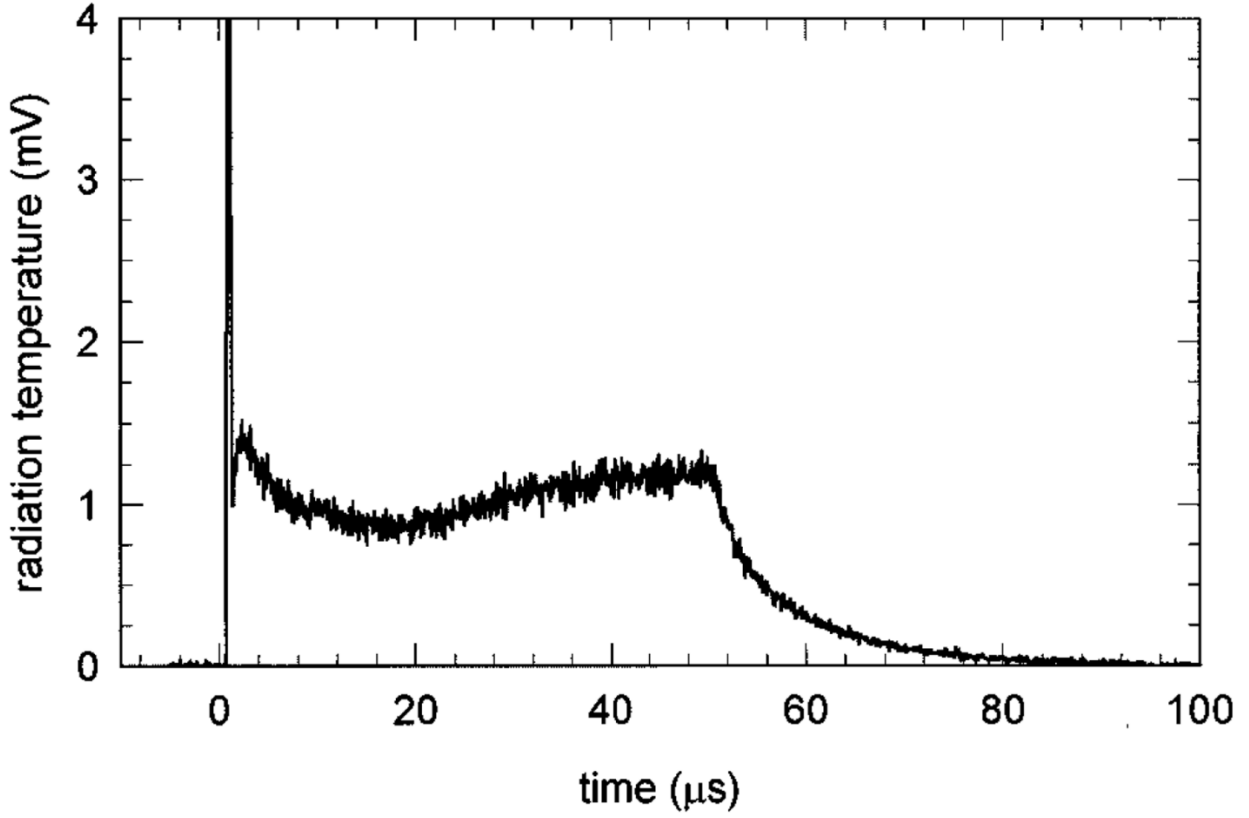
Fig. 1.6 Spike of the radiation temperature at the beginning of the pulse, representing an electron temperature (T_e) spike as high as 90-100 eV. Ar, 300 W, 20 mTorr, PRF = 100 kHz, DC = 50%. Reproduced from Ref. [21].
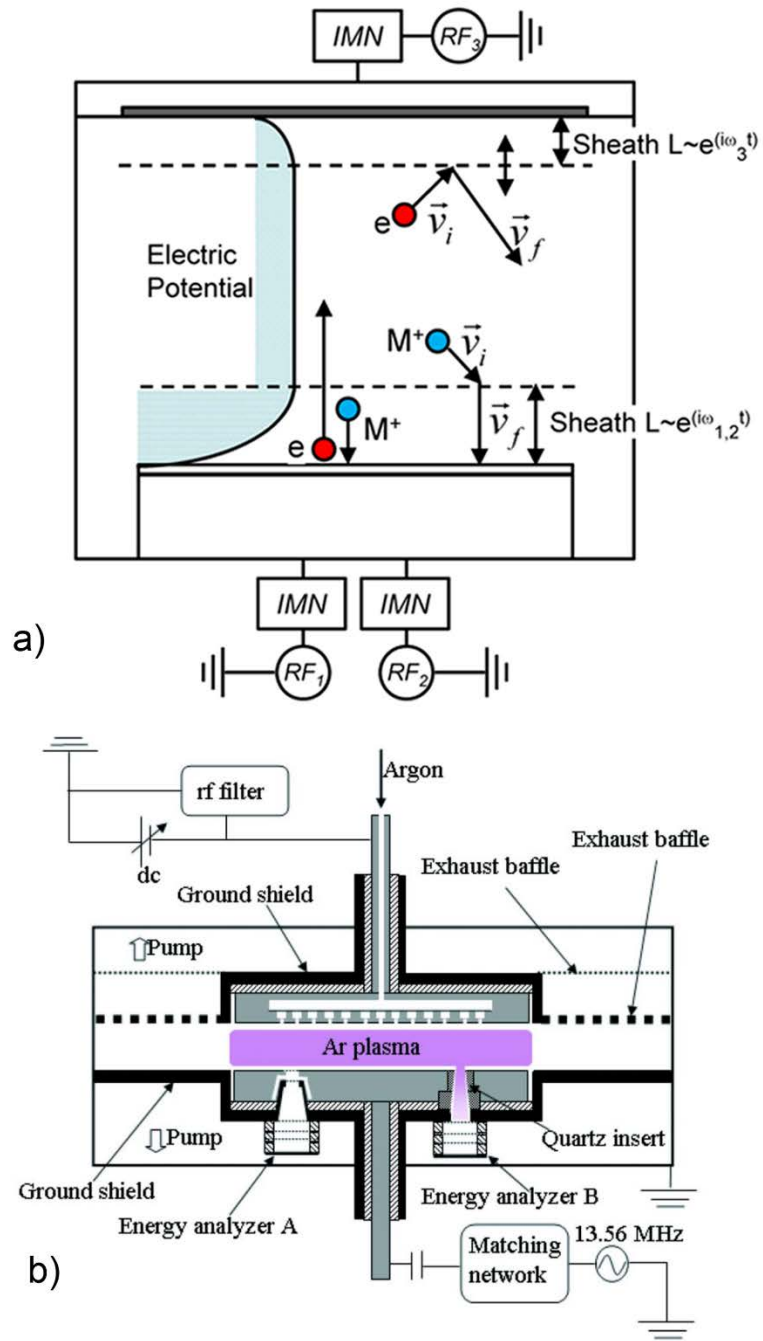
Fig. 1.7 Schematic of a) heating mechanisms in a CCP reactor and b) a CCP reactor setup in an experiment. Reproduced from Ref. [33].
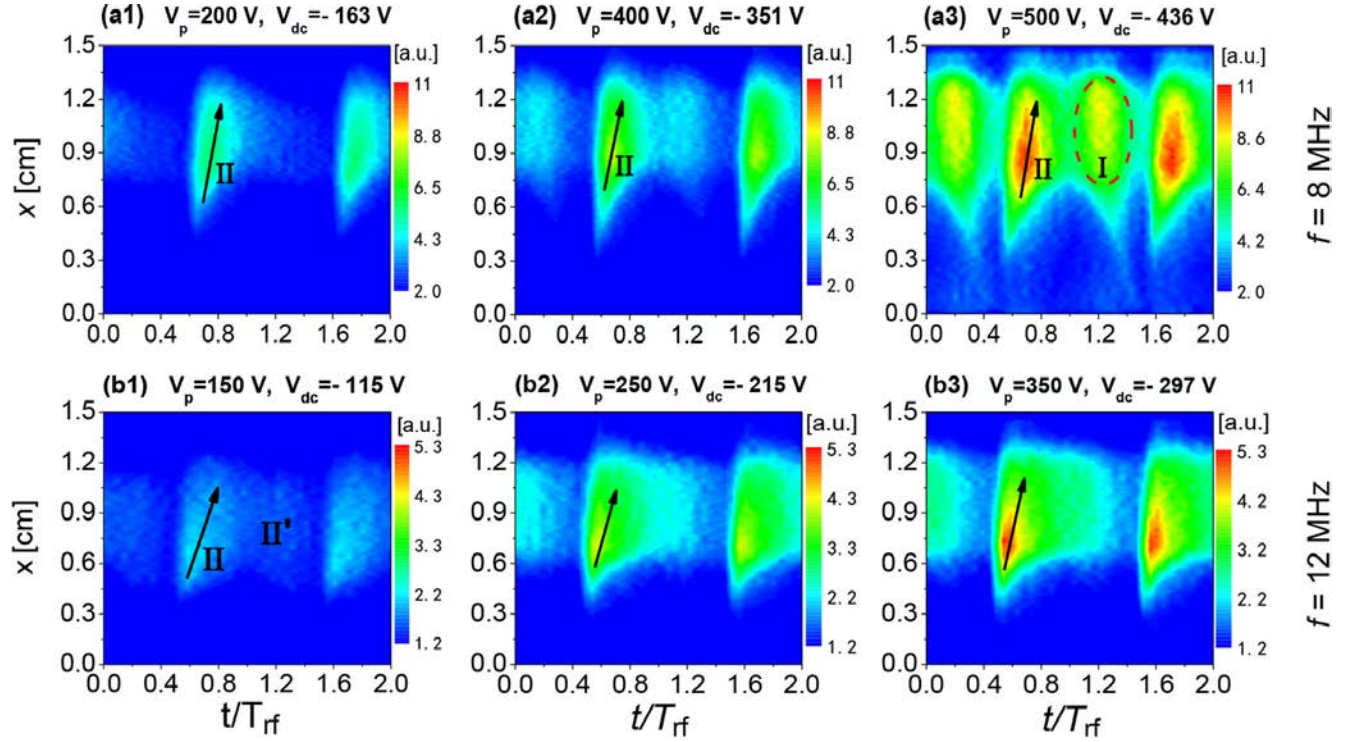
Fig. 1.8 Spatio-temporal evolutions of the electron impact excitation rate from the ground state into Ne2p$_1$ state within two RF cycles at different RF voltages for two driving frequencies, i.e. 8 MHz (first row) and 12 MHz (second row), at 50 Pa. A transition to γ-mode appears in (a3). Reproduced from Ref. [34].
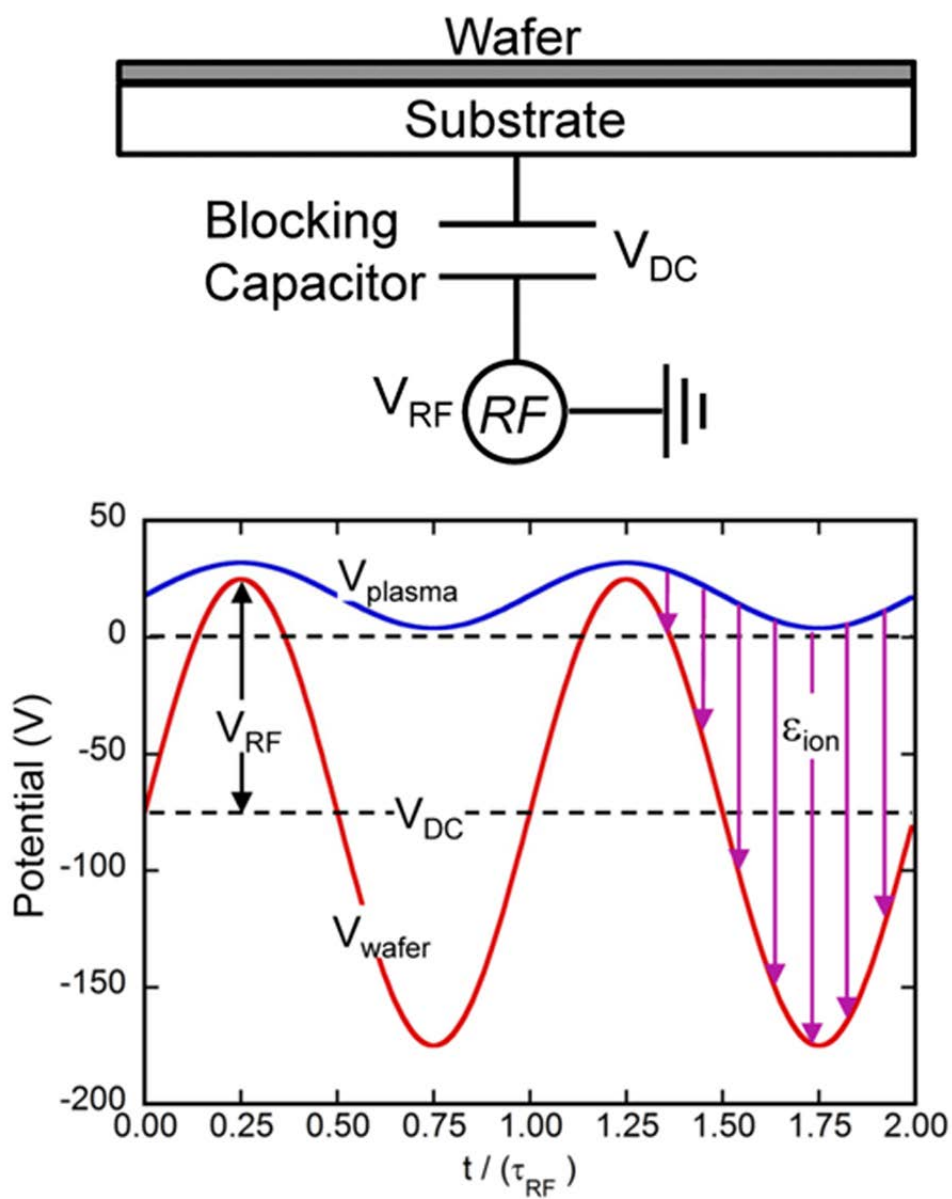
Fig. 1.9 The effect of DC-bias on the substrate potential and plasma potential in two RF periods (τ_{RF}).
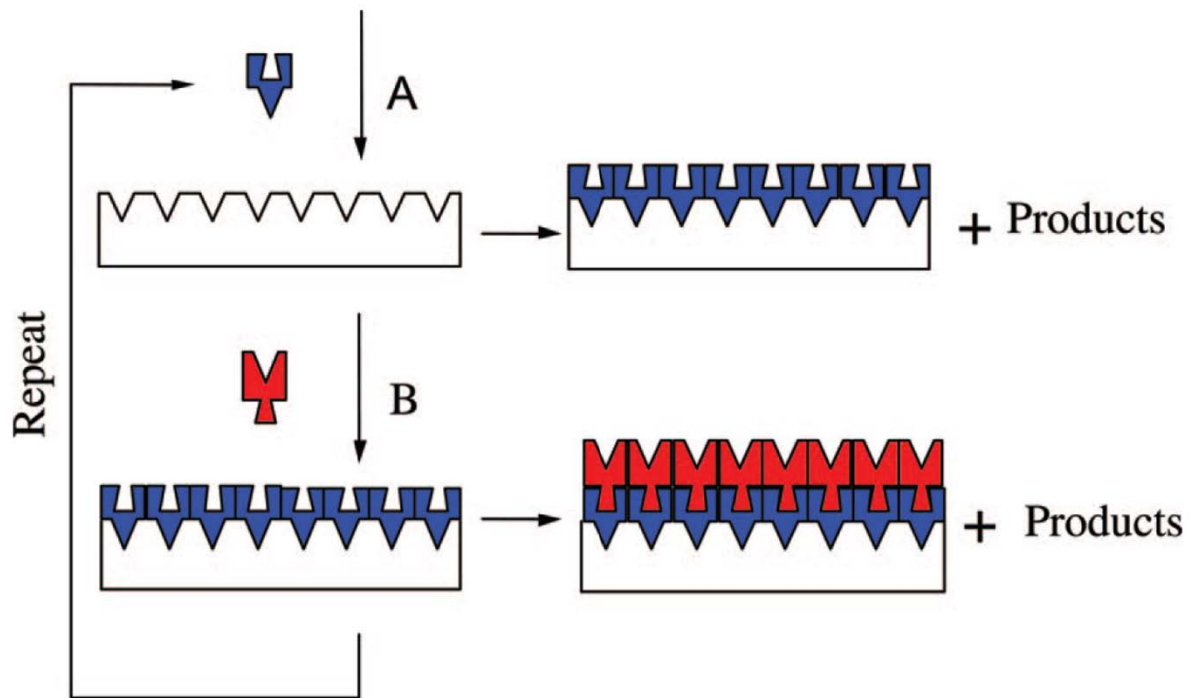
Fig. 1.10 Schematic of the AB binary sequence of ALD. The self-limiting ensures a maximum deposition rate of one mono-layer per cycle. Reproduced from Ref. [50].

1.8 References

1. F. F. Chen, Introduction to Plasma Physics and Controlled Fusion Volume 1: Plasma Physics, Plenum Press, New York (1984), p. 3.

2. J. P. Boeuf, J. Phys. D: Appl. Phys. **36**, R53 (2003).

3. A. Bogaerts, E. Neyts, R. Gijbels, and J. van der Mullen, Spectrochim. Acta Part B **57**, 609-658 (2002).

4. M. A. Lieberman and A. J. Lichtenberg, Principles of Plasma Discharges and Materials Processing 2nd Edition, John Wiley & Sons, New Jersey (2005), p. 9.

5. I. Adamovich et. al., J. Phys. D: Appl. Phys. **50**, 323001 (2017).

6. T. Makabe and Z. L. Petrovic, Plasma Electronics: Applications in Microelectronics Device Fabrication 2nd Edition, CRC Press, Boca Raton (2014), p. 3.

7. R. R. Schaller, IEEE Spectrum **34**, 52 (1997).

8. B. Wu, A. Kumar, and S. Pamarthy, J. Appl. Phys. **108**, 051101 (2010).

9. H. C. M. Knoops, T. Faraz, K. Arts, and W. M. M. Kessels, J. Vac. Sci. Technol. A **37**, 030902 (2019).

10. T. E. Sheridan and J. Goree, Phys. Fluids B **3**(10), 2796 (1991).

11. Jeffery I. Steinfeld, Molecules and Radiation: An Introduction to Modern Molecular Spectroscopy, 2d ed. © MIT Press, 1985.

12. S. Dujko, R. D. White, Z. L. Petrovic and R. E. Robson, Plasma Sources Sci. Technol. **20**, 024013 (2011).

13. J. Hopewood, C. R. Guarnieri, S. J. Whitehair, and J. J. Cuomo, J. Vac. Sci. Technol. A **11**, 152 (1993).

14. F. Soberón, F. G. Marro, W. G. Graham, A. R. Ellingboe, and V. J. Law, Plasma Sources Sci. Technol. **15**, 193-203 (2006).

15. D. Sudhir, M. Bandyopadhyay, W. Kraus, A. Gahlaut, G. Bansal, and A. Chakraborty, Rev. Sci. Instrum. **85**, 013510 (2014).

16. T. Ma, T. List, and V. M. Donnelly, J. Vac. Sci. Technol. A **36**, 031305 (2018).

17. E Despiau-Pujo, M. Brihoum, P. Bodart, M. Darnon, and G. Cunge, J. Phys. D: Appl. Phys. **47**, 455201 (2014).

18. J. P. Booth, H. Abada, P. Chabert, and D. B. Graves, Plasma Sources Sci. Technol. **14**, 273 (2005).

19. C. Petit-Etienne, E. Pargon, S. David, M. Darnon, L. Vallier, O. Joubert, and S. Banna, J. Vac. Sci. Technol. B **30**, 040604 (2012).

20. S. Banna et al., IEEE Trans. Plasma Sci. **37**, 1730 (2009).

21. G. A. Hebner, and C. B. Fleddermann, J. Appl. Phys. **82**, 2814 (1997).

22. B. Ramamurthi, and D. J. Economou, J. Vac. Sci. Technol. A **20**, 467 (2002).

23. M. Darnon, G. Cunge, and N. S. J. Braithwaite, Plasma Sources Sci. Technol. 23, 025002 (2015).

24. T. Gans, M. Osiac, D. O'Connell, V. A. Kadetov, U. Czarnetzki, T. Schwarz-Selinger, H. Halfmann, and P. Awakowics, Plasma Phys. Control. Fusion **47**, A353 (2005).

25. G. Cunge, B. Crowley, D. Vender, and M. M. Turner, Plasma Sources Sci. Technol. **8**, 576 (1999).

26. M. Lee, and C. Chung, Plasma Sources Sci. Technol. **19**, 015011 (2010).

27. M. M. Turner, and M. A. Lieberman, Plasma Sources Sci. Technol. 8, 313 (1999).

28. M.Lee, and C. Chung, Phys. Plasmas **13**, 063510 (2006).

29. A. M. Daltrini, S. A. Moshkalev, T. J. Morgan, R. B. Piejak, and W. G. Graham, Appl. Phys. Lett. **92**, 061504 (2008).

30. E. Kawamura, M. A. Lieberman, A. J. Lichtenberg, and D. B. Graves, Plasma Sources Sci. Technol. **21**, 045014 (2012).

31. T. List, T. Ma, P. Arora, V. M. Donnelly, and S. Shannon, Plasma Sources Sci. Technol. **28**, 025005 (2019).

32. S. V. Singh, and C. Pargmann, J. Appl. Phys. **104**, 083303 (2008).

33. L. Xu, L. Chen, M. Funk, A. Ranjan, M. Hummel, R. Bravenec, R. Sundararajan, D. J. Economou, and V. M. Donnelly, Appl. Phys. Lett. **93**, 261502 (2008).

34. G.-H. Liu, Y.-X. Liu, L.-S. Bai, K. Zhao, and Y.-N. Wang, Phys. Plasmas **25**, 023515 (2018)

35. J. Schulze, Z. Donkó, D. Luggenhölscher, and U. Czarnetzki, Plasma Sources Sci. Technol. **18**, 034011 (2009).

36. S. Y. Moon, J. K. Rhee, D. B. Kim, and W. Choe, Phys. Plasmas **13**, 033502 (2006).

37. S. Kechkar, P. Swift, S. Kelly, S. Kumar, S. Daniels, and M. Turner, Plasma Sources Sci. Techno. **26**, 065009 (2017).

38. D. O'Connell, T. Gans, E. Semmler, and P. Awakowicz, Applied Physics Letters, **93**(8), 081502 (2008).

39. P. C. Boyle, A. R. Ellingboe, and M. M. Turner, J. Phys. D: Appl. Phys. **37** 697 (2004).

40. K. Denpoh, Jpn. J. Appl. Phys. **53**, 080304 (2014).

41. V. Georgieva, A. Bogaerts, and R. Gijbels, Physical Review E **69**, 026406 (2004).

42. B. G. Heil. U. Czarnetzki, R. P. Brinkmann, and T. Mussenbrock, J. Phys. D: Appl. Phys. **41**, 165202 (2008).

43. B. B. Sahu, and J. G. Han, Physics of Plasmas **23**, 053514 (2016).

44. P. Diomede, D. J. Economou, T. Lafleur, J. P. Booth, and S. Longo, Plasma Sources Sci. Technol. **23**, 065049 (2014).

45. D. G. Voloshin, Y. A. Mankelevich, O. V. Proshina, and T. V. Rakhimova, Plasma Process. Polym. **14**, 1600119 (2017).

46. P. Saikia, H. Bhuyan, M. Escalona, M. Favre, B. Bora, M. Kakati, E. Wyndham, R. S. Rawat, and J. Schulze, J. Appl. Phys. **123**, 183303 (2018).

47. S. Sharma, S. K. Mishra, P. K. Kaw, and M. M. Turner, Phys. Plasmas **24**, 013509 (2017).

48. M. Belyansky, Handbook of Thin Film Deposition 4ᵗʰ edition, Elsevier (2018), ch. 8.

49. S. M. George, Chem. Rev. **110**, 111-131, (2010).

50. S. M. George, A. W. Ott, and J. W. Klaus, J. Phys. Chem. **100**, 13121 (1996).

51. R. W. Johnson, A. Hultqvist, and S. F. Bent, Materi. Today **17**, 236 (2014).

52. D. M. Hausmann, E. Kim, J. Becker, and R. G. Gordon, Chem. Mater. **14**, 4350 (2002).

53. F. Boehler, D. H. Triyoso, I. Hussain, B. Antonioli, and K. Hempel, Phys. Status Solidi C **11**, 73 (2014).

54. R. A. Ovanesyan, D. M. Hausmann, and S. Agarwal, J. Vac. Sci. Technol. A **35**, 021506 (2017).

55. S. W. Lee, K. Park, B. Han, S. H. Son, S. K. Rha, C. O. Park, and W. J. Lee, Electrochem. Solid-State Lett. **11**, G23 (2008).

56. A. Kobayashi, N. Tsuji, A. Fukazawa, and N. Kobayashi, Thin Solid Films **520**, 3994 (2012).

57. M. Putkonen, M. Bosund, O. M. E. Ylivaara, R. L. Puurunen, L. Kilpi, et al., Thin Solid Films **558**, 93 (2014).

58. M. Gebhard et. al., ACS Appl. Mater. Interfaces **10**, 7422 (2018).

59. Z. Zhu, P. Sippola, O. M. E. Ylivaara, C. Modanese, M. D. Sabatino, K. Mizohata, S. Merdes, H. Lipsanen, and H. Savin, Nanoscale Res. Lett. **14**, 55 (2019).

60. Y.-S. Lee, J.-H. Han, J.-S. Park, and J. Park, J. Vac. Sci. Technol. A **35**, 041508 (2017).

61. Y.-C. Jeong, S. B. Baek, D.-H. Kim, J.-S. Kim, and Y. C. Kim, Appl. Surf. Sci. **280**, 207 (2013).

62. K.-M. Jeon. J.-S. Shin, J.-Y. Yun, S. J. Lee, and S. W. Kang, J. Vac. Sci. Technol. A **32**, 031511 (2014).

63. A. Mallikarjunan, H. Chandra, M. Xiao, X. Lei, R. M. Pearlstein, H. R. Bowen, M. L. O'Neill, A. Derecskei-Kovacs, and B. Han, J. Vac. Sci. Technol. A **33**, 01A137 (2015)

64. M. Putkonen et. al. Thin Solid Films **558**, 93 (2014).

65. B. B. Burton, S. W. Kang, S. W. Rhee, and S. M. George, J. Phys. Chem. C **113**, 8249 (2009).

66. D. J. Economou, Plasma Process. Polym. **14**, 1600152 (2017).

67. E. Kawamura, M. A. Lieberman, A. J. Lichtenberg, and P. Chabert, J. Vac. Sci. Technol. A **38**, 023003 (2020).

68. Y.-X. Liu, E. Schüngel, I. Korolov, Z. Donkó, Y.-N. Wang, and J. Schulze, Phys. Rev. Lett. **116**, 255002 (2016).

69. M. J. Kushner, J. Phys. D: Appl. Phys. **42**, 194013 (2009).

70. H. C. Kim, F. Iza, S. S. Yang, M. Radmilović-Radjenović, and J. K. Lee, J. Phys. D: Appl. Phys. **38**, R283 (2005).

71. R. Schneider, Phys. Scr. **T124**, 76 (2006).

72. N. Degtyarenko, and A. Pisarev, Phys. Procedia **71**, 30 (2015).

73. S. Rauf, T. Sparks, and P. L. G. Ventzek, J. Appl. Phys. **101**, 033308 (2007).

74. E. C. Neyts, and P. Brault, Plasma Process. Polym. **14**, 1600145 (2017).

75. W. Guo, and H. H. Sawin, J. Phys. D: Appl. Phys. **42**, 194014 (2017).

Chapter 2: Description of the Models

The modeling of Low Temperature Plasmas provides insight into the minute physics that occurs during material processing. This makes a physics-based plasma model an essential tool in the early stage of reactor and process design. In this thesis, two plasma models were used: the Hybrid Plasma Equipment Model (HPEM), and the Monte Carlo Feature Profile Model (MCFPM). A detailed description of the HPEM is provided in this chapter, followed by a brief overview of the MCFPM.

2.1 Hybrid Plasma Equipment Model

The HPEM hybrid model contains several modules [1]. Each module addresses one area of the LTP physics hierarchically interacting with other modules. The modules that are used for the simulation in this thesis are Electromagnetics Module (EMM), Electron Energy Transport Module (EETM), Fluid Kinetics Poisson Module (FKPM), and Plasma Chemistry Monte Carlo Module (PCMCM). A schematic of the HPEM is given in Fig. 2.1. The simulation starts with an estimation of the densities of various species and their distribution. This provides the initial conductivity of the plasma to the EMM.

The EMM module calculates the electromagnetic fields $\vec{E}(\vec{r}, \varphi)$ and $\vec{B}(\vec{r}, \varphi)$ produced by antenna in materials and the plasma, where $\vec{r}$ is the spatial dependency and φ is the time dependency. A circuit model is used to represent the impedance matching network. This circuit model can capture various properties such as power reflection. The EM field calculated in the

EMM is transferred to the Electron Energy Transport Module (EETM). In the EETM, the behavior of the electrons is attained kinetically using a Monte Carlo simulation. The electron impact reaction rates $k(\vec{r},\varphi)$ and the electron impact source terms $S(\vec{r},\varphi)$ are then calculated and transferred to the Fluid Kinetics Poisson Module (FKPM). Within the FKPM, the densities $N(\vec{r})$, velocities $\vec{v}(\vec{r})$, and the temperatures $T(\vec{r})$ of the heavy particles are produced. The heavy particle reaction rate coefficients and source functions are also generated in this module. With the information for charge densities in the plasma and on the materials, Poisson's equation is solved in the FKPM, and this provides the electrostatic electric field $\overrightarrow{E_s}(\vec{r},\varphi)$ and the plasma potential $\Phi_P(\vec{r},\varphi)$. The electrostatic E-field and ionization sources are passed to the Plasma Chemistry Monte Carlo Module (PCMCM), where the pseudoparticles of ions and neutrals are launched and tracked using the Monte Carlo approach. The energy and angular distributions (EADs) of the heavy particles and electrons are logged on certain surfaces in the PCMCM.

In the HPEM, modules are coupled using a time-slicing technique. When performing a simulation, the evolution of the plasma is captured by executing modules with a unit of a global iteration. During each global iteration, modules are called and variables are updated with different time steps. For example, in a μs global iteration, FKPM is operated once, with several updates of electron impact reaction rates $k(\vec{r},\varphi)$ from EETM. This technique enables simulation in longer time scale without sacrificing much accuracy.

2.1.1 Electromagnetics Module (EMM)

The inductively coupled electromagnetic field is calculated in the EMM using the frequency-domain Maxwell's equations. The time-varying electric field $\vec{E}$ is obtained by solving the following wave equation using the finite difference method

$$-\nabla(\frac{1}{\mu}\nabla \cdot \vec{E}) + \nabla \cdot (\frac{1}{\mu}\nabla \vec{E}) = \omega^2 \varepsilon^2 \vec{E} + i\omega(\vec{j}_{coil} + \overline{\overline{\sigma}} \cdot \vec{E}), \qquad (2.1)$$

where μ is the permeability, ε is the permittivity, ω is the radian frequency of the applied power, and i is the imaginary unit. The last term $\vec{j}_{coil}$ represents the conduction current in the coil and $\overline{\overline{\sigma}} \cdot \vec{E}$ is the conduction current from the plasma. The $\overline{\overline{\sigma}}$ is the conductivity tensor with the form:

$$\overline{\overline{\sigma}} = \frac{\sigma_0}{(\alpha^2 + |B|^2)} \times \begin{pmatrix} \alpha^2 B_r^2 & \alpha B_z + B_r B_\theta & -\alpha B_\theta + B_r B_z \\ -\alpha B_z + B_r B_\theta & \alpha^2 + B_\theta^2 & \alpha B_r + B_\theta B_z \\ \alpha B_\theta + B_r B_z & -\alpha B_r + B_\theta B_z & \alpha^2 + B_z^2 \end{pmatrix}, \qquad (2.2)$$

where

$$\sigma_0 = \frac{e^2 n_e}{m_e} \frac{1}{v_m + i\omega}, \qquad (2.3)$$

$$\alpha = \frac{m_e}{e}(v_m + i\omega), \qquad (2.4)$$

B is the static magnetic field, n_e is the electron density, m_e is the electron mass, e is the elementary charge, and v_m is the electron momentum collision frequency [2]. For a simulation of the inductively coupled plasma, the electromagnetic field is calculated in the EMM as a function of position and phase in an RF period. Because no static magnetic field is used regarding the work in this thesis, the conductivity is isotropic and equals σ_0. Using the electric field calculated by Eq. (2.1), the magnetic field is derived as:

$$\vec{B} = (i/\omega)\nabla \times \vec{E}, \qquad (2.5)$$

Assuming the collisional power deposition through the azimuthal electric field, this electric field from Eq. (2.1) is then normalized to provide desired power through $\vec{j}_e \cdot \vec{E}$.

The EMM also contains a circuit model with which the power supply is interfaced to the plasma reactor. A schematic of the circuit representation of the impedance matching network,

antenna, reactor, and plasma is in Fig. 2.2. The antenna is modeled as a discretized transmission line. The geometry of the antenna determines its inductance. This inductance depends on the overall diameter, height, number of turns, and the thickness of the wire. It is divided into 100 discrete series segments, each of which has an appropriate fraction of the total resistance of the antenna. Each segment contains a series impedance, Z_{Sn}, consisting of the resistance (R_{An}) and physical inductance (L_{An}) of the antenna. The impedance Z_{Sn} also contains transformed values of resistance and inductance from the plasma [3]. The transformed impedance of the plasma, Z_T, is [4]

$$Z_T = \left(\frac{\omega M}{Z_P} \right)^2 \left(-i\omega L_P + R_P \left(1 - i\frac{\omega}{v_m} \right) \right), \quad M^2 = k_A L_A L_P , \tag{2.6}$$

$$Z_P^2 = \left(\omega L_P + \frac{\omega}{v_m} R_P \right)^2 + R_P^{\ 2} , \tag{2.7}$$

where R_P is the plasma resistance, k_A is the antenna transformer coupling coefficient, L_A and L_P are the inductance of the coil and plasma, respectively. The effective plasma resistance R_P was given by

$$R_P = \frac{\int \vec{j}_\theta \cdot \vec{E}_\theta \, d^3 r}{\left(\int \vec{j}_\theta \cdot d\vec{A} \right)^2} , \tag{2.8}$$

The numerator is the volume integrated inductively coupled power, and the denominator is the area integrated azimuthal current. The consequences of the skin depth and the nonlinearities in the plasma are accounted for by including the spatial dependence and phase differences between the current and the electric field.

From each discrete segment of the transmission line representation of the antenna, an impedance Z_{Cn} is implemented to represent the capacitance and series resistance directed to the

ground. This impedance is the capacitive coupling from the antenna. The reactance of Z_{Cn} consists dominantly of the series capacitances of the air gap between the antenna and dielectric window of the ICP reactor, the window, and the plasma sheath at the surface of the window. The resistance of Z_{Cn} results from the capacitively coupled conduction current flowing to the ground. The impedance of each element Z_k is calculated during the execution of FKPM. A brief description of the calculation of Z_k is provided as follows.

For each turn k of the antenna, the voltage amplitude V_{ok} and phase ϕ_{Vk} are determined from the circuit model. The voltage $V_k(t) = \text{Re}\left(V_{ok}\exp\left(i\left(\omega t + \varphi_{Vk}\right)\right)\right) = V_{ok}\cos\left(\omega t + \varphi_{Vk}\right)$ is used as the boundary condition for solving Poisson's equation. The displacement current flowing out of each turn of the coil is logged as

$$I_k(t) = \int \varepsilon_0 \frac{d\left(\vec{E}(t)\cdot\hat{n}\right)}{dt} dA , \tag{2.9}$$

where $\hat{n}$ is the normal vector of the coil surface, $\vec{E}(t)$ is the time-varying electric field obtained by solving Poisson's equation, and A is the surface area of the coil. The current $I_k(t)$ is then Fourier transformed to provide frequency-domain current with an amplitude I_{ok} and phase φ_{Ik}. The impedance is then

$$Z_k = \frac{V_{ok}}{I_{ok}}\exp\left(i\left(\varphi_{Vk} - \varphi_{Ik}\right)\right), \tag{2.10}$$

For pure H-mode, nearly all the power is coupled to the plasma inductively. The phase difference between the voltage and current, $(\varphi_{Vk} - \varphi_{Ik})$, is approaching 90°. For E-mode, when a finite amount of power is capacitively coupled to the plasma, the phase difference is $(\varphi_{Vk} - \varphi_{Ik}) \in (-90°, 0°)$. The value of Z_k is distributed to the transmission line segments in the

circuit model, meaning each Z_{Cn} is a fraction of the total impedance Z_k. The cycle-averaged capacitively coupled power is

$$P_c = \sum_k P_k = \sum_k \frac{1}{\tau_{rf}} \iint \varepsilon_0 V_k(t) \frac{d\left(\vec{E}(t)\cdot\hat{n}\right)}{dt} dAdt,$$ (2.11)

where τ_{rf} is the RF period. The circuit model also produces P_A (resistive losses in the antenna coils), P_M (resistive losses in the matchbox) and Z_M, the input impedance to the impedance matching network. The power dissipated by the inductive power coupling is

$$P_I = \int \frac{1}{2} \sigma(\vec{r}) E_\theta^2(\vec{r}) d^3r,$$ (2.12)

With Z_M, the electric field reflection coefficient is calculated as

$$\Gamma = \frac{Z_M - Z_0}{Z_M + Z_0},$$ (2.13)

The total power deposited in the system is

$$P_T = \left(1 - |\Gamma|^2\right) P_S = P_M + P_A + P_I + P_C,$$ (2.14)

where P_A is the resistive power dissipated in the antenna, and P_M is the resistive power dissipated in the impedance matching network. Recognizing that E_θ scales linearly with the antenna current and P_I scales with E_θ^2, the current flowing into the impedance matching network is renormalized so that Eq. (2.14) is satisfied. With the renormalized values, the circuit and wave-equations are again solved. This process is iterated several thousand times till convergence. The final values of V_k, E_θ and φ are returned to the FKPM for the next iteration for time integration of the fluid equations for densities, momenta, and energy.

For a perfect match of the P_S, $Z_M = Z_0$. In the HPEM, matching is produced by adjusting C_P and C_S such that $\text{Re}(Z_M) = Z_0$ and $\text{Im}(Z_M) = 0$. Typically, Z_0 is 50 Ω based on the industrial

standard. From a procedural perspective, C_P and C_S can be repeatedly tested to minimize the value of Γ. However, one can analytically compute Z_M based on the circuit values and plasma conditions, and solve for the values of C_P and C_S that produce the match. The solutions of C_P and C_S depend on the design of the IMN, details for solving C_P and C_S are provided in the Appendix.

Finding the impedance match can be accomplished through adjusting the matching circuit though it can also be done by varying the operating RF frequency. In the HPEM, this approach is accessible through fixing the IMN and performing a frequency sweep. The impedance of the load is then updated and the reflection coefficient is calculated for each frequency. The frequency that provides the smallest reflection is then chosen as the new operating frequency until the fractional variation of the load impedance is higher than the user defined threshold. Finally the frequency sweep will be performed again and the operating frequency will be updated.

2.1.2 Electron Energy Transport Module (EETM)

The EETM calculates the rate coefficient from electron impact reactions $k(\vec{r}, \varphi)$ and corresponding source function $S(\vec{r}, \varphi)$ by using the electromagnetic fields $\vec{E}(\vec{r}, \varphi)$, $\vec{B}(\vec{r}, \varphi)$ provided by EMM, and the electrostatic electric field $\vec{E}_S(\vec{r}, \varphi)$, as well as heavy particle densities $N(\vec{r})$ provided by the FKPM. The EETM then obtains the electron properties by using the electron Monte Carlo Simulation (eMCS) to compute electron energy distribution functions (EEDFs). Another method for attaining the electron properties is by solving the electron energy equation, which is performed in the FKPM. In any case, secondary electron emission caused by

heavy particle bombardments on surfaces exposed to the plasma are always addressed using the eMCS.

The eMCS is a fully kinetic approach to resolving the electron dynamics. The pseudoparticles representing the electrons are initially released with random velocities following a Maxwellian distribution. The positions chosen for the electrons are weighted by the electron densities in different parts of the reactor. The governing equation for the electron dynamics is the Lorentz equation

$$\frac{d\vec{v}_e}{dt} = \frac{e}{m_e}(\vec{E} + \vec{v}_e \times \vec{B}),$$ (2.15)

where $\vec{v}_e$ is the electron velocity and $\vec{E}$ and $\vec{B}$ are the total local electric and magnetic fields (electromagnetic and static).

The energy grid technique is applied to collect collision frequencies and the statics of the electrons. The electron energy is divided into several uneven ranges, e.g., 0-5, 5-10, 10-50, 50-300, and 300-1000 eV bearing in mind that bulk electrons typically have energy of less than 50 eV. The high energy range is used to capture the secondary electrons. These electrons are accelerated by the sheath, depending on the bias voltage and plasma potential, secondary electrons can have high energy up to several keV. Each energy section is further divided into energy bins and a collision frequency is calculated for each energy bin

$$v_i = \left(\frac{3\varepsilon_i}{m_e}\right)^{1/2} \sum_{j,k} \sigma_{ijk} N_j,$$ (2.16)

where ε_i is the average energy in bin i, σ_{ijk} is the cross-section of the species j of process k at energy ε_i, and N_j is the density of the species j. The concept of a null collision is applied in the eMCS to optimize the calculation of collision frequencies. A null collision frequency is defined

as the difference between the maximum collision rate and the real collision frequency. Because the maximum collision rate is a known parameter, including the null collision makes the total collision frequency independent of the electron velocity. Hence, the time intervals between collisions are governed merely by the probability law $\Delta t = -\ln(r)/\nu_{mj}$ [5]. The r is a random number within (0,1), and ν_{mj} is the maximum collision frequency within an energy bin j. The types of the collisions are determined by comparing the series of random numbers with the normalized collision frequencies. If the collision is found to be a null collision, no properties of the electrons are changed. Otherwise, the electron properties are updated according to the reactions that occur [6].

In the eMCS, the EEDFs are recorded to each energy bin i and spatial bin l

$$F_{il} = \sum_j w_j \delta\left[\left(\varepsilon_i \pm \frac{1}{2}\Delta\varepsilon_i\right) - \varepsilon_i\right]\delta\left[(\vec{r}_l \pm \Delta r) - \vec{r}_l\right], \tag{2.17}$$

The w_j involves the weighting of particles calculated based on the number of particles each pseudoparticle represents, the time step for updating particle trajectory, and spatial weighting. The EEDF $f_e(\varepsilon, \vec{r})$ is obtained at each spatial bin at the end of the eMCS by using

$$\sum_i F_{ij}\Delta\varepsilon_i = \sum_i f_e(\varepsilon, \vec{r})\varepsilon_i^{1/2}\Delta\varepsilon_i = 1, \tag{2.18}$$

Secondary electrons are always tracked in the method described above. Unlike bulk electrons, the secondary electrons are released perpendicular to the surface. They are no longer tracked when they strike a surface or when their energy is reduced to a value lower than the lowest excitation threshold. In the latter case, these secondary electrons are placed into a source function for bulk electrons.

The eMCS can provide highly accurate electron properties, especially when a large number of pseudoparticles are used. However, it can be computationally expensive. To ease the

computational burden, the application programming interface (API) OpenMP is used to enable parallel computing. The OpenMP is a multi-threading parallel computational platform implementing the fork-join model, as shown in Fig. 2.3 [7]. At the start of the parallel section, the master thread distributes the job to a number of slave threads. Each slave thread performs a fraction of the work and returns its results to the master thread at the end of parallel computation. Because multiple threads are working simultaneously, the parallel computation can provide up to 10 times in the speed of some simplified examples using ten threads.

The subroutines in the eMCS can be categorized into three sections: initialization subroutines (IS), particle trajectories and collisions subroutines (PS), and diagnostic and post-processing subroutines (DPS). In the eMCS, IS is called first to initialize the particle properties, followed by several repeated calls of PS. Then the DPS is called after each call of PS. Note that pseudoparticles representing electrons have no interactions with each other, making it suitable for parallel computing. The eMCS is reconstructed such that the PS is included in one big loop. In this loop, parallel computing is performed. The arrays storing the particle properties are separated by IS into several thread-aware arrays. Each array is then passed to a slave thread. By doing this, the probability of memory-sharing between the threads is significantly reduced. The properties of the pseudoparticles are then updated in the PS in the individual thread. After each PS, in the call of DPS, the thread-aware arrays are reconstructed back to their initial structure. Parallelizing the entire PS rather than each small loop in PS minimizes the computational overhead. Naturally, the speed-up is especially significant when a large number of pseudoparticles are used.

2.1.3 Fluid Kinetics Poisson Module (FKPM)

The heavy particle densities, electron energy equation and Poisson's equation are resolved in the FKPM. As an alternative to the eMCS, in the FKPM, the electron energy

distribution $f_e(\varepsilon, \vec{r}, \varphi)$ is obtained through solving the Boltzmann equation using the two-term approximation.

$$\frac{\partial f_e}{\partial t} = -\vec{v}\nabla_r f_e - \frac{e\left(\vec{E} + \vec{v}\times\vec{B}\right)}{m_e}\cdot\nabla_v f_e + \left(\frac{\partial f_e}{\partial t}\right)_{collisions}, \tag{2.19}$$

In Eq. (2.19), ∇_r is the spatial gradient, and ∇_v is the gradient in the velocity space. The last term on the right-hand side of the equation includes all the collisional terms. f_e from Eq. (2.19) are compute for a wide range of the normalized electric field (E/N), where E is the local electric field, and N is the gas density. A table of rate coefficients versus T_e is then created. This table is interpolated during execution of the code. Consequently, the electron temperature (T_e) is obtained using the equation

$$\frac{\partial(\frac{3}{2}n_e k_B T_e)}{\partial t} = \nabla\kappa\nabla T_e + \nabla\cdot(\vec{\phi}_e T_e) = P_e, \tag{2.20}$$

where k_B is the Boltzmann constant, κ is the thermal conductivity and $\vec{\phi}_e$ is the electron flux. The total power shunted to electrons is

$$P_e = \vec{j}_e\cdot\vec{E} = e\vec{\phi}_e\cdot\vec{E}, \tag{2.21}$$

There are two methods to express the electron flux: the simple drift-diffusion, and Scharfetter-Gummel (S-G) expression. The simple drift-diffusion form of the electron flux is

$$\vec{\phi}_e = e\mu_e n_e \vec{E} - D_e\nabla n_e, \tag{2.22}$$

where μ_e is electron mobility, and D_e is the electron diffusion coefficient. The S-G method is widely used to describe the transport of charged particles in the fluid model [7]. With a S-G expression, the flux between the mesh points i and $i+1$ is

$$\vec{\phi}_{i+1/2} = \frac{\alpha\bar{D}[n_{i+1} - n_i\exp(\alpha\Delta x)]}{1 - \exp(\alpha\Delta x)}, \tag{2.23}$$

with

$$\alpha = -e\bar{\mu}\left(\frac{\Phi_{i+1} - \Phi_i}{\Delta x}\right),$$ (2.24)

where $\bar{D}$ is the averaged diffusion coefficient between vertex i and $i+1$, $\bar{\mu}$ and Δx are the averaged mobility and the length of this interval, and Φ_i is the potential on vortex i.

The densities of the heavy particles are attained by solving continuity, momentum, and energy equations. For species i with a source term S_i

$$\frac{\partial N_i}{\partial t} = -\nabla \cdot \vec{\phi}_i + S_i,$$ (2.25)

$$\frac{\partial \vec{\phi}_i}{\partial t} = \frac{\partial(N_i\vec{v}_i)}{\partial t} = -\frac{1}{m_i}\nabla(kN_iT_i) - \nabla \cdot (N_i\vec{v}_i\vec{v}_i) + \frac{q_i}{m_i}N_i(\vec{E}_s + \vec{v}_i \times \vec{B})$$

$$-\nabla \cdot \bar{\bar{\mu}}_i - \sum_j \frac{m_j}{m_i + m_j}N_iN_j(\vec{v}_i - \vec{v}_j)v_{ij},$$ (2.26)

$$\frac{\partial N_i\varepsilon_i}{\partial t} = -\nabla \cdot \bar{\bar{\kappa}}\nabla T_i - p_i\nabla \cdot \vec{v}_i - \nabla \cdot (N_i\vec{v}_i\varepsilon_i) + q_i\vec{\phi}_i\vec{E} - (\bar{\bar{\mu}}_i\nabla \cdot \nabla\vec{v}_i)$$

$$-\sum_{m,j} k_{mij}N_iN_j\varepsilon_i + \sum_{m,j,l} k_{mjl}N_jN_l\Delta\varepsilon_{mjl},$$ (2.27)

where $\vec{\phi}$ is the flux, N is the density, $\vec{v}$ is the velocity, m is the mass, T is the temperature, $\bar{\bar{\mu}}$ is the viscosity, p is the pressure, and ε is the energy.

Because the charge density directly affects the electrostatic field $\vec{E}_S$, it is convenient to solve Poisson's equation in the FKPM along with the update of charged particle densities. In the HPEM, the Poisson's equation is semi-implicitly solved using linear interpolation of ion charge densities in the time domain

$$\nabla \cdot \left[\varepsilon\nabla\Phi(t + \Delta t)\right] = -\rho(t + \Delta t) = -\rho(t) - \Delta t\frac{\partial\rho}{\partial t}\bigg|_{t+\Delta t},$$ (2.28)

where ρ is the charge density. Because both the surface of a material and the plasma can hold the spatial charge, ρ is expressed as

$$\rho(t) = \rho_m(t) + \sum_i q_i N_i(t),$$ (2.29)

where the first term is the charge density from the solid material, and the second term is the charge from the plasma. q_i is the charge of ion i and N_i is the ion density. By solving Poisson's equation semi-implicitly, there is no requirement of time step Δt to be smaller than the dielectric relaxation time, which is, on the other hand, required for the explicit method [8]. If Scharfetter-Gummel fluxes are used, the $\left.\dfrac{\partial \rho}{\partial t}\right|_{t+\Delta t}$ term can be written as

$$\left.\frac{\partial \rho}{\partial t}\right|_{t+\Delta t} = \frac{\partial \rho_m(t')}{\partial t} - q_{e,j}\nabla \cdot \left(\vec{\phi}_e(t) + \frac{\partial \vec{\phi}_e}{\partial \Phi}[\Phi_s(t+\Delta t) - \Phi_s(t)] \right)$$

$$- \sum_i q_i \nabla \cdot \left(\vec{\phi}_i(t) + \frac{\Delta t}{2}\frac{\partial \vec{\phi}_i(t)}{\partial t} \right),$$ (2.30)

where $q_{e,j}$ represents the charge of electrons and ions, respectively, Φ_s is the electrostatic potential. t' means that the charge density is evaluated at the current time step t, but the potential is evaluated at the time step $t + \Delta t$.

The Jacobian term $\dfrac{\partial \vec{\phi}_e}{\partial \Phi}$ from Eq. (2.30) is numerically expressed by applying a small change of the potential, and then divide the corresponding electron flux fluctuation with this potential change. The first two terms of the partial derivative are kept as the value of $\dfrac{\partial \vec{\phi}_e}{\partial \Phi}$. Typically, the test variation $\Delta \Phi_{i,j}$ is smaller than 5% of the local potential. The numerical expression of the Jacobian term is

$$\frac{\partial \vec{\phi}_{i,j}}{\partial \Phi_{i+1,j}} = \frac{\vec{\phi}_{i,j}(\Phi_{i+1,j} + \Delta\Phi_{i+1,j}) - \vec{\phi}_{i,j}(\Phi_{i+1,j})}{\Phi_{i+1,j}},$$ (2.31)

where i and j are the coordinates of the mesh in the radial and axial direction. The equations mentioned above are solved using either Successive-Over-Relaxation or direct sparse matrix method [9,10].

The charge density is an essential component of the boundary condition. In the FKPM, the charge density on a surface is collected as the sum of the spatial charge in a dielectric material, the ion and electron fluxes to the surface, the secondary electron emitted from the surface, and the conduction current within the material. The potential on a powered material is the instantaneously applied potential superpositioned with the DC-bias V_{dc}.

$$\Phi(t + \Delta t) = \Phi_{RF}(t) + V_{dc},$$ (2.32)

where $\Phi_{RF}(t)$ is the RF potential at time t. As discussed in the Introduction, the magnitude of V_{dc} depends on the asymmetry of the reactor. In the HPEM, V_{dc} is calculated as

$$V_{dc} = \frac{1}{C}\int \sum_i m_i \left[\sum_j \vec{\phi}_j (q_j + q\gamma_{ij}) \cdot \hat{n} + \frac{\partial(\varepsilon\vec{E}\cdot\hat{n})}{\partial t} \right] dt,$$ (2.33)

where C is the magnitude of the blocking capacitance, i is the index of the materials, and j is the index of the particles. The first term on the right-hand side is the conduction current carried by ion and secondary electron fluxes. γ_{ij} is the secondary electron emission coefficient of material i when bombarded with particle j. $\hat{n}$ is the normal vector of the electrode surface. The second term is the displacement current on the electrode. m_i can be -1 or +1 depending on which side of the circuit the electrode is located. That is, if the electrode is on the powered end, $m_i = 1$, else if the electrode is electrically close to the ground, $m_i = -1$.

The power on the electrode is

$$\overline{P}_{rf} = \frac{1}{\tau} \iint V(t) \left[j(\vec{r},t) + \frac{d\left(\varepsilon \vec{E}(\vec{r},t)\right)}{dt} \right] dtdA \,, \tag{2.34}$$

where *V(t)* is the time-dependent voltage, *j* is the conduction current density, τ is the RF integration time, and *A* is the surface area of the electrode. The second term in Eq. (2.34) is the displacement current on the electrode, where ε is the electrode permittivity and $\vec{E}$ is the time-varying electric field.

When more than one frequency is applied to the same electrode, the power deposition is calculated individually for each power source. The current on the electrode is Fourier analyzed to distinguish the frequency components.

$$I_k = \sum_{n=0}^{N-1} i_n e^{-i2\pi k \frac{n}{N}}, k = 0,1,2,\cdots,N-1 \tag{2.35}$$

where *N* is the number of time bins used to resolve the RF cycles. Typically, the RF cycle is divided into 10^3-10^4 bins. With this current mapping in the frequency domain, the time domain current with a radian frequency of ω is expressed as

$$I(t) = \sum_{i=1}^{m} \sum_{j=1}^{n} I_{ij} \cos(j\omega_{ij}t + \phi_{ij}) \,, \tag{2.36}$$

where *m* is the total number of frequencies, *n* is the number of harmonics considered for each frequency, and ϕ_{ij} is the phase of the jth harmonic of frequency *i*. Sequentially, the time domain current is multiplied with the voltage, and the RF period averaged power deposition of frequency ω is

$$\overline{P}_{\omega i} = \frac{1}{\tau} \int I_{\omega i}(t) \cdot V(t) dt \,, \tag{2.37}$$

Finally, the total power on the electrode is the summation of the power from all frequencies.

2.1.4 Plasma Chemistry Monte Carlo Module (PCMCM)

The PCMCM is usually executed after the plasma reaches a quasi-steady state, though it can also be executed throughout the simulation. It is used to record the energy and angular distributions (EADs) of both charged and neutral species in the plasma or on the plasma-material interface [11]. The electric field, the density of species, and the relevant source functions are used in the PCMCM to move and track the pseudoparticles.

The PCMCM is operated kinetically using the Monte Carlo Simulation technique. Pseudoparticles are launched at targeted locations with densities weighted by the source functions of the corresponding species. The initial velocity of a species is isotropic, with a magnitude that replicates the temperature calculated in the FKPM using the Maxwell-Boltzmann distribution. The electric and magnetic field are linearly interpolated in both space and time domains, and used to advance pseudoparticle trajectories. Same as in the eMCS, collisions in the PCMCM are also handled using the null-collision technique. A series of random numbers are used to determine the collision frequencies and type of reaction from each collision.

The time step used to integrate the trajectory of pseudoparticles is calculated to be the minimum of the time between collisions, the time required for a pseudoparticle to move across a specified fraction of the mesh cell, and a fraction of the smallest RF period. In a bulk plasma, the fraction of a mesh cell a pseudoparticle is allowed to travel in each time step is between 0.2 – 0.5. As the pseudoparticle enters the sheath, it is accelerated to a high velocity by the electric field in a short period of time. Therefore, the fraction of a mesh cell a pseudoparticle is allowed to travel is constrained to ensure an accurate energy and angular distributions (EADs) recording.

Charge exchange collision is a common occurrence in the sheath. During a charge exchange collision, an energetic ion accelerated by the sheath collides with a neutral particle. The ion then losses its charge but preserves its initial kinetic energy. Consequently, a duo of a

hot neutral and a cold (thermal) ion is created. The hot neutrals bring a significant amount of kinetic energy to the surface that can activate the surface sites or cause further damage through subsequent bombardments. Due to the combined importance of ions and neutrals, both the IEADs and neutral energy and angular distributions (NEADs) are recorded in the PCMCM.

2.1.5 Surface Kinetics Module (SKM)

Reactions at the interface of plasma with a solid material (e.g., wall, wafer, electrode, etc.) can be addressed using a Surface Site Balance Model (SSBM) within SKM. The SSBM consists of the rates of reactions between fractional surface sites and gas phase fluxes, or between different surface sites. The relative sticking coefficient of the gas phase species in the plasma is updated depending on fractional surface coverage [11]. The incident flux ($\vec{\phi}_{in}$) to a surface is provided by FKPM. A surface reaction generally has the form

$$A(g) + B(s) \rightarrow C(s) + D(g) + E(g), \tag{2.38}$$
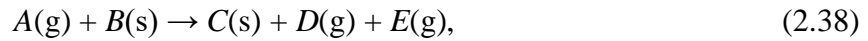
where g stands for gas phase species, and s denotes the surface sites. The rate of ith reaction between gas phase species A and surface sites B on material m is:

$$R_{im} = \alpha_i \phi_{Am} \theta_{Bm}, \tag{2.39}$$

where α_i is the reaction rate of ith reaction, ϕ_{Am} is the flux of gas phase species A on material m, θ_{Bm} is the fractional coverage of surface site B on material m. The fractional coverage of surface sites is updated by summing up the reaction rates.

The surface coverage ratio, of all the surface sites, is attained by integrating the rate equations of the corresponding sites using a third-order Runge-Kutta technique. The fractional surface coverage along with the gas phase fluxes from the surface, $\vec{\phi}_{out}$, is returned to the FKPM, through which the surface reactions feedback to the plasma. The reaction probability of gas phase species on the surface is the summation of the rates of reactions with it as a reactant.

2.2 Monte Carlo Feature Profile Model (MCFPM)

The Monte Carlo Feature Profile Model (MCFPM) is a voxel-based feature scale simulator used to investigate the physics of topologically evolving targets. It is compatible with both 2-dimensional (2D) and 3-dimensional (3D) simulations, while in this thesis, only the 3D geometry is used. A detailed explanation of the MCFPM is provided in Ref. [12]. Only a brief description of the model is given in the following paragraphs.

In the MCFPM, the feature profile is mapped using cubic voxels. Each voxel preserves its assigned material properties. Pseudoparticles with EADs obtained from the HPEM output are typically introduced at the top of the simulation domain. These pseudoparticles are then tracked until they hit the solid material on the surface. Based on the species of the colliding pair, the incident energy of the gas phase species, and the reaction probability, the outcome of the bombardment is determined. Two processes that lead to surface evolvement are deposition and sputtering. In the deposition process, an additional voxel representing the deposited species is added to the initial mesh. In a sputtering process, the voxel indicating the solid reactant is removed from the mesh, and the gas phase product is either tracked as a pseudoparticle using the Monte Carlo technique or returned as a background species.

The properties of these fluxes are logged at the bottom of the feature in a defined window. The number of bombarding particles within this window is calculated by counting the pseudoparticles hitting the surface, and scaling it with the number of particles each pseudoparticle represents. This value is then normalized by dividing it by the sampling area. The fluxes at the bottom of the feature are attained by multiplying the normalized particle number with the velocity components perpendicular to the solid surface. The height of the bottom solid surface is determined by averaging the heights of the top-most voxel from each

mesh column within the test area. This height of the surface is periodically recorded, and the deposition or etch rate is obtained by dividing the height change with the time interval between recordings. The number of particles leaving the feature is measured by the number of pseudoparticles passing through the top boundary of the simulation domain.

2.2.1 Co-deposition

In a semiconductor fabrication process, sometimes, sterically large molecules are used. For example, when depositing SiO_2 film using the PE-ALD technique, organic silicon precursors such as BTBAS ($[NH(C_4H_9)]_2SiH_2$), TIPS ($[(CH(CH_3)_2]_3SiH)$), and BDEAS ($SiH_2[N(CH_2CH_3)_2]_2$) are used. All of these compounds are more than twice the size of single silicon radicals. With a complete surface reaction, the silicon is the only particle that is deposited on a surface. However, occasionally, if the surface reaction is incomplete, the ligand group from the precursor remains on the surface, causing a steric hindrance. This phenomenon is addressed in the MCFPM by considering co-deposition sites.

In a co-deposition process, extra voxels are added to the mesh to represent the ligand group along with the deposition of the primary species (silicon). Depending on the dimension of the simulation domain, a search of the mesh region centered with the primary deposited site is performed in a 3×3 square (2D) or $3 \times 3 \times 3$ cube (3D) for possible co-deposition locations. A series of random numbers are then used to determine the sequence of this search. The co-deposited ligand groups can occupy up to 2 (2D) or 8 (3D) voxels in the mesh. When the co-deposited sites occupy more than one voxel, the location of each voxel is independently searched. Once added to the mesh, the ligand group is treated the same as other surface materials, with specified physical properties (e.g., mass, charge, mobility, etc.) and reactions with the gas phase particles.

The occurrence of co-deposition is probable only when the tagged surface site is deposited from the specific reactants. For example, in a SiO_2 PE-ALD process, the ligand group is introduced to the surface during precursor dosing. When a silicon radical is deposited, the ligand group from the precursor is assumed to react with the hydroxyl group on the target surface, and to volatilize as part of the gas phase product. However, if there are not enough hydroxyl groups on the surface, the ligand group will continue to bond with the silicon and stay on the solid surface. In this example, the primary deposition site is the silicon, and the prerequisite reactant is the silicon precursor. The precursor requirement is necessary because silicon can be deposited through various paths. Other than from the precursor, silicon can also be deposited from gas-phase silicon radicals sputtered by the energetic ions. In this case, the probability of co-deposition of the ligand group should be zero since the ligand group does not exist in the reactant. In the MCFPM, all the reactions are mapped with their corresponding reactants and products enabling use of the reactants as the prerequisite condition in the co-deposition process.

Because the MCFPM is a voxel-based model, all the materials are discretely treated using an aligned voxel mesh in the space domain. Therefore, the microscopic material structure is not resolved. However, the occurrence of a steric hindrance strongly depends on the microscopic properties of the reactants. The structure of the surface material, the neighboring components near the positions where the reaction occurs, and the orientation of the gas phase reactant during a collision are all vital factors that affect the steric hindrance. In the MCFPM, a probability is assigned to the co-deposition reactions to provide extra control and to accommodate the elements that are not included in the model. A series of random numbers ranging from 0 to 1 is used to

determine whether the co-deposition occurs. The random number is compared with the co-deposition probability and co-deposition occurs when the random number is smaller.

2.2.2 Energetic Particle Surface Reaction

In the MCFPM, any reactions between gas-phase species and surface sites are mapped in a probability array. When a pseudoparticle hits the surface, a random number is generated and compared with a given reaction probability, which then determines which reaction is to occur. Most of the reactions used in this thesis have a constant reaction probability although it is important to remember that an energetic particle surface reaction probability is energy and angular dependent [13, 14]

$$p(E_i, \theta) = p_0 \left(\frac{E_i - E_{th}}{E_r - E_{th}} \right)^n f(\theta), \quad (2.40)$$

where E_i is the particle energy, θ is the incident angle, p_0 is the reference probability, E_r is the reference energy, E_{th} is the threshold energy, and $f(\theta)$ is the angular dependent function. The exponential term n is typically 0.5. When bombarding on the surface, energetic particles can cause physical sputtering or chemical enhanced etching, any of which may have different angular dependence. In this thesis, using a PE-ALD process, physical sputtering dominates the likely energetic particle surface reactions, and a reaction probability is at the maximum value when the incident angle is around 60˚. In our case, this reaction probability decreases with a decreasing incident angle and is zero for glazing collisions.

If the target feature has an aspect ratio greater than 1, an energetic particle can experience several collisions on the sidewall before reaching the bottom of the feature. Through this process, the particle losses its energy. The preserved energy E_s of a sputtered particle after striking the surface is

$$E_s(\theta) = E_i \left(\frac{E_i - E_c}{E_{ts} - E_c} \right) \left(\frac{\theta - \theta_c}{90^\circ - \theta_c} \right),$$ (2.41)

where E_{ts} is the threshold energy for specular scattering, E_c is the cut off energy of diffusive scattering, and θ_c is the lower angular boundary for specular scattering. Particles with $E_i > E_{ts}$ preserve all the energy, and particles with $E_i < E_c$, or $\theta < \theta_c$ are treated as to be diffusively scattered.
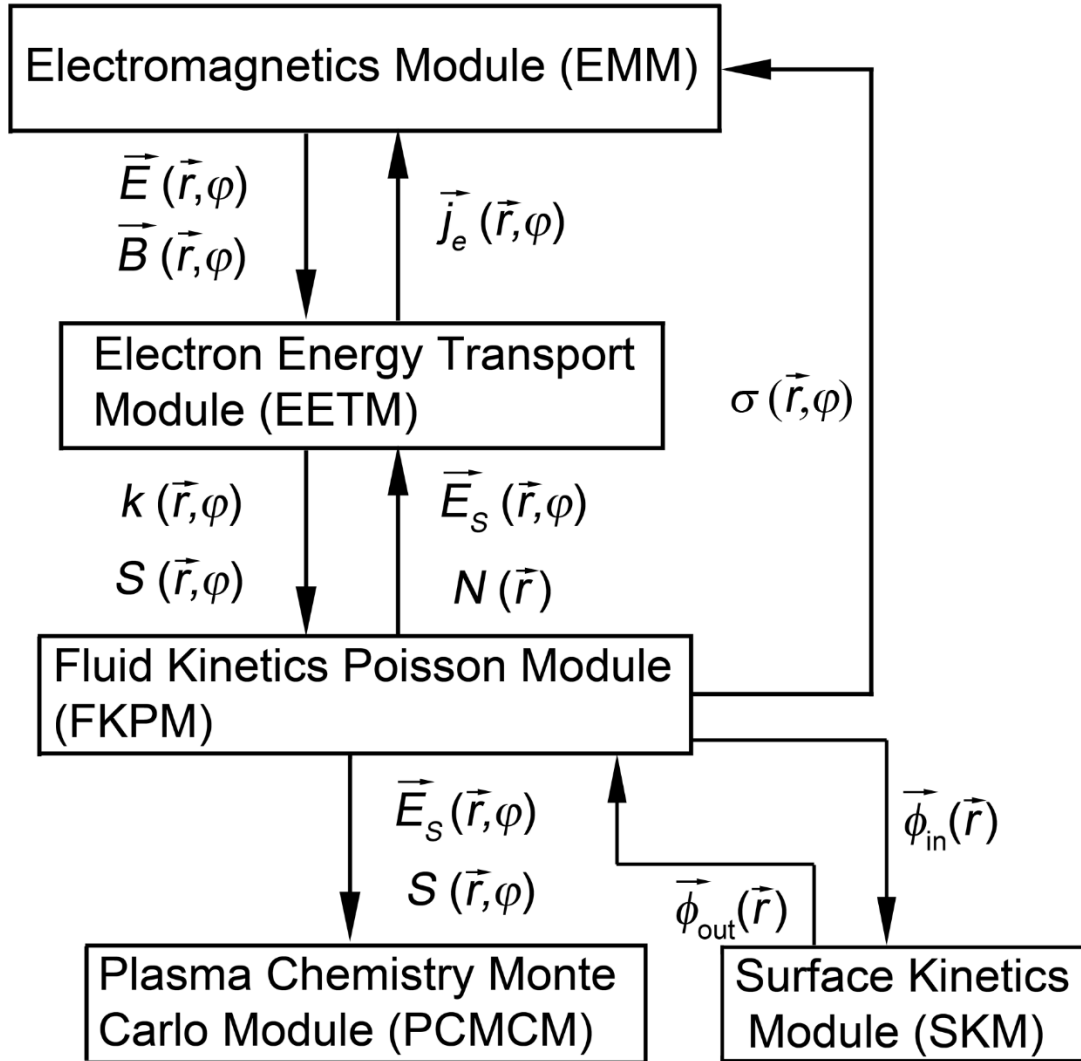
Fig. 2.1 The flow chart of the Hybrid Plasma Equipment Model (HPEM) used in this thesis.
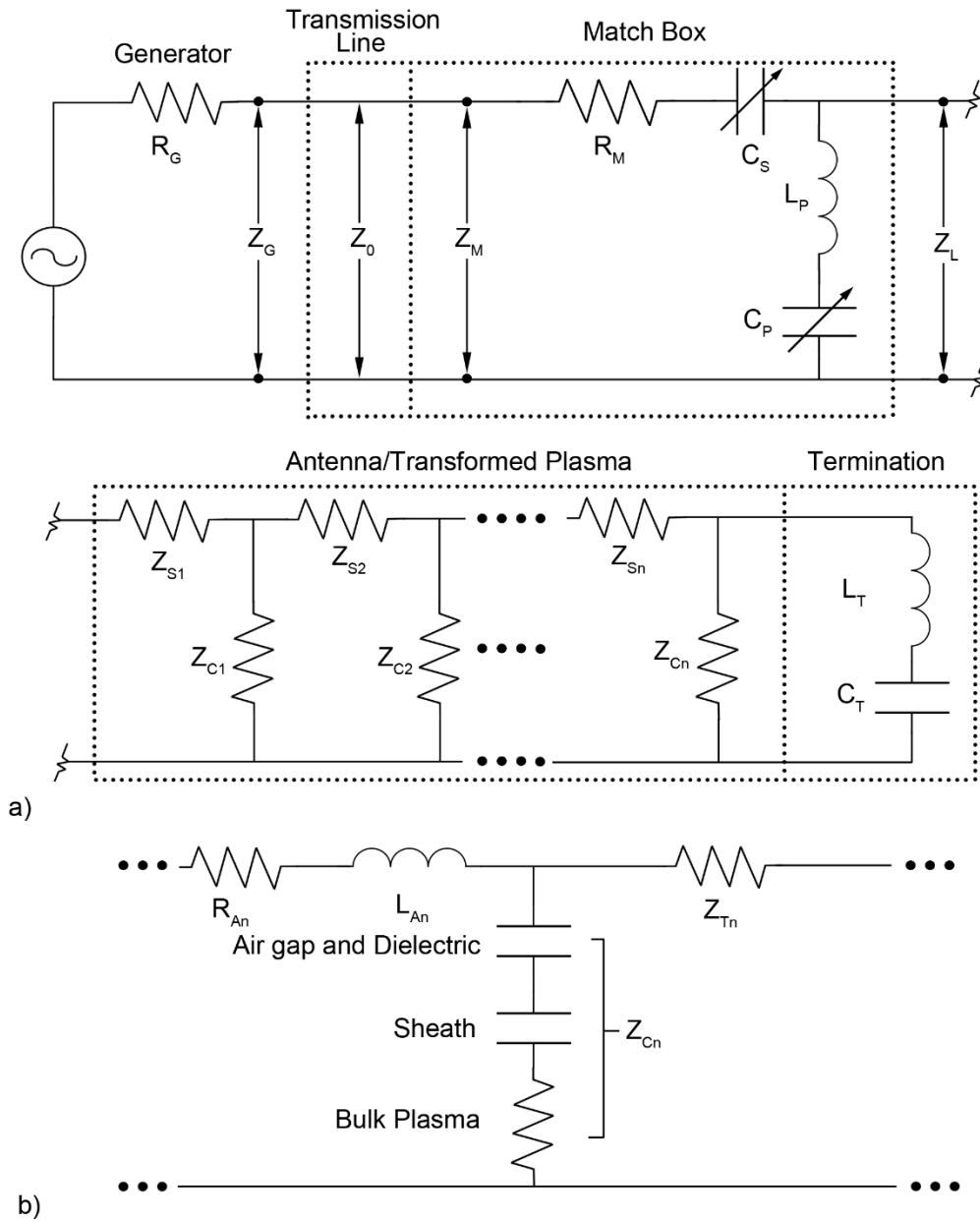
Fig. 2.2 a) Schematic of the circuit model and b) the detail of each segment representing 1/100 of an antenna.
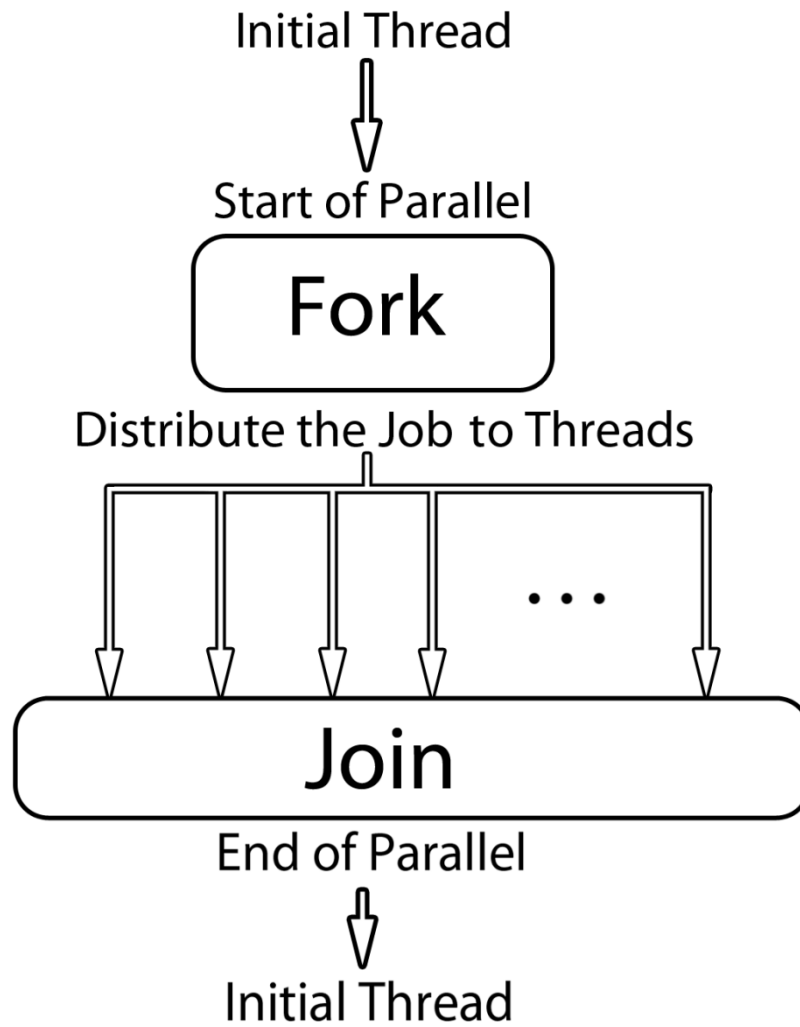
Fig. 2.3 Schematic of the fork-join model used in OpenMP for parallel computation.

2.4 References

1. M. J. Kushner, J. Phys. D: Appl. Phys. **42**, 194013 (2009).

2. R. L. Kinder and M. J. Kushner, J. Vac. Sci. Technol. A **17**, 2421 (1999).

3. M. J. Kushner, W. Z. Collison, M. J. Grapperhaus, J. P. Holland, and M. S. Barnes, J. Appl. Phys. **80**, 1337 (1996).

4. R. B. Piejak, V. A. Godyak, and B. M. Alexandrovich, Plasma Sources Sci. Technol. **1**, 179 (1992).

5. S. L. Lin, and J. N. Bardsley, J. Chem. Phys. **66**, 435 (1977).

6. S.-H. Song, and M. J. Kushner, Plasma Sources Sci. Technol. **21**, 055028 (2012).

7. R. Chandra, R. Menon, L. Dagnum, D. Kohr, D. Maydan, and J. Mcdonald, Parallel Programming in OpenMP. New York: Morgan Kaufmann (2000).

8. P. L. G. Ventzek, T. J. Sommerer, R. J. Hoekstra, and M. J. Kushner, Appl. Phys. Lett. **63**, 605 (1993).

9. W. H. Press, B. P. Flanney, S. A. Teukolsky, and W. T. Vetterling, Numerical Recipes: The Art of Scientific Computing, Cambridge University Press, 1987.

10. SLAP Sparse Matrix Library: https://www.netlib.org/.

11. D. Zhang, and M. J. Kushner, J. Vac. Sci. Technol. A. **19**, 524 (2001).

12. C. Huard, Y. Zhang, S. Sriraman, A. Paterson, K. J. Kanarik, and M. J. Kushner, J. Vac. Sci. Technol. A **35**, 031306 (2017).

13. C. C. Cheng, K. V. Guinn, V. M. Donnelly, and I. P. Herman, J. Vac. Sci. Technol. A **12**, 2630 (1994).

14. C. F. Abrams, and D. B. Graves, J. Appl. Phys. **86**, 2263 (1999).

Chapter 3: Insights to Plasma Transients in Low-High Pulsed Power Inductively Coupled Plasmas*

3.1 Introduction

Inductively coupled plasmas (ICPs) represent a critical technology for plasma etching for semiconductor fabrication, particularly for the manufacture of conductors and compound materials, and for atomic layer etching [1-5]. Typical operating conditions include rare gas-halogen gas mixtures and pressures of a few to tens of mTorr. Power deposition is up to a few kW in chambers accommodating 300 mm diameter wafers. As the critical dimension (CD) of semiconductor devices continues to decrease and more exotic materials are used, finer control is required over the plasma produced reactive fluxes to the wafer.

An increasingly applied method to control reactive fluxes to the wafer is the use of pulsed-power. Typical pulse repetition frequencies (PRF) are up to 5-10 kHz and duty cycles (DC), which are the fraction of the pulse period power is on, are typically tens of percent. Pulsed power enables high peak power during the power-on portion of the cycle while leveraging unique plasma chemical reactions during the power-off portion of the period [6-8]. When combined with continuous or pulsed biases on the substrate, unique combinations of reactant fluxes and ion energies onto the wafer can be produced to accelerate ions onto the wafer [9,10].

Pulsed ICPs have been particularly effective in minimizing damaging the wafer during processing. For example, Ishikawa found that in an SiO_2 etching process carried out in an Ar

---

ICP, there was less UV damage when using pulsed power compared to continuous wave (CW) due to the lower UV dose during the power-off period [11]. Petit-Etienne et al. studied silicon recesses during plasma etching with both CW and pulsed-power using $HBr/O_2/Ar$ plasmas [12]. They found that when using synchronous pulsed-power, the recess loss of Si could be better controlled due to a decreased ion flux while maintaining neutral fluxes. They also concluded that using pulsed-power may also minimize chamber wall sputtering due to the lower ion flux, which then reduced contamination of the substrate [13]. Bodart et al. investigated the consequences of PRF and DC on radical densities in Cl_2/HBr plasmas [14]. They found that in the high PRF regime, changing DC could effectively control the fragmentation of the feedstock gases, whereas in the low frequency regime the effect of DC on the plasma chemistry was small.

Pulsed ICPs have also been extensively investigated through modeling. In an early work, Ramamurthi et al. developed a two-dimensional continuum model to study pulsed ICPs sustained in Cl_2 [15]. A highly electronegative ion-ion plasma core with an electropositive edge was observed in the afterglow of the discharge. A spike in T_e was observed at the beginning of the power pulse, which agreed well with experiments. The authors concluded that some plasma properties, such as negative ion density, are strongly dependent on the spatial distribution of the plasma core, also noting the need to control electric probe positions in experiments to obtain a complete perspective of these complex processes. Due to the strong spatial dependence of plasma properties in an electronegative discharge, the separation of the electronegative core and electropositive periphery was accounted for in a volume-averaged model developed by Kim et al. [16]. That model predicts a decreased ratio of neutral-to-ion flux as the aspect ratio of the discharge increases in an O_2 plasma, further demonstrating the importance of geometry and the spatial conditions in electronegative plasmas. To better understand the transient behavior of a

pulsed-power driven electronegative plasma, Thorsteinsson et al. performed a computational investigation of an Ar/Cl$_2$ plasma using a global model [17]. They concluded that improvements in etch selectivity when using a pulsed-power Cl$_2$ plasma result from the increase of the radical to ion ratio compared to CW operation. This control can be further refined by varying mole fractions in Ar/Cl$_2$ mixtures, a practice that provides some limited ability to tune the electron temperature.

A commonly observed behavior of T_e in a pulsed ICPs is that at the beginning of the power pulse T_e spikes to a value above that in the quasi-steady state. For example, in the modeling by Ramamurthi et al., this spike in T_e was observed in a pulsed Cl$_2$ ICP [15]. T_e peaked to 5 eV at the beginning of the pulse and then rapidly decreased to the quasi-steady value of 2 eV in about 10 μs. This phenomenon was observed in early experiments performed by Ashida et al. [18]. In a pulsed ICP sustained in Ar at 5 mTorr, Langmuir probe measurements indicated a peak in T_e at the leading edge of the pulsed period up to 7 eV, with the quasi-steady state temperature being 3.5 eV. Darnon et al. noted that in their experiments the overshoot of T_e at the beginning of the pulse is more significant when the pulse repetition PRF is low [19]. A low PRF provides a longer afterglow, and thus a lower electron density, n_e, at the beginning of the next pulse. This lower n$_e$ then produces the overshoot of T_e. With the spike of T_e in a pulsed plasma being well documented, its behavior is used as a test of the accuracy of experimental measurements [20]. However, the spatial dependence of the spike of T_e is not often documented.

Although there are several advantages of using pulsed-power for electronegative ICPs, there are also several challenges. Due to the low electron density at the end of the afterglow and at the beginning of power pulse, E-H (capacitive-to-inductive) transitions can occur at the beginning of each pulse. At the beginning of the pulse when the electron density is low, the

electromagnetic skin depth can be larger than the dimensions of the reactor, and electromagnetic coupling is inefficient. Power is electrostatically and capacitively coupled to the plasma through the voltage drop from the coil to the plasma bulk. This is the E-mode. As the electron density n_e increases, the skin depth decreases and power becomes coupled to the plasma inductively through the electromagnetic field. This is the H-mode. During the onset of the E-mode, large oscillations can occur in the plasma potential and plasma density, and electrostatic waves can be launched from beneath the antenna. When operating close to the transition between the E- and H-modes, ionization instabilities may occur which produce periodic maxima in the plasma density [21].

The E-H transition in ICPs was experimentally investigated by Cunge et al. [22] who observed a hysteresis in the mode transition as a function of power. It was observed that the power absorbed by the plasma has a nonlinear dependence on the electron density. In a later work, Chabert et al. investigated this instability in SF_6 and Ar/SF_6 plasmas with a combination of experimental and modeling work [21]. They concluded that multistep ionization plays an important role in ionization balance, induces nonlinearity in the plasma and produces hysteresis behavior during the E-H mode transition

One of the origins of the E-H transition in electronegative ICPs and its associated instabilities is the need to reignite the plasma at the beginning of each period in pulsed plasmas. One strategy to circumvent the E-H transition while also modulating power is to use a high-low power scheme [23]. Using this method, the pulsed power format consists of a high-power portion of the pulsed period followed by a low power portion of the pulsed period - that is, non-zero power. The intent of the non-zero power is to maintain the plasma's conductivity at a high enough value so that the system remains in H-mode throughout the pulsed period. However,

even high-low power pulsing may have instabilities. List et al. found that in high-low power modulated Cl_2 ICPs, the plasma may extinguish at the beginning of the low-power period and then reignite after 10s of microseconds to a few ms [23]. They called this phenomenon "ignition delay", the cause of which is believed to be related to the ability of the supply to deliver power to the time varying impedance of the plasma.

In this chapter, we discuss results from a computational investigation of high-low pulse power formats for ICPs sustained in Ar/Cl_2 gas mixtures. We found that in high-low pulsed plasmas, T_e undergoes a transient during both power transitions. For long enough high- and low-power periods, T_e, is effectively constant during the pulse. However, T_e, has a momentary maximum when power transitions from low-to-high, are similar to the leading edge of conventional pulsed ICP. T_e, also has a momentary minimum when power transitions from high-to-low. This response of T_e to power transitions highly depends on location with respect to the electromagnetic skin-depth and the fractional dissociation in the Cl_2-containing plasma. Within the skin-depth, the transients in plasma properties (T_e and n_e) during power transitions are distinctly observed. With increasing distance from the skin-depth, the transients disperse in space and dissipate in magnitude. These responses of the plasma to pulsed power can be controlled through gas mixture and the pulsed power format. Decreasing the Cl_2 mole fraction, lengthening the power ramp time, and increasing the low-power diminish the transients and produce a more spatially uniform plasma.

A brief model description is in Sec. 3.2. Plasma properties as a function of high-low power format and gas mixture are discussed in Sec. 3.3. Concluding remarks are provided in Sec. 3.4.

3.2 Description of the Model

Note: The computational investigation was performed using the HPEM (Hybrid Plasma Equipment Model). Details of this model are discussed in Sec. 2.1 and Ref. [24], while a brief description follows focusing on the options used in this study.

In this work, the model employed uses the Electromagnetics Module (EMM), Fluid Kinetics Poisson Module (FKPM), and Electron Monte Carlo Simulation Module (eMCS) within the Electron Energy Transport Module (EETM). The inductively coupled electric field is produced in the EMM from a frequency domain solution of Maxwell's equation. The densities, fluxes and temperatures of the heavy particles (neutrals and ions), densities of electrons and electrostatic potential are produced in the FKPM. This information is then transferred to the eMCS for electron energy distributions (EEDs) throughout the reactor. Electron trajectories including electron collisions in the time and spatially varying electric and magnetic fields are computed. Transport of both bulk and secondary electrons from surfaces is addressed. Electron-electron collisions are included such that the Maxwellian nature of the EEDs is captured in regions of high electron density.

The species included in this work are Ar, $Ar(1s_5)$, $Ar(1s_4)$, $Ar(1s_3)$, $Ar(1s_2)$, $Ar(4p)$, $Ar(4d)$, Ar^+, Ar_2^+, Ar_2^*, Cl_2, $Cl_2(v)$, Cl_2^+, Cl, Cl^+, $Cl(4s)$, $Cl(4p)$, $Cl(3d)$, Cl^-, and electrons.

3.3 Characteristics of Low-High Pulsed Power ICPs

The geometry of the ICP reactor used in this investigation is shown in Fig. 3.1a. The system is a conventional ICP reactor with a stovetop 4-turn coil located at 0.4 cm above a dielectric window. The cylindrical reactor radius is 7.6 cm and the chamber height is 15.6 cm. A wafer of a radius of 3.7 cm is positioned on a grounded substrate 13 cm below the dielectric Al_2O_3 window. A 1.8 cm wide Al_2O_3 focus ring surrounds the substrate. The dielectric constant

of the alumina is 9.8 and that of the wafer is 11.8. The dielectric has a negligible conductivity while the wafer has a conductivity of $10^{-3}/\Omega$-cm. The substrate supporting the wafer is not powered so that any modulation of the plasma is attributed to power changes from the coil. The gas inlet is in the sidewall at 0.4 cm below the dielectric window and the annular pump is at the bottom of the reactor with a 2.1 cm width. The feedstock gas enters the chamber at ambient temperature (300 K). A pressure sensor is embedded in the sidewall at 3.9 cm above the substrate to monitor the local pressure, and that measurement is used to throttle the output flow rate to maintain the specified pressure. The inner wall of the reactor is coated with the dielectric yttria (Y_2O_3) to decrease the sticking coefficient of radicals, thus increasing the precursor densities in the plasma bulk. The dielectric constant of yttria is about 13. The actual thickness of the yttria coating of a few microns cannot be resolved by the mesh, and so the dielectric constant of the yttria used in the model was increased to 10^4 so that the capacitance (F/cm^2) of the yttria material would be the same as the thin film. The reactor is surrounded by air with electrical ground planes situated at large enough distances so that the electromagnetic waves produced by the coil are not perturbed by the surrounding ground planes.

The secondary electron emission coefficients of both the alumina window and the Y_2O_3 sidewall coating were 0.05 for ions and 0.01 for excited state species having energy greater than the work function of the material. (Photoelectron emission was not included.) A parametric study was conducted for varying the secondary electron emission coefficient from one third to three times of these base case values. There was little impact on the plasma density or spatial distribution of the plasma. The ionization by secondary electrons is 1-2 orders of magnitudes smaller than the ionization by bulk electrons.

The applied power profile, shown in Fig. 3.1b, is a high-low pulsed format that modulates

the 13.56 MHz radio frequency current applied to the antenna. For the work in this chapter, all the applied power is inductively coupled to the plasma. That is, we did not include capacitive coupling from the coils and so were able to assume H-mode power deposition. This assumption was validated by performing limited simulations with full electrostatic coupling from the antenna. In the base case, the high-power is 160 W and the low-power is 96 W. (With high power, the power density, W/cm^3, is similar to industrial reactors used for microelectronics fabrication.) The pulse repetition frequency (PRF) is 5 kHz and the duty cycle (DC) is 50%. Note that the power takes 10 μs to ramp from low-to-high or from high-to-low power. The ramp-up and ramp-down times are evenly split between the high- and low-power periods so a 50% DC is strictly enforced. For the base case, the feedstock gas used is an $Ar/Cl_2 = 5/95$ mixture with a flow rate of 22 sccm. The pressure is held constant at 20 mTorr. The reaction mechanism used for the Ar/Cl_2 plasma investigated here is the same as in Ref. [25]. The recombination coefficient on surfaces for ground state Cl to recombine to form Cl_2 was 0.05. Excited states of Cl and Ar quenched on surfaces to form their ground states with unity probability. $Cl_2(v)$ quenched on all surfaces to form ground state Cl_2 with 0.5 probability. All charged species recombine on surfaces with no reflection, depositing charge on dielectric surfaces.

The 2D profiles of the electron density (n_e), electron temperature (T_e) and ionization source by bulk electrons (S_e) are shown in Fig. 3.2. The figures shown are at the end of the high- and low-power periods, corresponding to the times of 100 μs and 200 μs shown in Fig. 3.1b. In the base case, the position with the highest power deposition is at mid-radius of the reactor at 1 cm below the dielectric window. As the power changes from 96 W to 160 W, the maximum power density increases from 0.8 to 1.4 W/cm^3, leading to an increase in the maximum electron

71

density from 6.3×10^{10} cm^{-3} to 1.3×10^{11} cm^{-3}. Using these values of n_e and the momentum transfer collision frequency (ν_m) of 2 to 4×10^7 s^{-1}, the skin depth (δ) of the EM wave in the plasma is 1.5 to 2.0 cm, which is much smaller than the height of the reactor (13 cm). Consequently, the pulsed power has little direct impact on the plasma dynamics in the several cm above the wafer.

For example, the ionization source by bulk electrons (S_e) decreases by a factor of 100 within 5.0 cm from the dielectric window, indicating the plasma density above the substrate is not directly sustained by the pulsed power but rather results from transport of charged species from the top of the reactor. The plasma near the substrate can at best be sustained by power that is convected from the top of the reactor by non-local electron transport and by electron thermal conduction, or by Penning ionization due to metastable species that transport from the top of the reactor.

The dominant positive and negative ions in the base case are Cl_2^+ and Cl^-. Their densities and the gas temperature (T_{gas}) are shown in Fig. 3.3 at the end of the low- and high-power portions of the pulsed cycle. The axial densities of electrons and Cl^- at mid-radius of the wafer are shown in Fig. 3.4 at the end of the low- and high-power periods. The maximum Cl_2^+ density has only a small increase, 1.6×10^{11} cm^{-3} to 1.8×10^{11} cm^{-3}, as the input power transitions from low (96 W) to high (160 W). The increase in the negative ion density is also small, 1.5×10^{11} cm^{-3} to 1.6×10^{11} cm^{-3}. The electronegativity of the plasma, the ratio of the negative ion density to electron density, decreases from 2.4 at low power to 1.2 at high power. The Cl^- density is relatively stable through one full period due to the high dissociative attachment rate of Cl_2 by thermal electrons which can occur throughout the reactor. Losses of Cl^- are dominated by ion-ion recombination since the negative ion is trapped in the plasma by there being a positive

plasma potential throughout the pulsed period. The peak plasma potential is 13 V during low power and 14 V during high power. Unlike pulsed systems where the power is turned off, the plasma potential does not dissipate during the low-power period which would then allow negative ions to diffuse out of the plasmas. With the Cl_2^+ density also fairly stable through the period, the loss term of the Cl^- is also fairly constant. ,

The maximum gas temperature is modulated during the pulsed cycle by about 170 K (752 K during low power and 920 K during high power). Heating is nearly instantaneous with the application of power while the dominant gas cooling is by thermal conduction to the walls. (There are small additional contributions due to injection of cool gas and pumping of hot gas.) These thermal heating and cooling time scales are short compared to the gas convective time scale, and so there is less modulation in the gas density. As a result, there are pressure oscillations during the pulsed period [26].

The aspect ratio of the ICP reactor has important implications on the local densities of charged particles. In this work, the reactor has a fairly large aspect ratio (height divided by radius) with the power deposition and electron impact ionization being limited to a few cm at the top of the reactor within the electromagnetic skin depth. Transport processes then convect power and density from the skin depth to the lower portion of the reactor. For example, n_e and T_e are shown at mid-radius of the wafer as a function of time for different heights in Fig. 3.5. Within the electromagnetic skin depth (height = 11 cm), n_e is fairly constant during the high- and low-power periods with a change in density commensurate with the change in power. At locations further from the skin depth, the electron density is smaller while the relative modulation in n_e is also smaller. Moving further from the source, there is an increasing positive slope in n_e as a function of time during the high-power pulse and an increasingly more negative slope in n_e as a

function of time during the low-power pulse. These trends result from the finite transport time for the excess electron density produced during the high-power to translate to the bottom of the reactor. The time for transport of the electrons from the top to the bottom of the reactor is commensurate with the pulsed period. Therefore, the increase and decrease in plasma density that is experienced in real-time with power modulation at the top of the reactor is averaged over the cycle at the bottom of the reactor.

The high- and low-power periods are long enough, 100 μs, that the plasma in the skin depth comes into a quasi-steady state during both the high- and low-power periods. For quasi-steady state conditions, the electron temperature T_e is determined by a balance between sources by electron impact ionization and Penning reactions, and losses by attachment, recombination and transport out of the skin depth. In the skin depth, the fractional dissociation, 47%, is nearly constant during the high- and low-power periods, and the change in gas rarefaction between the high- and low-power, 15%, is not large. As a result, T_e during the low- and high-power periods is similar – the value at which sources and losses balance each other. The power deposition is, to first order, $n_e k_L(T_e) N_g$, where $k_L(T_e)$ is the rate coefficient for power loss (which increases with increasing T_e) and N_g is the gas density. With T_e and N_g being similar during the low- and high-power, then a change in power requires a change in n_e. The change in n_e is downwards when going from high-to-low power and upwards when going from low-to-high power. These transitions in turn require that T_e momentarily decrease below the self-sustaining value in transitioning from high-to-low power to lower the electron density. Similarly, T_e must momentarily increase above the self-sustaining value when transition from low-to-high power to increase electron density.

A similar interpretation of the need for spikes (up or down) in T_e, comes from the

perspective of power dissipation. With an instantaneous, step-function increase in power deposition, there is not sufficient time for the electron density to increase to accommodate the increase in power. To enable the increase in power deposition, T_e must increase, which usually also increases the rate of power dissipation per electron. Similarly, if there is an instantaneous decrease in power, there is insufficient time for the electron density to decrease to accommodate the decrease in power. To enable the decrease in power deposition, T_e must decrease, which usually also decreases the rate of power dissipation per electron. The duration of the spikes in T_e (up or down) is then the time required for the electron density to change from the low-to-high values (and vice-versa).

These spikes in T_e are shown in Fig. 3.5, and occur dominantly in the skin depth where power deposition is maximum – positive spike for low-to-high power and negative spike for high-to-low power. When translating lower in the reactor and further from the skin depth, T_e decreases due to collisional power loss. The local heating sources are superelastic collisions (a small contribution), thermal conduction by bulk electrons or non-local transport in the tail of the EED. The spikes in T_e also dissipate and broaden in time, as thermal conductivity and convection translate the pulse of hotter electrons (low-to-high power) or cooler electrons (high-to-low power) to lower heights. The end result is that T_e appears to have periodic waves close to the wafer.

The EEDs at the end of the high- and low-power periods are shown in Fig. 3.6. At the top of the reactor, the EEDs are almost Maxwellian due to the high e-e collision frequency and higher T_e. Moving away from the power source, the EEDs gradually shift to bi-Maxwellian with a lower temperature bulk (1.0 eV) and higher temperature tail (1.9 eV). The bulk T_e decreases in translating lower in the reactor due to the lower frequency of e-e collisions and collisional power

loss. The tail of T_e is relatively constant (or decreases less than the bulk T_e) as the tail is sustained by non-local transport of high energy electrons that are accelerated in the skin depth and have longer mean free paths. There are no significant differences between the EEDs at the end of the low- and high-power periods. First, the T_e is essentially the same in the skin depth at the end of the low- and high-power periods, and so the power deposition-per-electron is the same. As a result, the EED in the skin depth is essentially the same. Lower in the reactor, the tail of the EED has a higher temperature at the end of the high-power period compared to the low-power period. This is likely a result of the higher thermal conductivity afforded by the higher electron density.

3.3.1 Gas Mixture

In a pure rare gas mixture at low pressure (without dimer ions), loss of electrons and ions is dominated by diffusion to surfaces where they recombine. If in a pulsed system, the period is shorter than the time for ions to diffuse to surfaces, then the plasma source is effectively averaged over the pulse period. The plasma density will then not directly track the variation in power deposition. When increasing the Cl_2 mole fraction in a Ar/Cl_2 gas mixture, the rate of electron loss by dissociative attachment increases and the electron density is more modulated during the pulsed period. This increased rate of modulation of the plasma density then requires a larger modulation in T_e.

The Cl_2 mole fraction in the Ar/Cl_2 gas mixture was varied from 20% to 80%, and the resulting electron densities are shown in Fig. 3.7 at the end of the high-power part of the cycle. The electron densities and temperatures at heights of 11 cm and 2 cm above the substrate are shown in Figs. 3.8 and 3.9 during the pulsed cycle. The PRF (5 kHz), duty cycle (50%) and low/high power (96 W/160 W) are the same as in the base case.

With the increase in Cl_2 mole fraction, the power deposition per electron increases and so

76

on this basis alone, for a given power density, the electron density decreases. We see this trend in the electromagnetic skin depth where power deposition is maximum – n_e increases from 1.6×10^{11} cm^{-3} for an Ar/Cl$_2$ = 20/80 mixture to 7.9×10^{11} cm^{-3} for an Ar/Cl$_2$ = 80/20. As electrons diffuse out of the power deposition region, the T_e of these electrons decrease more rapidly with increasing Cl$_2$ mole fraction. For Cl$_2$, which is a thermally attaching gas, the rate of dissociative attachment increases with decreasing T_e, and this lowers the average electron density even further. As a result, there is a more severe gradient in electron density between the top and bottom of the reactor with a larger Cl$_2$ mole fraction. For the Ar/Cl$_2$ = 80/20 mixture, n_e decreases by a factor of 2.2 from the top to the bottom of the reactor. For the Ar/Cl$_2$ = 20/80 mixture, this decrease is by a factor of 7.5.

The electron density at the top of the reactor (height = 11 cm) is essentially in phase during the pulse-period – increasing when the power is high and decreasing when the power is low. With the power deposition being limited to the skin depth, there is a time-delay (phase offset) for the increase in plasma density to propagate from the top of the reactor to the bottom of the reactor. This delay is 10-15 μs for the Ar/Cl$_2$ = 80/20 mixture and decreases with increasing mole fraction. At the same time, the degree of modulation in the plasma density decreases from the top of the reactor to the bottom of the reactor. In the skin depth, the electron density is modulated by a factor of 2. Above the substrate, the modulation is a factor of 1.5. The phase delay and decrease in modulation in plasma density are both a consequence of the finite propagation time for the pulse of higher electron density during the high-power period to propagate across the reactor.

In transitioning from low-to-high power, which requires an increase in plasma density, T_e must increase at least momentarily above the quasi-state self sustaining values. In transitioning

from high-to-low power, which requires a decrease in plasma density, T_e must at least momentarily decrease below the quasi-state self sustaining values. The magnitudes of these momentary increases and decreases in T_e get larger with increasing Cl_2 mole fraction. T_e in the skin depth (height = 11 cm) as a function of Cl_2 mole fraction is shown in Fig. 3.9a. The leading positive spike of T_e (low-to-high power) increases by about 0.2 eV between a mole fraction of 20% and 80%. This increase is required to offset the additional electron losses by dissociative attachment.

The initial positive spike in T_e produces excess ionization that persists during the high-power pulse. Based on the additional losses inherent to the more chlorine rich $Ar/Cl_2=20/80$ mixture, one would expect T_e to be higher during the pulse in than in more dilute mixtures. This is not the case, as T_e is marginally lower for the chlorine rich mixtures during the pulse. The excess ionization produced by the positive leading spike in T_e enables a lower T_e in the chlorine rich mixtures during the high-power pulse. During the low-power period, T_e is higher for higher Cl_2 mole fractions. In transitioning from high-to-low power, there is no ionization excess and so T_e is higher in the more chlorine rich mixtures to offset the additional electron losses.

T_e for different Cl_2 mole fractions at 2 cm above the substrate is shown in Fig. 3.9b. The electron transport time from top-to-bottom of the reactor is 10-20 μs, which is also about the duration of the leading spikes and decreases in T_e in the skin depth. As a result, these spikes and decreases in T_e are dissipated and averaged over the high- and low-power periods by the time the transients reach the substrate. The end result is that there are imperceptible spikes (positive or negative) in T_e above the substrate. However, the low-to-high power positive spike in T_e, and the high-to-low power negative spike in T_e in the skin depth, when convected to the substrate, produces a temperature that is 0.1 to 0.2 eV higher during the high-power than during the low-

78

power.

With there being increasing collisional losses with increasing Cl_2 mole fractions while the electrons transport from the source region to the substrate, T_e above the substrate decreases by 0.7 eV with increasing mole fraction (20% to 80%). A portion of this decrease can be attributed to the lower electron thermal conductivity due to the lower electron density with a large Cl_2 mole fraction. The lower thermal conductivity reduces the diffusion of thermal energy from the source region to the substrate.

3.3.2   Power Ramp-Down Time

For the pressures and gas mixtures investigated in this chapter, the time for the system to respond to step function changes in power deposition is the response time τ_R = 10-30 µs. If the change in power is over times longer than τ_R, then the plasma will track the change in power in a quasi-steady state manner. That is, the electron density and temperature will be nearly in equilibrium with the instantaneous power. When ramping down in power, there must still be a decrease in T_e below the self-sustaining value to enable a decrease in plasma density; and there must be increases in T_e above self-sustaining when ramping up in power. However, for long enough ramp times these changes may be imperceptible. If the power ramping time, τ, is commensurate or shorter than τ_R, then the T_e must undergo significant excursions in order to increase power dissipation while increasing electron density (ramp up) or decrease power dissipation while decreasing electron density (ramp down).

The power ramp-down time, τ, was varied from 10 µs to 80 µs while the ramp-up time remained at 10 µs. The corresponding T_e at heights of 11 and 2 cm are shown in Fig. 3.10, and the corresponding n_e are in Fig. 3.11. The low- and high-power periods are long enough that the quasi-steady state electron densities are nearly the same, independent of ramp time τ. Having

said that, larger values of τ result in higher average power deposition. (Between a ramp time of 10 and 80 μs, the average power increases from 128 W to 139 W.) As a result, there is proportionately more dissociation of the Cl_2 and more gas heating, which results in the electron density being about 10% higher with the longest ramp time. That aside, the conditions for low-to-high power are nearly the same for all ramp times. As a result, the initial spikes in T_e in the skin depth (height = 11 cm) are also nearly independent of τ.

As τ increases from 10 to 80 μs, the length of power-down period begins to exceed the plasma response time τ_R. In doing so, the downward spike in T_e becomes less severe – 0.3 eV for τ = 10 μs to less than 0.1 eV for τ = 80 μs. If we extend τ to 100 μs, the change in T_e falls within the statistical noise of the simulation. Above the substrate, T_e shows the transit time delay and smoothing of the initial spike for the low-to-high power transition (discussed above). During the low power period, T_e is higher for τ = 80 μs compared to shorter ramp times due to the lack of the downward spike in T_e. However, all of these variations are within 0.15 eV.

With the exception of the aforementioned increase in n_e due to the higher average power for large τ, n_e in the skin depth closely tracks the ramping down of the power. At 2 cm above the substrate, the averaging of power deposition over the electron transit time of 10-30 μs from the skin depth makes the electron density less well correlated with the ramp-down time.

3.3.3 Magnitude of Low Power

For what are otherwise the same conditions, if the lengths of the low- and high-power periods are long enough to achieve the steady state, T_e should be independent of the magnitude of power during the low- and high-power periods. That value of T_e is given by ionization sources being balanced by losses. In practice, there are average power affects that must be considered. For example, consider keeping the high-power constant and varying the low-power.

Increasing low power increases the average power deposition, which results in more dissociation of Cl_2, more gas heating and higher average plasma density. More dissociation of Cl_2 reduces the rate of electron loss by dissociative attachment. More gas heating produces rarefaction that increases losses by diffusion and reduces ion-ion neutralization rate coefficients. Higher plasma densities increase the rates of dissociative recombination and ion-ion neutralization. The end effect on T_e becomes case specific.

Electron temperatures at heights of 11 cm in the skin depth, and 2 cm above the wafer, are shown in Fig. 3.12 while varying the low-power (P_L) from 32 W (20% of the high-power) to 160 W, which is equal to the high power. The electron densities for these conditions are shown in Fig. 3.13. When increasing P_L from 32 W to 160 W, the average power deposition increases from 96 W to 160 W, the fractional dissociation of Cl_2 increases from 38% to 44%, and the gas temperature increases from 568 to 573 K. The increase in fractional dissociation of Cl_2 largely enables the quasi-steady state value of T_e in the skin depth to decrease by 0.13 eV when P_L increases from 32 W to 160 W. With this increase in the fraction dissociation of Cl_2, the electron density during the constant high-power 160 W increases from 9.4×10^{10} cm^{-3} for $P_L = 32$ W to 1.4×10^{11} cm^{-3} for $P_L = 160$ W.

The low- to high-power spike in T_e increases from zero for $P_L = 160$ W, as this is a continuous plasma, to 0.85 eV for $P_L = 32$ W. This increasing overshoot in T_e with decreasing P_L is required to avalanche the plasma from progressively lower plasma densities to that for the high-power. For example, for $P_L = 32$ W, the electron density increases by factor of 6.9 from low- to high-power. The magnitude of the high- to low-power decrease in T_e intensifies with P_L decreasing from 160 to 32 W. Reducing P_L requires a larger change in n_e which is produced by a larger negative excursion of T_e below the steady state. The high- to low-power decrease in T_e is

0.9 eV for $P_L = 32$ W and 0.26 eV for $P_L = 96$ W.

T_e also has a small decrease in its steady state value in the skin depth (height = 11 cm) during the high- and low-power periods. There is a 0.13 eV decrease in T_e from $P_L = 160$ W to $P_L = 32$ W. This change is largely a result of the higher average power with $P_L = 160$ W producing more dissociation of Cl_2 and therefore fewer attachment losses. However, above the substrate (height = 2 cm) there is significant variation of T_e for different P_L. For example, at the end of the high-power period, T_e is 0.1 eV lower for $P_L = 32$ W compared to $P_L = 160$ W. This is the opposite trend compared to the skin depth (height = 11 cm) where $P_L = 160$ W has the lower T_e. The net change in T_e from the skin depth to the wafer (from high to low P_L) is a decrease of 0.23 eV. With $P_L = 32$ W, the average power is lower, the dissociation of Cl_2 is lower, the Cl_2 density is higher and the electron density is lower. As a result, there are more collisional losses and less thermal conduction from the skin depth as electrons transport down towards the substrate. The aggregate end result is a lower T_e.

During the low-power period above the substrate, the decrease in T_e ($P_L = 32$ W compared to $P_L = 160$ W) is 0.35 eV whereas in the skin depth, T_e for $P_L = 160$ W is lower by 0.13 eV. The net change in T_e is 0.5 eV from the skin depth to the wafer, about twice the change as during the high-power period. Since the fractional dissociation is essentially the same during the high- and low-power periods, the larger decrease in T_e can be attributed to lower thermal conductivity due to the lower electron density with $P_L = 32$ W. This lower thermal conductivity is likely also responsible for the slow increase in T_e during the high-power portion of the pulse.

The densities of all the cations (Cl_2^+, Cl^+, Ar^+, and Ar_2^+), density of Cl^- and the ratio of the densities of the dominant cation Cl_2^+ and Cl^+ ($\alpha = [Cl_2^+]/[Cl^+]$) in the skin depth (height = 11 cm) are shown in Fig. 3.14 for different values of P_L. Among the cations, the dominant species

are Cl_2^+ and Cl^+, which have densities 2-3 orders of magnitude higher than the densities of Ar^+ and Ar_2^+. During the high-power part of the cycle, the cation density is nearly constant whereas the Cl^- density increases by 30% from P_L = 160 W to P_L = 32 W. The decrease in Cl^- density with increasing P_L is partly due to the increase in fractional dissociation of Cl_2 (53% to 73%) with increasing power – low Cl_2 density translates to lower rates of dissociative attachment – and increased rarefaction in the skin depth at higher power. $\alpha = [Cl_2^+]/[Cl^+]$ is particularly sensitive to the P_L and increases with decreasing P_L. Again, this is in part explained by the lower fractional dissociation at low P_L. The lower fractional dissociation not only reduces the rate of ionization of atomic Cl but also increases the rate of charge exchange of Cl^+ with Cl_2 to form Cl_2^+.

3.4 Concluding Remarks

In this chapter, an inductively coupled plasma, driven by a low-high pulsed power sustained Ar/Cl_2 mixtures at 20 mTorr, was computationally investigated. Similar to an on-off pulsed plasma, the electron temperature T_e spikes in the electromagnetic skin depth at the beginning of the high-power portion of the cycle. A downward spike of T_e occurs in the skin depth during power transition from high-to-low power, while T_e is nearly the same value (and constant) during the low- and high-power periods. T_e is largely determined by a balance between electron heating from the electric field, and power losses, which in the skin depth includes both collisions and advection out of the skin depth. With the gas density nearly constant during the pulsed cycle the increase in T_e above the steady-state value is required at the leading edge of the low-to-high power period to increase the ionization rate to reach a higher plasma density required to sustain the high-power portion. Analogously, a decrease in T_e below the steady-state value is required at the leading edge of the high-to-low power period to decrease the rate of ionization and increase the rate of attachment. As the low-to-high (and high-to-low) power

ramping time increases and exceeds the energy relaxation time, the leading edge transients in T_e become less severe. For long ramping times, the transients become nearly indistinguishable.

The response of the plasma to the low-high and high-low power changes is highly spatially dependent. For example, the spikes of T_e are distinct in the skin depth while being elongated transients near the substrate. Similarly, the modulation in electron density in the skin depth closely tracks power deposition while n_e is dispersed in time near the substrate. Both transients in T_e and n_e are delayed near the substrate relative to the skin depth. The electron transport time across the reactor, (10-30 µs) coincides with the time of the power transition, and so produces a delay in the transients in the skin depth. During this transport in density and temperature across the reactor, power is collisionally dissipated while thermal conduction disperses the heat pulse. As a result, the spikes (positive and negative) in temperature, and steps in electron density originating in the skin depth, are dispersed in time and in space upon reaching the substrate.

For pulse repetition rates in ICPs that are high enough that the gas density and mole fractions do not significantly change during the pulses. Spikes of T_e (positive or negative) should be expected during power transitions. However, these spikes are really only required in the skin depth where power deposition occurs. The magnitude, duration and phase of the transients in T_e and n_e are at first functions of distance from the skin-depth, and second, a function of the absolute plasma density that controls the thermal conduction of electron power from the skin depth. A third consideration is the non-local transport of electrons in the tail of the energy distribution function which have a longer mean-free-path than the electrons in the bulk of the distribution. For conditions where non-local effects dominate, the convection of electron power from the skin depth to lower in the reactor will be more rapid and efficient.

84

The results discussed in this chapter demonstrate the importance of considering spatial- and time-dependent dynamics when optimizing ICPs sustained with pulsed-power. The dynamics that are experienced during power transitions at positions within the skin depth of the electromagnetic wave launched into the plasma can be very different from those at more remote locations. For plasma processing applications, optimizing the flux of reactants to the substrate is the ultimate goal. In this regard, it is recommended to directly measure the plasma properties by the substrate rather than interpret them from the measurements performed near the power source. This is particularly important when using pulsed power, during which large transients can occur in the skin depth but these transients do not survive to the substrate. Applying a low-high power profile, instead of off-on pulsed power, and moderately extending the power transition time can mitigate the severe oscillations of plasma properties during power transitions.

3.5 Figures
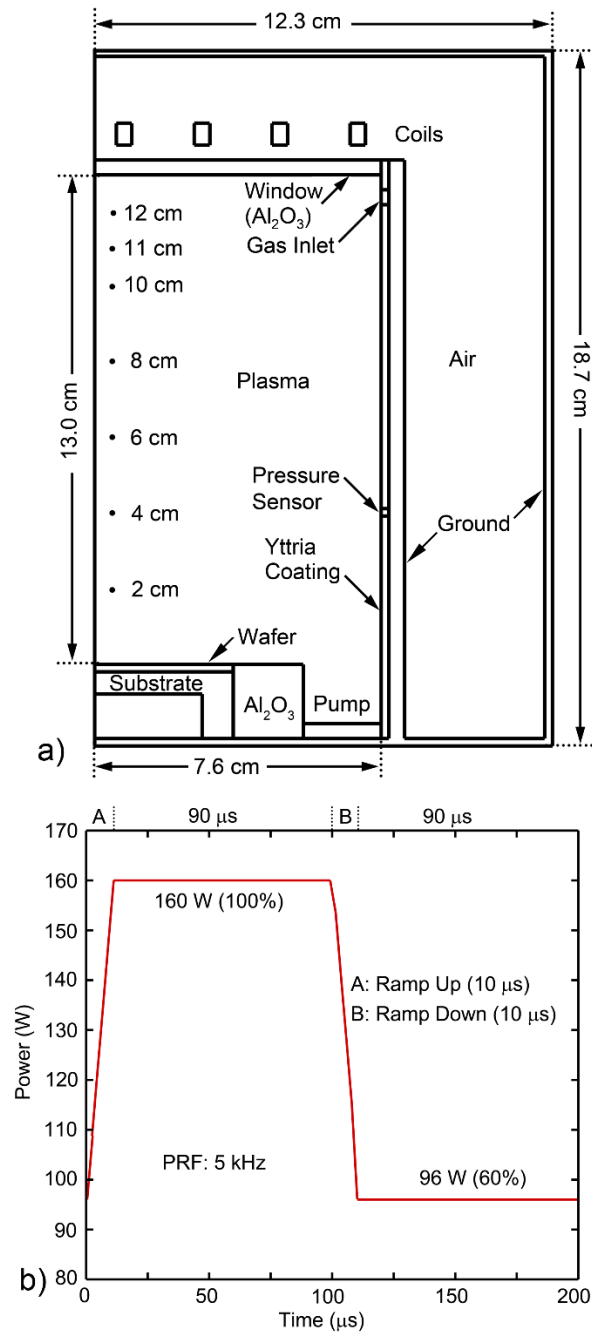
Fig. 3.1 Geometry and power profile used in the model. a) The geometry is an inductively coupled plasma having a 4 –turn antenna. The dots (with dimensions) indicate where plasma properties are shown. b) Pulse power profile for the base case.
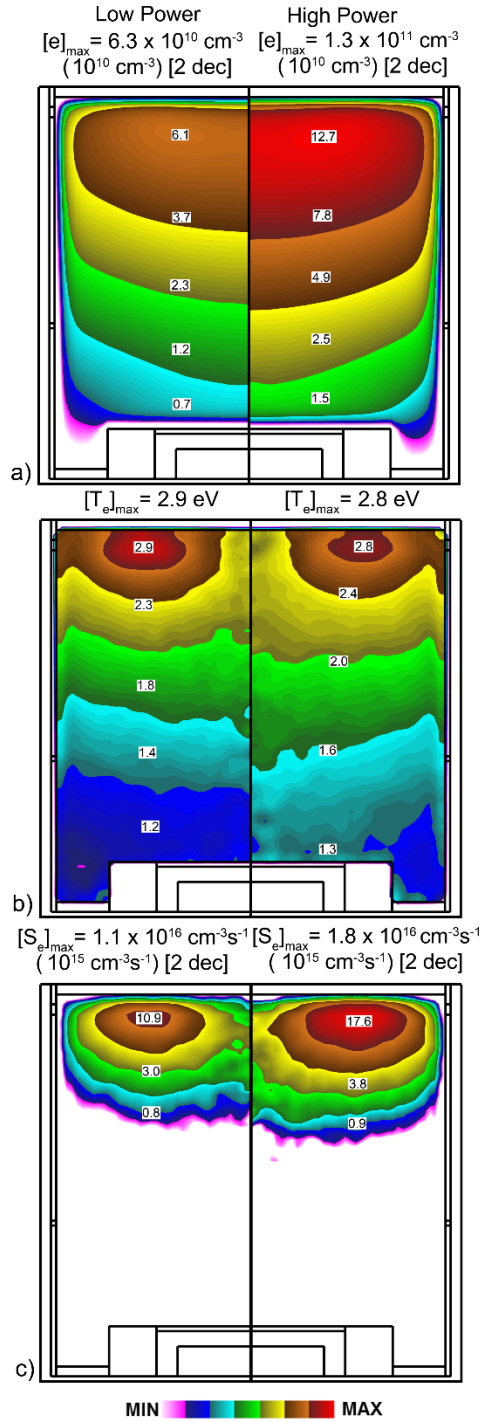
Fig. 3.2 Plasma properties for the base case (Ar/Cl$_2$ = 5/95, 20 mTorr, 96 W - 160 W) at 0 µs (end of the low-power) and 100 µs (end of the high power) during the power pulse. a) Electron density, b) electron temperature and c) ionization source by collisions of bulk electrons. Maximum value, range of values plotted and units for contour labels are indicated in each image.
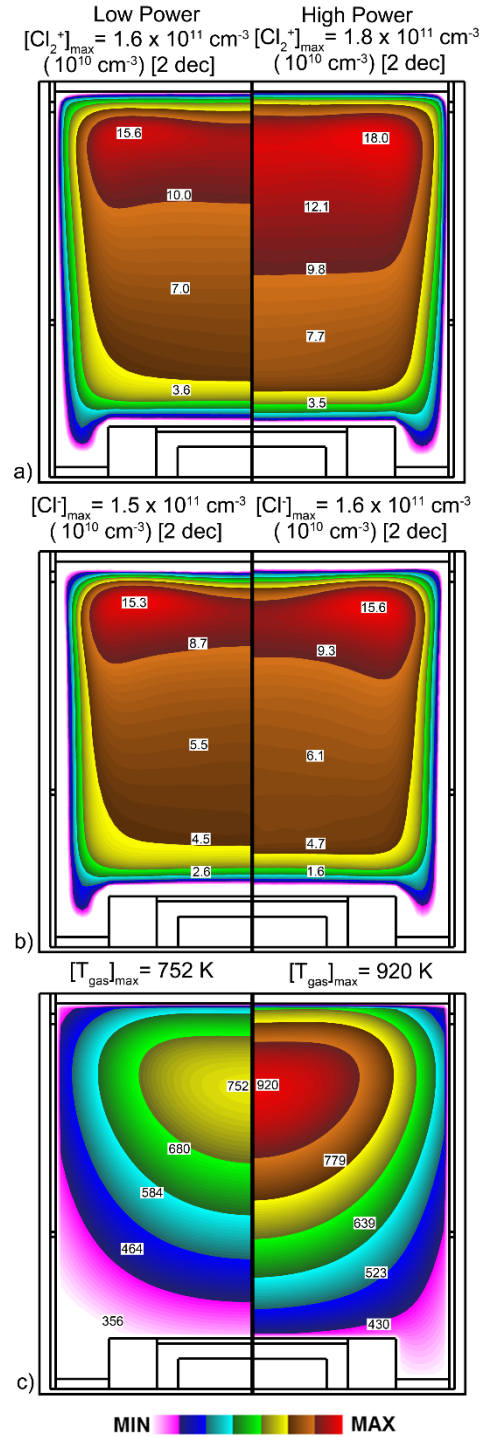
Fig. 3.3 Plasma properties for the base case (Ar/Cl$_2$ = 5/95, 20 mTorr, 96 W – 160 W) at 0 µs (end of the low-power) and 100 µs (end of the high power) during the power pulse. a) Cl$_2^+$ density, b) Cl$^-$ density and c) gas temperature. Maximum value, range of values plotted and units for contour labels are indicated in each image.
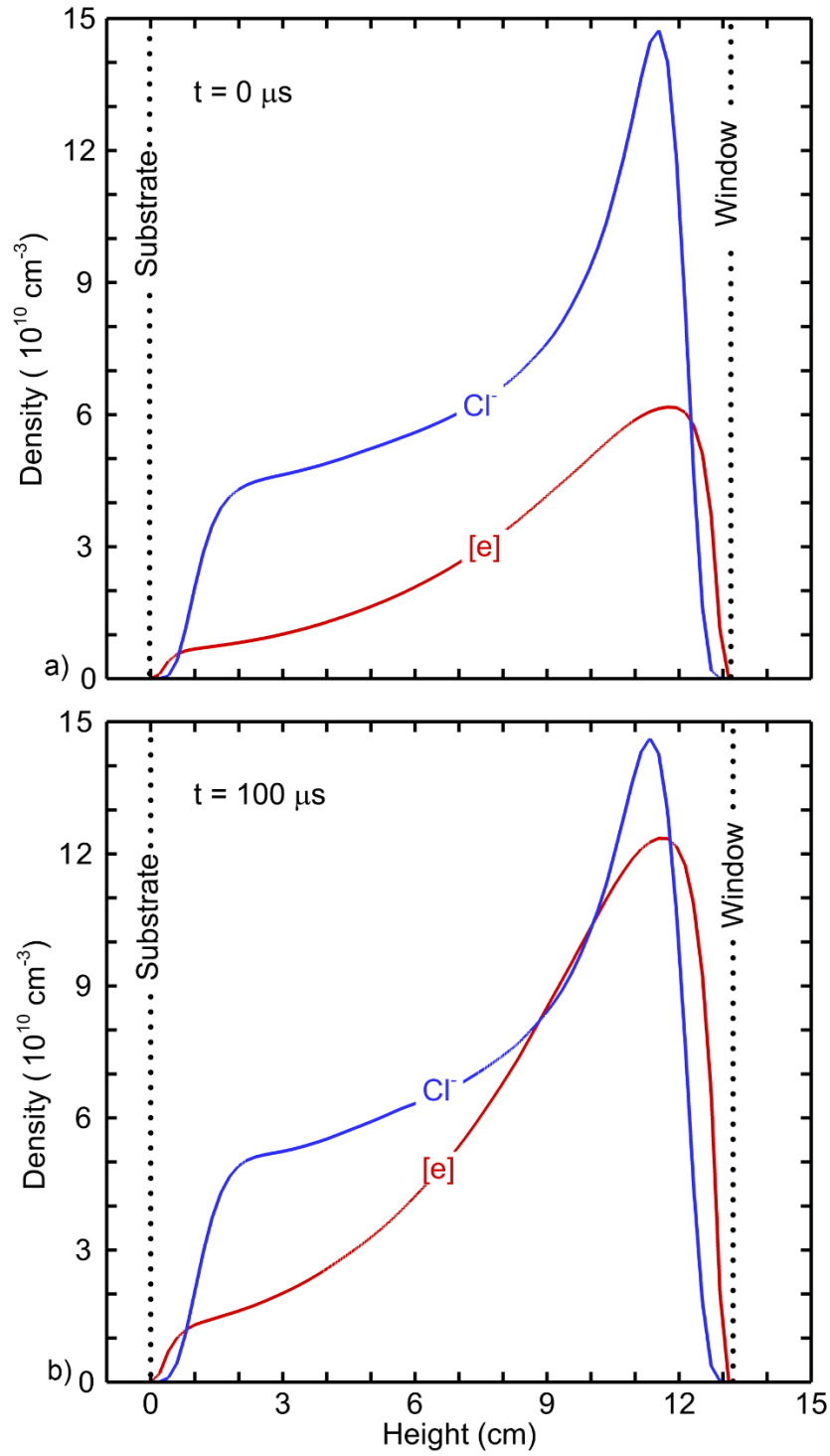
Fig. 3.4 Axial distribution of electron and Cl⁻ densities at mid-radius of wafer at a) end of the low-power pulse (0 μs) and b) end of the high-power pulse (100 μs).
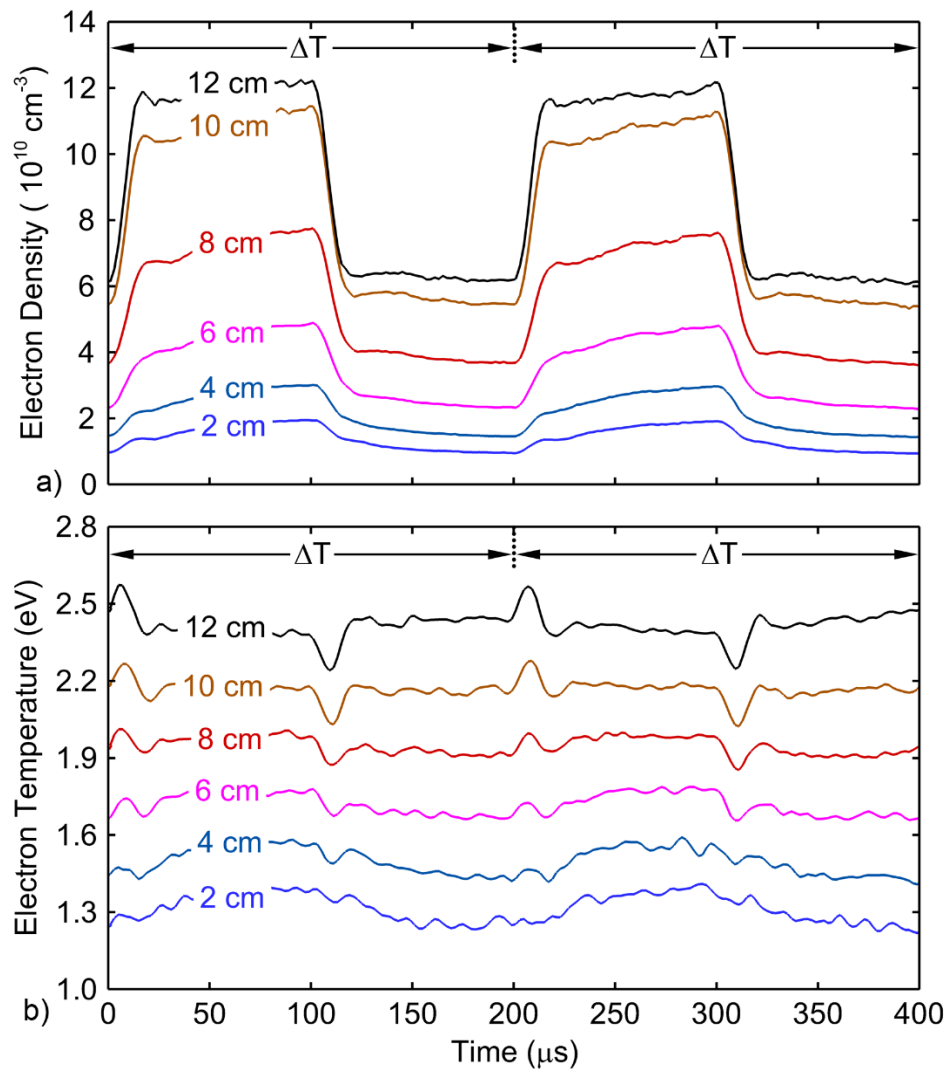
Fig. 3.5 Time dependence of a) electron density and b) electron temperature at different heights above the substrate and mid-radius over 2 pulse periods (Ar/Cl2 = 5/95, 20 mTorr, 96 W - 160 W).   These heights are noted in Fig. 3.1.   The results for electron temperature have been numerically smoothed.
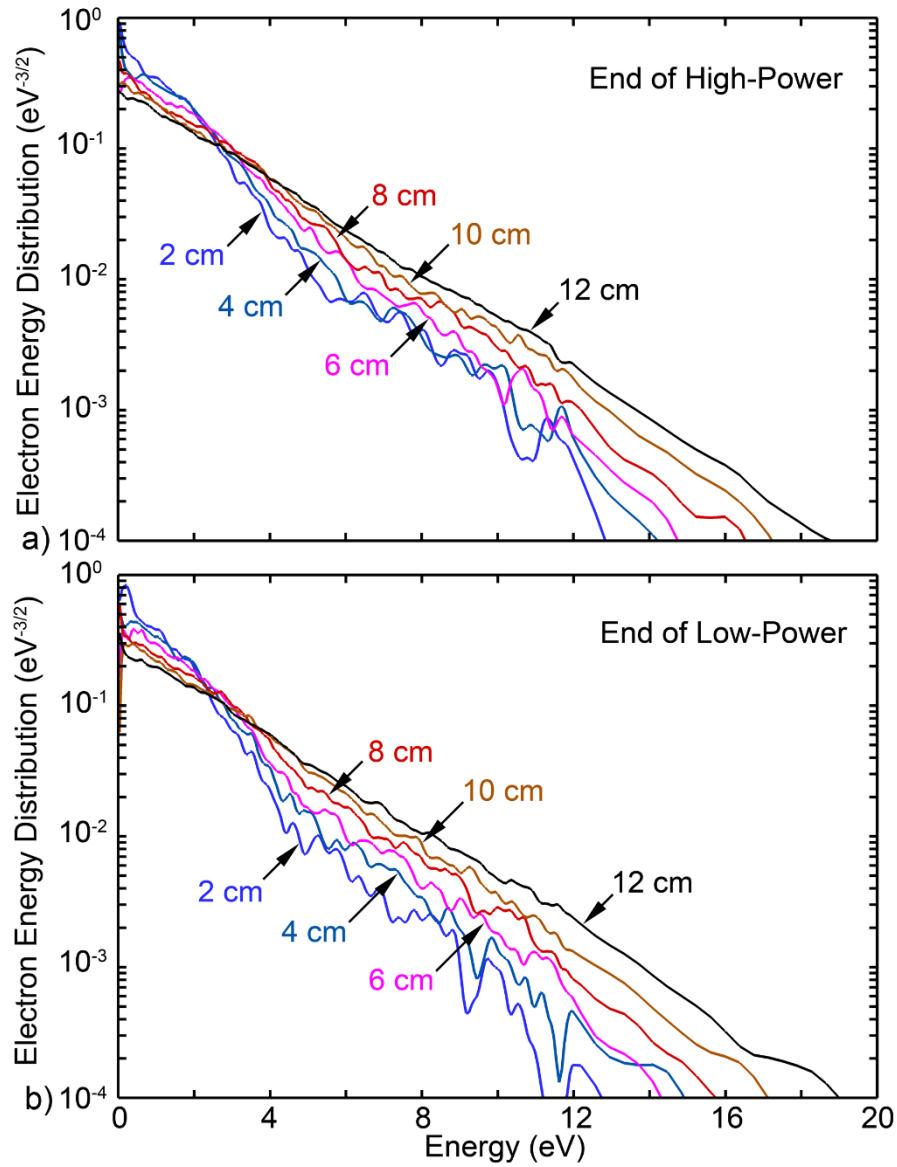
Fig. 3.6 Electron energy distributions (EEDs) at different heights above the substrate at mid-radius of the wafer at the a) end of the low-power pulse (0 μs) and b) end of the high power pulse (100 μs). (Ar/Cl$_2$ = 5/95, 20 mTorr, 96 W - 160 W.) These heights are noted in Fig. 3.1. The EEDs have been numerically smoothed.
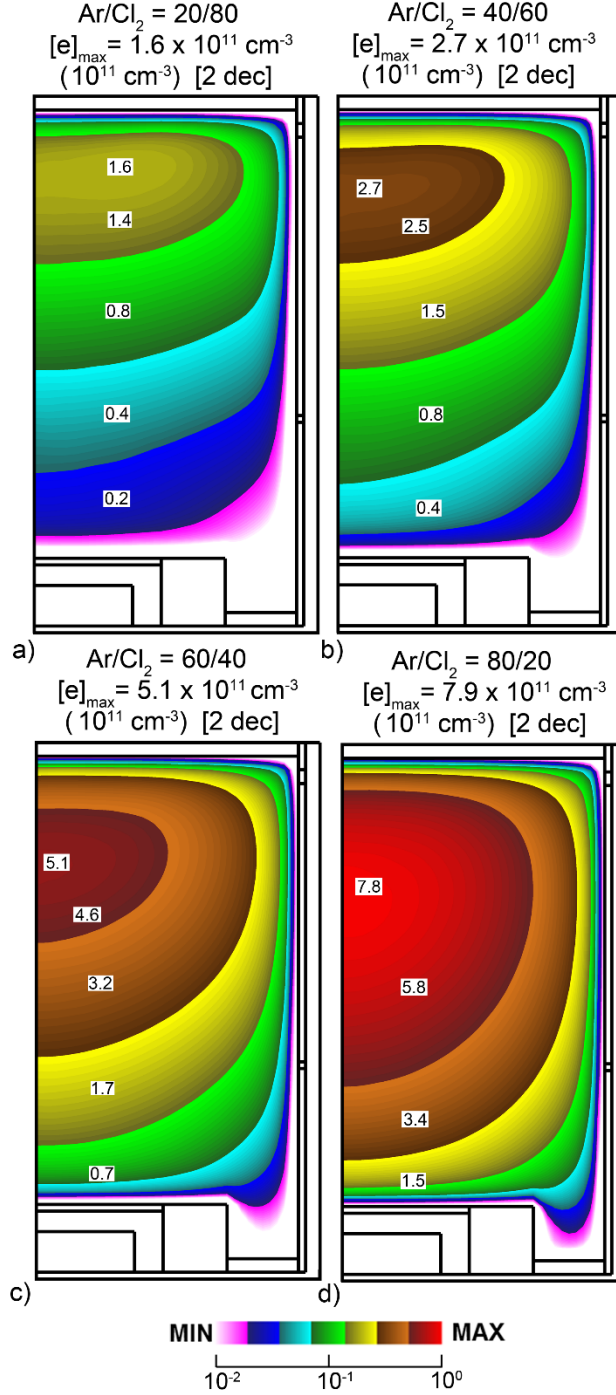
Fig. 3.7 Electron density at the end of the high-power pulse (100 μs) for gas mixtures of Ar/Cl$_2$ = a) 20/80, b) 40/60, c) 60/40 and d) 80/20. (20 mTorr, 96 W - 160 W.) The contours are plotted on a 2-decade log scale with the maximum value in each frame noted. Contour labels have units of 10^{11} cm^{-3}.
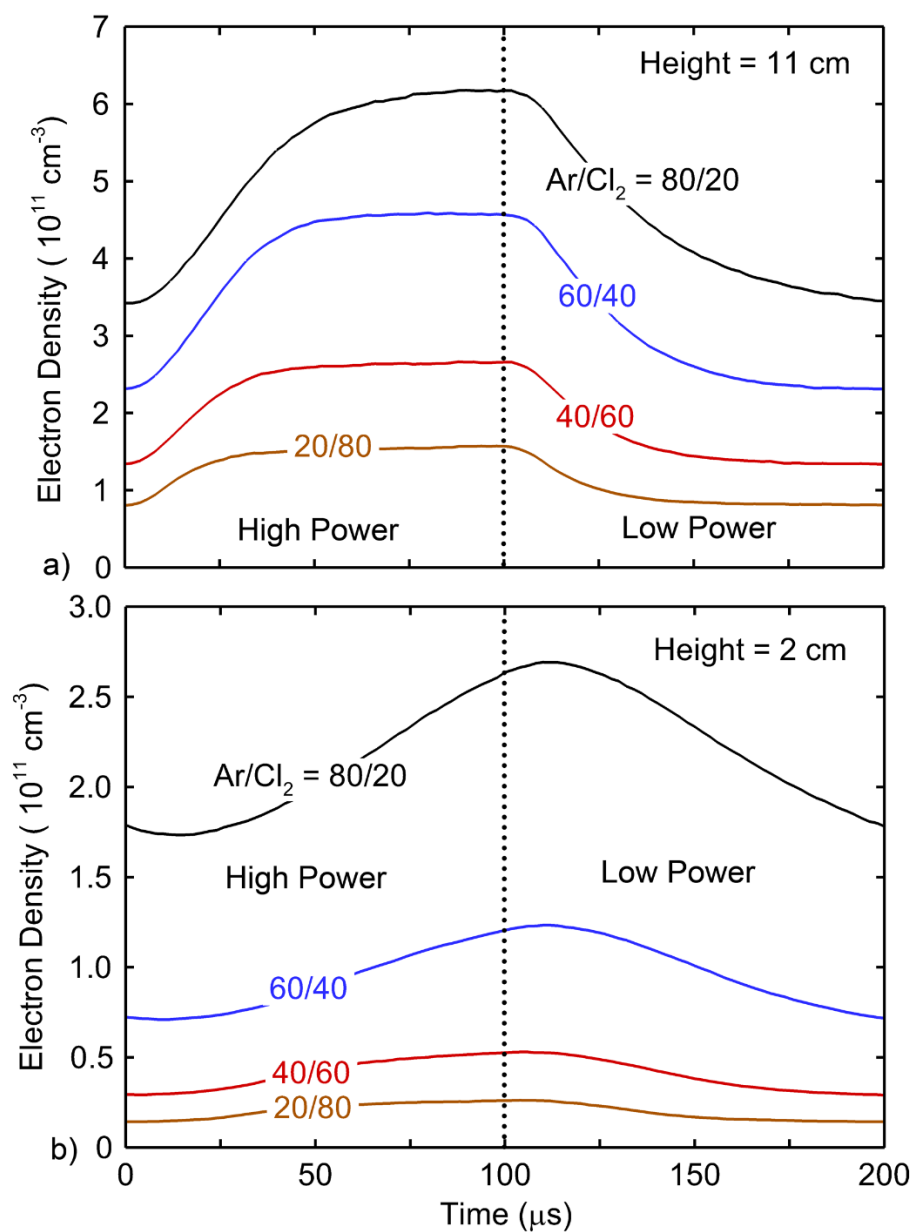
Fig. 3.8 Electron density as a function of time for different values of the Cl_2 mole fraction at a) 11 cm above the substrate and b) 2 cm above the substrate. (20 mTorr, 96 W - 160 W.)
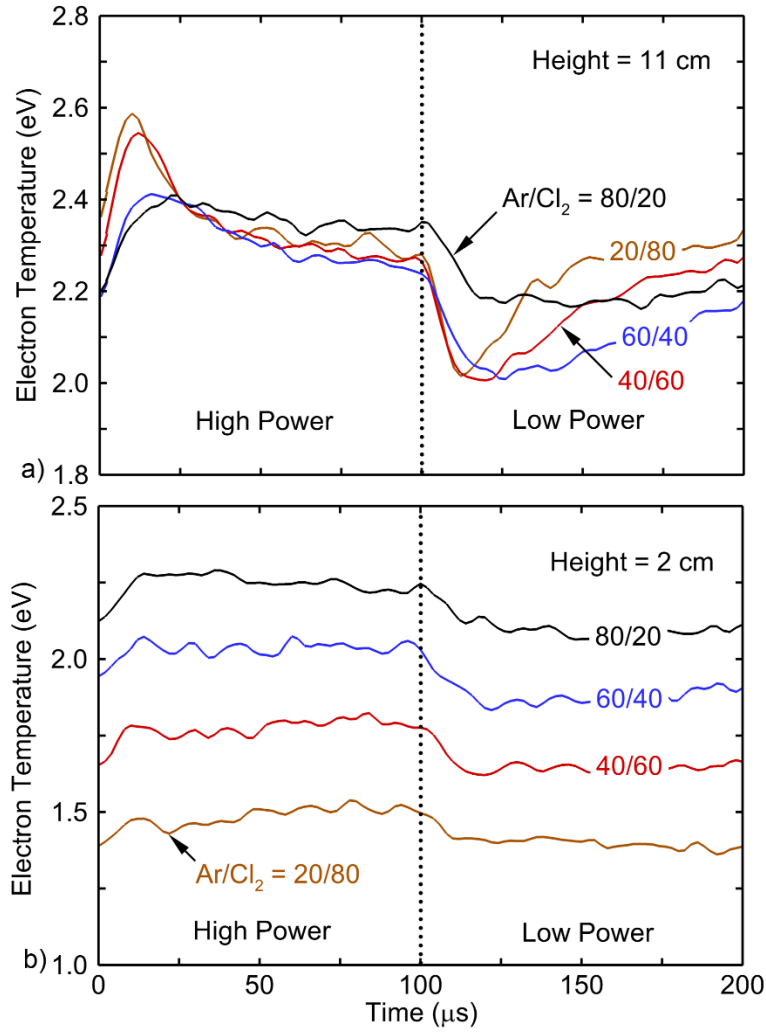
Fig. 3.9 Electron temperature as a function of time for different values of the Cl_2 mole fraction at a) 11 cm above the substrate and b) 2 cm above the substrate. (20 mTorr, 96 W - 160 W.) The values for T_e have been numerically smoothed.
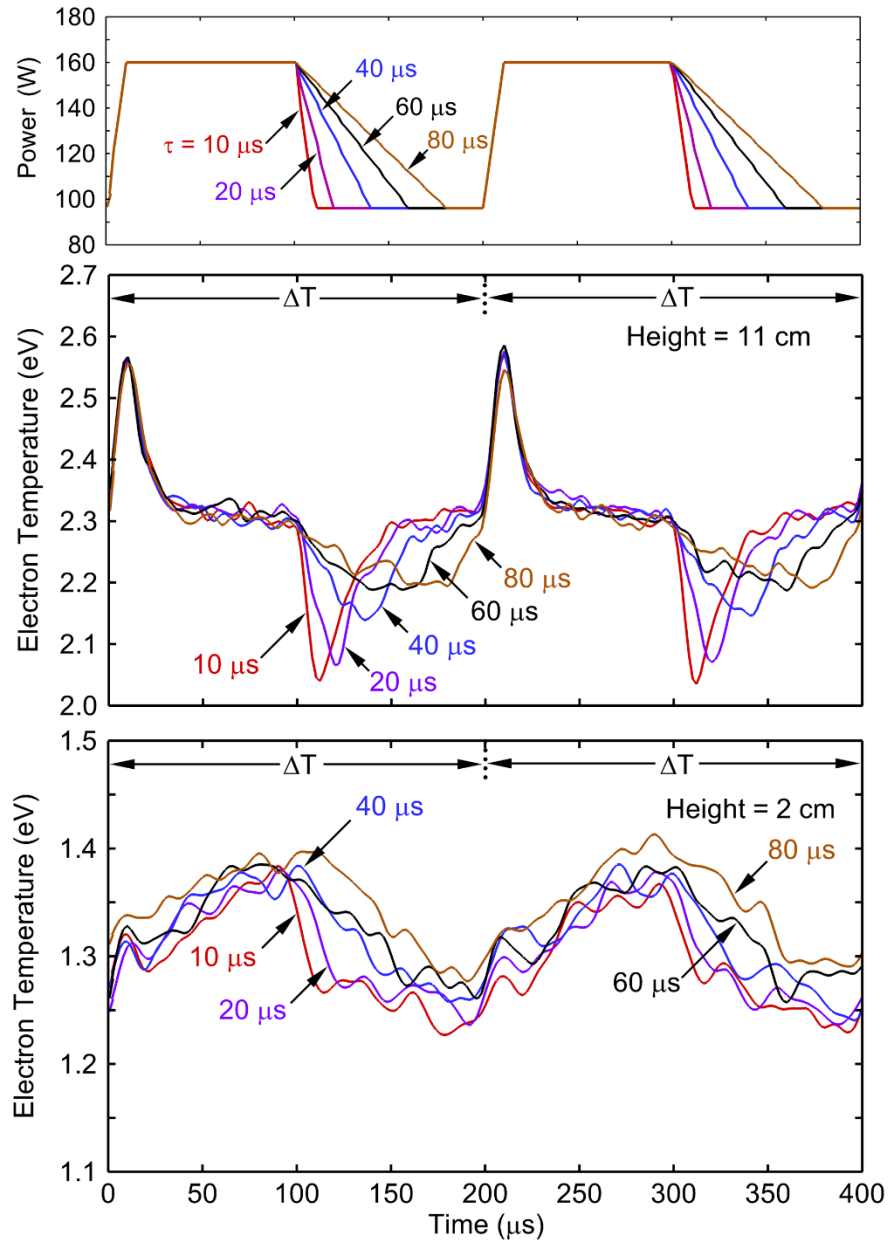
Fig. 3.10 Electron temperature while varying the power ramp-down time. a) Power profiles for ramp-down times from 10 to 80 μs. Electron temperature for different ramp-down times at b) 11 cm above the substrate and c) 2 cm above the substrate. (Ar/Cl$_2$ = 5/95, 20 mTorr, 96 W - 160 W.) These values of T_e have been numerically smoothed.
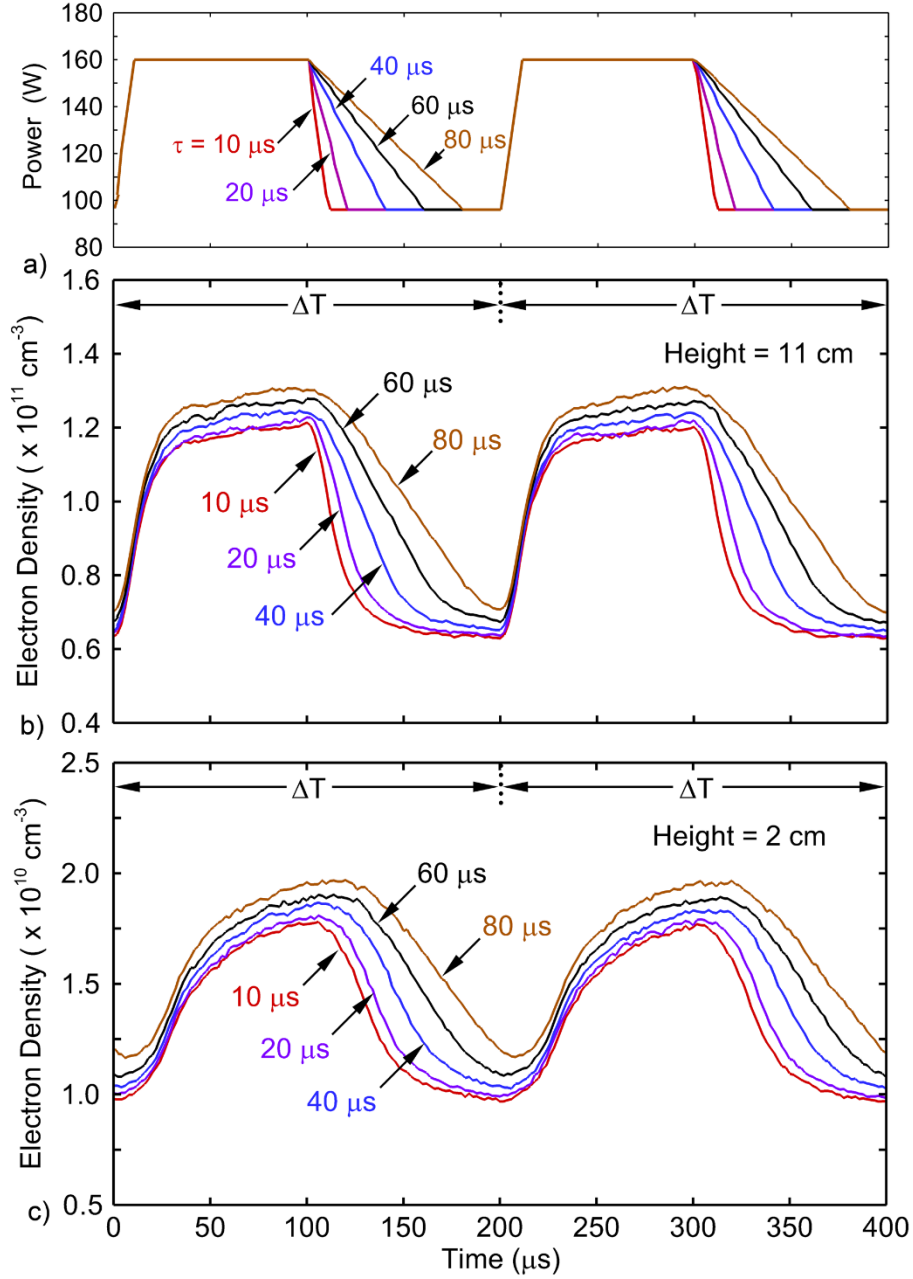
Fig. 3.11 Electron density while varying the power ramp-down time. a) Power profiles for ramp-down times from 10 to 80 µs. Electron density for different ramp-down times at b) 11 cm above the substrate and c) 2 cm above the substrate. (Ar/Cl$_2$ = 5/95, 20 mTorr, 96 W - 160 W.)

96
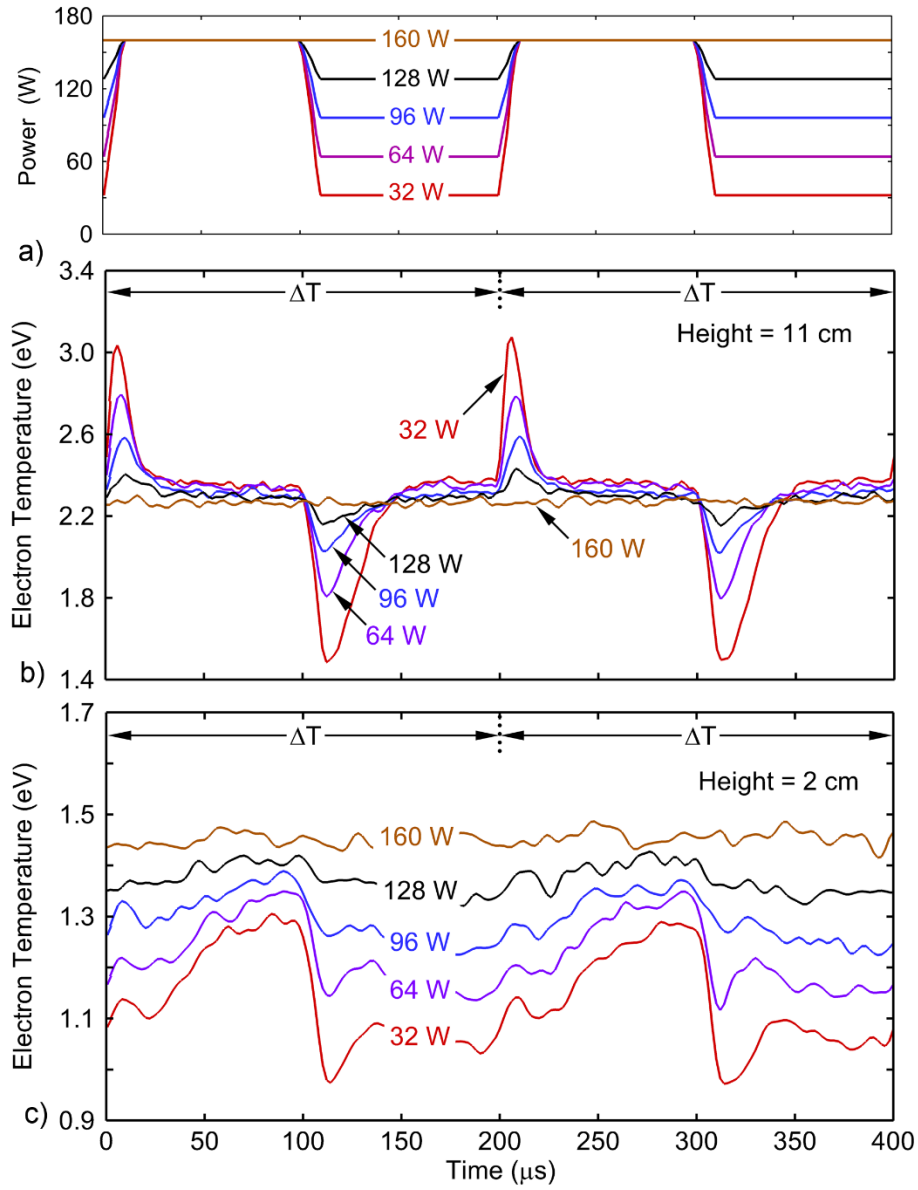
Fig. 3.12 Electron temperature while varying the low power during the cycle. a) Power profiles for low powers of 32 W to 160 W. Electron temperature for different low powers at b) 11 cm above the substrate and c) 2 cm above the substrate. (Ar/Cl$_2$ = 5/95, 20 mTorr, 160 W high power.) These values of T_e have been numerically smoothed.
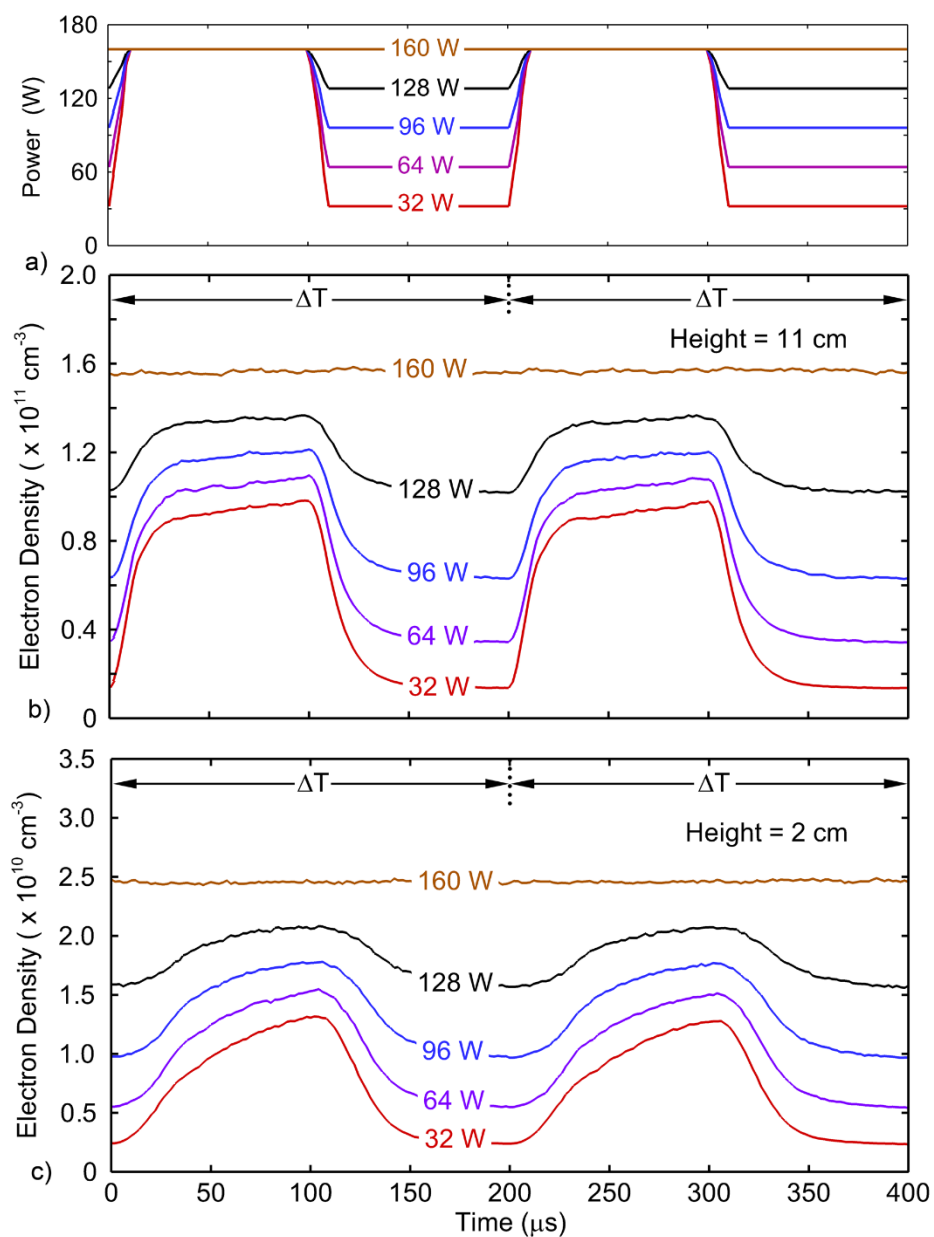
Fig. 3.13 Electron density while varying the low power during the cycle. a) Power profiles for low powers of 32 W to 160 W. Electron density for different low powers at b) 11 cm above the substrate and c) 2 cm above the substrate. (Ar/Cl$_2$ = 5/95, 20 mTorr, 160 W high power.)
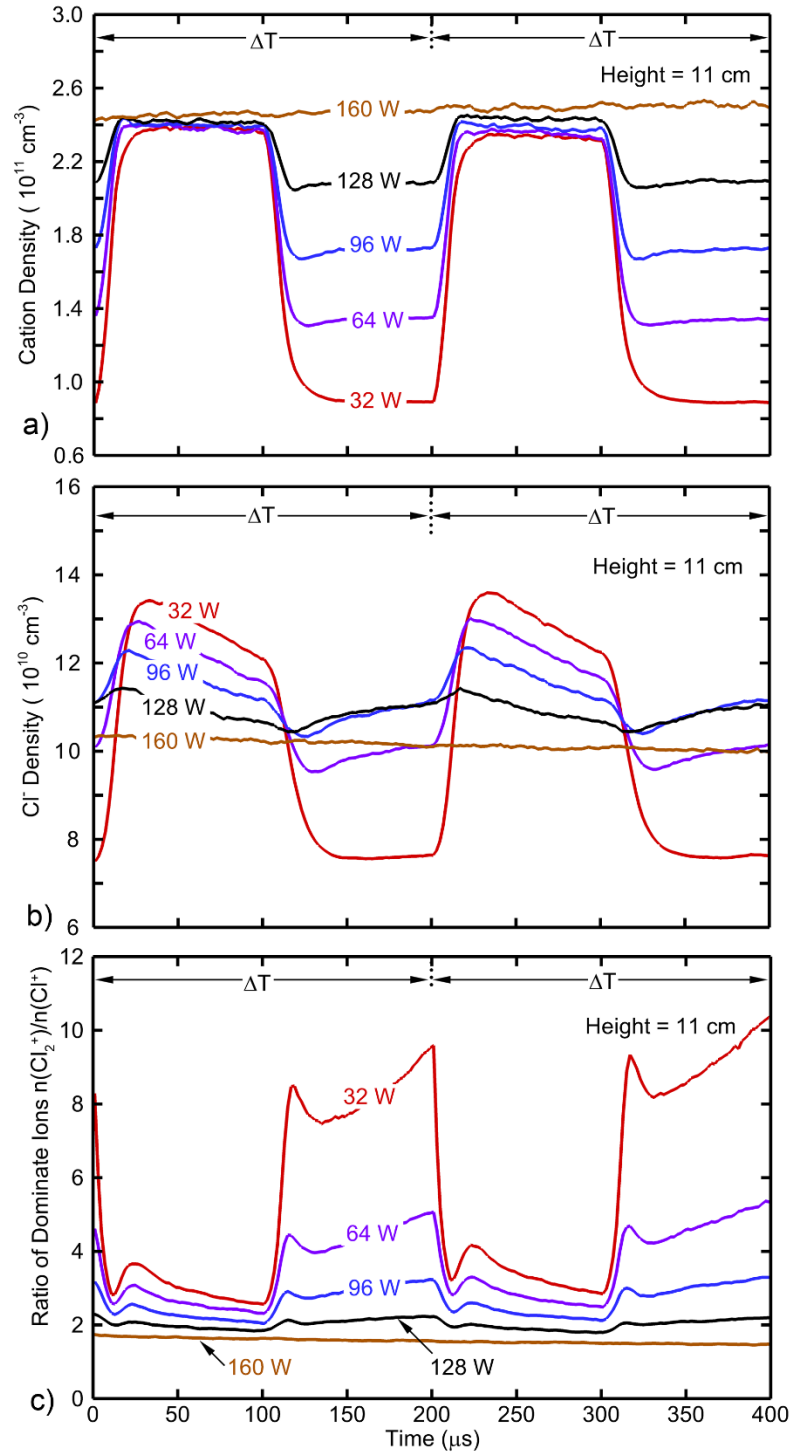
Fig. 3.14 Plasma properties 11 cm above the substrate while varying the low power during the cycle. (Ar/Cl$_2$ = 5/95, 20 mTorr, 160 W high power.) a) Total cation density, b) Cl$^-$ density and c) ratio $\alpha = n_{Cl_2^+}/n_{Cl^+}$.

3.6 References

1. A. Agarwal, P. J. Stout, S. Banna, S. Rauf, and K. Collins, J. Vac. Sci. Technol. A **29**, 011017 (2011).

2. A. Agarwal, P. J. Stout, S. Banna, S. Rauf, and K. Collins, Appl. Phys. Lett. **100**, 044105 (2012).

3. S. Banna, A. Agarwal, G. Cunge, M. Darnon, E. Pargon, and O. Joubert, J. Vac. Sci. Technol. A **30**, 040801 (2012).

4. V. M. Donnelly, and A. Kornblit, J. Vac. Sci. Technol. A **31**, 050825 (2013).

5. K. J. Kanarik, T. Lill, E. A. Hudson, S. Sriraman, S. Tan, J. Marks, V. Vahedi, and R. A. Gottscho, J. Vac. Sci. Technol. A **33**, 020802 (2015).

6. T. Ma, T. List, and V. M. Donnelly, J. Vac. Sci. Technol. A **36**, 031305 (2018).

7. E Despiau-Pujo, M. Brihoum, P. Bodart, M. Darnon, and G. Cunge, J. Phys. D: Appl. Phys. **47**, 455201 (2014).

8. J. P. Booth, H. Abada, P. Chabert, and D. B. Graves, Plasma Sources Sci. Technol. **14**, 273 (2005).

9. C. Petit-Etienne, E. Pargon, S. David, M. Darnon, L. Vallier, O. Joubert, and S. Banna, *J.* Vac. Sci. Technol. B **30**, 040604 (2012).

10. S. Banna et al., IEEE Trans. Plasma Sci. **37**, 1730 (2009).

11. Y. Ishikawa, Y. Ichihashi, S. Yamasaki, and S. Samukawa, J. Appl. Phys. **104**, 063306 (2008).

12. C. Petit-Etienne, M. Darnon, L. Vallier, E. Pargon, G. Cunge, F. Boulard, and O. Joubert, J. Vac. Sci. Technol. B **28**(5), 926 (2010).

13. C. Petit-Etienne, M. Darnon, P. Bodart, M. Fouchier, G. Cunge, E. Pargon, L. Vallier, O. Joubert, and S. Banna, J. Vac. Sci. Technol. B **31**, 011201 (2013).

14. P. Bodart, M. Brihoum, G. Cunge, O. Joubert, and N. Sadeghi, J. Appl. Phys. **110**, 113302 (2011).

15. B. Ramamurthi, and D. J. Economou, J. Vac. Sci. Technol. A **20**, 467 (2002).

16. S. Kim, M. A. Lieberman, A. J. Lichtenberg, and J. T. Gudmundsson, J. Vac. Sci. Technol. A **24**, 2025 (2006).

17. E. G. Thorsteinsson, and J. T. Gudmundsson, J. Phys. D: Appl. Phys. **43**, 115202 (2010).

18. S. Ashida, M. R. Shim and M. A. Lieberman, J. Vac. Sci. Technol A. **14**, 391 (1996).

19. M. Darnon, G. Cunge, and N. S. J. Braithwaite, Plasma Sources Sci. Technol. **23**, 025002 (2014).

20. J. B. Boffard, S. Wang, C. C. Lin and A. E. Wendt, Plasma Sources Sci. Technol. **24**, 065005 (2015).

21. P. Chabert, A. J. Lichtenberg, M. A. Lieberman, and A. M. Marakhtanov, Plasma Scources Sci. Technol. **10**, 478 (2001).

22. G. Cunge, B. Crowley, D. Vender, and M. M. Turner, Plasma Sources Sci. Technol. **8**, 576 (1999).

23. T. List, T. Ma, P. Arora, V. M. Donnelly, and S. Shannon, Plasma Sources Sci. Technol. **28**, 025005 (2019).

24. M. J. Kushner, J. Phys. D: Appl. Phys. **42**, 194013 (2009).

25. P. Tian, and M. J. Kushner, Plasma Sources Sci. Technol. **26**, 024005 (2017).

26. G. Cunge, D. Vempaire, and N. Sadeghi, Appl. Phys. Lett. **96**, 131501 (2010).

Chapter 4: Power Matching to Inductively Coupled Plasmas[†]

4.1 Introduction

The combined impedance of the plasma reactor and the plasma in low pressure plasma processing for microelectronics fabrication, using both capacitively and inductively coupled plasmas (ICPs), is typically non-linear [1-2]. Common combined impedances can range from 100's of mΩ to 100's of Ω and up to kilo-ohms of reactance. These conditions make it difficult to deliver power to the plasma from conventional power supplies and transmission lines that typically have fixed impedances of 50-75 Ω. The electric field reflection coefficient, Γ_R, is the electric field reflected from the plasma reactor relative to the electric field delivered by the power supply through a transmission line (typically a coaxial cable) to the plasma reactor. The reflection results from the output impedance of the power supply and transmission line differing from that of the plasma reactor,

$$\Gamma_R = \frac{Z_L - Z_0}{Z_L + Z_0},\tag{4.1}$$

where Z_L is the impedance of the load (in this case, the combined impedance of the plasma reactor and the plasma) and Z_o is the output impedance of the power supply and transmission line [3]. Since Z_L has reactive contributions, Γ_R typically has both real and imaginary components from which both the magnitude and relative phase of the forward and reflected waves can be

---

[†] The results discussed and portion of the text appearing in this chapter were previously published in the paper by Chenhui Qu *et al.*, "Power matching to pulsed inductively coupled plasmas", J. Appl. Phys. 127, 133302 (2020).

determined. Typically only the magnitude of reflection $|\Gamma_R|$ is used to characterize matching efficiency.

The usual remedy to maximize power transfer to a plasma processing reactor (and minimize reflection) is to employ an impedance matching network (IMN) between the transmission line and plasma reactor [4-6]. The IMN usually contains reactance (capacitors and inductors) both in series and parallel to the load with the goal of making the input impedance to the IMN be the same as the power supply termination impedance and transmission line impedance. In doing so, the reflection coefficient is minimized. In practice impedance matching is complicated by both the non-linear characteristics of the plasma and the increasingly common use of multiple frequencies and pulsed power. Even if driven with a single frequency, the non-linear response of the plasma to that single frequency power will produce higher harmonics in current, thereby making reproducible impedance matching more challenging [7,8].

The use of pulsed power further complicates matching as the plasma contribution to Z_L can change by orders of magnitude during the pulsed cycle. For example, pulsed ICPs as used in microelectronics fabrication operate at pressures of tens of mTorr in attaching gas mixtures such as Ar/Cl_2 powered with radio frequency (RF) supplies of a few to tens of MHz. The pulsed repetition frequency (PRF), pulses per second, can be hundreds of Hz to tens of kHz. Duty cycle (DC), the fraction of time the power is applied per cycle, can be 10-50%. The end result is that the electron density at the time the power is applied at the leading edge of the pulse can be as low as 10^8 cm^{-3} whereas later during the pulse, the electron density can exceed 10^{11} cm^{-3} [9,10]. These densities can increase across these three decades during a few to 10s or 100s of μs depending on the power delivery system and reactor design. The reactor contribution to Z_L for an ICP is typically dominated by the positive reactance of the inductance of the antenna, though

the antenna will also have resistance.

Z_L for a pulsed ICP has additional dynamics due to the E-to-H (capacitive-to-inductive) transition that occurs during the transient in plasma density at the beginning of a pulsed period [11-15]. If the electron density at the beginning of a power pulse is too low, the electromagnetic skin depth, δ_P, may exceed the dimensions of the reactor which then makes inductive coupling of power from the antenna problematic. For these conditions, the antenna simply acts as an electrode which electrostatically and capacitively couples power into the plasma through the dielectric window between the antenna and the plasma [11]. This is the E-mode during which power can be dominantly coupled into the plasma by sheath oscillation (much like a capacitively coupled plasma) with power mainly deposited by ion acceleration from the plasma into the dielectric window under the antenna [15]. During the capacitive E-mode, the reactance of the plasma is negative. As the electron density increases, δ decreases which increases the fraction of power that is inductively coupled until the power is dominantly delivered by electron acceleration in the electromagnetic field within δ of the antenna. This is the H-mode during which the reactance of the plasma is positive. In practice there may be mixed-mode coupling, both E-mode and H-mode during quasi-steady state operation of the ICP [11,12]. The degree of E- and H-mode coupling depends on factors such as the voltage across the antenna, the proximity of antenna to the plasma, the shape of the antenna, gas pressure and composition, and the use of a Faraday shield between the antenna and plasma [16].

The E-H transition in ICPs has been addressed both experimentally and theoretically [17-25]. When measuring the electron energy distribution (EED), Chung et.al. found that during E-mode, the EED evolves from bi-Maxwellian to Druyvestein-like structure when increasing pressure [26]. During the H-mode, having a significantly larger electron density with a higher

rate of e-e collisions, the EED remains essentially as a Maxwellian. To smoothen the severity of the E-H transition, Singh et al. investigated use of a Faraday shield to minimize capacitive coupling from the antenna [16]. When using the Faraday shield, the plasma potential at low power was lower, indicating lower capacitive coupling while the electron density was lower. During H-mode, the antenna current and voltage decreased when using the Faraday shield. Had the plasma been operating purely in H-mode, there would not have been a decrease in current when using the Faraday shield, which then implies that even in H-mode, there was mixed E- and H-mode coupling.

Kempkes et al. investigate the effect of the power modulation on the E-H transition using rectangular and triangular power waveforms [27]. They found that even with smoothly varying power (triangular waveform) abrupt E-H transitions occurred. Kawamura et al. performed 2-dimensional (2D) simulations of E-H transitions in ICPs sustained in Cl_2 [28]. They found ionization instabilities and modulations in electron density attributed to rapid transitions between E- and H-modes.

The E-H transition often displays hysteresis behavior. The transition between the low E-mode electron density to the high H-mode electron density occurs at different powers if increasing power (occurs at a higher power) or decreasing power (occurs at a low power). The power deposition from both inductive and capacitive coupling was theoretically analyzed by Lee et al. [29], who found that the pressure and the dimensions of the reactor affected the power for the E-H transition. The combined effects of electron density, collision frequency and skin depth of the electromagnetic wave contributes to nonlinear dependence of mode transition on operating conditions. The hysteresis of the E-H transition was experimentally investigated by Daltrini et al. [30]. They suggest that rather than being an intrinsic characteristic of the plasma, the

hysteresis behavior can be affected by the power loss in the matching system, suggesting the need to include circuit analysis when investigating these transitions.

The E-to-H transition is another complicating factor in matching pulsed power to the ICP reactor. The change in Z_L due to the E-to-H transition in addition to the reduction in the resistance of the plasma is typically over shorter times than the components in the match box can be changed. The end result is that power delivery cannot be efficiently matched to the plasma reactor during the entire pulsed cycle. The values of components in the match box are typically chosen to match at a particular time during the pulsed cycle – this is called set-point matching. If the match is chosen early in the pulsed period, the E-mode may be emphasized while there is a mismatch during the latter part of the pulsed cycle. If the set-point is late during the pulse period, the E-mode may be suppressed but there is also a longer time to ramp up the plasma density when power is mismatched early in the pulse.

In this chapter, some results from a computational investigation of the dynamics of power matching to pulsed ICPs of the type used in microelectronics processing (etching, deposition) are discussed. A model for the circuit and match box has been employed in a 2-dimensional simulation of the ICP. It was found that under perfect matching conditions, there is a smooth transition between the E- and H-modes, in contrast to several experimental results. This suggests that a sharp transition between modes is not a fundamental plasma transport issue, but rather may be related to power delivery. It was found that when using pulsed power, the power delivery is highly dependent on the time during the pulse at which the set-point is matched. Matching early in the pulsed period leads to a faster re-ignition of the plasma, while emphasizing E-mode characteristics during the onset of the pulse. There is also poor matching during the H-mode. Matching later in the pulsed period leads to better power delivery overall, at the cost of longer

106

ignition delay. The rapid application of power when operating in E-mode can launch electrostatic waves due to the need to establish a sheath to dissipate the applied voltage. The pulsed duty-cycle, matchbox parameters, and antenna shape play key roles in power matching inductively coupled plasmas.

A brief model description is provided in Sec. 4.2. Matching to pulsed ICPs with E-H transitions is discussed in Sec. 4.3. Concluding remarks are in Sec. 4.4.

4.2 Description of the Model

This computational investigation was performed using the Hybrid Plasma Equipment Model (HPEM) complemented by a model for the matchbox. The HPEM is discussed in detail in Chapter 2 and Ref. [31], thereby only a brief description will be provided here. In this case we utilize three modules – the Electromagnetics Module (EMM), Electron Energy Transport Module (EETM) and the Fluid-Kinetics Poisson Module (FKPM). The frequency domain wave equation for inductively coupled electric field is solved in the EMM. In this 2-dimensional simulation, the current flowing in the antenna is in the azimuthal direction θ, producing components at the fundamental frequency of the magnetic field in the (r,z) [radius, height] directions and of the electric field, E_θ, in the θ direction. The conduction currents are provided by a circuit model. The Poisson's equation is solved in the FKPM coincident with the update of all charged and neutral species densities. Complex conductivities are transferred back to the EMM to solve the wave equation.

The schematic of the circuit representation for the matchbox, reactor and plasma is shown in Fig. 4.1. As described in Sec. 2.1.1, the antenna is represented as a discretized transmission line in the circuit model. Its inductance is calculated based on its geometry, and divided into 100

107

segments. Each of these segments has an fraction of the total inductance of the antenna. In this work, four paths of power flow are considered: power loss in the matchbox (P_M), power loss on the antenna (P_A), inductively coupled power (P_I), and capacitively coupled power (P_C).

An ideal matching condition is represented when the power refection coefficient, Γ, is zero. The circuit components for such a condition are solved as $Z_M = Z_0$, where Z_M is the input impedance of the matchbox and Z_0 is the intrinsic impedance of the power source. The choices of the circuit components in the matchbox are circuit dependent. That is, the solutions of the circuit components are subject to the architecture chosen for the matchbox. For the matchbox used in this chapter as shown in Fig. 4.1, the capacitors C_P and C_S are adjusted to approach the perfect matching, and the solutions are:

$$C_p = \frac{-B \pm \sqrt{B^2 - 4AC}}{2A}, \tag{4.1}$$

$$C_s = -\frac{\mathrm{Re}(Z_L)^2 \left(1 - \omega^2 L_p C_p\right)^2 + \left[\omega C_p |Z_L|^2 - \mathrm{Im}(Z_L)\left(1 - \omega^2 L_p C_p\right)\right]^2}{\omega\left(1 - \omega^2 L_p C_p\right)|Z_L|^2 \left[\omega C_p |Z_L|^2 - \mathrm{Im}(Z_L)(1 - \omega^2 L_p C_p)\right]}, \tag{4.2}$$

where

$$A = [\mathrm{Re}(Z_0) - R_M]\left\{|Z_L|^2 \omega^4 L_p^2 + \omega^2 |Z_L|^4 + 2\omega^3 L_p \mathrm{Im}(Z_L)|Z_L|^2\right\} - \mathrm{Re}(Z_L)\omega^4 L_p^2 |Z_L|^2, \tag{4.3}$$

$$B = 2\omega^2 L_p \mathrm{Re}(Z_L)|Z_L|^2 - 2\omega|Z_L|^2\left[\mathrm{Re}(Z_0) - R_M\right]\left[\omega L_p + \mathrm{Im}(Z_L)\right], \tag{4.4}$$

$$C = \left\{\left[\mathrm{Re}(Z_0) - R_M\right] - \mathrm{Re}(Z_L)\right\}|Z_L|^2, \tag{4.5}$$

4.3 Matching to Pulsed ICPs with E-H Transitions

For computationally investigating the fundamental phenomena of E-H matching, we chose a simple ICP geometry and a relatively small chamber. This layout for an ICP reactor

powered by a spiral planar antenna is a standard design used for plasma assisted semiconductor fabrication [35-37]. Industrial systems are typically larger to accommodate wafers up to 30 cm in diameter. Our choice of a smaller chamber for this investigation was based on wanting a fine enough mesh to capture the dynamics of the E-H transitions while also enabling computation of a sufficient number of pulsed periods to reach the quasi-steady stated. The details of our investigation are sensitive to the size and topology of the reactor. For example, antenna and chamber impedance are both functions of size and layout, which would affect the specific values of match box parameters, and necessitate a different termination impedance. The spacing of the antenna from the dielectric window affects capacitive coupling, as discussed below. Having said that, the systematic trends we discuss apply to more complex and larger reactors. For example, we have performed limited studies on industrial size ICP reactors [38] and the systematic trends we discuss here are essentially the same.

A schematic of the reactor is shown in Fig. 4.2. The chamber has an internal diameter of 22.5 cm, height (substrate to window) of 12 cm and is powered by a 3-turn antenna having radii of 2.5, 5.3 and 8.0 cm. The coils have thickness of 0.45 cm and height of 1.15 cm, and sit above the 0.8 cm thick quartz window ($\varepsilon/\varepsilon_0 = 4$) with an air gap of 0.4 cm. The total inductance of the antenna is $L_C = 0.95$ μH. The antenna-plasma coupling coefficient is $k_C = 0.75$. The entire inner surface of the window serves as gas inlet showerhead with the pump port occupying an annulus between 6.9 and 11.1 cm on the bottom of the chamber. A pressure sensor is located in the outer wall 2 cm above the pump port. All other surfaces are grounded metal.

Unless otherwise noted, the gas mixture is $Ar/Cl_2 = 65/35$ at a pressure of 25 mTorr. Ar/Cl_2 gas mixtures are commonly used for conductor etching. The gas inlet flowrate is 200 sccm. The outlet flow rate is adjusted so that the pressure at the sensor is 25 mTorr. As

discussed below, our results are sensitive to the conductivity of the plasma at the start of the power pulse, and that conductivity is sensitive to gas mixture. When using pure Cl_2 plasmas, a thermal electron attaching gas, the system can transition to an ion-ion plasma during the afterglow with a negligible electron density. These conditions then require "re-ignition" of the plasma on every power pulse. Although this may in fact be the case for many industrial systems, the re-ignition requirement adds another constraint and complexity. We therefore chose a gas mixture for which there would be significant change in conductivity during the afterglow but not to the degree that re-ignition is required.

The reaction mechanism is the same as discussed in Ref. 32. An important point for the study in this chapter is that Cl_2 is a thermal electron attaching gas for which the rate coefficient for dissociative electron attachment increases with decreasing electron temperature, T_e. So for otherwise the same conditions, rates of attachment are small when power is applied during a pulse and T_e is large. Rates of attachment are large when the power is off and T_e is small.

The fixed circuit elements are coil resistance $R_C = 0.1$ Ω, termination impedances $C_T = 100$ nF and $L_T = 5$ nH, and inductance on match box $L_P = 100$ nH. The internal resistance of the match box was neglected by setting $R_M = 10^{-6}$ Ω so that P_M is negligible. This allows for the independent study of impedance matching impact on plasma transients. In practice, matching network impedances can have 100s to 1000s of mΩ of real resistance, and consume a significant amount of power delivered by the supply. Typically, these dissipative losses are accounted for in the series elements, where the larger dissipative components tend to reside, and where the current through the elements tends to be higher, as opposed to the shunt components. The inner coil of the antenna was connected to the match box, and the outer coil of the antenna was connected to ground through the series termination components C_T and L_T.

4.3.1 Continuous Power Baseline

With the base case values for circuit and operating conditions, the continuous wave (CW) characteristics of the ICP reactor were first investigated as a function of power delivered from the supply. Using perfect match values for C_P and C_S, $\Gamma = 0$, and $P_S = P_T$. The electron density, inductive power and capacitive power are shown in Fig. 4.3 for a total power deposition of 5 W and 200 W. Note that the capacitive power deposition plotted is actually the time average of the capacitive and resistive (bulk) power deposition. The calculation of local power deposition of $p = \vec{j} \cdot \vec{E}$ is unable to distinguish between the capacitive and resistive heating. Given the spatial distribution and the negative sign of the reactance of Z_k, the capacitive power is clearly dominated by sheath heating at higher total power.

For 5 W, the voltages on the coils (inner to outer) are 147 V, 112 V and 44 V. The total capacitive power is 3.19 W (63.8% of the total), inductive power is 0.86 W (17.2 %), and resistive antenna losses 0.95 W (19%), a power division that indicates E-mode operation. On a relative basis, antenna losses are larger at lower total power due to the higher relative antenna current required to sustain the plasma. The capacitive component includes contributions from both ion and electron acceleration by the sheath and bulk Joule heating. With the largest voltage and capacitive current from the inner coil, the capacitive heating is maximum under that coil (3.8 mW/cm^3) adjacent to the dielectric with resistive current flowing through the plasma to produce Joule heating of 0.7 mW/cm^3 in the center of the plasma. Sheath heating also occurs along the metal boundaries. With the peak electron density of 6×10^8 cm^{-3}, inductive power deposition extends to the middle of the reactor (electric field skin depth $\delta = 7.4$ cm) with a maximum value of 3 mW/cm^3. The voltages on the 3 coils of the antenna are nearly in phase. However, with different voltage amplitudes and different adjacent sheath thickness, particularly with respect to

111

ground, there is some recirculation of current between the antenna coils that produces a net negative power deposition in the upper outer radius of the reactor.

For 200 W total power, the voltages on the coils (inner to outer) are 334 V, 276 V and 112 V. The total capacitive power is 9.7 W (4.8% of the total), inductive power is 188.2 W (94.1%), and resistive antenna losses 2.1 W (1.1%), a power division that indicates H-mode. With a higher electron density (peak 6.8×10^{10} cm^{-3}) the plasma is more conductive and capacitive heating is largely limited to the periphery of the reactor. The higher plasma density also reduces the electric field skin depth to $\delta = 0.7$ cm.

The capacitive power has a cycled averaged layer of negative power deposition parallel to the dielectric window, in addition to that in the upper right corner, that was not observed at lower power. At the high power, the electron flux directed towards the dielectric is dominated by the ambipolar flux originating from the electron sources produced by inductive coupling. The electron ambipolar flux is retarded by the ambipolar electric field that points from the center of the plasma towards boundaries. This is the same direction as the electric field that produces electron heating due to expansion of the capacitive sheath under the window. During expansion of the capacitive sheath, power is expended in slowing the ambipolar driven electron flux in addition to accelerating electrons out of the sheath region. This negative power deposition is not observed at the lower power in the absence of the large ambipolar electron flux produced by inductive coupling.

The division of power deposition between capacitive and inductive; and average electron density are shown in Fig. 4.4a for $P_T = 5\text{-}200$ W for perfect match conditions and continuous power. The values of C_P and C_S to obtain perfect matches and ionization efficiency are shown in Fig. 4.4b. (Ionization efficiency is average plasma density divided by power deposition in the

plasma, and is a relative measure of efficiency.) These results are typical of the E-H transition. At low power deposition, the electron density is low, the skin depth is large and sheath is thick. The low electron density and large skin depth reduces (on a relative basis) the inductive power deposition and the thick sheath (on a relative basis) increases the capacitive power deposition. The thicker sheaths produce a larger sheath velocity, and capacitive power deposition scales with the square of the sheath speed. As noted above, for $P_T = 5$ W, 77% of the power is capacitive and 11% is inductive. The power dissipation by the coil is about 12%. With increasing power deposition, the electron density increases, skin depth decreases and sheath thickness shrinks, all of which contribute to lower capacitive power deposition and higher inductive power deposition. We do not observe a sharp, step-function increase in electron density that can be identified as the E-H transition. The power at which the E-H transition occurs is then somewhat a qualitative judgement. The fraction of power dissipated by inductive coupling exceeds 50% at $P_T = 25$ W, and exceed 90% at $P_T = 140$ W. To achieve the perfect match, the values of the matching elements C_P decreases by about 20% and C_S increases by a factor of 2.5.

Over the range of $P_T = 5$-200 W, the average electron density increases from 2.8×10^8 cm^{-3} to 2.3×10^{10} cm^{-3}, a factor of nearly 100 increase, for P_T increasing by a factor of 40. A portion of the increase in electron density results from an increase in ionization efficiency, plotted here as the total electron density divided by the total power deposition in the plasma. This efficiency increases by a factor of nearly 3. At low P_T, the fraction of power dissipated by resistive coil and capacitive heating is large. No ionization occurs from coil heating, and the efficiency of ionization by capacitive coupling is low due to ion acceleration in the sheaths, characteristic of the E-mode. The efficiency remains relatively constant until the H-mode begins, at which time the efficiency increases. At high power deposition, a true H-mode occurs,

as the majority of power is dissipated by electron heating in the bulk which is intrinsically more efficient at producing ionization.

With there always being a perfect match when changing P_S, there is a relatively smooth transition from dominantly E-mode to dominantly H-mode with increasing power. To obtain this perfect match with increasing power, the value of C_S smoothly increases (33 pF to 155 pF) and C_P smoothly decreases (267 pF to 168 pF). Experimentally, it is often observed that there is a rapid, almost impulsive, increase in electron density with a rapid switch between E-mode and H-mode when a critical power is delivered from the supply. Based on fundamental plasma transport, there is no requirement for such a sharp transition to occur.

In practice, the transition in apparent ionization efficiency may be exacerbated by the difficulty in matching between the E-mode and H-mode. If the circuit is better able to match to the H-mode (positive reactance) than E-mode (negative reactance), then the ionization efficiency will make a rapid and impulsive increase when the H-mode begins to dominate. There may also be heating of electrical components that can change their impedance. Another factor that may influence the apparent ionization efficiency is changes in plasma conditions due to the power deposition. For example, when operating at constant pressure, higher power deposition produces more gas heating which reduces the gas density and so reduces the electron collision frequency. In chemically active mixtures, more power deposition produces more dissociation and so there are different species with which electrons collide.

To demonstrate these possibilities, two parameterizations were performed. In the first, a parameterization over power (P_T = 5-200 W) was conducted with the match box settings chosen to provide a perfect match at 150 W (C_P = 162 pF, C_S = 135 pF) which then produces mismatches at other powers. The resulting ionization efficiency is shown in Fig. 4.5. For these

conditions the circuit is mismatched at lower powers, producing a large reflection coefficient, and a corresponding low ionization efficiency. With power increasing towards 150 W, the reflection coefficient decreases, H-mode begins to dominate and so the ionization efficiency increases.

In the results shown in Fig. 4.4, the length of time for the simulation was deliberately chosen to be long enough so that the plasma properties came into a quasi-steady state; while being short enough that there was no significant dissociation of the feedstock gases and gas temperature excursions were not significantly different. These conditions correspond to a short residence time of the gas in the plasma, τ_{res}. In this way, a side-by-side comparison of different powers could be performed without the complication of the impact of changing gas temperatures, gas densities and gas compositions on matching. In actual practice, when changing power one does have these complications of gas heating producing rarefaction and different degrees of dissociation of the gas.

The parameterization in Fig. 4.4 was repeated when computing for a sufficient time that all plasma properties including gas temperature and composition come into a steady state. This would correspond to at large τ_{res}. With the large τ_{res}, for $P_T = 5$ W, the average gas temperature was $T_g = 330$ K (for a wall temperature of 325 K) and fractional dissociation of Cl_2 was 1.3%. For $P_T = 200$ W, $T_g = 635$ K and fractional dissociation was 27%. The resulting ionization efficiency, also shown in Fig. 4.5, increases by a factor of 4.5 from low to high power. The majority of this increase in efficiency results from the decrease in Cl_2 mole fraction (due to dissociation) and decreases in gas density (gas heating), which then decreases the rate of attachment. These results emphasize the difficulty of performing side-by-side comparisons of E-H behavior when changes in power deposition also change fundamental properties of the plasma

in addition to electron density.

4.3.2 Set Point Matching to ICPs

In this section, we discuss matching of a pulsed ICP for the same operating conditions as the CW studies (Ar/Cl$_2$ = 65/35, 25 mTorr). The standard conditions for pulsed ICP operation were a pulse repetition rate (PRF) of 13.3 kHz (period of 75 µs), duty cycle 35% and forward power delivered from the supply during the power on period of P_S = 250 W. As a base case, we used perfect match conditions by instantly adjusting C_P and C_S to produce Γ=0 throughout the pulse period. The maximum in the plasma potential, the electron density, Cl$^-$ density and positive ion densities are shown in Fig. 4.6a during the power pulse and immediate afterglow. The modes of power dissipation are shown in Fig. 4.6b. The resistive and reactive components of the impedance Z_L, and perfect matching values of C_P and C_S are shown in Fig. 4.6c.

At the beginning of the power pulse, the plasma conditions are essentially an ion-ion plasma where the positive ion density is nearly equal to the negative ion density, [M$^+$]≈[Cl$^-$]=4.5 × 10^{10} cm^{-3}. The small electron density at the beginning of the pulse, $n_e = 2 \times 10^8$ cm^{-3} results from Cl$_2$ being a thermally attaching gas, which reduces the electron density during the afterglow through dissociative electron attachment producing Cl$^-$. During the power pulse the negative ion density [Cl$^-$] is relatively constant. With the electron temperature $T_e \approx 2.5 - 3.5$ eV during the power pulse, the thermal dissociative attachments rates are small compared to ionization rates. The increase in electron density is nearly matched by the increase in positive ion density.

With this low initial electron density, power is initially capacitively coupled. During the first 3 µs, the capacitive power exceeds that of the inductive power and the plasma operates in E-mode. The E-mode is additionally indicated by the oscillation in the plasma potential, Φ_P, with an amplitude as large as 450 V in the same manner as a capacitively coupled plasma. The

116

maximum antenna voltage amplitude (inner turn) is 1080 V. There is some oscillation in the voltage amplitude on the antenna, which is due to the rapid increase in electron density, which changes the plasma impedance sufficiently to lower the antenna voltage, which lowers the electron density which induces an increase antenna voltage. This oscillation is likely magnified by the iterative numerical technique used to link the plasma portion of the simulation with the circuit.

As the electron density increases, the electromagnetic skin depth decreases and sheath under the coils thins, the fraction of capacitive power dissipation decreases. By 5 µs, the electron density is high enough, 1×10^{10} cm^{-3}, and skin depth short enough that power is dominantly inductively coupled and the plasma operates dominantly in H-mode. Due to the proximity of the antenna to the dielectric window, approximately 5% of the total power continues to be capacitively coupled even during H-mode. This is similar to CW operation. In the quasi-steady state during the pulse, the proportion of capacitively coupled power decreases by a few watts but is otherwise nearly constant. Upon termination of the power, both the capacitive and inductive power decrease in nearly the same proportion while remaining in H-mode. The power decreases quickly enough that the electron density does not appreciably change, and so the skin depth remains short enough to allow H-mode operation. This represents a hysteresis-type of behavior. The plasma remains in H-mode during decreasing power at the same power deposition that corresponded to E-mode during the beginning of the pulse.

As the plasma density increases at the leading edge of the power pulse and operation transitions to H-mode, the oscillation in Φ_P decreases to an amplitude of 10-20 V. This modulation of Φ_P is on top of the quasi-dc plasma potential of about 20 V. This dc value of plasma potential results from the ambipolar nature of the plasma transport ($T_e > T_{ion}$, $m_e < m_{ion}$).

117

An indication of purely H-mode operation without capacitive coupling would be quasi-dc plasma potential without significant oscillation. Since the power deposition resulting from E_θ and electron heating are harmonic, there can be harmonic oscillation in T_e and so there would be some small oscillation in Φ_P even in purely H-mode. However, in this case, the majority of oscillation in Φ_P is due to capacitive coupling.

With perfect match conditions, C_P decreases during the power pulse from 290 pF to 160 pF, accompanied by an increase in C_S from 50 pF to 160 pF. The combined load impedance, Z_L (which includes the antenna coil and plasma) has a positive reactance due to the inductance of the antenna. This reactance decreases during the plasma pulse in response to the capacitive component of the antenna current through the plasma. The resistive component increases in response to the power deposition in the plasma.

The impedance of the variable capacitors in RF matching networks is typically changed by a mechanical process (e.g., changing the overlap area between two plates). The speed of the mechanical movement of these variable capacitor systems is largely determined by the driving motors, with end-to-end movement typically on the order of hundreds to thousands of milliseconds. Impedance control algorithms working in conjunction with these mechanical limits will typically produce a tuning transient with a comparable characteristic time. With plasma-induced impedance transients having time scales that are orders of magnitude shorter that what can be achieved by these mechanically driven system, it is typically not possible to change the values of C_S and C_P rapidly enough to achieve a perfect match throughout the power pulse. Typically set-point matching is employed in which values of C_S and C_P are chosen to minimize Γ at a particular instant during the power pulse. We investigated the consequences of set-point matching. Computationally, this was achieved by selecting values at given times for C_S and C_P

118

from the perfect-match case. For example, plasma reactor properties are shown in Fig. 4.7 when values for C_S and C_P were chosen for set-point matches from early to late in the pulse. These times, relative to the start of the power pulse, were 1.5, 3.25, 7 and 21 µs. Since the progression of the plasma prior to the time of the matching point is not exactly the same as for the case with perfect matching, the reflection coefficient at the match point may not be exactly zero.

For a matching point of $t_M = 1.5$ µs, the reactor properties at the match point are a forward power of 82.7 W and $\Gamma = 0.013$. The maximum capacitive power of 62.2 W occurs at the match point. The resistive power is 9.6 W and inductive power is 8.5 W, indicating operation in the E-mode. (Note that Γ is finite due to the plasma properties being different than for the perfect match that provided the values of C_S and C_P.) As the plasma density begins to increase, the E-mode dissipates and H-mode begins. With this increase in plasma density, the values of C_S and C_P required to achieve a match deviate from the set-point values. The reflection coefficient then monotonically increases until the H-mode is fully established at $t = 6$-7 µs, after which Γ is relative constant at 0.5. At the end of the pulse, the electron density is 1.15×10^{10} cm^{-3} compared to the perfect match value of 2.4×10^{10} cm^{-3}. This decrease in electron density is due to the reduction in power deposition following that $\Gamma = 0.5$.

As t_M increases, the peak capacitive power decreases, there is a larger delay in the onset of inductive power deposition and the maximum inductive power increases, as shown in Fig. 4.8. The delay in onset of the H-mode results from there being less ionization produced during the E-mode. With a larger t_M, there is a larger mismatch that produces a larger Γ early in the pulse, which reduces power deposition and ionization. For example, for $t_M = 2.5$ µs, the peak capacitive power of $P_C = 70$ W occurs at 2 µs when the inductive power is $P_I = 41$ W and $\Gamma = 0.03$. Just prior to the end of the maximum delivered power at 23 µs, $P_C = 9.3$ W, $P_I = 108$

and $\Gamma=0.46$. For $t_M = 21$ µs, the peak capacitive power of $P_C = 21$ W occurs at 2.6 µs when the inductive power is $P_I < 1$ W and $\Gamma = 0.76$. At 23 µs, $P_C = 12$ W, $P_I = 235$ and $\Gamma < 0.001$. For $t_M > 7$ µs, the set-point values of C_S and C_P are well matched to the H-mode, and so $\Gamma < 0.01$ for $t > 10\text{-}15$ µs for the remainder of the power pulse. The electron density at the end of the power pulse is nearly that of the perfect match.

4.3.3   Matching for Different Duty Cycles

Matching early during the power pulse is sensitive to the electron density at the onset of power, and this is particularly problematic in thermally attaching gas mixtures such as Ar/Cl_2. During the inter-pulse period, the electron temperature decreases, which increases the rate of attachment and increases electron loss. The lower electron density at the onset of power for the next pulse makes the system appear to be more capacitive to the matching network. This sensitivity can be demonstrated by varying the duty cycle of the pulsed power.

For the same peak power during the power pulse, a shorter duty cycle translates to lower average power deposition and less fractional dissociation of Cl_2. The larger density of Cl_2 results in more attachment during a longer inter-pulse period, resulting in a lower initial electron density at the beginning of the next pulse. For example, the electron density and plasma potential Φ_P during the pulsed period are shown in Fig. 4.9 for different duty cycles (25% to 65%). Note that the time scales are shifted in Fig. 4.9b by increments of 10 ns. in order to show the plasma potentials more clearly. The electron density at the beginning of the pulsed cycle is 1×10^8 cm^{-3} for a duty cycle of 25% and 1×10^9 cm^{-3} for a duty cycle of 65%. The magnitude of oscillation of Φ_P indicates the severity of capacitive coupling.

When varying duty cycle, the same set-point match is used corresponding to $t_M = 7$ µs and a duty cycle of 35%. Duty cycles shorter than 35% produce smaller initial electron densities.

However, the system already starts in the E-mode, and so there is little change in the oscillation of the Φ_P. Increasing duty cycle increases the initial electron density, which enables some H-mode coupling early during the pulse. This H-mode coupled power reduces the power coupled into the E-mode which then reduces the oscillation in Φ_P. This reduction in capacitive power does come at a cost of increasing the reflection coefficient. At the time of the nominal match conditions for a duty cycle of 35%, the reflection coefficient at $t = 7$ μs is $\Gamma = 0.01$. For a 25% duty cycle, is $\Gamma = 0.02$ (still small) whereas for a duty cycle of 65%, the reflection coefficient is $\Gamma = 0.08$.

4.3.4   Ion Energy Distribution on Dielectric Window During E-mode

A consequence of early matches that allow significant power into the E-mode is large ion fluxes incident onto the dielectric window while there is still significant oscillation in the plasma potential. These conditions produce energetic ions onto the window which can result in sputtering and erosion. For example, the ion energy distributions (IEDs) incident onto the window with a duty cycle of 25% are shown in Fig. 4.10. At the beginning of the pulse, the plasma potential rises from about 10 V when the sheath beneath the window is thick. The resulting IED is largely thermal with an extended tail. As the plasma density increases, which thins the sheath, and plasma potential increases with the capacitive coupling, the IED extends to as high as 200 eV, for a plasma potential peaking at 375 V during the E-mode. The maximum in the IED does not directly correspond to the maximum in plasma potential due to the locations within the thick sheath that ions are produced and due to the transient charging of the dielectric. As the H-mode is established and the plasma potential decreases, the maximum energy of the IEDs also begins to decrease. By the end of the power pulse, the peak of the IED occurs at 18 eV. In the afterglow where the plasma potential decreases below 10 V, the peak in the IED

occurs at 5 eV.

When matching early in the pulse, capacitive coupling is emphasized, there is more power dissipated in ion acceleration and there are more energetic of ions incident on all inside surfaces of the reactor, and on the window in particular. These energetic ions could be potentially damaging to the window and other surfaces. These energetic fluxes are then another consideration in choosing an early match. Having said that, even with t_M being small, the E-mode dissipates before the plasma density reaches its maximum value. As such, the flux of energetic ions produced by capacitive coupling may not be large, thereby reducing the likelihood for damage.

4.3.5 Antenna Placement

The capacitance between the antenna and the plasma consists of at least three series components – the capacitance of the air gap between the antenna and window, the capacitance of the window and the capacitance of the sheath. In practice, the capacitance of the antenna-window gap is more variable than that of the window. For example, placement of the antenna after maintenance must be extremely precise to replicate the capacitance of the antenna-window gap. The variable capacitance of the antenna-window gap then translates into variability in the plasma.

To demonstrate the sensitivity of matching pulsed ICPs to the placement of the antenna, the following procedure was followed. The gap between the bottom of the flat antenna and the window was varied from $d = 0$ (in contact with the window) to 8.2 mm. For each gap, calculations were first performed with perfect matching. The values of C_P and C_S for each gap size were then chosen as the perfect match values at $t_M = 20$ μs. The simulations for gaps sizes of $d = 0 - 8.2$ mm were then repeated with these fixed values C_P and C_S. The resulting

capacitive power P_C and inductive power P_I during the power pulse are shown in Fig. 4.11.

With increasing values of the gap, d, the series capacitance of the gap-window pair decreases. With $d = 0$ (maximum capacitance), E-mode power is dissipated at the leading edge of the power pulse. This capacitive power produces ionization, which then enables the inductive power to begin earlier leading to an onset of the H-mode. As the gap size d increases, the series capacitance also decreases. This decrease in capacitance of the gap limits current, then decreases the E-mode power at the leading edge of the power pulse and increases the reflection coefficient. With lower E-mode power deposition, the increase in electron density is slower. This slow rate of increase in electron density means that more time is required for the electron density to increase to the point that inductive power dominates and the H-mode begins. During the quasi-steady state portion of the pulse where the circuit is well matched to the plasma, the small values of d allow for larger capacitive power deposition, which then reduces the inductive power deposition.

For all values of the antenna-window gap, there is nearly a perfect match late in the pulse – all forward power is dissipated either in the plasma or in the antenna. However, the manner of deposition, fraction of power dissipated as P_C and P_I, is sensitive to the height of the antenna above the window. In results not shown here, there is a similar dependence on the flatness of the antenna. An antenna that may be mounted at a small angle with respect to the window can be perfectly matched, however the fractions of power dissipated as P_C and P_I are a function of the orientation of the antenna. Reproducing performance when replacing an antenna requires both ensuring a match and also reproducing the fraction of power separately dissipated as P_C and P_I. In the case of pulsed plasmas, the power waveforms should also be reproduced.

4.3.6 Electrostatic Waves at Onset of E-mode

For thermally attaching gas mixtures, as in the Ar/Cl_2 mixture used in this investigation,

the onset of the E-mode at the leading edge of the power pulse produces an impulsive perturbation to the plasma that generates electrostatic waves. At the beginning of the power pulse, the plasma is essentially an ion-ion plasma with the positive and negative ion densities greatly exceeding the electron density. For example, for the base-case at the end of the afterglow, the positive and negative ion densities adjacent to the window are essentially equal at 3.4×10^{10} cm^{-3} whereas the electron density is 2×10^{8} cm^{-3}. The charge density (units of elementary charge, $q = 1.6 \times 10^{-19}$ C) is -2.5×10^{4} cm^{-3}. There essentially is no sheath as both positive ions have largely thermalized to the same temperature during the afterglow and the ions have nearly the same mobilities.

When the power is applied, a large voltage is generated across the antenna and capacitive coupling to the plasma occurs. The response of the plasma is to attempt to form a sheath to dissipate the capacitive voltage drop. During the first few RF cycles, the sheath is most easily formed by accelerating electrons adjacent to the dielectric into the plasma to produce a positive space charge region. During these first few cycles, the far more numerous positive and negative ions are nearly immobile and do not significantly separate to produce the charge density needed to create the sheath. With each half cycle, electrons are expelled from and attracted to the dielectric. The end result is launching of electrostatic waves into the ion-ion plasma.

The electron and charge density are shown in Fig. 4.12 during the first 6 cycles of the power pulse for the base-case with a match point of $t_M = 1.5$ μs. These conditions were chosen to emphasize the initial E-mode coupling for demonstration purposes. The electron density is shown as color-contours. The charge density ρ (units of elementary charge/cm^3) is shown with numerical labels with a line for $\rho = 0$ indicating a sign change in local charge density. As the power increases at the beginning of the pulse, the voltage on the coils increases with each

successive RF cycle. Electrons adjacent to all surfaces in contact with the plasma are expelled into the plasma in an attempt to form a sheath. This expulsion is most pronounced under the window adjacent to the coils but also occurs along the side walls and substrate. The expulsion first produces an electrostatic wave having $\rho < 0$. Since the electron density is 2-orders of magnitude less than the positive and negative ions, this wave can propagate through the plasma without significantly perturbing the overall charge balance. The anodic half of the cycle launches a positive electrostatic wave. With each cycle, a new wave is launched, producing layers of alternating charge propagating into the plasma. The waves appear to emanate from under the inner and middle coils where the voltage is the largest and the largest amount of charge must be expelled to form the sheath.

In time, the electron density increases and positive space charge sheath is formed under the dielectric while the initial electrostatic waves collisionally dissipate. The waves soon become chaotic (not shown) due to the disparity in coil voltages, each with slightly different phases. The oscillating voltage on each coil launches what appears to be a cylindrically expanding electrostatic wave of different magnitude. These individually expanding waves are close enough in phase that their sum appears to have only a slight curvature. However, on successive pulses, the disparity in voltage between the coils increases, producing expanding waves which intersect and become chaotic before dissipating.

These electrostatic waves will occur in any highly electronegative system in which a sharply rising negative voltage is applied to a surface. For example, in pulsed plasma doping (P^2LAD) systems, a multi-kV negative, nearly step-function pulse is applied to the substrate to accelerate ions into the wafer for shallow junction implantation [39]. Simulations of P^2LAD systems predict similar electrostatic waves, albeit more soliton-like due to the single transient

voltage [40]. In the ICP systems discussed here, the amplitude and duration of the waves are small, and so the effects on processing (e.g., etch rate or uniformity) are likely not large. Their effects on diagnostics and sensors could be problematic, particularly if the waves are not reproducible pulse-to-pulse.

4.4 Concluding Remarks

Power dissipation in CW and pulsed electronegative inductively coupled plasmas sustained in Ar/Cl_2 mixtures and the consequences of impedance matching were computationally investigated. During a pulsed cycle, the modulation in electron density determines the mode of power deposition – capacitive (E-mode) at low electron density where the electromagnetic skin depth is large and inductive (H-mode) at high electron density where the electromagnetic skin is small. Even with perfect power transfer from the supply to the plasma, there is a natural E-H mode that occurs at the beginning of the pulsed period.

When considering matching, the increase in plasma density and spatial distribution of the plasma changes the impedance of the plasma reactor during pulsing, which then changes the matching requirements to deliver power from the supply. Since components in the match box are typically fixed during the pulsed period, components in the match box are set to match the plasma at particular time during the pulsed period. If the match box is chosen to match the impedance at the onset of the power pulse, E-mode is emphasized and a fast plasma ignition is expected due to efficient power deposition during power ramp-up. However, the tradeoff is a high power reflection coefficient during the majority of the power-on period as a consequence of the impedance mismatch to the H-mode plasma. In contrast, matching the higher power H-mode produces more net power transfer from the supply to the plasma, but delays the onset of the H-mode due to the mismatch of power in the E-mode.

Duty cycle during pulsing has important implications on power matching. In general, the shorter the duty cycle, the lower the electron density at the beginning of the next power pulse. This is particularly the case for mixtures using gases that attach thermal electrons, such as Cl_2. The lower electron density with a shorter duty cycle promotes E-mode operation at the start of the next power pulse.

In highly electronegative gases, the plasma at the beginning of the power pulse is essentially an ion-ion plasma. The impulsive application of power in a purely an E-mode results in launching of electrostatic waves during the leading RF cycles. The response of the plasma to the high voltage on the antenna during the E-mode is to form a sheath. The electrostatic waves result from the expulsion of the remaining electrons from nearby surfaces in an attempt to form a sheath. These waves are more severe when the afterglow is long and electronegativity is high.

Capacitance is largely a function of geometry and so the capacitance between the antenna and the plasma is a function of the gap length between the coil and dielectric window. A big gap produces a small capacitance and decreases the capacitive power that can be deposited during the E-mode. That decrease in power reduces the initial increase in electron density which then delays the onset of the H-mode.

The results discussed in this chapter demonstrate that impedance matching to a plasma, especially when using pulsed power, is a complex process. Changes in both operating conditions (duty cycle) and geometry (distance between the antenna and dielectric window) were found to impact the formation of the plasma and the power dissipation, which then affect plasma properties such as plasma density and collision frequency that determine the impedance of the plasma. Therefore, impedance matching networks with fixed components are not able to achieve a match over the entire pulsed period. Even when matching can be achieved, reset of the IMN

may be necessary for even slight modifications of the operating conditions or the setup of the reactor. For example, after preventative maintenance, a slight change in the arrangement of reactor components such as the antenna may produce a change in matching requirements.

Different match box setups lead to distinctive plasma behavior. In a pulsed power sustained plasma, choosing the circuit components in the match box to match the plasma impedance early in the pulse may produce faster ignition but risks impedance mismatch during the latter part of the pulse. Matching during the latter part of the pulse optimizes power delivery during the quasi-steady state with the tradeoff of delayed plasma formation. Matching the early part of the pulse benefits plasmas sustained by pulsed power with small duty cycles, while matching the late part of the pulse is suitable for plasmas sustained by power with long duty cycles or if the power supply is not able to accommodate higher levels of reflected power.

Power matching to transient systems will be challenging as long as the matching requires mechanical changes in components. These mechanical changes simply cannot be made rapidly enough to track the change in plasma impedance. As pulsed plasmas become even more prevalent in semiconductor manufacturing, advanced matching techniques, such as frequency tuning, will be required to minimize mode transitions and instabilities.

4.5 Figures
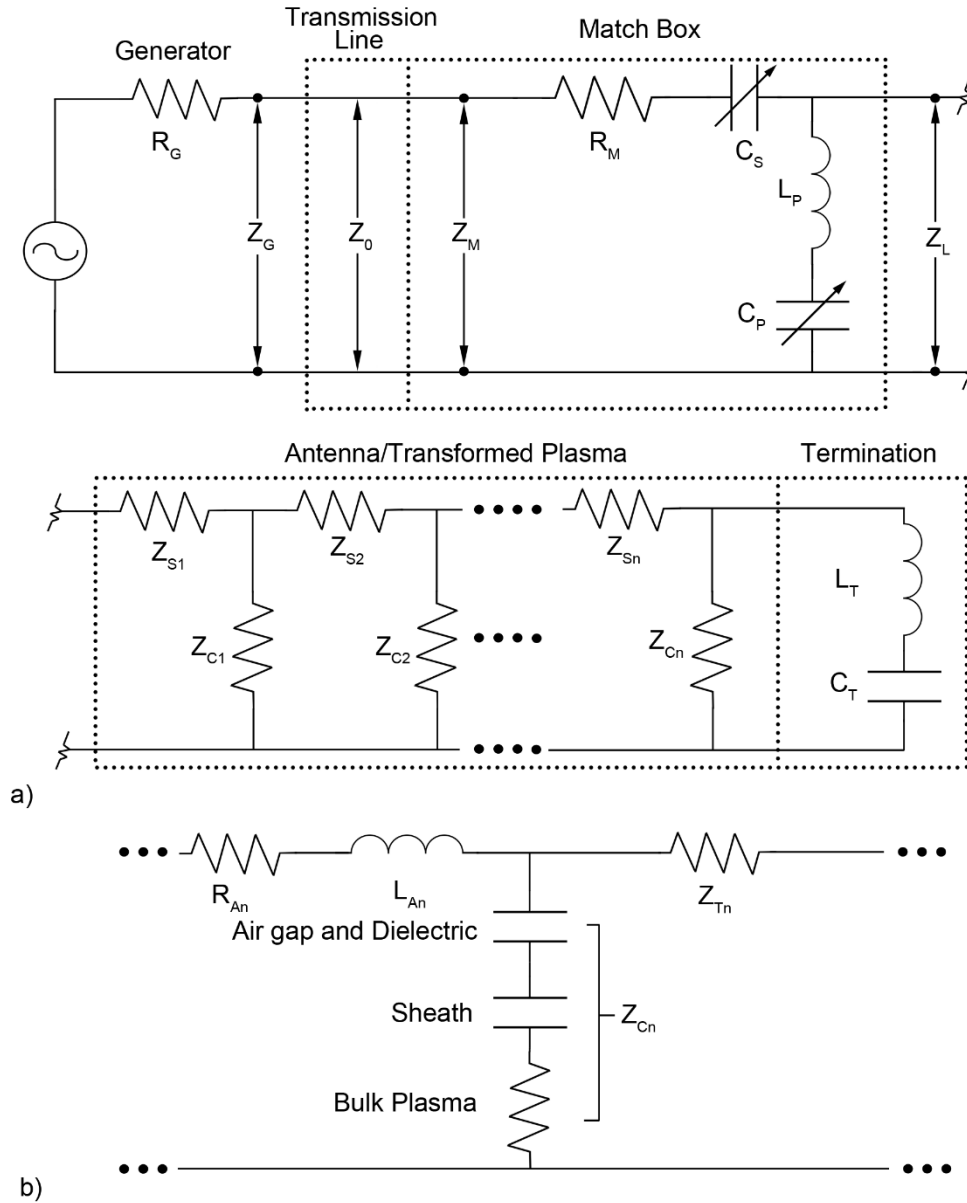
Fig. 4.1 Circuit schematic a) The circuit consists of impedances of the power generator, transmission line, matchbox, antenna, plasma, and termination circuit components. The antenna and transformed plasma impendances area represented by a discrete transmission line with each segment have having serial impedance Z_{sn} and parallel impendance due to capactive coupling, Z_{cn}. b) The Z_{sn} components consist of the physical resistance (R_{An}) and inductance (L_{An}) of the antenna, and the transformed impedance (resistance and inductance) of the plasma, Z_{Tn}. The impedance due to capacitive coupling, Z_{cn}, has components due to the air gap and dielectric, sheath and bulk resistance of the plasma.
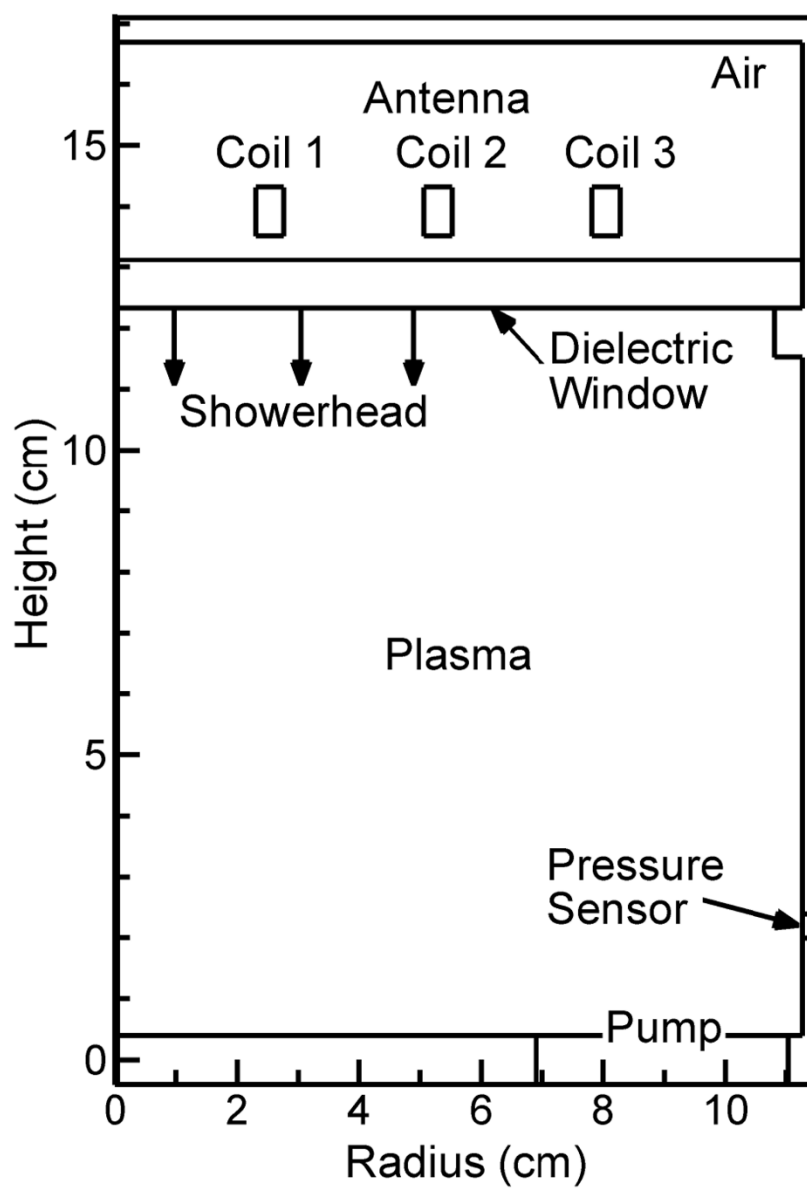
Fig. 4.2 Geometry of the cylindrically symmetric ICP reactor.
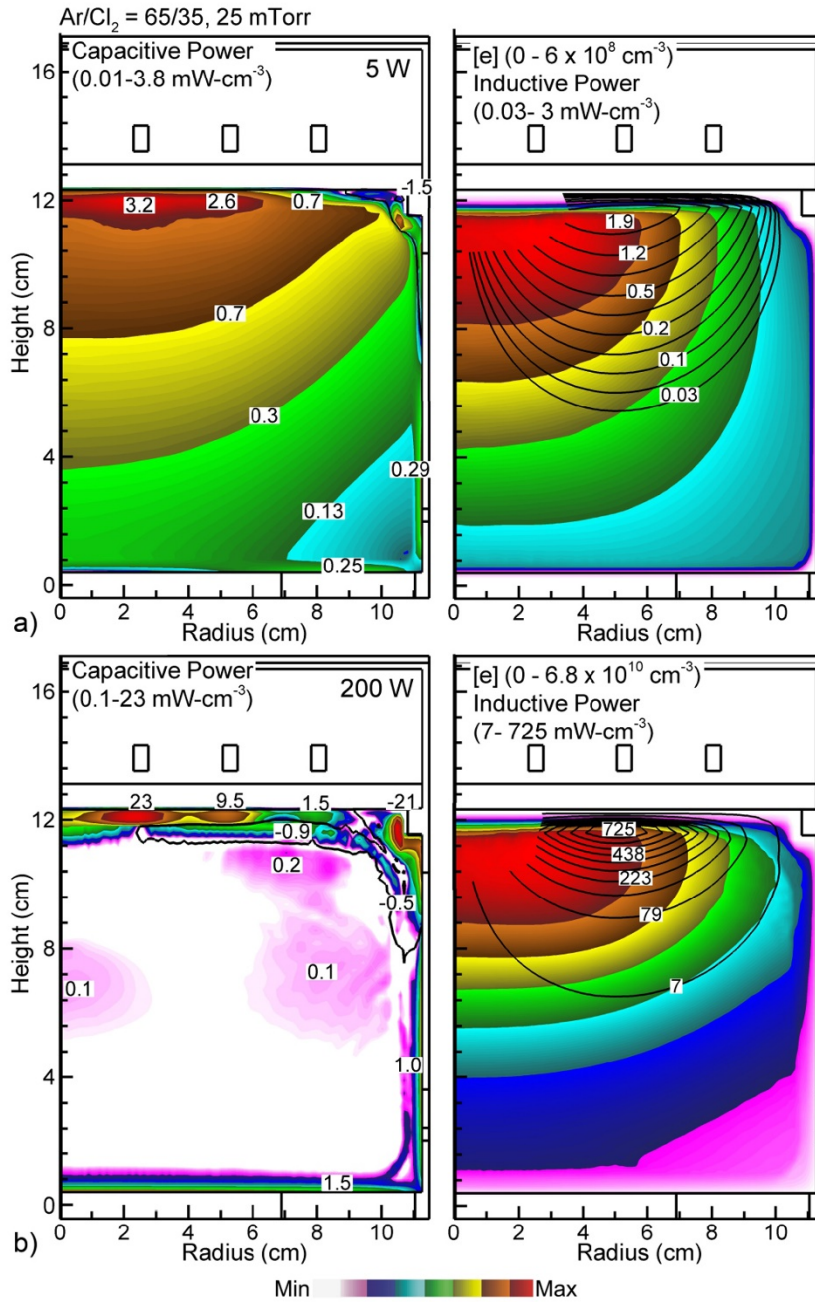
Fig. 4.3 Capacitive and inductive power deposition, and electron density when plasma is sustained with at total continuous power of a) 5 W and b) 200 W. (Ar/Cl$_2$ = 65/35, 25 mTorr.) The match is perfect. The capacitive power is shown as color contours with a line separating positive and negative values. Contour labels are mW/cm^3. Electron density is shown as color contours. Inductive power deposition is shown as contour lines with labels in mW/cm^3. The contour lines are blanked near the axis to enable clear view of the sheath formed under the powered coil.
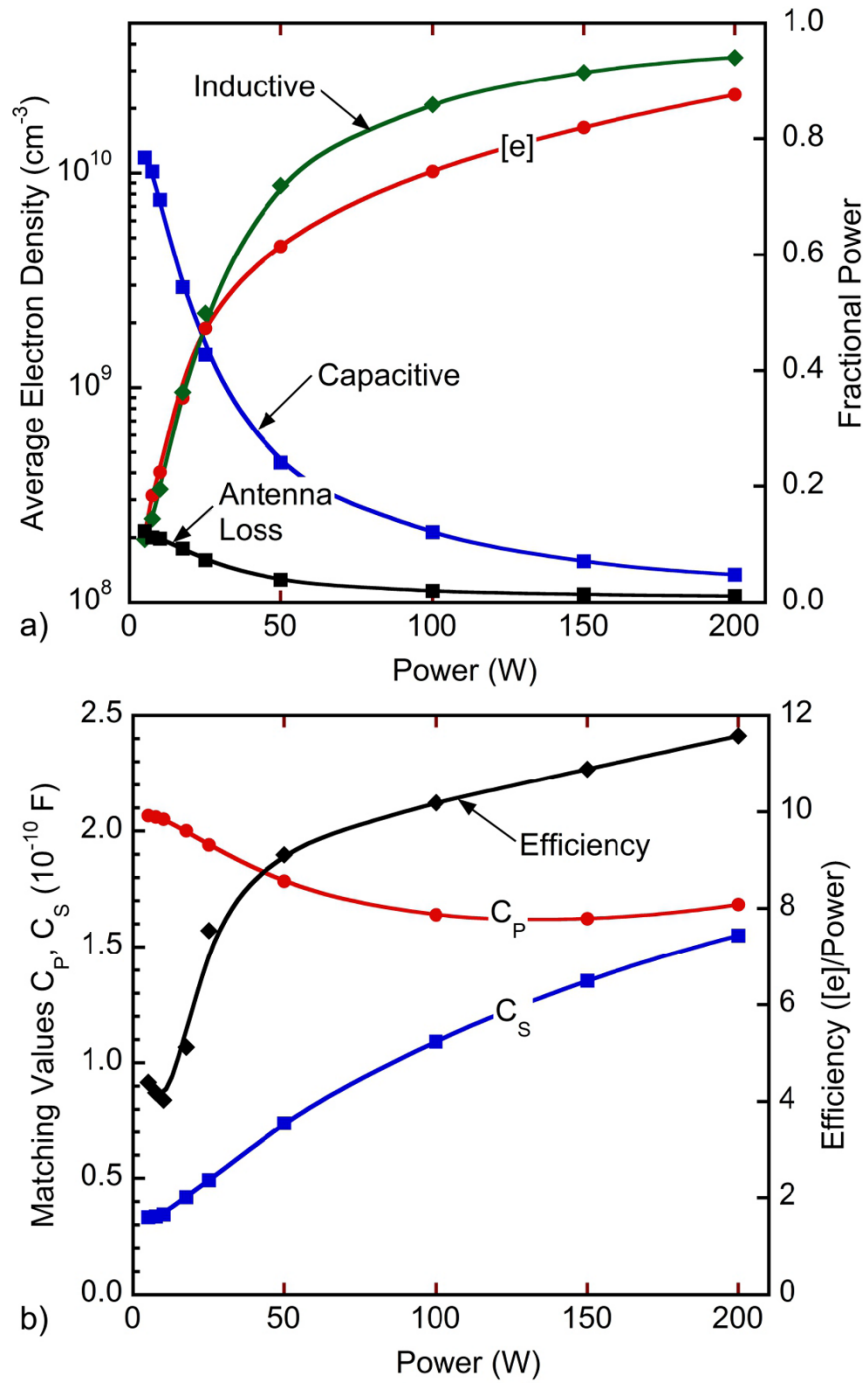
Fig. 4.4 Plasma and circuit properties as a function of CW power deposition for perfect matching ($Ar/Cl_2 = 65/35$, 25 mTorr). a) Electron density and fraction of power deposition due inductive H-mode, capacitive E-mode and antenna heating. b) Analytical solutions for C_P and C_S for a perfect match and the ionization efficiency. The ionization efficiency is total electron density divided by power deposition in the plasma, and is a relative measure of efficiency.
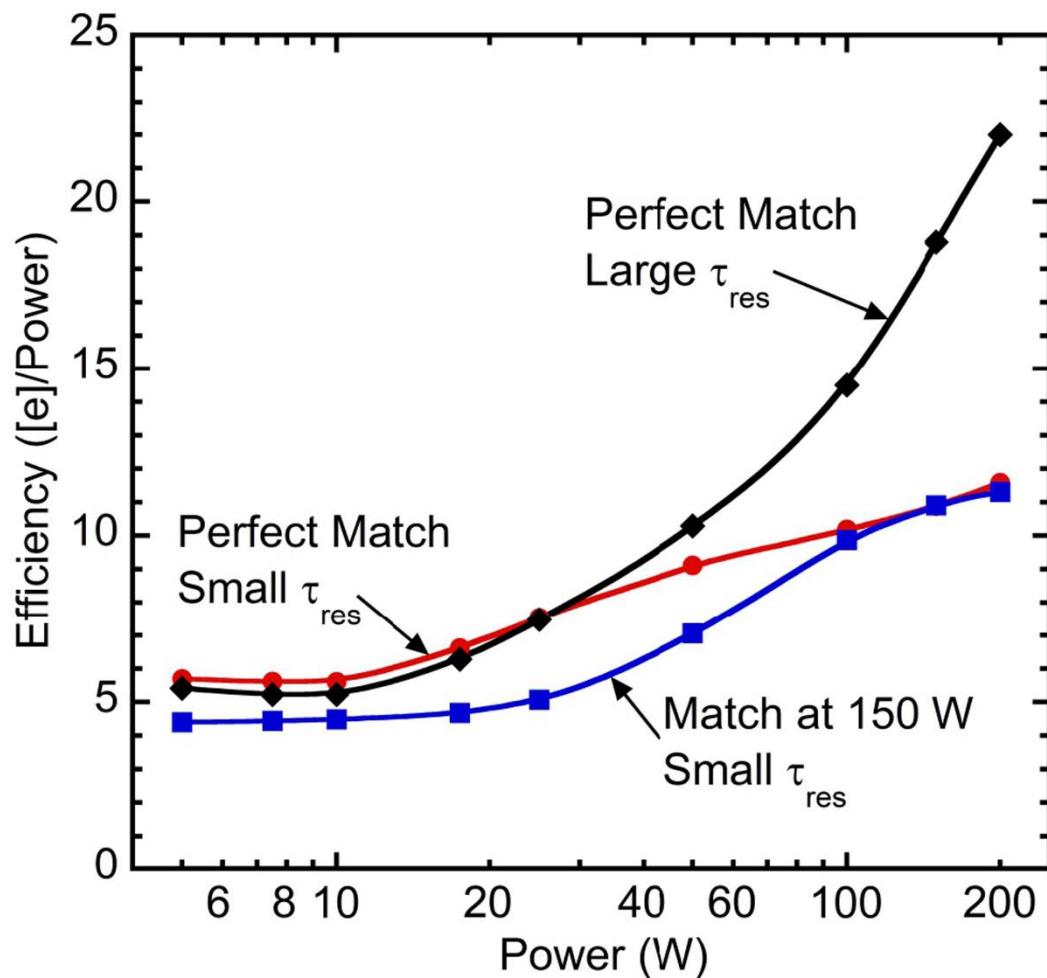
Fig. 4.5 Ionization efficiency as a function of CW power (Ar/Cl$_2$ = 65/35, 25 mTorr). Cases are shown for perfect matches for small and large residence time (τ_{res}) and with circuit values for a perfect match at 150 W with small τ_{res}. The ionization efficiency is total electron density divided by power deposition in the plasma, and is a relative measure of efficiency.
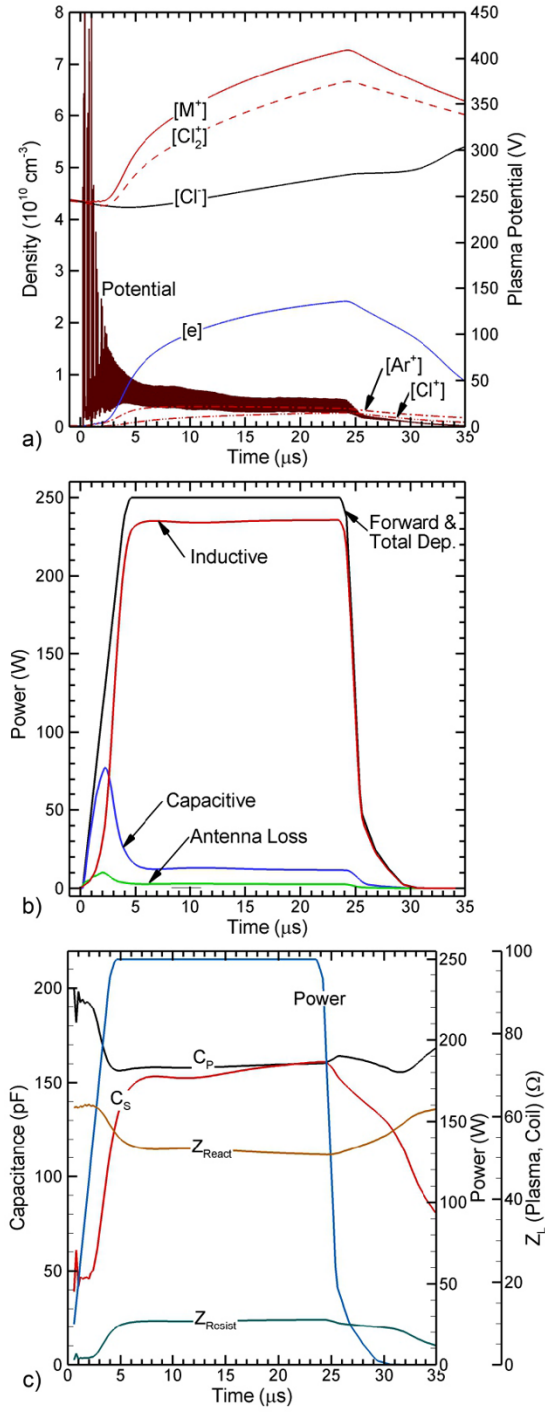
Fig. 4.6 Plasma and circuit values for a pulsed ICP with perfect matching. a) Electron and ion densities, and plasma potential, b) modes of power deposition and c) C_P and C_S for perfect match conditions, and reactive and resistive components of the impedance Z_L. The pulse repetition frequency is 13.3 kHz, duty cycle of 35% and forward power during the pulse is P_S=250 W, shown in c).

134
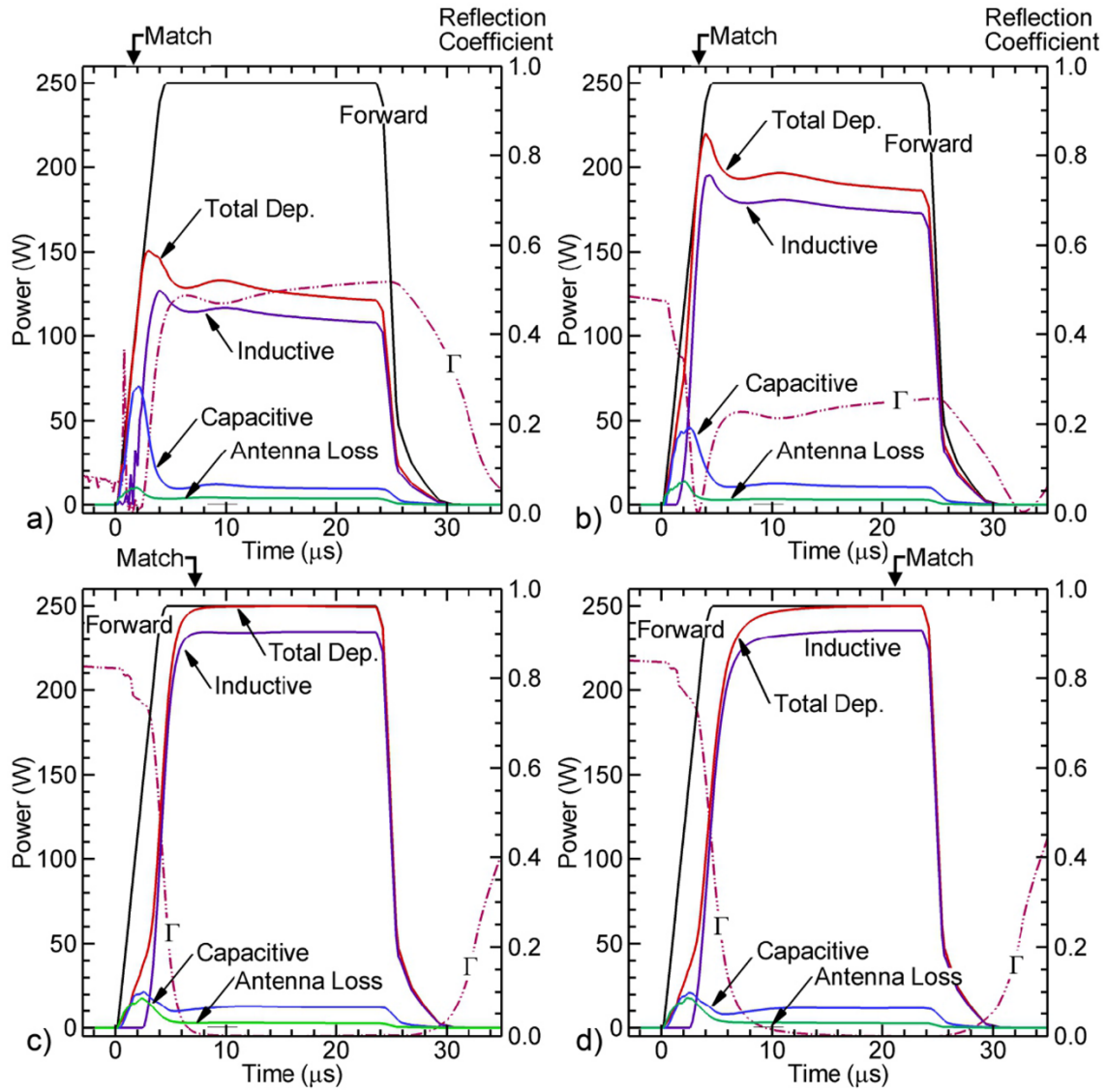
Fig. 4.7 Modes of power deposition, total power deposition and power reflection coefficient Γ when C_P and C_S are chosen to match at t_M = a) 1.5, b) 3.25, c) 7 and d) 21 µs into the pulse. (Ar/Cl$_2$=65/35, 25 mTorr, PRF = 13.3 kHz, DC = 35%, P_S = 250 W.)
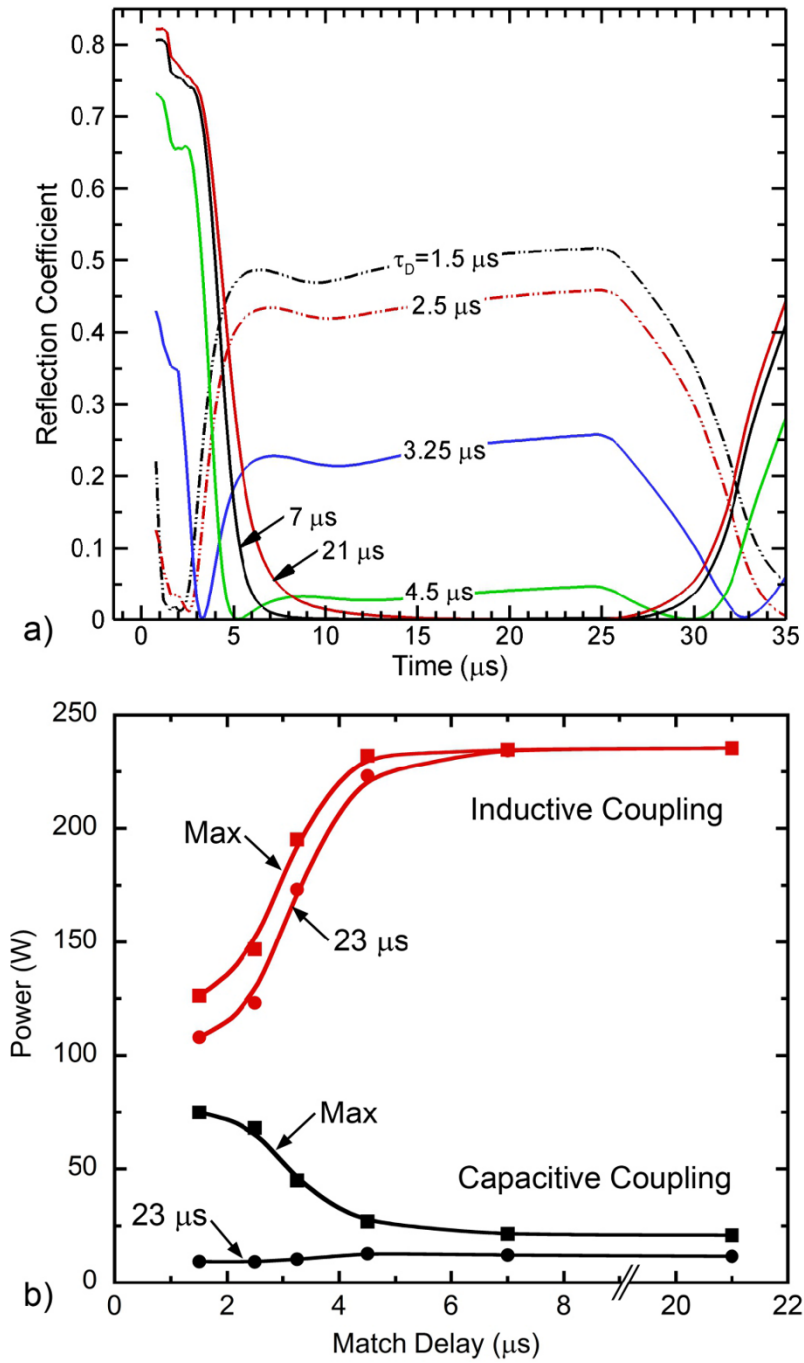
Fig. 4.8 Circuit values and power deposition as a function of matching time. a) Power reflection coefficients through one pulsed period when matching at different t_M. b) Inductive and capacitive power at their maximum value and at the end of pulse (t = 23 µs) with varying match time t_M. (Ar/Cl$_2$ = 65/35, 25 mTorr, PRF = 13.3 kHz, DC = 35%, P_S = 250 W.)
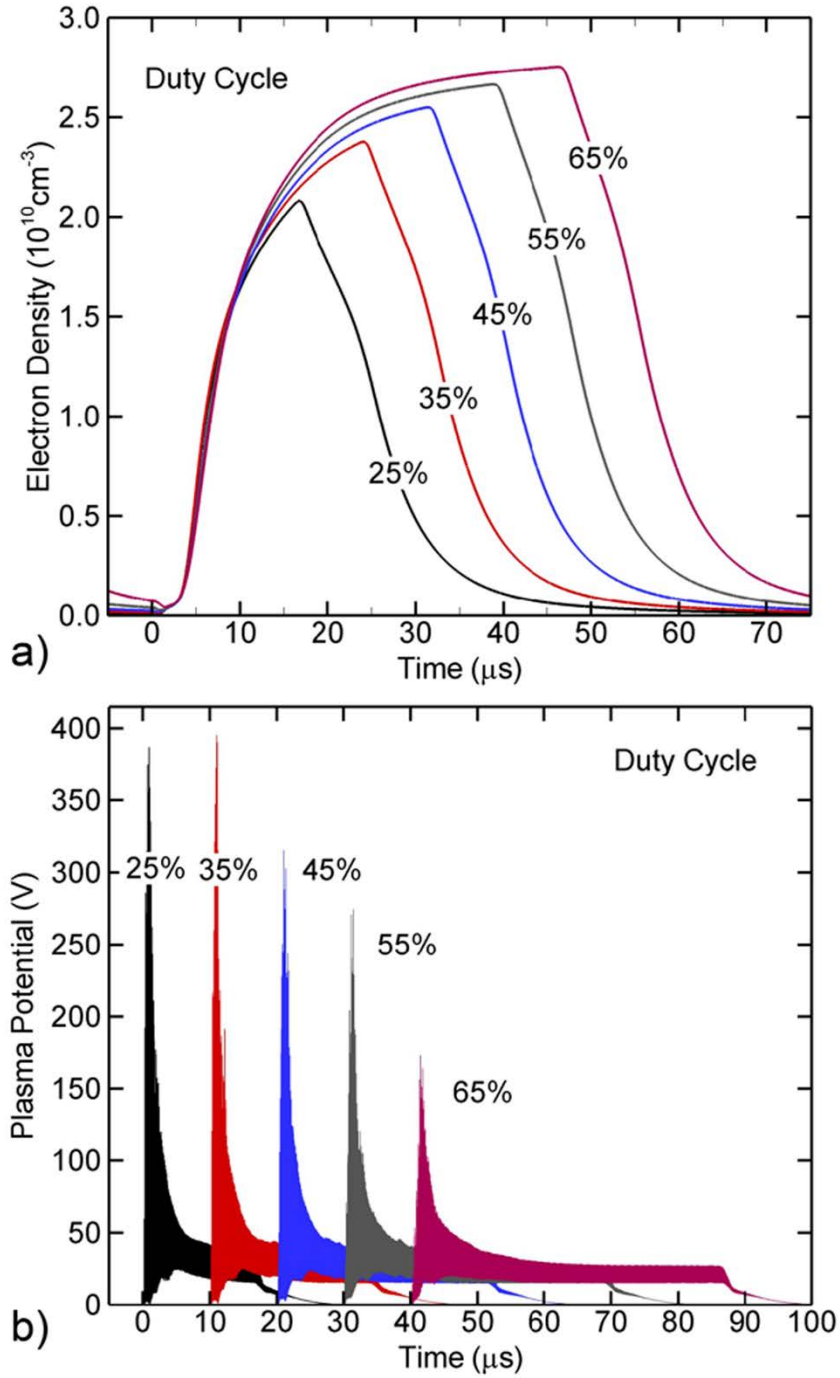
Fig. 4.9 Plasma properties when varying duty cycle (25 to 65%) during a pulsed period. The circuit match values correspond to a duty cycle of 35% with the match time at $t_M = 7$ µs. a) Electron density and b) plasma potential. For clarity, the plots for plasma potential have been shifted by increments of 10 ns. (Ar/Cl$_2$=65/35, 25 mTorr, PRF = 13.3 kHz, P_S = 250 W).
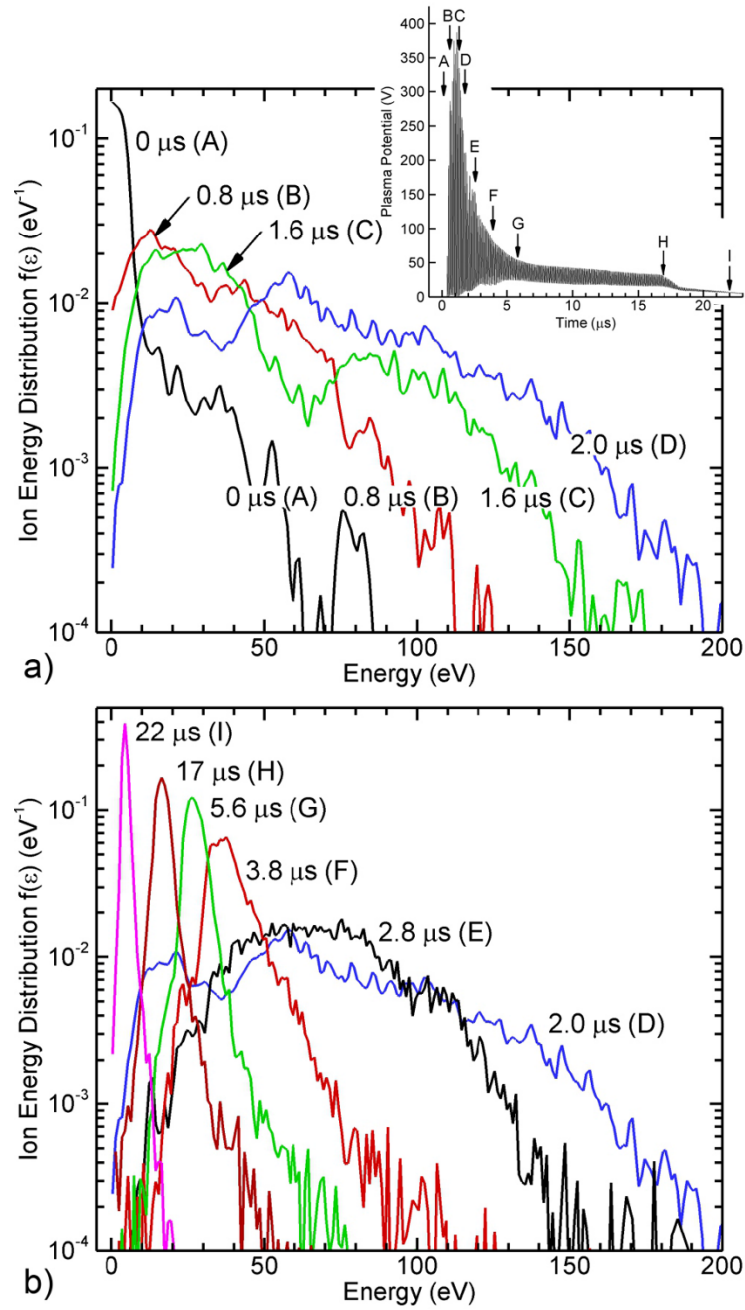
Fig. 4.10 Ion energy distribution (IED) incident onto the dielectric window at different times during the pulse. a) 0-2.0 µs, and b) 2.0-22 µs. The inset shows the plasma potential. The labels A-H are the locations in the pulsed cycle at which the IEDs are plotted. (Ar/Cl$_2$ = 65/35, 25 mTorr, PRF = 13.3 kHz, DC = 25%).
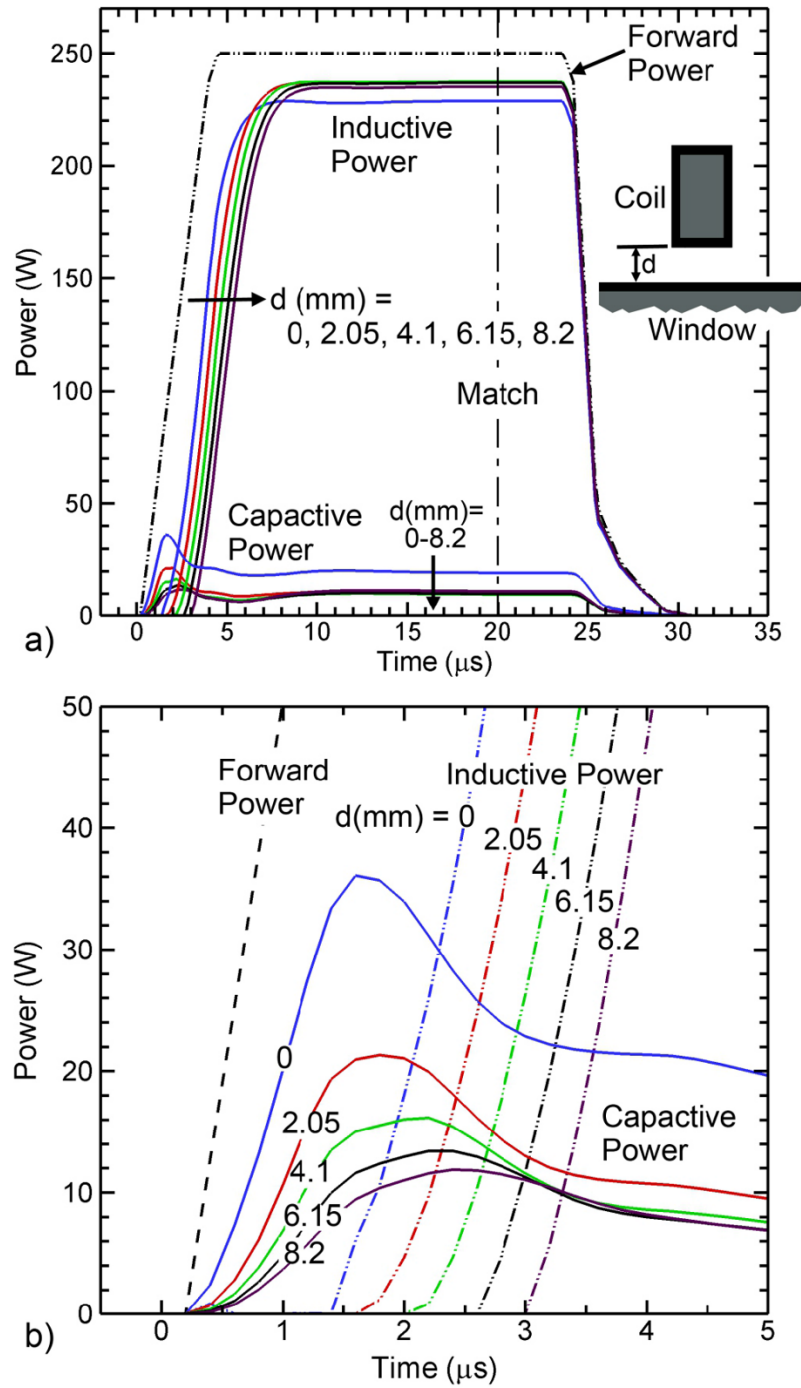
Fig. 4.11 Inductive and capacitive power deposition for different gaps, d, between the coils and the top of the dielectric window. Heights range between $d = 0$ to 8.2 mm. a) Power over the entire power-on period and b) power during the first 5 µs. The circuit match values correspond to the match time $t_M = 20$ µs. (Ar/Cl$_2$ = 65/35, 25 mTorr, PRF = 13.3 kHz, DC = 35%, $P_S = 250$ W.)
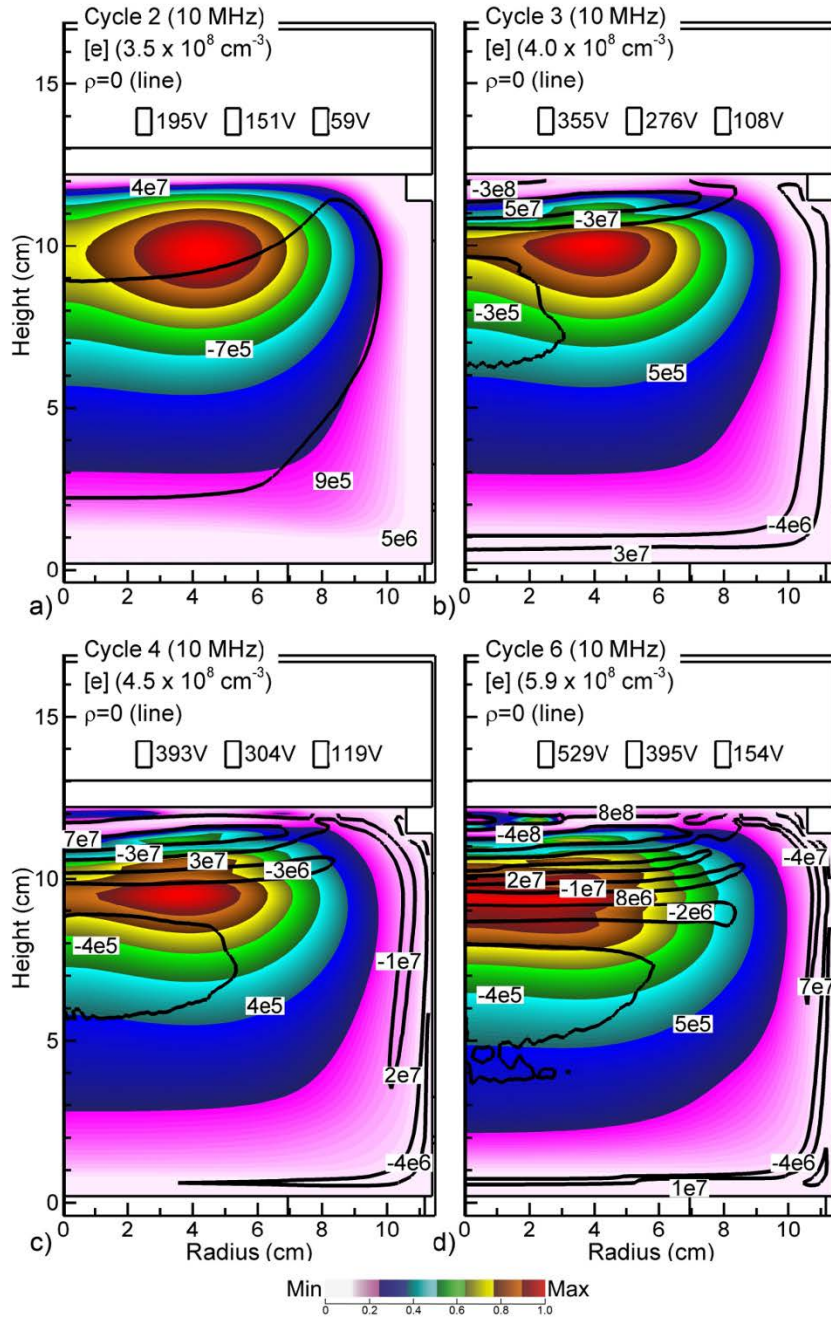
Fig. 4.12 Electron density (color contours) and charge density over the first few RF cycles of a pulsed period. a) 2nd, b) 3rd, c) 4th and d) 6th cycles. The circuit match values correspond to the match time t_M = 1.5 µs. The charge density ρ is shown by labels in units of q (1.6 × 10^{-19} C)/cm^3 with a line denoting $\rho = 0$. (Ar/Cl$_2$ = 65/35, 25 mTorr, PRF = 13.3 kHz, DC = 35%, P_S = 250 W). The impulsive power deposition launches electrostatic waves.

4.6 References

1. P. Chabert, J. L. Raimbault, J. M. Rax, and M. A. Lieberman, Phys. Plasmas **11**, 1775 (2004).

2. J. Gudmundsson, and M. A. Lieberman, Plasma Sources Sci. Technol. **7**, 83 (1998).

3. K. Kurokawa, IEEE Trans. Microw. Theory Tech. **13**, 194 (1965).

4. S. Xu, K. N. Ostrikov, Y. Li, E. L. Tsakadze, and I. R. Jones, Phys. Plasmas **8**, 2549 (2001).

5. F. Schmidt, J. Schulze, E. Johnson, J. Booth, D. Keil, D. M. French, J. Trieschmann, and T. Mussenbrock, Plasma Sources Sci. Technol. **27**, 095012 (2018).

6. J. Franek, S. Brandt, B. Berger, M. Liese, M. Barthel, E. Schüngel, and J. Schulze, Rev. Sci. Instrum. **86**, 053504 (2015).

7. T. Mussenbrock, R. P. Brinkmann, M. A. Lieberman, A. J. Lichtenberg, and E. Kawamura, Phys. Rev. Lett. **101**, 085004 (2008).

8. J. Schulze, B. G. Heil, D. Luggenhölscher, R. P. Brinkmann, and U. Czarnetzki, J. Phys. D: Appl. Phys. **41**, 195212 (2008).

9. L. Liu, S. Sridhar, V. M. Donnelly, and D. J. Economou, J. Phys. D: Appl. Phys. **48**, 485201 (2015).

10. C. Xue, D. Wen, W. Liu, Y. Zhang, F. Gao, and Y. Wang, J. Vac. Sci. Technol. A **35**, 021301 (2017).

11. Th Wegner, C. Küllig, and J. Meichsner, Plasma Sources Sci. Technol. **26**, 025006 (2017).

12. Th Wegner, C. Küllig, and J. Meichsner, Plasma Sources Sci. Technol. **26**, 025007 (2017).

13. J. Wang, Y. Du, X. Zhang, Z. Zheng, Y. Liu, L. Xu, P. Wang, and J. Cao, Phys. Plasmas **21**, 073502 (2014).

14. M. A. Lieberman, and A. J. Lichtenberg, *Principles of Plasma Discharges and Materials Processing*, 2nd ed. (John Wiley & Sons, Inc., Hoboken, New Jersey, 2005).

15. P. Chabert, and N. Braithwaite, *Physics of Radiofrequency Plasmas*, (Cambridge: Cambridge University Press, 2011).

16. S. V. Singh, and C. Pargmann, J. Appl. Phys. **104**, 083303 (2008).

17. T. Gans, M. Osiac, D. O'Connell, V. A. Kadetov, U. Czarnetzki, T. Schwarz-Selinger, H. Halfmann, and P. Awakowicz, Plasma Phys. Control. Fusion **47**, A353 (2005).

18. G. Cunge, B. Crowley, D. Vender, and M. M. Turner, Plasma Sources Sci. Technol. **8**, 576 (1999).

19. M. Lee, and C. Chung, Plasma Sources Sci. Technol. **19**, 015011 (2010).

20. M. M. Turner, and M. A. Lieberman, Plasma Sources Sci. Technol. **8**, 313 (1999).

21. T. Czerwiec and D. B. Graves, J. Phys. D: Appl. Phys. **37**, 2827 (2004).

22. Th Wegner, C. Küllig, and J. Meichsner, Plasma Sources Sci. Technol. **24**, 044001 (2015).

23. P. Chabert, A. J. Lichtenberg, M. A. Lieberman, and A. M. Marakhtanov, Plasma Sources Sci. Technol. **10**, 478 (2001).

24. U. Kortshagen, N. D. Gibson, and J. E. Lawler, J. Phys. D: Appl. Phys. **29**, 1224 (1996).

25. E. Despiau-Pujo and P. Chabert, Plasma Sources Sci. Technol. **18**, 045028 (2009).

26. C. Chung and H. Chang, Appl. Phys. Lett. **80**, 1725 (2002).

27. P. Kempkes, S. V. Singh, C. Pargmann, and H. Soltwisch, Plasma Sources Sci. Technol. **15**, 378 (2006).

28. E. Kawamura, M. A. Lieberman, A. J. Lichtenberg, and D. B. Graves, Plasma Sources Sci. Technol. **21**, 045014 (2012).

29. M. Lee and C. Chung, Phys. Plasmas **13**, 063510 (2006).

30. A. M. Daltrini, S. A. Moshkalev, T. J. Morgan, R. B. Piejak, and W. G. Graham, Appl. Phys. Lett. **92**, 061504 (2008).

31. M. J. Kushner, J. Phys. D **42**, 194013 (2009).

32. P. Tian and M. J. Kushner, Plasma Sources Sci. Technol. **26**, 024005 (2017).

33. M. J. Kushner, W. Z. Collison, M. J. Grapperhaus, J. P. Holland and M. S. Barnes, J. Appl. Phys. **80**, 1337 (1996).

34. R. B. Piejak, V. A. Godyak and B. M. Alexandrovich, Plasma Sources Sci. Technol. **1**, 179 (1992).

35. T. Ohba, W. Yang, S. Tan, K. J. Kanarik, and K. Nojiri, Jpn. J. Appl. Phys. **56**, 06HB06 (2017).

36. D. J. Coumou, S. T. Smith, D. J. Peterson, and S. C. Shannon, IEEE Transactions on Plasma Science, **47**, 2102 (2019).

37. D. Metzler, C. Li, S. Engelmann, R. L. Bruce, E. A. Joseph, and G. S. Oehrlein, J. Vac. Sci. Technol. A **34**, 01B101 (2016).

38. S. J. Lanham and M. J. Kushner, "Investigating Mode Transitions in Pulsed Inductively Coupled Plasmas", 64th American Vacuum Society International Symposium, Paper PS-WeA10, Tampa, FL, November 2017.

39. S. B. Felch, Z. Fang, B.-W. Koo, R.B. Liebert, S.R. Walther and D. Hacker, Surf. Coat. Technol. **156**, 229 (2002).

40. A. Agarwal and M. J. Kushner, J. Appl. Phys. **101**, 063305 (2007).

Chapter 5: Impedance Matching to a Pulsed Inductively Coupled Plasma Using Set-point Matching and Frequency Tuning

5.1 Introduction

Low pressure plasmas are widely used in industrial applications for microscale device fabrication. Efficiently applying sufficient power to the plasma is necessary to produce high plasma densities, which requires a low power reflection coefficient (Γ). The power reflection coefficient is,

$$\Gamma = \left| \frac{Z_L - Z_0}{Z_L + Z_0} \right|^2 ,$$
(5.1)

where Z_L is the combined impedance of plasma, antenna/electrodes, and any circuit components used in the power transmission line, and Z_0 is the output impedance of the power supply, which typically is 50 Ω. In an inductively coupled plasma (ICP) reactor, to reduce Γ, an impedance matching network (IMN) ideally consisting of non-resistive passive circuit components is often implemented between the power supply and plasma reactor. By changing the impedance of the IMN, Z_L can be tuned to minimize Γ. The power delivery to the plasma is then,

$$P = P_0(1 - \Gamma),$$
(5.2)

where P_0 is the output power from the power supply. The maximum power delivery is attained when $Z_L = Z_0$. Employing an IMN is a commonly used and effective method to maximize the power delivery to a plasma [3-7].

However, certain challenges emerge when the plasma switches between multiple states

144

during operation, for example, when the plasma is sustained with pulsed power [8-12]. In consider a plasma pulsed with 100s W at 10s mTorr pressure at 10s of kHz, both the real and imaginary parts of the plasma impedance can experience severe oscillations up to 10s Ω to 100s Ω during power transitions. These oscillations result from the significant difference between electron densities (n_e) between when power is on and off. At the leading edge of the power pulse, the electron density can increase from lower than 10^8 cm^{-3} to more than 10^{11} cm^{-3} within several μs. This increase of electron density produces high electron plasma frequency (ω_{pe}) and plasma conductivity (σ_p), and low plasma impedance,

$$\omega_{pe} = \left(\frac{e^2 n_e}{\varepsilon_0 m_e} \right)^{1/2},$$
(5.3)

$$\sigma_p = \frac{\varepsilon_0 \omega_{pe}^2}{j\omega + \nu_m},$$
(5.4)

where e is the elementary charge, ε_0 is the permittivity of free space, m_e is the electron mass, ω is the radiofrequency (RF) of the input power, and ν_m is the electron-neutral collision frequency [13]. If the duty-cycle (DC) of a pulse (the fraction of a period power is on) is small, or the period is short, it is likely that electron and ion densities will fail to reach the quasi-steady state before power is turned off again [11-12]. Consequently, the plasma impedance will continuously change during power-on, making it difficult for an IMN with fixed components to instantaneously match the impedance. If the power has a high-low pulsing profile—wherein instead of having zero power input during power-off, a low-power is applied to maintain the plasma—the different plasma impedances during the high- and low-power periods will pose even more challenges to the IMN [10]. To that end, real-time impedance matching techniques with an agile impedance adjustment rate is needed to optimize power delivery.

One approach to improve the impedance matching to a plasma load with a changing

145

impedance is to use multiple IMNs that match different Z_L [14]. For example, in a high-low pulsed power ICP reactor, two IMNs can be used to match the impedances of the plasma during high- and low-power periods. The IMN is switched between two architectures at each power transition. Using this technique, the power reflection will be greatly reduced compared to when the IMN is fixed. However, switching circuit components in the IMN is often a mechanical process that cannot be performed rapidly (often 100s to 1000s ms). Meaning matching the impedance by modifying the IMN is difficult if the plasma load is pulsed at high pulse repetition frequency (PRF). If the IMN fails to synchronize with the impedance of the plasma, unpredictable instabilities in the plasma can occur.

Another method of impedance matching to a plasma in near real-time is to fix the components of the IMN but modify the frequency of the power delivered from the power supply [15-16]. Both the impedance of the plasma and the circuitry have fairly significant reactive components, making it reasonably efficient to impedance match by frequency tuning. The advantage of using frequency tuning is the high tuning speed, The frequency tuning itself can be done in a time as short as 10s μs as the tuning can be performed electronically without any mechanically moving parts. Additionally, the fractional change of frequency that is required is usually small. For a plasma operating at 10s MHz, without orders of magnitude variation in operating conditions (power, pressure, gas flow rate etc.), the required frequency change to obtain matching during a pulse is often less than several MHz.

In this chapter, we discuss results from computational investigations of impedance matching with both a fixed IMN and with frequency tuning performed on a 15 mTorr Ar ICP. The plasma is produced in the ICP reactor ICAROS, and sustained by a pulsed power having PRF = 5 kHz, DC = 50%, and power of 50 W. Employing a fixed IMN was found to produce a

146

reasonable impedance matching result, but mismatch occurs when the impedance of the load shifts away from the target impedance of the IMN. This issue is then addressed by applying frequency tuning for a real-time impedance match. The power profile was varied to test the capability of frequency tuning to correct an impedance mismatch. Specifically, the pulsed power ranges from 30-80 W, power ramp time during power transition is varied from 4-80 µs, and DC is adjusted from 40-60%. In all cases, frequency tuning was found to help maintain a low power reflection coefficient. A brief description of the model is provided in Sec. 5.2. Results of the investigation of power deposition with only IMN and a combination of IMN and frequency tuning with varying pulse profiles are provided in Sec. 5.3. Concluding remarks are in Sec. 5.4.

5.2 Description of the Model

The computational platform used in this work is the Hybrid Plasma Equipment Model (HPEM). The details of this model are discussed in Chapter 2 and Ref [17]. Only a brief description is provided here.

The modules from the HPEM that are used in this work are the Fluid Kinetics Poisson Module (FKPM), Electromagnetics Module (EMM), and Electron Energy Transport Module (EETM). The inductively coupled electromagnetic field is obtained by solving the frequency-domain Maxwell's equation in the EMM. The continuity, momentum, and energy equations for the heavy particles are solved in the FKPM to update the heavy particle densities. With the charge density provided, Poisson's equation is also addressed in this module to provide the electrostatic potential. Boltzmann's equation is solved in the EETM for the electron energy distribution function (EEDF). Cross sections are averaged over the EEDF to provide impact rate coefficients. Electron energy equation is solved for the electron temperature.

A circuit model in the EMM is used to represent the IMN in the power transmission line

147

from the power supply to the ICP reactor. The impedances of the plasma downstream of the antenna are calculated having both inductive and capacitive components. A user-specified IMN is implemented between the antenna and power supply. The values of circuit components in the IMN are analytically calculated to produce a perfect impedance matching condition ($Z_L = Z_0$). This is accomplished by matching both the real and imaginary parts of Z_L and Z_0. When using frequency tuning, circuit components in the IMN are fixed, while the frequency of the radiofrequency (RF) provides minimum reflection coefficient is obtained by a minimization search. Both the test range (f_{range}) and step (Δf) are user-defined values. Frequency tuning is only performed when the fractional change of load impedance exceeds a threshold ε, which is by default 0.01.

The plasma species included in this model are Ar, Ar($1s_5$), Ar($1s_4$), Ar($1s_3$), Ar($1s_2$), Ar(4p), Ar(4d), Ar_2^*, Ar^+, Ar_2^+ and electrons, where Ar_2^* is a lumped excited state of the argon dimer.

5.3 Plasma Characteristics with Set-Point Matching and Frequency Tuning

The geometry of the ICP reactor used in this work is shown in Fig. 5.1. and represents the ICAROS reactor designed by Prof. Steven Shannon at North Carolina State University. This cylindrically symmetric reactor is relatively small, with the plasma chamber having a radius r = 4.8 cm and height z = 14.3 cm. Pure Ar is used at a flow rate of 10 sccm at a pressure of 15 mTorr. Gas is injected from the top of the reactor and is pumped out at the bottom. The speed of the pump is adjusted to maintain constant pressure. The wall of this reactor is alumina, with a dielectric constant $\varepsilon r = 9.8$. A 4-turn solenoidal coil provides power to the plasma. Here, the top coil is connected to the power supply, such that the voltage on the coil decreases from top to bottom. The bottom coil is connected to ground through a 0.35 nF capacitor. Pulsed power with

a pulse repetition frequency (PRF) of 5 kHz and duty cycle (DC) of 50% is applied to the plasma. The default power transition time (τt) is 4 μs, meaning that the power takes 4 μs to ramp from zero to full power, and from full power to zero. By default, the radiofrequency (RF) is 13.56 MHz. The reactor is surrounded by air. The outer-most boundary of the computational domain is metal, which provides boundary conditions for solutions of Poisson's equation and the wave equation.

The 2-dimensional distributions of electron density (n_e) and power density as well as the spatially averaged n_e and electron temperature (T_e) are shown in Fig. 5.2. Here, all power is delivered to the plasma ($\Gamma = 0$). The peak electron density is 1.4×10^{11} cm^{-3}. The peak power density of 0.17 W/cm^3 is close to the wall adjacent to the coils as the skin depth is only a few cm. Capacitive power coupling is not included in this work. That is, power is not electrostatically coupled to the plasma from the voltage drop on coils. The spatially averaged electron density and electron temperature are plotted over one pulse period (200 μs). T_e spikes at the beginning of the pulse when n_e is low ($< 4 \times 10^{10}$ cm^{-3}) in order to avalanche the electron density from its low prepulse value. This spike of T_e diminishes after 10 μs as n_e increases. Note that even though T_e is stabilized through almost the entire power-on period, n_e continues to increase, indicating that the plasma is not in a quasi-steady state. The plasma impedance changes with n_e and produces an electrically dynamic load, which then produces an impedance mismatch if no impedance matching system has been implemented.

The IMN implemented between the coils and power supply is shown in Fig. 5.3. From left to right are the power supply, impedance matching network, and the load impedances from the coils, plasma, and the reactor. The output impedance of power supply, R_G, is a standard 50 Ω impedance with no reactive component. R_{loss} represents the stray resistance in the IMN.

However, in this work, R_{loss} is set to 0 to provide a lossless IMN. The inductance L_P in the IMN is a constant 0.7 μH, while the capacitances C_S and C_P are analytically solved to produce a perfect impedance match condition. A detailed solution of C_S and C_P is provided in the Appendix. Briefly, C_S and C_P are solved by matching the combined impedance of all the non-power supply components to R_G. The loads following the IMN are the coils and plasma, whose impedances are automatically calculated in the HPEM. The impedance of the coil is geometry dependent, and the plasma impedance is a function of plasma geometry, density and impact collision frequency (v_m). Z_P is approximated as that of the window. The last two components, L_T and C_T, are the termination components representing the impedance between the antenna and ground. In this work, $L_T = 0$, and $C_T = 350$ pF.

Values of C_P and C_S in this IMN are solved through the power-on part of the pulse for a perfect match. The results are shown in Fig. 5.4, where Im(Z_L) and Re(Z_L) are the real and imaginary parts of the load impedance Z_L. Significant oscillations of Z_L occur during power transitions as both n_e and the collision frequency (v_m) experience rapid changes. As shown in Eq. (5.4), a change of n_e and v_m directly affects the electrical properties of the plasma. Because the plasma impedance is one of the major components of Z_L, the ignition and decay of the plasma then produce changes in the power reflection coefficient. Z_L stabilizes as plasma approaches the quasi-steady state, with Re(Z_L) remaining constant at 25 Ω, and Im(Z_L) slightly decreasing from 46 Ω (20 μs) to 41 Ω (100 μs). This variation of Im(Z_L) suggests that the increase in n_e during power-on mainly affects the reactance of the plasma. To have a perfect match, the value of C_P remains nearly constant, with only minor increases from 52 pF at 10 μs to 63 pF at 100 μs. C_S is increases by a factor of 1.4, from 182 pF to 253 pF, which indicates that an impedance mismatch will occur if the IMN has fixed values of C_S and C_P.

The power deposition and reflection with the fixed IMN are shown in Fig. 5.5. The method of using a fixed IMN for impedance matching is referred to as set-point matching. With set-point matching, C_P and C_S are obtained from the result shown in Fig. 5.4 to perfectly match at a specific time during the pulse. Set-point values of C_P and C_S are chosen at $\tau_M = 10$ and 90 μs, and are designated as match points. When $\tau_M = 10$ μs, the plasma ignites rapidly and reaches the near quasi-steady state within 20 μs. Because the IMN is selected to match the impedances at $\tau_M = 10$ μs, the reflected power (P_{ref}) drops to 0 at that time, after the initial spike when the plasma first ignites. The impedance of the plasma becomes relatively stable 50 μs after the leading edge of the pulse (Fig. 5.4). Matching early in the pulse produces a non-zero power reflection coefficient Γ through the entire power-on period, starting from $\tau = 10$ μs. In this case, with $\tau_M = 10$ μs, 2.6 W out of 50 W input power is reflected back to the power supply at $\tau = 90$ μs, which translates to a power reflection coefficient of $\Gamma = 5\%$. To minimize this power reflection, a match point is chosen late in the pulse, at $\tau_M = 90$ μs. As shown in Fig. 5.5b, this approach successfully brings power reflection down to almost zero when $\tau > 40$ μs. However, the mismatch early in the pulse challenges plasma ignition. Compared to $\tau_M = 10$ μs, the initial power reflection spike lasts longer when matching at $\tau_M = 90$ μs. Even though the integral of the reflected power (P_{ref}) in the entire power-on period is not large ($\approx 10\%$), the slower plasma ignition might be problematic.

To better optimize power delivery, a near real-time impedance matching technique is needed, along with set-point matching. To accomplish this, we implemented frequency tuning. Typically, the power reflection coefficient is sensitive to the change of frequency, as shown in Fig. 5.6a. Power reflection can be significantly reduced by a small adjustment in operating frequency. In practice, frequency tuning can be done much faster than adjusting the components

in the IMN (μs versus s). In the HPEM, frequency tuning is performed using a search algorithm. A diagram of this process is shown in Fig. 5.6b. Frequency tuning is performed when the fractional variation of the load impedance exceeds the threshold ε, which is 0.01 here.

Results with frequency tuning along with set-point matching are shown in Fig. 5.7. The range for the frequency tuning is $f_{range} = 4$ MHz, meaning that the frequency can be varied from 11.56 to 15.56 MHz. As the model indicates, with frequency tuning, almost perfect power matching is attained regardless of the choice of match points. Power reflection of less than 30 W occurs in the first 4 μs for both cases ($\tau_M = 10$ and 90 μs). The finite power reflection during start up is a consequence of the frequency have reached its lower limit of 11.56 MHz. However, because of its small magnitude and short duration, this power reflection does not have a significant effect on the plasma. The choice of match points affects the preciese frequency during frequency tuning. When frequency tuning is employed, 13.56 MHz is the frequency near the match points because the components in the IMN are chosen when the input power is at 13.56 MHz. By matching at different times, the peak-to-peak frequency oscillation decreases from 3.5 MHz for $\tau_M = 10$ μs to 2 MHz for $\tau_M = 90$ μs. In practice, frequency tuning with a tuning requires at least 10 μs. Therefore, choosing the match point that requires the smallest peak-to-peak frequency oscillation will reduce power reflection by reducing the number of frequency changes. For example, when $\tau_M = 10$ μs, if the frequency is tuned to match early pulse to operate at 13 MHz and remains at this frequency until mid-pulse at ≈ 60 μs, the offset of 2 MHz from the ideal frequency during power-on will produce a significant impedance mismatch. Conversely, if $\tau_M = 90$ μs and the frequency is tuned to 13 MHz in the early pulse, it only creates ≈ 0.6 MHz frequency offset in the mid-pulse. This considerably reduces the impedance mismatch.

In the following sections, power delivery to the plasma is computationally investigated by considering power magnitude, power transition time, and duty cycle while using set-point only impedance matching, and a combination of set-point matching and frequency tuning. The IMNs used are the same as it from the base case (50 W, DC = 50%, τ_t = 4 μs) when matching in the late pulse at τ_M = 90 μs.

5.3.1 Power Magnitude

The power magnitude of the pulse was varied from 30 to 80 W while the duty cycle (50%) and transition time (4 μs) remained the same as the base case. To quantify the power deposition, power efficiency η is defined as,

$$\eta = \frac{\int_0^{\tau_P} P_{dep} dt}{\int_0^{\tau_P} P_{forward} dt},$$

(5.5)

where τ_P is the pulsing period, P_{dep} is the power deposition in the plasma, and $P_{forward}$ is the power output from the power supply. As a function of $P_{forward}$, η is plotted in Fig. 5.8. Even in the absence of frequency tuning, the power efficiency remains at a relatively high value of > 90% when $P_{forward}$ > 50 W. This is because the electrical properties of the plasma do not change significantly at high plasma density and so Z_L is relatively stable. For example, as power increases from 50 to 80 W, Re(Z_L) stays at 25 Ω while Im(Z_L) moderately increases from 35 to 41 Ω, which induces a minor impedance mismatch and leads to a slight decrease of η. Even though the IMN is chosen to match the late pulse when $P_{forward}$ = 50 W, the highest power efficiency with a set-point match occurs when $P_{forward}$ = 60 W. Although the impedance is perfectly matched at the end of the pulse when $P_{forward}$ is 50 W, η is lower at $P_{forward}$ = 50 W than 60 W. The power reflection produced by the impedance mismatch during other parts of the pulse is larger when $P_{forward}$ is 60 W. Instead of obtaining perfect match conditions at a specific

match point, when choosing IMN values, the goal should be to minimize the reflection coefficient through the entire period.

Without frequency tuning, the power deposition efficiency drops to almost zero as the pulse power decreases from 50 to 30 W. The electron density and power reflection coefficient with and without frequency tuning are shown in Fig. 5.9, when the pulse power is 30, 40, and 50 W. Note that when power is 40 W, even without frequency tuning, the plasma nearly reaches a quasi-steady state density at the end of the pulse. At $\tau = 90$ µs, $Z_L = (24 + j44)$ Ω when the power is 40 W, compared to $Z_L = (25 + j41)$ Ω when the power is 50 W. These values of closed Z_L suggest that when $P_{forward} = 40$ W, using the same IMN setup as in the base case can also optimize power delivery late in the pulse. As shown in Fig. 5.9b, the power reflection coefficient when $P_{forward}$ is 40 W (Γ_{40W}) is only 5% at $\tau = 100$ µs. The low power deposition efficiency with a decreasing power is caused by the impedance mismatch early in the pulse. At $\tau = 10$ µs, $Z_L(40$ W$) = (21 + j47)$ Ω, while $Z_L(50$ W$) = (24 + j51)$ Ω. The difference in Z_L, especially in relation to the resistive components, produces a severe impedance mismatch, which results in a high reflection coefficient and a low power deposition efficiency. A low power deposition efficiency early in the pulse delays plasma formation and increases in n_e. Therefore, at 40 W, it takes a longer time for the plasma to reach a quasi-steady state.

The impact of the impedance mismatch early in the pulse is maximized when $P_{forward} =$ 30 W. In this case, without frequency tuning, plasma fails to ignite as the power reflection coefficient remains high (Fig. 5.9b). However, with frequency tuning, the power reflection coefficient at 30 W (Γ_{30W}) is reduced to 80% at the leading edge of the pulse, which shortly increases to 95% and then abruptly decreases to less than 10% in 10 µs. The final decrease of Γ_{30W} is enabled by the power deposition early in the pulse. Even though Γ_{30W} is still higher than

154

80% in the first 5 μs, the small amount of power deposited in the plasma enables plasma ignition and the increase of n_e, which facilitates the impedance matching and further enables the increase of plasma density.

5.3.2 Power Transition Time

Another parameter that is often varied in a pulsing profile is the power transition time (τ_t). The power transition time was varied from 4 to 80 μs as the power turns on, and remains constant at 4 μs when the power is turned off. For all cases, full power is 50 W, and the duty cycle is 50%. Therefore, average power decreases with an increase of τ_t.

The power deposition efficiency η as a function of τ_t is shown in Fig. 5.10a. Without frequency tuning, η decreases from 93% to 14% as τ_t increases from 4 to 80 μs. This is caused by the long period of time with low input power. The power reflection coefficients when τ_t is 4, 40 and 80 μs are shown in Fig. 5.10b. Without frequency tuning, the power reflection coefficient remains at a high value through out the power transition. This is because the low power density produces a low plasma density, which leads to an impedance mismatch that enhances power reflection and results in even less power deposition to the plasma, again preventing an increase in n_e. When $\tau_t = 80$ μs and there is no frequency tuning, power cannot transfer to the plasma until the last 20 μs of the pulse when $P_{forward}$ reaches 50 W. Even then, the minimum power reflection coefficient is 60%, which translates to a power deposition of 20 W. The end result is a 20 μs spike of $n_e \approx 1.6 \times 10^{10}$ cm^{-3} at the end of each pulse with 86% of the total power reflected back to the power supply.

Applying frequency tuning proves helpful in reducing the power reflection coefficient. A low frequency is needed for impedance matching when n_e is low; however, the lower boundary of the RF is 11.56 MHz, which means there is a minimum n_e requirement for a functional

155

frequency tuning. In this work, that electron density is $\approx 10^{10}$ cm^{-3}, however n_e takes a longer time to reach this density with a longer τ_t. When $\tau_t = 80$ µs, frequency tuning starts to reduce Γ_R at 30 µs when $P_{forward} = 18$ W and nearly all of the power before 30 µs is reflected. The longer the power transition time is, more power is reflected. As τ_t increases from 4 to 80 µs, η decreases from 99% to 87% when frequency tuning is implemented. These results demonstrate that frequency tuning or real-time impedance matching is likely to be most impactful when the power profile has a large fraction in the low-power regime, such as a sawtooth waveform.

5.3.3 Duty Cycle

In this section, the duty cycle of the pulse ranges from 40% to 60%. The peak power is 50 W, and the power transition time is 4 µs, the same as in the base case. Therefore, the average power increases with an increase in the duty cycle. The power deposition efficiency η as a function of the duty cycle is shown in Fig. 5.11a.

Changing the duty cycle mainly affects the time the plasma stays in the quasi-steady state. The longer the duty cycle, the longer the time the plasma is in the quasi-steady state. The components of the IMN were chosen to match the load impedance Z_L when the plasma is stabilized at the end of the pulse. The impact of frequency tuning becomes insignificant when the duty cycle is long. The plasma can reach the quasi-steady state with a DC = 40% (Fig. 5.11). As a result, the power deposition efficiency $\eta > 90\%$ without frequency tuning. In these cases, frequency tuning can still optimize power delivery to the plasma during the first 40 µs, when some level of impedance mismatch occur.

As the duty cycle decreases, the impact of frequency tuning becomes more significant when a longer fraction of the pulse is mismatched. Note that increasing the duty cycle also decreases the inter-pulse period, meaning the plasma has a shorter time to dissipate, and the

initial plasma density will be higher at the leading edge of the pulse. Without frequency tuning, as the duty cycle increases from 40% to 60%, the initial electron density increases from 1.5 to 1.9×10^{10} cm^{-3}. However, since the plasma takes only $\approx$ 20 µs to reach the high-density state, the different n_e at the beginning of the pulse has little impact on power delivery.

5.4 Concluding Remarks

A computational investigation of power deposition in an Ar ICP sustained in the reactor ICAROS with 50 W power pulsed at 5 kHz was performed using the HPEM simulation platform. Two impedance matching techniques were employed: set-point matching using a fixed components in the impedance matching network (IMN), and a combination of set-point matching with a close to real-time frequency tuning. The circuit components in the IMN are first analytically solved for the perfect match and then fixed to match the impedance at a certain time during the pulse. Real-time frequency tuning is then employed with the set-point match to correct impedance mismatches.

We found that using set-point matching alone produces impedance mismatch and results in power reflection at times other than the match point. When frequency tuning is applied, the choice of match point affects the tuning range in such a way that a late match point in a quasi-steady state results in the need for smaller frequency adjustments. The impact of frequency tuning on power deposition with varied power magnitude, power transition time, and duty cycle were discussed. With the IMN set to match the impedance of the quasi-steady state, frequency tuning is found to be most impactful during transients when the input power is low. Therefore, frequency tuning is recommended if the pulse power is low, the power transition time is long, or the duty cycle is short. Impedance match early in the pulse is desirable because a severe

mismatch will extend the time that the plasma reaches the steady state. Therefore, frequency tuning, especially in the early pulse, is recommended.

To summarize, impedance matching not only maximizes the power delivered to the plasma reactor but also minimizes the power reflected back to the supply. Minimizing the reflected power becomes ever more important as power levels increase in plasmas processing – now exceeding 10-20 kW. In addition to minimizing reflected power to protect the power supply, optimum impedance matching enables consistent power pulsing profiles to the plasma. For example, optimum matching helps to avoid issues such as *dropping a pulse*, in which due to impedance mismatch at the onset of applied power, the plasma does not ignite during the pulse. In this chapter, the effects of set-point matching and frequency tuning for impedance matching in plasma processing are discussed. However, these results may also apply to other pulsed power plasma applications. For example, pulsed power thrusters are used in electric propulsion (EP) for accelerating and station keeping of satellites and spacecraft. EP uses plasma exhaust to accelerate the spacecraft. In these systems, minimizing mass is exceedingly important. Minimizing mass is typically achieved by maximizing the efficiency of all on-board systems, which includes the power transfer that generates the plasma.
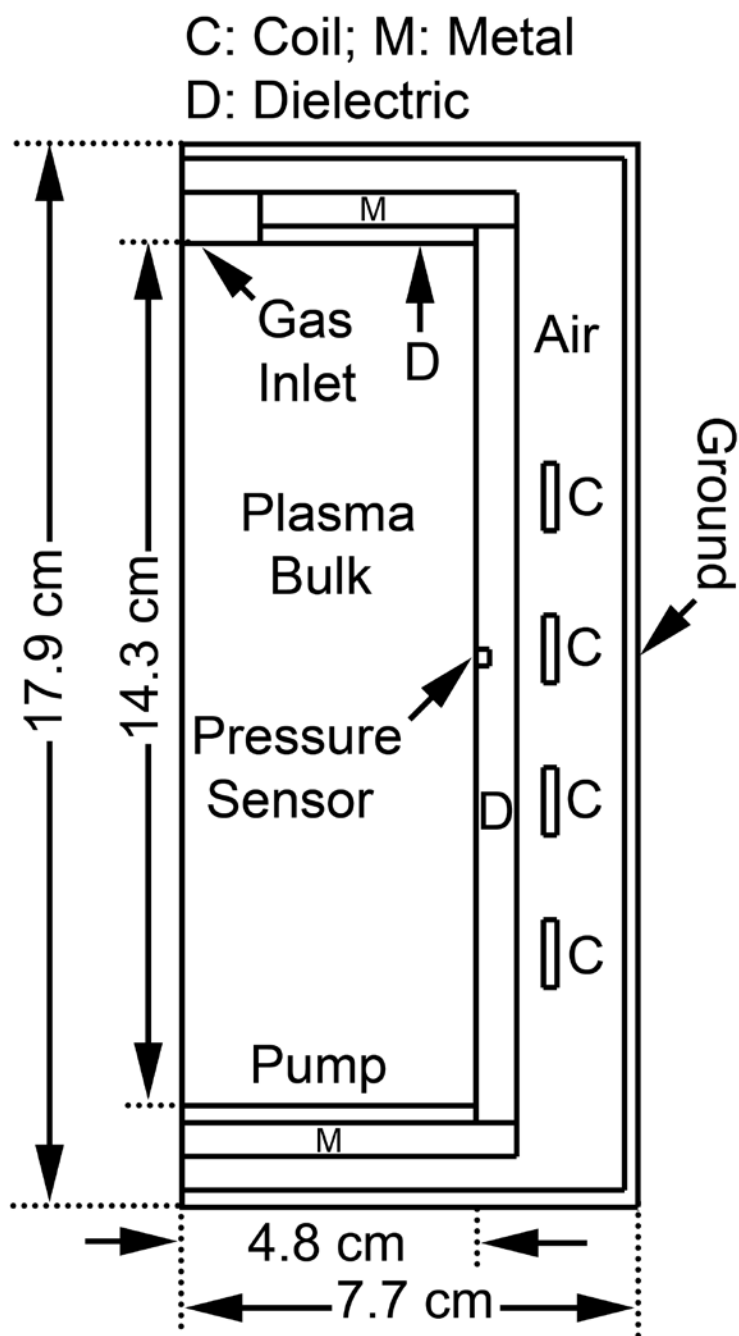
Fig. 5.1 Geometry of the inductively coupled plasma (ICP) reactor used in this work.
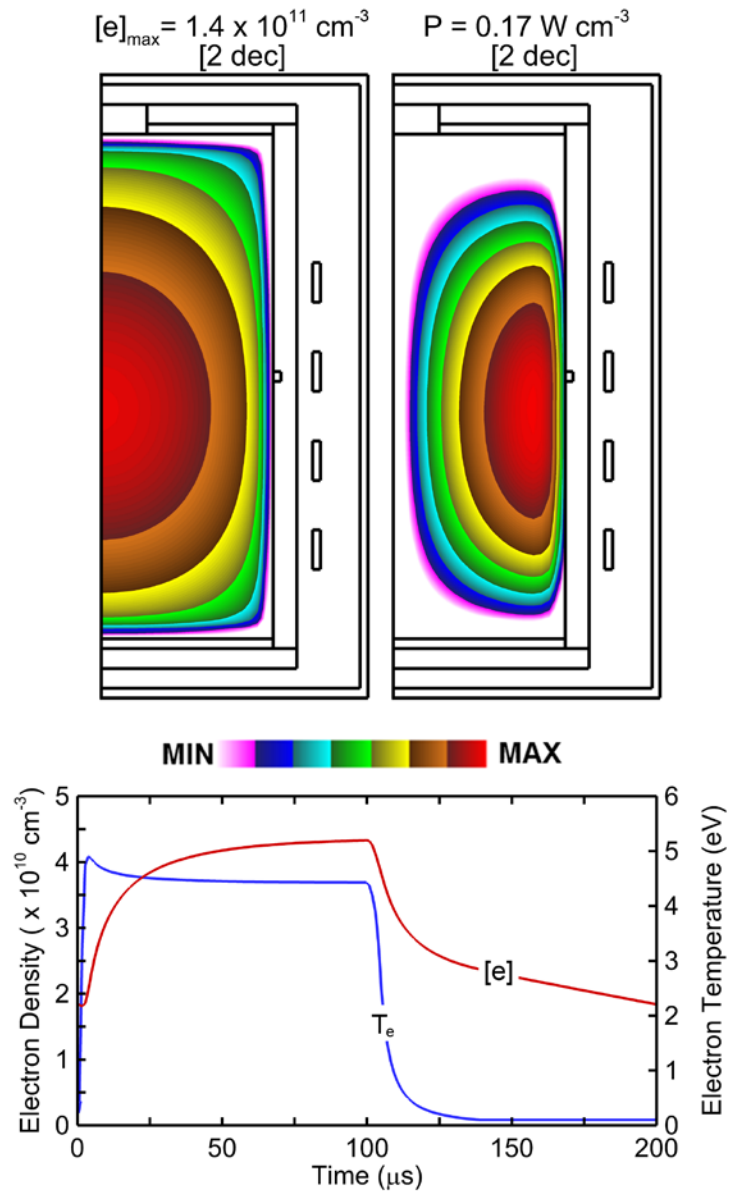
Fig. 5.2 Distributions of electron density and power density, and spatially averaged electron density and electron temperature. Ar, 15 mTorr, 50 W, PRF = 5 kHz, DC = 50%.
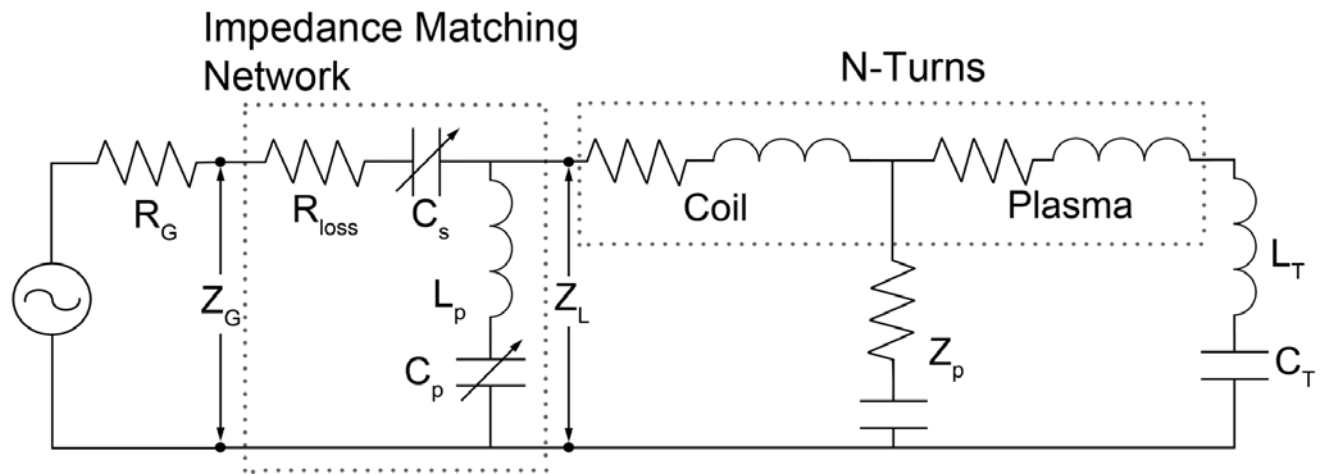
Fig. 5.3 Diagram of power transmission line with power supply, impedance matching network, and load impedance consisting of the coil, plasma, and termination circuit components.
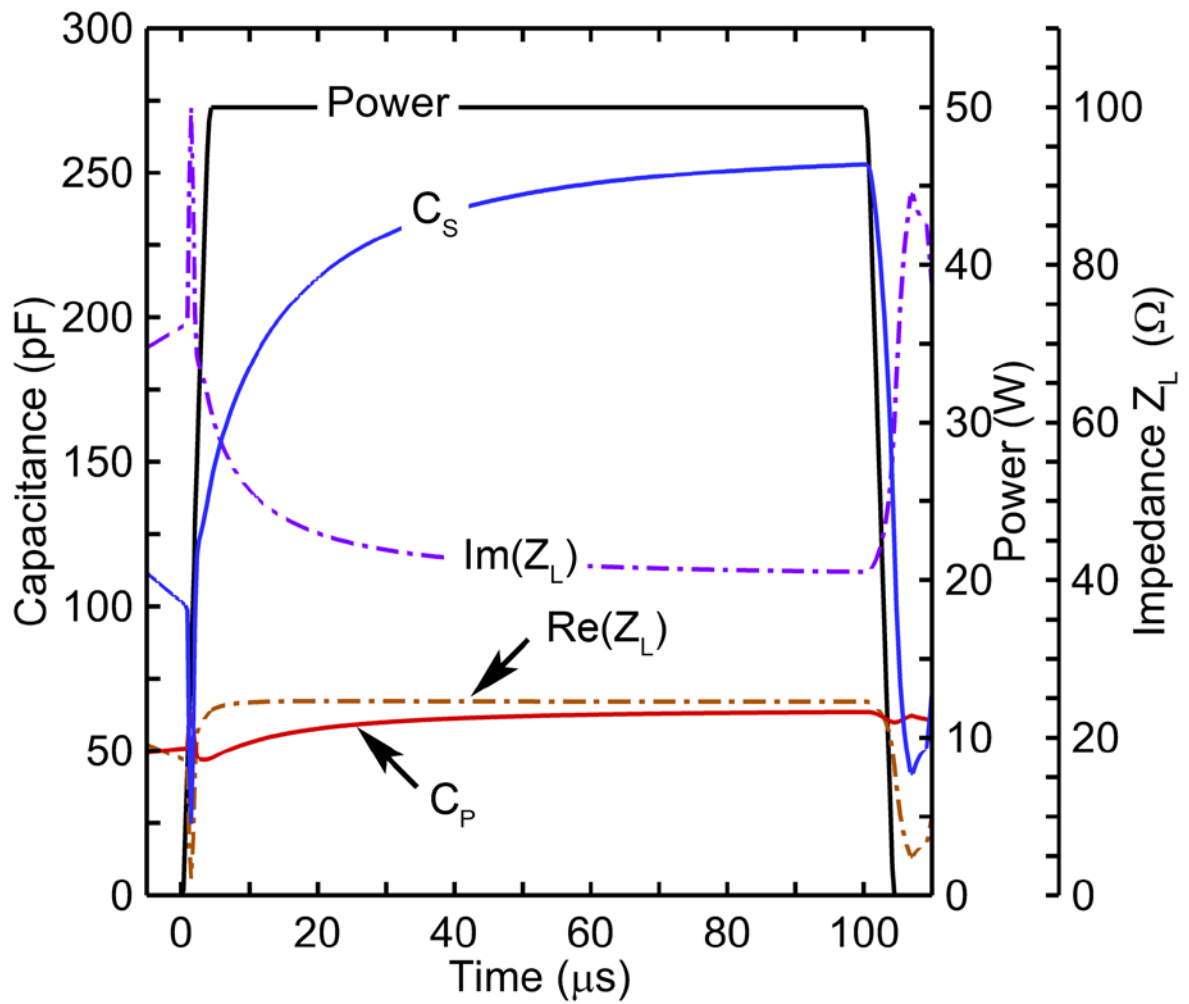
Fig. 5.4 Real and imaginary parts of the load impedance (Z_L) and the capacitances in the matching network (C_P and C_S) required for the impedance match. Ar, 15 mTorr, 50 W, PRF = 5 kHz, DC = 50%.
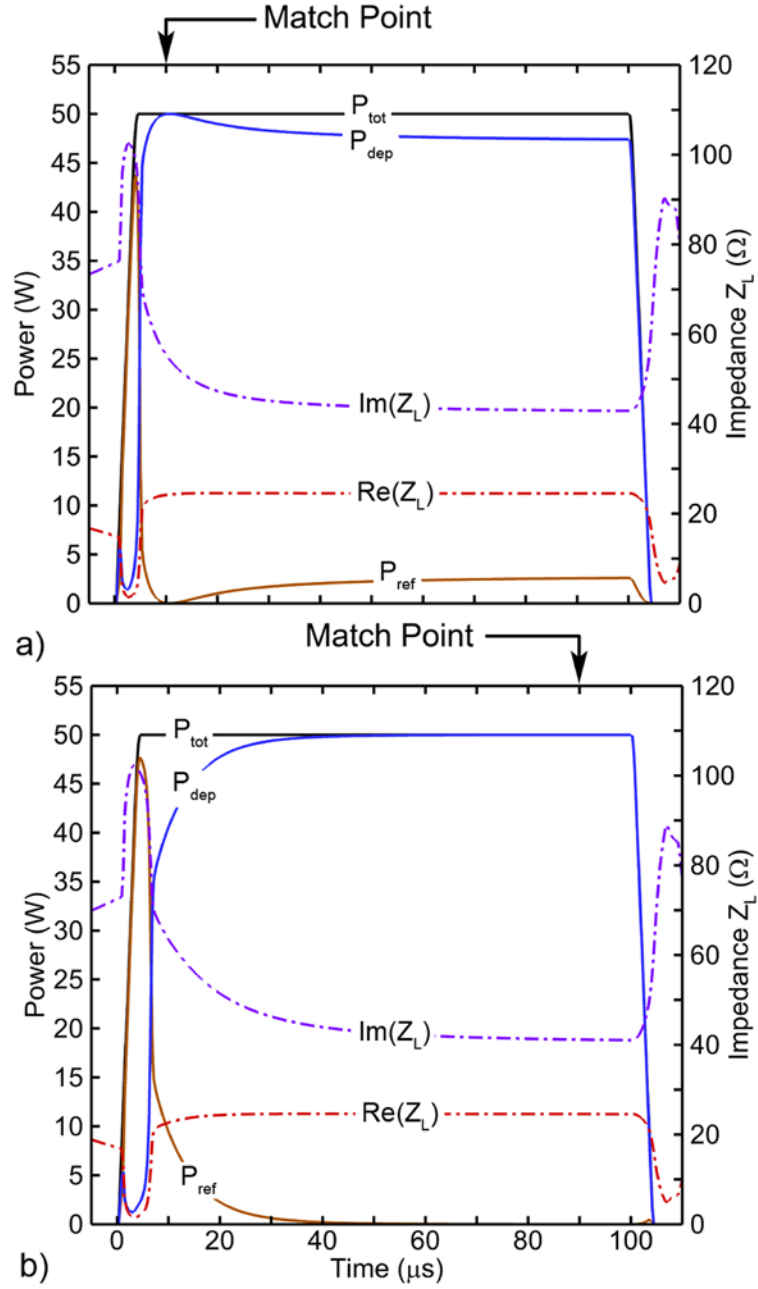
Fig. 5.5 Power deposition (P_{dep}) and reflection (P_{ref}) and load impedance when the impedance matching network is chosen to match a) in the early pulse at $\tau = 10$ μs and b) in the late pulse at $\tau = 90$ μs. Ar, 15 mTorr, 50 W, PRF = 5 kHz, DC = 50%.
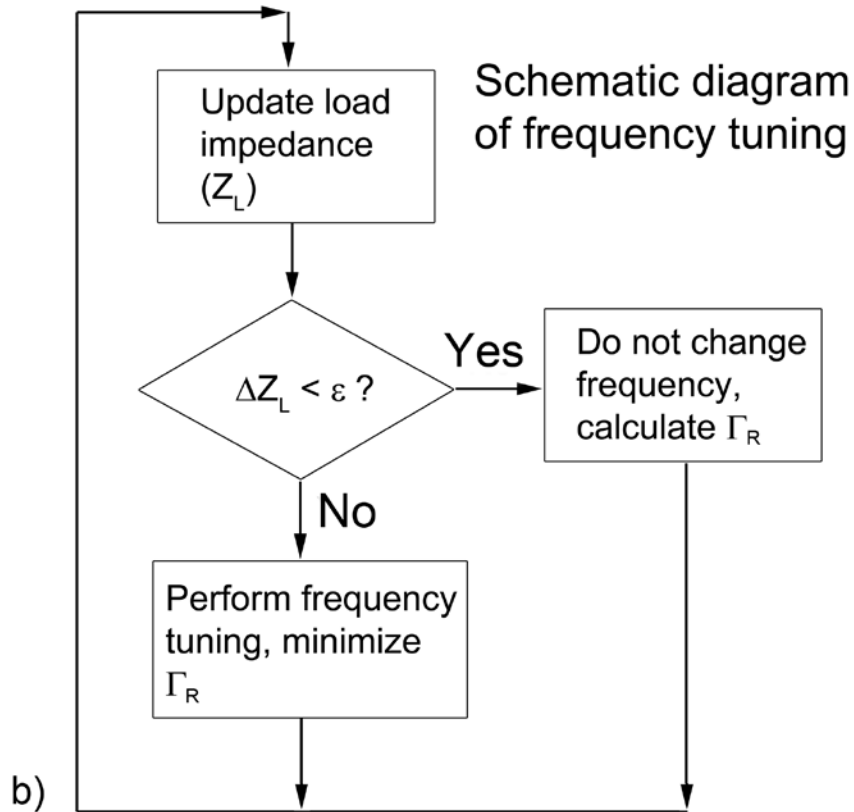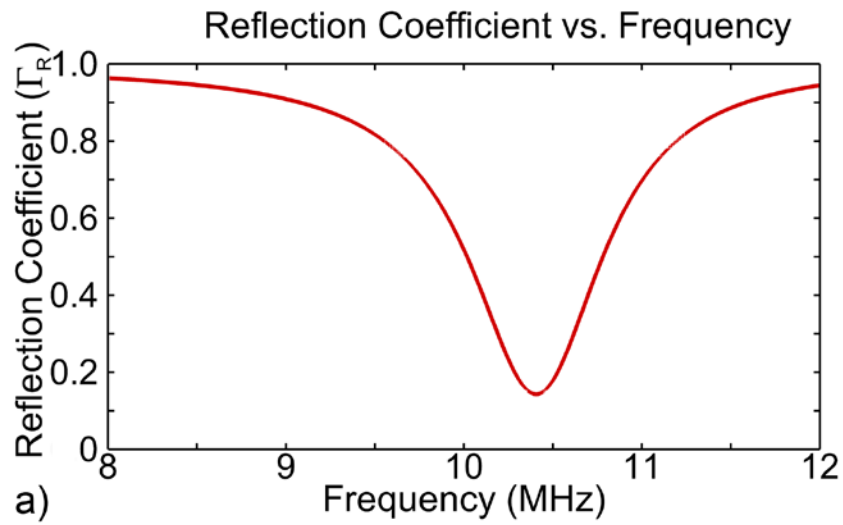
Fig. 5.6 a) A typical response of power reflection coefficient (Γ) with radiofrequency, and b) a schematic diagram of frequency tuning in the HPEM.
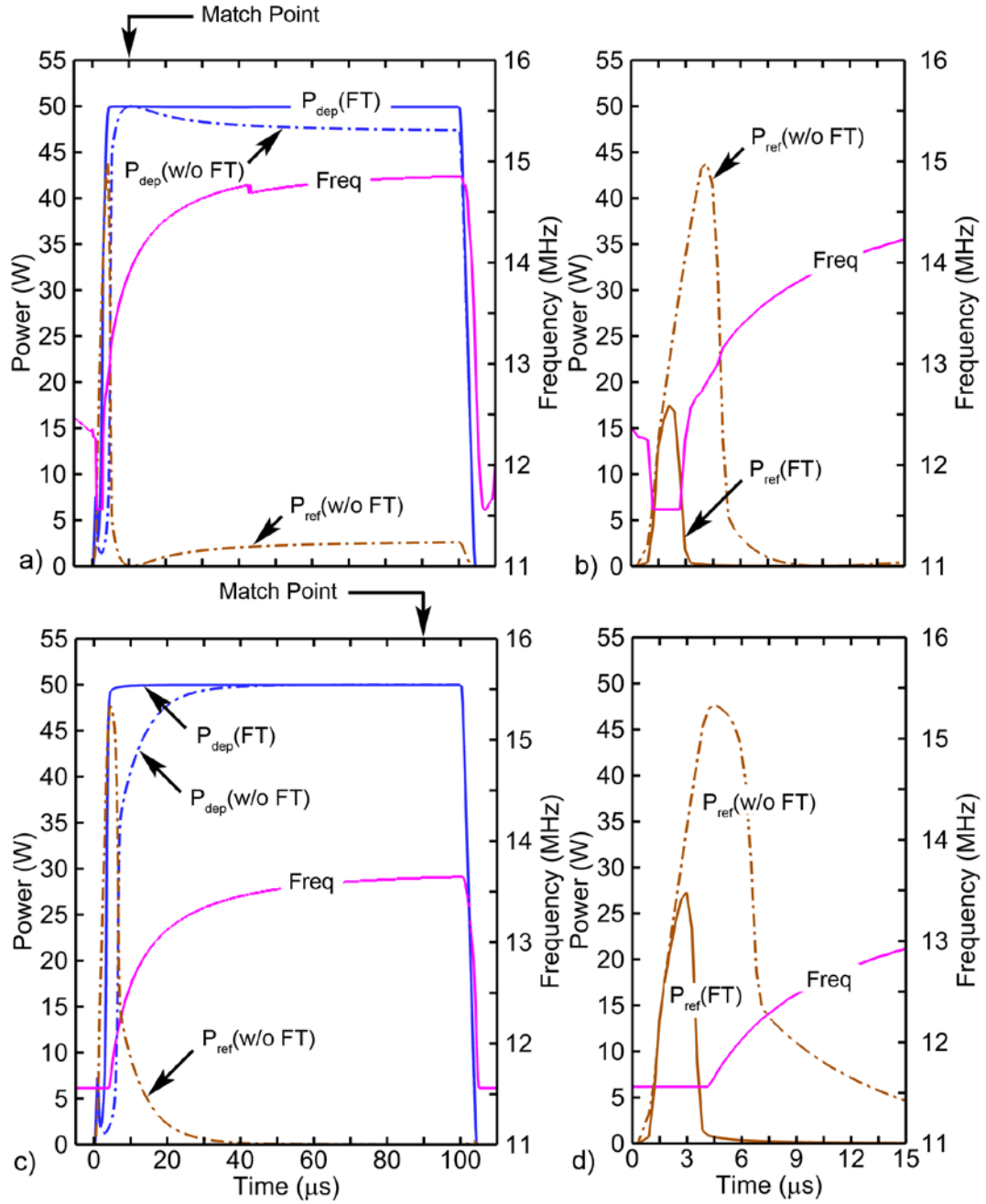
Fig. 5.7 Power deposition (P_{dep}) and reflection (P_{ref}) with (FT) and without (no FT) frequency tuning when a) b) IMN is chosen to match early in the pulse at $\tau = 10$ µs and when c) d) IMN is chosen to match late in the pulse at $\tau = 90$ µs.
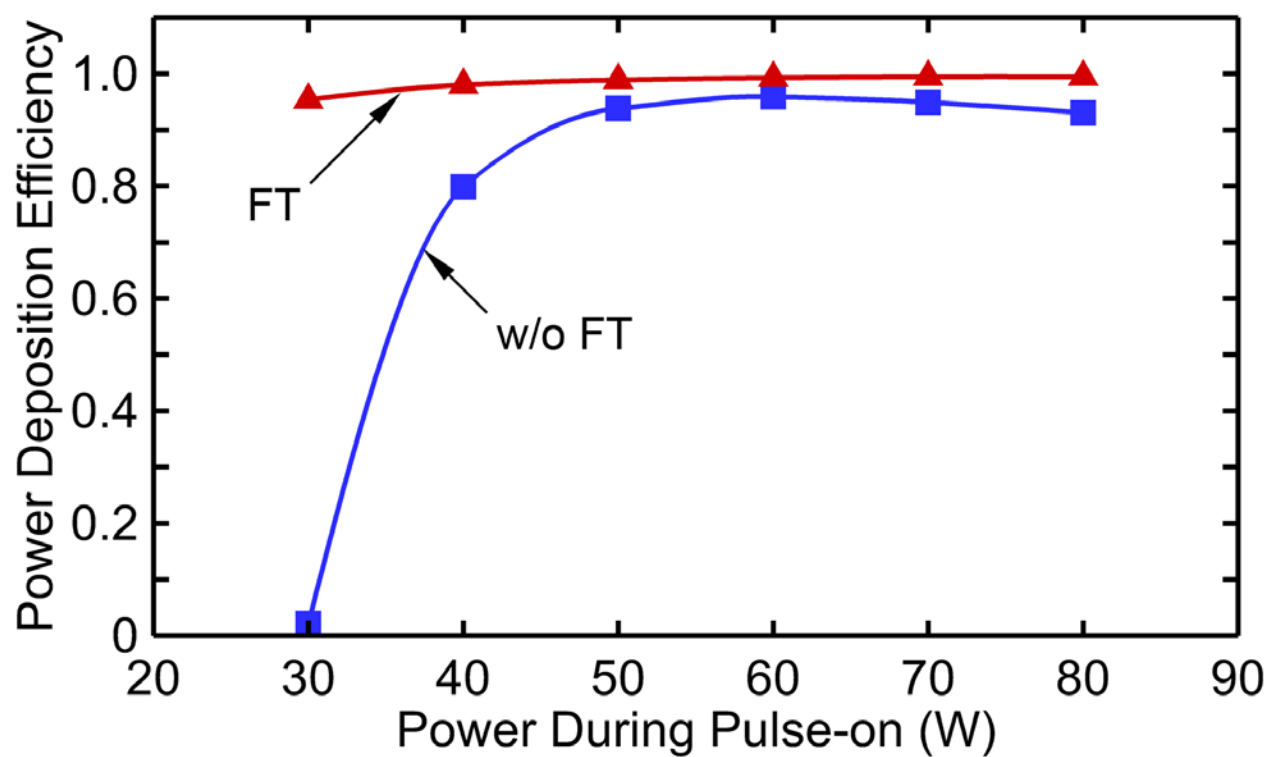
Fig. 5.8 Power deposition efficiency with and without frequency tuning with different powers. Ar, 15 mTorr, PRF = 5 kHz, DC = 50%.
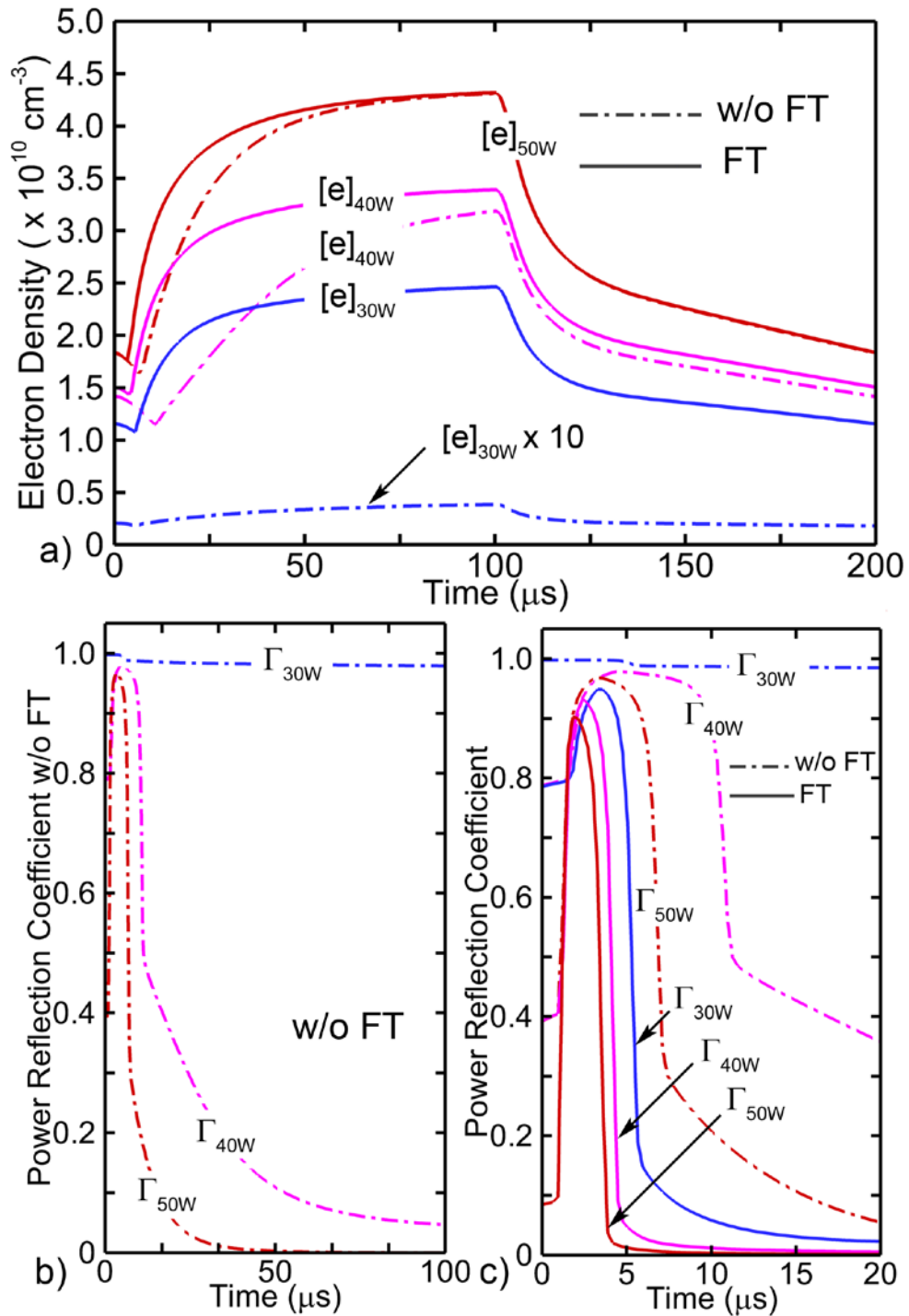
Fig. 5.9 a) Spatially averaged electron density b) power reflection coefficient without frequency tuning and c) power reflection coefficient in the first 20 μs with and without frequency tuning. Ar, 15 mTorr, PRF = 5 kHz, DC = 50%.

167
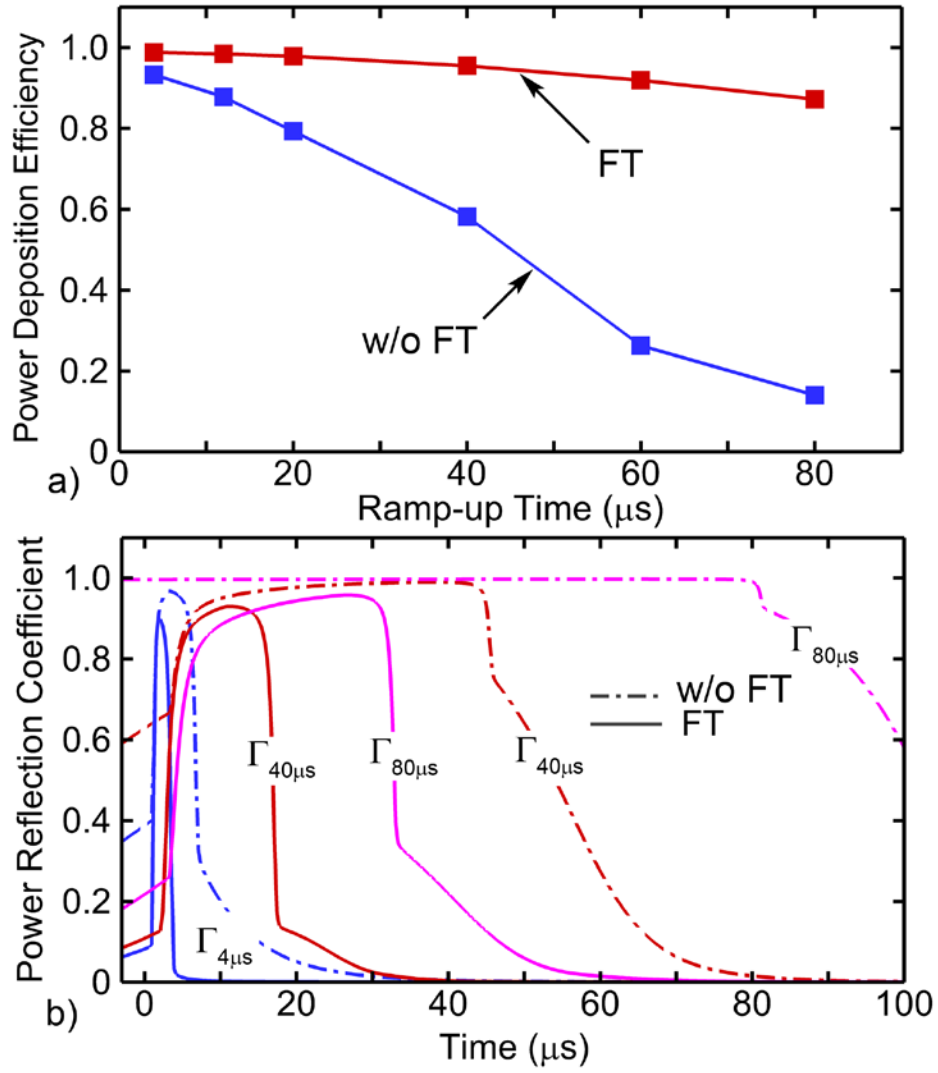
Fig. 5.10 a) Power deposition efficiency as a function of power transition time (τ_t) and b) power reflection coefficient when τ_t = 4, 40, and 80 µs. Ar, 50 W, 15 mTorr, PRF = 5 kHz, DC = 50%.
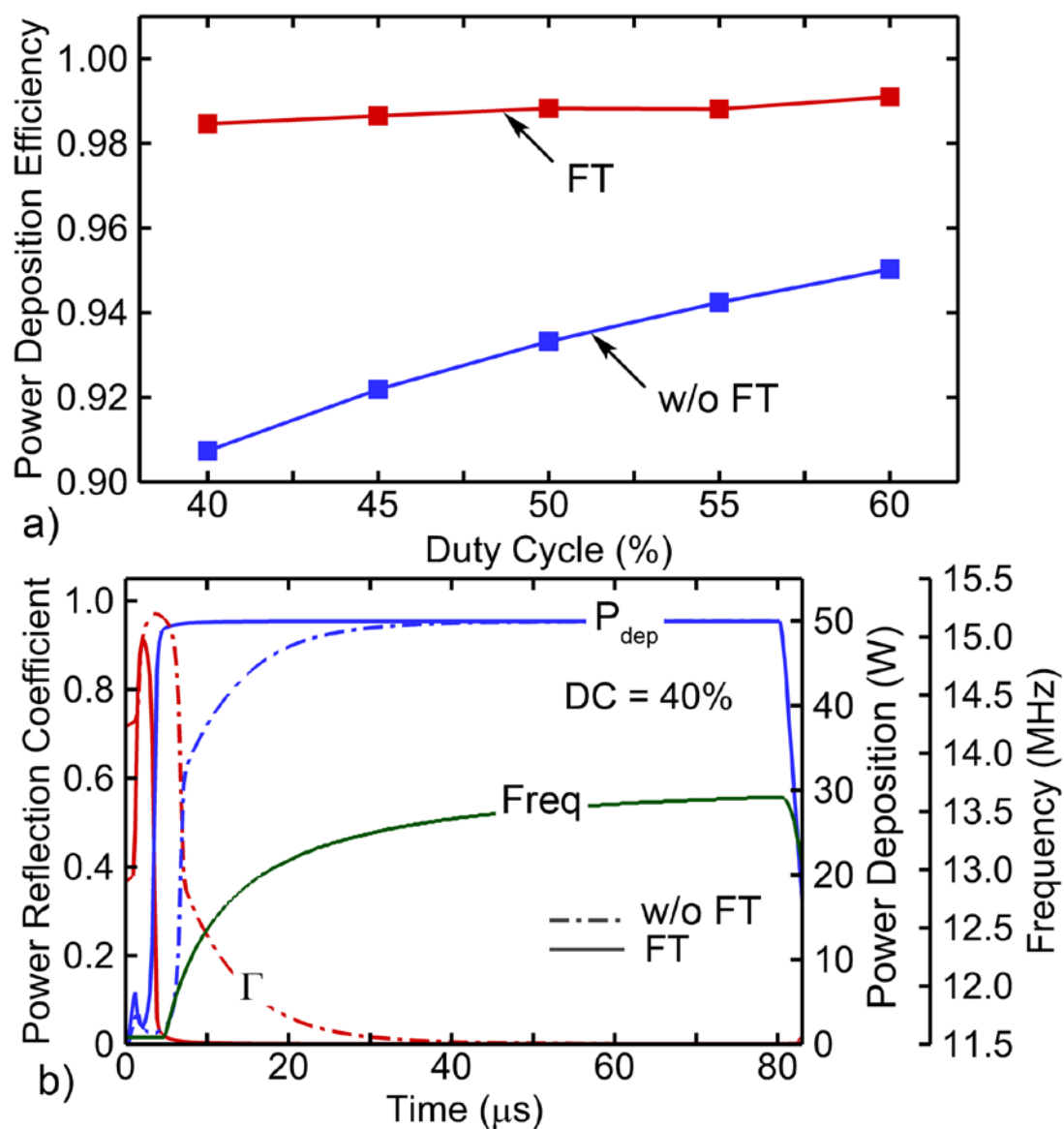
Fig. 5.11 a) Power deposition efficiency as a function of duty cycle and b) power deposition, power reflection, and frequency with and without frequency tuning when DC = 40%. Ar, 50 W, 15 mTorr, PRF = 5 kHz.

5.6 References

1. I. Adamovich et. al., J. Phys. D: Appl. Phys. **50**, 323001 (2017).

2. B. Wu, A. Kumar, and S. Pamarthy, J. Appl. Phys. **108**, 051101 (2010).

3. F. Schmidt, J. Schulze, E. Johnson, J.-P. Booth, D. Keil, D. M. French, J. Trieschmann, and T. Mussenbrock, Plasma Sources Sci. Technol. **27**, 095012 (2018).

4. M. Long, IEEE Plasma Sci. **34**, No. 2 (2006).

5. J. Hopwood, Plasma Sources Sci. Technol. **3** 460 (1994).

6. D. Petreus, A. Grama, S. Cadar, E. Plaian, and A. Rusu, 12th Int. Optim. Elect. Electron. Equipment Conf. pp. 1317-1322 (2010).

7. J. G. Yang, N. S. Yoon, B. C. Kim, J. H. Choi, G. S. Lee, and S. M. Hwang, IEEE Plasma Sci. **27**, No. 3 (1999).

8. L. Liu, S. Sridhar, V. M. Donnelly, and D. J. Economou, J. Phys. D: Appl. **48**, 485201 (2015).

9. J. S. Seo, K. N. Kim, K. S. Kim, T. H. Kim, and G. Y. Yeom, Jpn. J. Appl. Phys. **54**, 01AA10 (2015).

10. T. List, T. Ma, P. Arora, V. M. Donnelly, and S. Shannon, Plasma Sources Sci. Technol. **28**, 025005 (2019).

11. B. Ramamurthi, and D. J. Economou, J. Vac. Sci. Technol. A **20**, 467 (2002).

12. M. A. Lieberman, and S. Ashida, Plasma Sources Sci. Technol. **5**, 145-158 (1996).

13. M. A. Lieberman and A. J. Lichtenberg, Principles of Plasma Discharges and Materials Processing (John Wiley & Sons, Inc., Hoboken, NJ, USA, 2005).

14. A. Aghajanyan, A. Hakhoumian, N. Poghosyan, T. Poghosyan, and T. Zakaryan, Armen. J. Physics **8**, pp. 44-50 (2015).

15. K. Takahashi, Y. Nakano, and A. Ando, J. Phys. D: Appl. Phys. **50**, 265201 (2017).

16. K. Takahashi, K. Hanaoka, and A. Ando, Front. Phys. **7**, pp. 1-8 (2020).

17. M. J. Kushner, J. Phys. D: Appl. Phys. **42**, 194013 (2009).

Chapter 6: Customizing Capacitively Coupled Plasma Properties with a Triple-Frequency Power Source

6.1 Introduction

The use of capacitively coupled plasmas (CCPs) to enable reactive-ion etching (RIE) has been widely studied [1-4]. A typical CCP reactor consists of a pair of parallel plate electrodes separated by a few cm, an annular gas outlet surrounding the bottom electrode (substrate), and a showerhead for the gas inlet that overlaps with the top electrode. In conventional RIE, the bottom electrode is powered with up to several kW of radiofrequency (RF) power, and the top electrode is grounded. A negative DC bias voltage is usually self-generated on a blocking capacitor in series with the bottom electrode to balance current to the powered and grounded electrodes [2,5]. This bias voltage partly contributes to the ion acceleration and can accelerate the ion energy incident on the substrate from 100s to thousands eV.

Energetic ions play an essential role in the microchip etching process as they are the agent for both physical sputtering and surface activation. To optimize the RIE process, one needs precise control over the ion energy and angular distributions (IEADs) incident on the wafer. For example, with the shrinking device dimension (under 10 nm) and increasing aspect ratio (AR, the depth over the width) of the target features, a narrow ion angular distribution (IAD) is required to minimize scattering from the sidewalls [6-8]. If an ion enter a feature with a large incident angle (> 50˚), it will strike and be reflected from the sidewalls. Successive collisions result in a loss of energy and broadening of the angular distribution. This results in

bowing at the top of the feature and a lack of energetic ions at the etch front at the bottom, causing a widened opening and slow etch rate. The ion energy distribution (IED) has limitations both high- and low-energies. Too high of an ion energy leads to perhaps unwanted physical sputtering. Too low of an ion energy results in etch-stop [9,10].

IEADs can be modified by changing the plasma operating conditions. However, in a conventional single-frequency (SF) CCP, this usually leads to modification of the magnitude and composition of the ion flux. To decouple the IEADs from the magnitude of the ion flux, and to gain independent control of both, multi-frequency CCPs can be used. The goal is to have more control parameters so that a combination of the parameters can provide a wide range of IEADs and ion flux. In a CCP, electrons are mainly heated through stochastic heating such that hot electrons are created through the fast oscillation of the sheath. A sheath is a high electric field (E-field) region adjacent to a surface exposed to the plasma. Above the surface of a powered electrode, high frequency voltage, usually radiofrequency (RF), leads to a high sheath expansion velocity and a resulting high heating efficiency as well as a high plasma density. Unlike electrons, ions only respond to the low-frequency (LF) due to their larger mass. In a multi-frequency CCP, high-frequency (HF) power is used to control the plasma density while a range of LF powers are applied to the substrate to modify the IEADs. Applying harmonics of a fundamental frequency produces the electrical asymmetry effect (EAE) due to non-linear responses of the sheath to the non-sinusoidal voltage waveforms. The EAE provides an approach to control the DC bias, thereby offering additional control over IEADs [11-15].

The most basic multi-frequency CCP is a dual-frequency (DF) CCP where the power is applied to the plasma through two distinguishable frequencies [16-19]. Boyle et al. studied a DF-CCP using a particle-in-cell model with Monte Carlo collisions (PIC-MCC) [17]. It was

shown that the decoupling nature of the ion energy and flux is related to the low-to-high frequency ratio such that a greater separation of the two frequencies provides a more thorough decoupling between the IED and ion flux. In addition to the frequency ratio, the phase between frequencies (θ) can also be used as a method to control a DF-CCP [11, 20]. With investigations using an analytical model, Czarnetzki et al. reported that when applying the fundamental frequency (13.56 MHz) and its second harmonic (27.12 MHz) on the same electrode in a CCP, the ion energy has an almost linear dependence to θ, but the ion flux remains constant [11]. They suggested that varying θ induces significant deviations to the dynamics of power dissipation, and yet, time-averaged power deposition to the plasma is barely changed. Consequently, the acceleration of ions in the sheath, through which they obtain energy, is impacted by θ, but the ion flux remains constant.

Applying DF power can also have fundamental impacts on the plasma. Sahu et al. reported that while keeping the power input constant, if an ultrahigh-frequency (320 MHz) is added to a SF-CCP sustained by 200 W (13.56 MHz) power, the electron energy distribution function (EEDF) can be changed from a Druyvesteyn to a bi-Maxwellian structure [21]. They concluded that HF enhances stochastic heating and populates warm-electrons (11-15 eV). Despite the advantages of DF-CCP in an RIE process, O'Connell et al. warned that some level of HF-LF coupling can still occur, especially when both frequencies are applied to the same electrode [16]. Such an issue can be solved by distributing the powers to different electrodes and using multi-frequency (> 2) power for even more sophisticated control over the plasma.

Diomede et al. investigated a multi-frequency CCP in a geometrically symmetric reactor powered by a tailored voltage consisting of up to three harmonics of the fundamental frequency (15 MHz) [22]. They found that both the absolute value of the DC bias and the electron density

increase with an increasing number of harmonics. But the ion energy on the grounded electrode changes monotonically with the number of harmonics. The average ion energy increases with an increasing number of applied harmonics when the phase of the harmonics $\theta = \pi$, but decreases when $\theta = 0$. These results suggest using phase as a parameter for modifying plasma properties in a multi-frequency CCP. Lee et al. investigated the IED from a low-pressure triple-frequency (TF) CCP sustained in Ar with driving frequencies of 1, 30, and 120 MHz applied to the same electrode [23]. They concluded that the current density (for the current-driven source) or voltage (for a voltage-driven source) along with the frequency ratios, determine the average ion energy and the width of the IED, instead of the absolute values of frequencies.

Focused more on the function of each frequency in a multi-frequency CCP, Kawamura et al. investigated Ar discharges with the highest frequency, being up to 162 MHz. They also concluded that LF power predominantly determines sheath development while the HF power controls plasma production. They reported that the standing wave created by HF power optimizes the plasma distribution. The high plasma density in the center of the reactor, caused by the standing wave, counteracts the electrostatic effect at the edge of the wafer and improves plasma uniformity.

In this chapter, we investigate a TF-CCP sustained in an $Ar/CF_4/O_2$ gas mixture and driven by powers at 5, 10, and 80 MHz. A brief model description is provided in Sec. 6.2. Results from the simulation while varying power, pressure, high frequency, and geometry are discussed in Sec. 6.3. Concluding remarks are in Sec. 6.4.

6.2 Model Description

The model used in this chapter is a two-dimensional (2D) kinetic-fluid hydrodynamics simulation, the Hybrid Plasma Equipment Model (HPEM). A detailed description of HPEM is

provided in Chapter 2 and Ref [25]. Only a brief description is provided here.

The HPEM contains modules addressing different aspects of plasma physics. The modules used in this work are Fluid Kinetics Poisson Module (FKPM), Electron Monte Carlo Simulation (eMCS), Surface Kinetic Model (SKM), and Plasma Chemistry Monte Carlo Module (PCMCM). In the FKPM, the momentum, energy, and continuity equations of all the heavy particles (neutrals and ions) are solved, which provides the densities of these heavy particles along with their source terms. Poisson's equation is also addressed in the FKPM to provide the electrostatic potential. The SKM interacts with FKPM in a way that the FKPM provides the fluxes to a surface, and SKM uses that information to update the surface reaction probabilities that are used in the FKPM.

The transport of both bulk and secondary electrons are tracked in the eMCS, as discussed in Section 2.1.2 and Ref [26]. In the eMCS, trajectories of pseudoparticles that represent electrons are advanced in the electric field from the FKPM while undergoing statistically chosen collisions. In this work, 60,000 pseudoparticles are launched to provide statistically accurate spatially-dependent electron energy distribution functions (EEDFs), which are then used to produce electron transport and rate coefficients.

Both the ion flux and the IEADs can be obtained using PCMCM. In the PCMCM, similar to the eMCS, pseudoparticles representing ions are launched, moved, and tracked using a Monte Carlo approach. The number of pseudoparticles launched for each species is weighted by its corresponding source term. The electrostatic field solved for in the FKPM provides the acceleration. The IEADs of Ar^+, CF_3^+, CF_2^+, CF^+, F^+, O^+, O_2^+, and F_2^+ are recorded when striking the wafer. The IEADs discussed in this chapter averaged over the wafer and cross 0 degree.

In the HPEM, the power sources are independently controlled. For most cases discussed in this chapter, powers at each frequency are specified, and those corresponding voltages are adjusted to deliver the desired power. A 5 nF blocking capacitor is connected to the substrate to produce the DC bias. A $Ar/CF_4/O_2$ gas mixture is used as the feedstock gas, and the chemistry is discussed in detail in Ref [26]. The species are Ar, Ar($1s_5$, $1s_3$), Ar($1s_2$,$1s_4$), Ar(4p, 5d), Ar^+, CF_4, CF_3, CF_2, CF, C, F, F^*, F_2, SiF_4, SiF_3, SiF_2, CF_3^+, CF_2^+, CF^+, C^+, F^+, F_2^+, CF_3^-, F^-, O_2, $O_2(^1\Delta)$, O_2^+, O, O(^{1}D), O^+, O^-, CO, CO^+, COF, COF_2, CO_2, FO, and e.

6.3 Plasma Characteristic of TF-CCP

The reactor geometry used in this work is shown in Fig. 6.1. The reactor is cylindrical and is symmetrical across the central axis. The radius of the reactor is 29 cm, and the height is 7.4 cm. The wafer and the top electrode have a radius of 15.0 cm and are separated by 2.8 cm. HF power, 80 MHz and 500 W, is applied to the top electrode, and DF power with 5 and 10 MHz components is applied to the substrate, each delivering 400 W. The voltage at each frequency, time averaged plasma potential, and DC bias are in Table I. A quartz focus ring (relative dielectric constant $\varepsilon_r = 4$) surrounds the wafer. A sacrificial material with the same conductivity as the wafer (0.05 $\Omega^{-1}cm^{-1}$) is placed between the wafer and focus ring to smooth the sheath and help make the plasma uniform to the edge of the wafer. The wall of the reactor is grounded with a thin layer of dielectric coating ($\varepsilon_r = 50$). A fairly large ε_r is used here to compensate for the thickening of the dielectric layer by the finite mesh size, such that the capacitance of the dielectric coating remains large. In this geometry, the showerhead overlaps with the top electrode and feeds a gas mixture of $Ar/CF_4/O_2$ (75/15/10) evenly to the reactor at 500 sccm. The outlet pump is the annulus at the bottom of the reactor, surrounding the substrate. The pressure is measured by a sensor embedded in the chamber wall 0.8 cm above the pump,

which is used to adjust the pumping speed to sustain a constant pressure of 25 mTorr in the reactor.

The spatially averaged cation and neutral densities at the steady state are shown in Fig. 6.2. In the base case, the dominant ions are Ar^+ (2.4×10^{10} cm^{-3}) and CF_3^+ (2.0×10^{10} cm^{-3}). A high Ar^+ density results from the higher mole fraction of Ar in the feedstock gas. CF_4 has lower mole fraction, but CF_3^+ still has a fairly high density because ionization of CF_4 is dissociative and produces CF_3^+, and carbon fluorides have high charge exchange reaction rates with other ions such as Ar^+ and O^+. The low O_2 input limits the densities of oxygen species. Note that O_2^+ has a steady-state density of 4.0×10^9 cm^{-3}, an order of magnitude lower than Ar^+. The dominant neutrals are O, F, and F_2, as shown in Fig. 6.2b. O is mostly produced through the dissociative attachment reaction of O_2, and F is from the electron-impact dissociation reaction of CF_4.

In the base case, the peak plasma density reaches 1.1×10^{11} cm^{-3} at $r = 13.0$ cm, as shown in Fig. 6.3a. The electron density (n_e) peaks at the periphery instead of the center of the reactor, partly due to the electrostatic electric field (E-field) enhancement at the corners of the top electrode and the wafer. At 0.5 cm beneath the edge of the top electrode, the current density in both radial (J_r) and axial (J_z) are 10^{-3} A/cm^2, while at the same axial position but $r = 7.5$ cm, both J_r and J_z are an order of magnitude lower, at 10^{-4} A/cm^2, suggesting a possibly higher power deposition at the edge than the mid-radius of the electrodes. At 0.5 cm beneath the top electrode, the power density is $P = 0.06$ W/cm^3 at $r = 13$ cm, but only 0.03 W/cm^3 at $r = 7.5$ cm.

In an RIE process, energetic ions are essential for the chemical sputtering and surface activation. A -370 V DC bias is generated on the substrate, producing a time averaged 490 V potential drop across the sheath above the wafer as opposed to a smaller 125 V potential drop by

the top electrode. At 25 mTorr, the mean free path (λ) of Ar is about 0.2 cm, which is commensurate with the sheath width (0.6 cm). This means some ions can travel across the sheath with very few or no collisions. Such ions preserve most of their kinetic energy (100s eV) before impacting on the wafer.

Electron temperature (T_e) is uniform in the plasma bulk, as shown in Fig. 6.3b. The stochastic heating causes high T_e at the edge of sheaths with a value up to 3-4 eV. This high T_e drops rapidly towards the plasma bulk as hot electrons dissipate their energy through inelastic collisions with heavy particles (e.g., ionization and excitation). At the periphery of the plasma bulk ($r > 18$ cm), T_e is slightly higher due to the low n_e. However, because this high-temperature region is in the downstream of the gas flow, it does not significantly affect the bulk plasma and therefore is not discussed in detail.

In a CCP, hot electrons with energy high enough to ionize a ground or excited state species can be either bulk, or beam electrons. Bulk electrons are those in the plasma bulk that gain energy mainly through stochastic or ohmic heating. Beam electrons are emitted from a surface as the product of energetic particle bombardments on that surface. Beam electrons accelerated by the sheath can have energy up to the maximum sheath potential, making them affective at ionizing the neutral particles. The secondary electron emission coefficient (γ) by ions is 0.15 on the wafer, the showerhead, and the sacrificial material, 0.05 on the quartz, and 0.005 for the dielectric coating on the wall [27]. The ionization sources produced by the bulk and beam electrons are shown in Fig. 6.3c and d. The ionization is dominated by bulk ionization. Because bulk electrons are heated through sheath oscillation, the ionization source produced by bulk electrons (S_e) is dependent on the plasma distribution and peaks at 1.1×10^{16} cm^{-3}s^{-1} at $r = 14$ cm where the plasma density is high. In comparison, the ionization source for

beam electrons (S_{eb}) is uniform in both radial and axial directions. The high energy of beam electrons allows them to travel across the reactor and initiate ionizations in the mid-gap.

The increase of ion flux in the radial direction (47% from the center to the boundary) is caused by the rise of plasma density but is not high enough to compensate for the decrease of the secondary electron emission coefficient from 0.15 (electrodes and wafer) to 0.05 (quartz), a reduction to 1/3. The rate of secondary electron emission is determined by the ion flux and the secondary electron emission coefficients. S_{eb} decreases abruptly at the boundaries of the top electrode and wafer due to the reduction in rate of emission and the reduction in sheath voltage on the focus ring. Note that the ionization sources have small values outside the plasma bulk, suggesting the power is well confined between the electrodes.

The 2-dimensional (2D) Ar^+ distribution is shown in Fig. 6.3e. Similar to n_e, a peak Ar^+ density of 1.1×10^{11} cm^{-3} occurs below the edge of the top electrode where the bulk ionization is at its maximum. The E-field in the sheaths accelerates cations toward the surfaces, causing a low Ar^+ density near surfaces. Because the E-field in the sheaths points from the plasma to the wall, it repels anions instead of attracting them. Due to the low anion temperature (< 0.2 eV), it is nearly impossible for negative ions to climb the 100s V potential barrier of the sheath. Therefore, the anions are well confined in a thin layer between the electrodes. For example, as shown in Fig. 6.3f, F^- is trapped in a 1.5 cm thick slot in the mid-gap with a peak density of 9.0×10^{10} cm^{-3} at $r = 14$ cm where n_e is high. Unlike electrons, F^- is uniformly distributed across the reactor in the radial direction. In the base case, the F^- density is high enough to be commensurate with n_e, and the ratio $n(F^-)/n_e > 1$ in the center of the reactor, suggesting an ion-ion plasma composition. Unlike ions and electrons, the distribution of the neutral species is not directly affected by the E-field. For example, O is evenly distributed between the electrodes even within

179

the sheath (Fig. 6.3g). However, because any O^+ bombarding on a surface is likely returned to the plasma as O, and because the O^+ flux is higher on the wafer than on the top electrode, O density is higher in the bottom half of the gap than in the top half.

Due to their high densities, Ar^+ and CF_3^+ have the highest fluxes (Γ) among cations. At mid-radius of the wafer ($r = 7.5$ cm), $\Gamma_{Ar^+} = 4 \times 10^{15}$ cm^{-2}s^{-1} and $\Gamma_{CF_3^+} = 1.9 \times 10^{15}$ cm^{-2}s^{-1}. The IEADs of these two species are shown in Fig. 6.4a and b, plotted in a logarithmic scale with two orders of magnitude. The normalized IEDs are shown in Fig. 6.4c. Both Ar^+ and CF_3^+ have a narrow angular distribution of less than 5 degrees. Most ions hitting the wafer have energy between 300 to 750 eV. Ions with low energy (< 400 eV) either have had collisions as they cross the sheath, or are produced near or within the sheath through charge exchange reactions. On the other hand, energetic ions residing on the high-energy end of IEDs (> 600 eV) have encountered no or only a few collisions as they travel across the sheath. Both the IEADs of Ar^+ and CF_3^+ have a maximum at $\varepsilon = 400$ eV, agreeing well with the DC bias $V_{dc} \approx$ -400 V. At 25 mTorr, the transit time of ions across the sheath $\tau_{ion} \approx 0.3$ µs, close to the RF cycle of 5 MHz power, τ_{5MHz} = 0.2 µs. Therefore, if ions enter the sheath when the 5 MHz voltage is negative, they can be accelerated by both the DC bias and this negative voltage and reach energy higher than 400 eV, which produces the maximum extent of the CF_3^+ IED at 650 eV.

The electron energy distribution function (EEDF) is one of the most fundamental plasma properties. The EEDFs from positions depicted in Fig. 6.5b are shown in Fig. 6.5a. The radial position $r = 13.5$ cm was chosen because the peak n_e is at that radius. The EEDFs have noticeable high-energy tails (> 20 eV) near the sheaths ($z = 3.6$ and 6.0 cm) due to stochastic heating. This high-energy tail is suppressed in the center of the bulk plasma ($z = 4.8$ cm), where electrons are inefficiently heated by a small E-field (≈ 0.5 V/cm) from ohmic heating. In

addition to this low heating efficiency, in the plasma bulk, electrons can quickly lose their energy through inelastic collisions, preventing them from gaining enough energy to populate the high-energy tail of the EEDF. One counter-intuitive result is that even though the total power from the substrate is higher than the power from the top electrode, the fraction of high-energy electrons is higher near the top electrode. The upper position is 0.1 cm from the top electrode and the lower position is 0.3 cm above the substrate to accommodate the thinner sheath thickness by the top electrode. However, either moving the upper point 0.2 cm away from the top electrode or moving lower point 0.2 cm towards the substrate, does not appreciably change the EEDFs. This difference in EEDFs occurs because the radio frequencies 10s MHz are much smaller than the electron plasma frequency ω_{pe} (about 20 GHz). Therefore, electrons are capable of responding to the dynamics of the sheath and being heated each time the sheath expands. To that end, a high frequency translates to a higher sheath speed and therefore a higher stochastic heating efficiency. That is why EEDF has a higher high-energy tail near the top electrode, where the power has the higher frequency (80 MHz).

The EEDFs from different radial positions are shown in Fig. 6.6. Note that the height $z =$ 4.8 cm is chosen because the peak plasma density occurs there. The difference of the EEDFs from the center and the left point is small and appears Maxwellian. However, at $r = 18$ cm in the periphery of the bulk plasma, the EEDF appears to have a concave structure (Druyvesteyn distribution). Note that to have a Maxwellian distribution, elastic collisions such as electron-electron (e-e) collision should be the dominant collision [5]. Comparing with the center point (n_e $= 1.1 \times 10^{11}$ cm^{-3}), both left ($n_e = 7.5 \times 10^{10}$ cm^{-3}) and right ($n_e = 7.0 \times 10^{10}$ cm^{-3}) points have lower n_e, meaning that e-e collisions are not as dominant. However, the stochastic heating and secondary electron emission from the powered electrode and substrate provide high-energy

electrons at $r = 5$ cm (left point). Therefore, the high rate of heating raises the tail of the EEDF.

6.3.1 Power

Input power is one of the most commonly used variables for controlling the plasma. The 80 MHz power (P_{HF}) was varied from 50 to 1000 W, while the power from the substrate is held constant at 800 W with 400 W at each frequency. The voltage at each frequency, averaged plasma potential, and DC bias with varying P_{HF} are shown in Table I. The corresponding electron distribution and the ionization source by bulk electrons (S_e) are shown in Fig. 6.7. Both n_e and S_e increase with P_{HF}. As P_{HF} increases, S_e has a 5-fold increase in the center of the reactor, leading to a high n_e that balances the local maxima at the edge of the electrode. When $P_{HF} = 50$ W, n_e in the center of the reactor ($r = 1$ cm) is only 13% of the peak n_e. This ratio increases to 72% as P_{HF} increases to 1000 W, suggesting a much more uniform plasma distribution with high P_{HF}. Note that the location having the peak n_e moves inwards, with an increase of P_{HF}, implying the effect of electrostatic E-field enhancement at the edge of electrodes is weakened with an increasing P_{HF}. Because of the sheath thickness $s \propto n_e^{-1/2}$, a non-uniform plasma distribution when P_{HF} is low leads to a bending of the sheath edge. This may consequently cause tilting of IADs when the boundary of the sheath is not parallel to the surface of the wafer.

The EEDFs were recorded at upper and center points shown in Fig. 6.5b with varying P_{HF}. The EEDFs from the center point are almost identical when P_{HF} increases from 500 W to 1000 W. However, as P_{HF} decreases from 500 to 50 W, the EEDF perceptibly evolves from a Maxwellian distribution to a Druyvesteyn distribution with a concave structure. This is partly because when $P_{HF} = 50$ W, the recording point ($r = 13.5$ cm, $z = 4.8$ cm) is no longer within the high-density plasma center. When P_{HF} decreases from 500 to 50 W, n_e at the center point is

reduced by 66% from 1.1×10^{11} cm^{-3} to 3.7×10^{10} cm^{-3}. The lower n_e translates to low e-e elastic collision frequency, which produces a deviation of the EEDF from a Maxwellian distribution. At the upper point, near the sheath of the top electrode, the high-energy tail ($\varepsilon > 20$ eV) of EEDFs falls with lower P_{HF} due to its decreasing power density. The high-energy tail decreases when moving further away from the top electrode. As P_{HF} decreases from 1000 to 50 W, the power density decreases from 1.2 to 0.3 W/cm^3 at the upper point. The low power density causes less electron heating and thus smaller high-energy tails of EEDFs.

The 2D IEADs and the normalized IEDs of the dominant ions Ar$^+$ and CF$_3$$^+$ are shown in Fig. 6.9. For both species, the ion energy tends to decrease as the P_{HF} increases. As P_{HF} increases from 50 to 1000 W, the DC bias drops from -660 to -121 V, and the plasma potential increases from 138 to 167 V, providing a net decrease of 510 V potential drop across the sheath. The decreased sheath potential with an increasing P_{HF} results in lower ion bombardment energy. When P_{HF} is 1000 W, the peak Ar$^+$ energy is about 600 eV lower than that when P_{HF} is 50 W. The low plasma density also thickens the sheath. At the mid-radius ($r = 7.5$ cm) of the wafer, the sheath thickness $s = 0.9$ cm when $P_{HF} = 50$ W, but only 0.2 cm when $P_{HF} = 1000$ W. With the same pressure, the thicker the sheath, the more collisional the sheath becomes. A collisional sheath deviates ion trajectories and broadens the IAD. Therefore, the IAD is much broader when $P_{HF} = 50$ W. The breadth of the IAD decreases from 10° to 5° as the P_{HF} increases from 50 to 1000 W. If P_{HF} is between 500 and 1000 W, the IAD barely changes because the sheath thickness only moderately decreases with the increase of power.

6.3.2 Pressure

Chamber pressure affects collision frequency and the mean free path of both ions (λ_{ion}) and electrons (λ_e) and is another parameter that determines the plasma distribution and density. The pressure was varied between 15 and 50 mTorr. The corresponding electron distribution, and

the ionization source by bulk electrons (S_e), are shown in Fig. 6.10. The voltage at each frequency, averaged plasma potential, and DC bias with varying pressure are shown in Table I. Increasing the pressure from 15 to 50 mTorr, the peak n_e is decreased by 14%. As pressure increases from 15 to 50 mTorr, λ_e decreases from 1.7 cm to 0.7 cm at the edge of the sheath, meaning at 50 mTorr, the number of hot electrons reaching the mid-gap ($z = 4.8$ cm) is sharply decreased. This reduces the ionization and hence produces a low n_e. Note that when the pressure is 50 mTorr, S_e is confined to a thin layer near the top electrode, and its magnitude is halved compared with the S_e at the same position when the pressure is 15 mTorr. The decrease of S_e in the bulk plasma increases the relative importance of ionization by beam electrons (S_{eb}). When the pressure is 50 mTorr, at mid-gap ($r = 7.5$ cm and $z = 4.8$ cm), $S_{eb} = 1.7 \times 10^{15}$ cm^{-3}s^{-1}, surpassing $S_e = 1.3 \times 10^{15}$ cm^{-3}s^{-1}. S_{eb} becomes more important in high pressure because beam electrons with an energy of 100s eV having longer mean free path, allowing them to travel into and ionize the plasma bulk.

The EEDFs at the center point ($r = 13.5$ cm, $z = 4.8$ cm) with varying pressure are shown in Fig. 6.11a. As the pressure increases from 15 to 50 mTorr, the high-energy tail is suppressed as the result of the shortening of λ_e. A steeper slope of EEDF with increasing pressure translates to the lower T_e. As shown in Fig. 6.11b, the reactor averaged T_e drops from 3.1 to 2.7 eV as the pressure increases from 15 to 50 mTorr, while n_e decreases from 4.3 to 2.6 $\times 10^{14}$ cm^{-3}. Note that the gas mixture used in this work contains attaching gases such as F_2 and O_2, thereby increasing the pressure significantly enhances the attachment reactions, causing the decrease of n_e.

The IEADs and normalized IEDs of Ar$^+$ and CF$_3^+$ at pressures of 15, 30, and 50 mTorr are shown in Fig. 6.12. Increasing the pressure broadens the IADs because the sheath becomes

184

thicker and more collisional. As the pressure increases from 15 to 50 mTorr, the IAD is extended from 8° to 16°. The maximum ion energy increases with the increase in pressure. For example, as the pressure increases from 30 to 50 mTorr, the peak Ar^+ energy is increased from 780 to 850 eV. This increase of ion energy with pressure is caused by the increase of both plasma potential and the magnitude of DC bias on the substrate. As the pressure increases from 15 to 50 mTorr, the DC bias increases from -382 V to -450 V, and the plasma potential from 108 to 150 V. This high plasma potential and more negative DC bias creates high maximum ion energy when the pressure is 50 mTorr. However, at high pressure, the sheath is more collisional. Therefore, even though the maximum ion energy is almost 900 eV, the majority of ions still come with energy $\approx$ 400 eV. At 50 mTorr, the fraction of ions with energy less than 300 eV is more than that when the pressure is 15 mTorr, as shown in Fig. 6.12c, and d. Therefore, the average ion bombardment energy can be similar for cases with different pressures even though the maximum ion energy is significantly different.

6.3.3 Frequency

The driving frequency of the power source is considered to be one of the most important parameters in an rf-power driven CCP. The frequency from the top electrode was varied from 20 to 120 MHz, while the power from the substrate remains the same as in the base case (5 MHz 400 W and 10 MHz 400 W). The voltages at each frequency, averaged plasma potential and DC bias with varying HF are shown in Table I. The electron distribution and the ionization source by bulk electrons (S_e) are shown in Fig. 6.13. With the same input power, the peak value of the S_e and n_e barely changes with the HF. However, as the HF increases from 20 to 120 MHz, the spatial distribution of both n_e and S_e becomes more uniform. As discussed before, electrons can respond to the change of rf, and higher frequency has higher stochastic heating efficiency.

Therefore, as the HF increases, more hot electrons are created at the sheath edge, leading to a high ionization rate and high n_e in plasma bulk. Note that even though the power is fixed, the power dissipated to ions and electrons can vary under different operating conditions. In this work, the power delivered to electrons increases from 125, 328 to 355 W, as the HF increases from 20, 60, and 120 MHz, showing that increasing the driving frequency amplifies electron heating efficiency. However, the effect of the changing HF is not as significant when it rises from 60 to 120 MHz comparing to when it increases from 20 to 60 MHz, suggesting a saturation frequency above which n_e will not have significant change with the increase of frequency.

The EEDFs at the center point ($r = 13.5$ cm, $z = 4.8$ cm) are recorded as the HF increases from 20 to 120 MHz, as shown in Fig. 6.14. Similar to the effect of HF on n_e, increasing HF from 60 to 120 MHz only has a minor impact on EEDF. The low sensitivity of EEDF to a changing HF is because when the HF is higher than 60 MHz, the plasma properties are governed by the magnitude of power input instead of the heating efficiency. Even though the heating efficiency still increases, the impact is simply not significant enough to cause any substantial change to the plasma. Therefore, the similar n_e and the e-e elastic collision frequencies occur, resulting in nearly identical EEDF. On the other hand, if the HF decreases from 60 MHz, both n_e and the EEDF are affected by the decreasing stochastic heating efficiency, which causes a decrease of the hot electron density, hence low S_e and n_e. The power transferred to electrons when the HF is 20 MHz is only approximately 1/3 compared with that when the HF is 120 MHz. A low n_e translates to a low e-e collision frequency. Therefore, when the HF is 20 MHz, the EEDF in the bulk plasma has a concave structure, characterized by suppression on both the high and low energy ends.

The IEADs of Ar^+ and CF_3^+ on the wafer when the HF is 20, 60, and 120 MHz are shown

in Fig. 6.15. Ions gain their highest energy when the HF is 60 MHz. As the HF decreases from 60 to 20 MHz, the DC bias becomes less negative, from -320 V to -145 V. Meanwhile, the plasma potential increases from 151 to 316 V. With both DC bias and plasma potential considered, the sheath potential by the wafer is 10 V higher when the HF is 60 MHz, which provides slightly higher ion energy. However, the ion energy is not monotonically increased with the increase of the HF. As the HF increases from 60 to 120 MHz, the plasma potential decreases from 151 to 117 V, and the DC bias from -320 to -305 V. The net decrease of 49 V of sheath potential as HF increases from 60 to 120 MHz results in a decline of the maximum ion energy. Increasing HF still produces an increase of stochastic heating efficiency, thus high n_e, especially in the center of the reactor ($r < 5$ cm). With similar DC bias and higher power deposition into electrons, the plasma potential then decreases to reduce the power dissipated to ions, and maintain the constant power delivery to the plasma.

6.3.4 Gap Length

The effect of gap length between the top electrode and the substrate on the plasma was also investigated. The voltage at each frequency, averaged plasma potential, and DC bias when the gap length is varied are shown in Table I. The distributions of n_e and the ionization source by bulk electrons (S_e) when the gap length $d = 2.3$, 3.3, and 4.3 cm are shown in Fig. 6.16. The peak n_e barely changes with d because the power input is constant (1300 W). The plasma is more uniformly distributed with an increasing d, due to the weakened electrostatic effect at the edge of the electrodes and the decreased loss of charged particles with decreasing surface to volume ratio. When $d = 2.3$ cm, from 0.3 cm above the wafer, power density increases from 1.1 W/cm^3 at $r = 1$ cm to 2.3 W/cm^3 at $r = 14$ cm. This uneven power deposition leads to a non-uniform plasma distribution. When $d = 4.3$ cm, a wider gap minimizes the coupling between the top electrode and the substrate and weakens that electrostatic effect. When $d = 4.3$ cm, at 0.3 cm

187

above the wafer, power density is 1.9 W/cm^3 at $r = 1$ cm, and 2.0 W/cm^3 at $r = 14$ cm, with only a minor increase of 0.1 W/cm^3. A uniform power deposition leads to uniform S_e and n_e distributions. When $d = 4.3$ cm, n_e from mid-gap is almost constant across the reactor, which is desired for most applications. Increasing d also reduces the surface to the volume ratio of the reactor. In a low temperature plasma, the diffusion loss to the wall is one of the major sinks for the charged species. Reducing the surface to volume ratio effectively reduces the wall loss; therefore, despite the decreasing magnitude of S_e with the increasing d, n_e still increases.

The EEDFs with varying d was recorded at $r = 13.5$ cm at mid-gap for each case, shown in Fig. 6.17. The high-energy component is suppressed as d increases. Because the data is gathered at the mid-gap, increasing d increase the distance between the recording point and the sheath. Therefore, hot electrons created at the sheath edge are more likely to be cooled by collisions before reaching the position where EEDF is recorded. Also, power is more evenly distributed in the reactor when d is large. Therefore, the power density at $r = 13.5$ cm is lower with larger d as more power is delivered to the plasma in the center of the reactor ($r < 5$ cm). Consequently, fewer hot electrons are produced near the edge of electrodes, which also contributes to the suppression of the high-energy tail of EEDF at mid-gap when d increases.

The IEADs of the Ar$^+$ and the CF$_3^+$ as d increases from 2.3 to 4.3 cm are shown in Fig. 6.18. The ion energy increases with an increasing d as a result of a more negative DC bias. As d increases from 2.3, 3.3 to 4.3 cm, the DC bias changes from -300 V, -395 to -411 V, while the plasma potential increases from 126, 132, to 138 V. Note that the DC bias is a function of multiple parameters including areas of the grounded and powered surfaces, n_e at the edge of sheaths adjoining these surfaces and the RF voltage from the power source. Usually, in an SF-CCP, a well-confined plasma between the electrodes translates to a weak geometrical asymmetry

since the boundary of the bulk plasma is evenly distributed on the powered (bottom electrode) and grounded (top) surfaces, which usually have a similar surface area. However, in this TF-CCP setup, both the top electrode and the substrate are powered, meaning the main reactor itself, where the plasma is generated, is highly electrically asymmetric. Therefore, simply having the plasma confined between the electrodes does not guarantee a zero DC bias. In this particular setup, as d increases, the plasma is more confined between the electrodes, and the DC bias significantly increases. This is partly because as d increases from 2.3 to 3.3 cm, n_e by the grounded surface (above the pump) decreases to notably lower than that in the center of the bulk plasma, which leads to a more negative DC bias. Because the plasma potential has only a mild increase with d, the average ion energy is predominantly determined by the magnitude of DC bias. The IED shifts about 100 eV to higher energy as d increases from 2.3 to 3.3 cm. The IAD becomes slightly narrower with increasing d as the high DC bias generates higher acceleration perpendicular to the wafer surface. However, this decrease of the IAD with a varying d is insignificant since the sheath thickness barely changes.

6.4 Concluding Remarks

In this chapter, a low temperature TF-CCP sustained in $Ar/CF_4/O_2$ is computationally investigated under different operating conditions. The electrostatic electric field enhancement at the edge of the electrodes was found to raise the local plasma density. Changing operating conditions, such as increasing the HF or increasing HF power, can enhance the electron heating at the center of the reactor (< 5 cm), thereby weakening the electrostatic effect and leading to a more uniform plasma distribution. The electron energy distribution function (EEDF) was found to have a Maxwellian structure in the regions with high electron density (n_e) due to the high electron-electron (e-e) collision frequency. However, the EEDF has a concave structure

189

(Druyvesteyn) where n_e and the stochastic heating efficiency are low.

Ideally, in a multi-frequency CCP, the HF power governs the plasma density while the LF power determines the ion energy and angular distributions (IEADs) onto the wafer. However, varying HF power was found to have some effects on the IEADs. Increasing HF power directly increases the power density in the plasma, while increasing HF itself promotes the stochastic heating. Both of these result in an increase of n_e in the center of the reactor and a more uniform plasma distribution. A re-distributed plasma changes the symmetry of the reactor that in turn determines the DC bias. Therefore, varying the HF power (magnitude, frequency) often modifies the DC bias. Also, both the plasma potential and sheath thickness (s) are sensitive to the change of n_e, meaning they are also functions of the HF power. The plasma potential and DC bias together determine the potential drop across the sheath, which establishes the ion energy distribution (IED). The sheath thickness s affects the collisionality of the sheath and the energy width of the IED. For the same pressure, thicker s translates to a more collisional sheath, and a broader ion angular distribution (IAD). Evidently, the IEAD has a non-linear dependence on HF power. In general, low n_e results in high sheath potential and thick sheath, therefore a broad IAD and high ion energy. The dependence of IEADs on HF power was investigated varied from 50 to 1000 W. In practice, when using HF power to adjust plasma behavior, the range of the varying power is often not as big. Therefore, the effect of HF power on the IEADs will be less recognizable.

The effects of pressure and gap length (d) between the electrodes on the plasma were also investigated in this work. Increasing the pressure shortens the mean free path of electrons, thus reducing the ionization in the bulk plasma. Meanwhile, high pressure translates to a highly collisional sheath, which broadens the IAD. Increasing the gap length makes the plasma more

uniform and makes a more negative DC bias. The effect of gap length on IEADs saturates once $d > 3.3$ cm.

In conclusion, in a TF-CCP, the plasma properties can be adjusted by using different HF power, pressure, and reactor geometry. It has been confirmed that some coupling of HF power to the IEADs occurs, and fully independent control of plasma density and IEADs onto the wafer is hard to achieve. However, with only moderate adjustments of the operating conditions, the consequences of HF on IEADs can be minimized. Using a high power with high frequency, low pressure, and long gap length between the electrodes is recommended strategy to achieve uniform plasma distributions. A uniform plasma distribution across the reactor makes the DC bias less sensitive to changes in the HF power, which helps decouple the control of IEADs and the plasma density.

Table I. Voltage of Each Frequency, Plasma Potential and DC bias with Varying Conditions

The following table contains voltage at each frequency, time averaged plasma potential and DC bias with varying conditions. For each case, only one parameter differs from the base case, and that parameter is used to label the corresponding case. In the base case, HF = 80 MHz, P_{HF} = 500 W, pressure is 25 mTorr, gap length between top and bottom electrodes is 2.8 cm.

		Voltage (V_{5MHz})/V_{10MHz}/V_{HF}) /V	Potential /V	DC bias /V
	Base Case	448/357/117	128	-370
Power	50 W	768/488/44	138	-660
	200 W	619/437/77	124	-556
	700 W	362/310/141	142	-252
	1000 W	276/266/176	167	-121
Pressure	15 mTorr	438/336/108	108	-382
	20 mTorr	436/344/113	120	-372
	30 mTorr	468/375/120	136	-384
	40 mTorr	507/401/126	147	-414
	50 mTorr	541/418/129	150	-450
Frequency	20 MHz	440/367/342	316	-145
	40 MHz	491/390/192	203	-301
	60 MHz	444/347/144	151	-320
	100 MHz	431/347/103	119	-352
	120 MHz	396/330/96	117	-305
Gap Length	2.3 cm	396/330/116	126	-300
	3.3 cm	472/375/119	132	-395
	3.8 cm	476/378/121	136	-403
	4.3 cm	485/383/124	138	-411

6.5 Figures
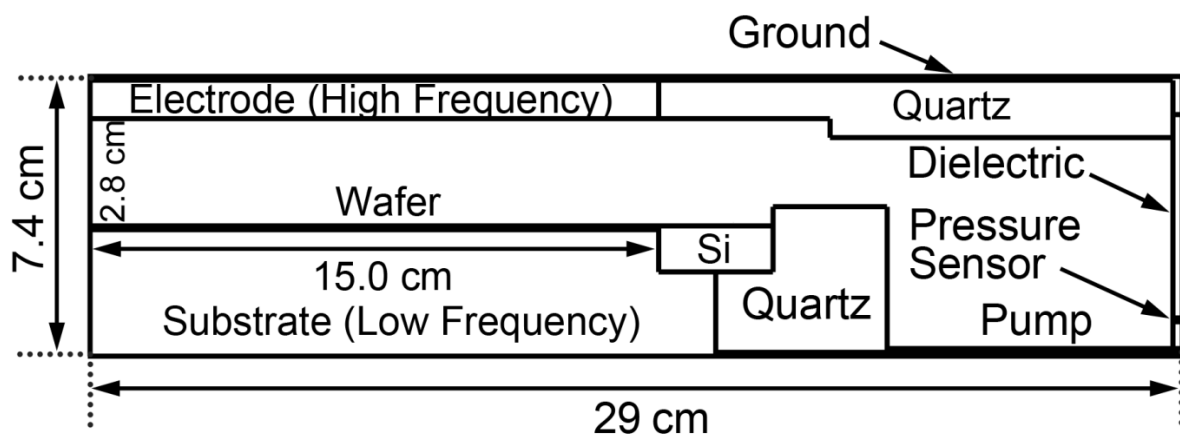
Fig. 6.1 Geometry of the reactor. 80 MHz power (500 W) is applied to the top electrode, 5 and 10 MHz power (400 W each frequency) are applied to the substrate. $Ar/CF_4/O_2$ (75/15/10), 25 mTorr.
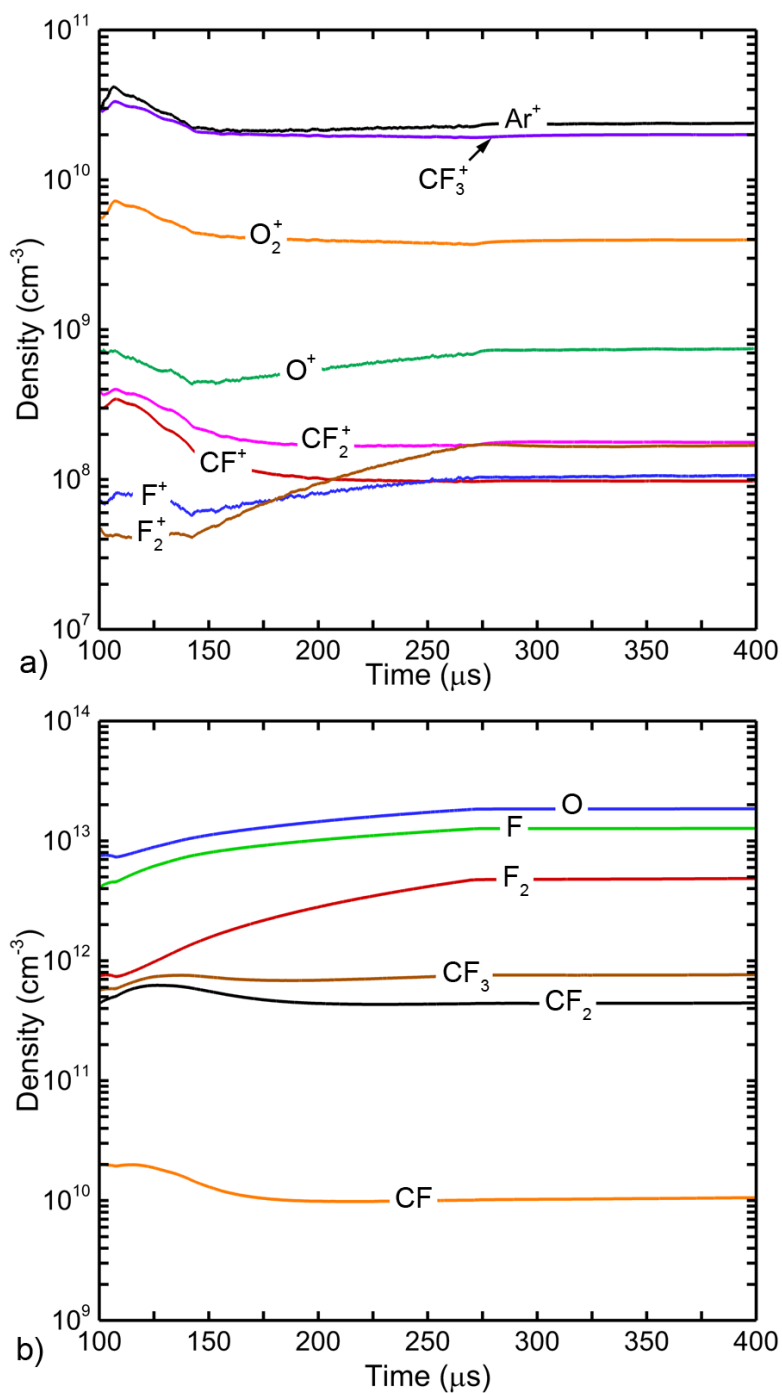
Fig. 6.2 Spatially averaged a) ion and b) neutral species' densities. An acceleration technique was used to help the plasma reach the quasi-steady state faster, causing rapid density changes in the first 250 μs. Ar/CF$_4$/O$_2$ (75/15/10), 25 mTorr, top electrode: 500 W (80 MHz), substrate: 400 W (5 MHz), 400 W (10 MHz).
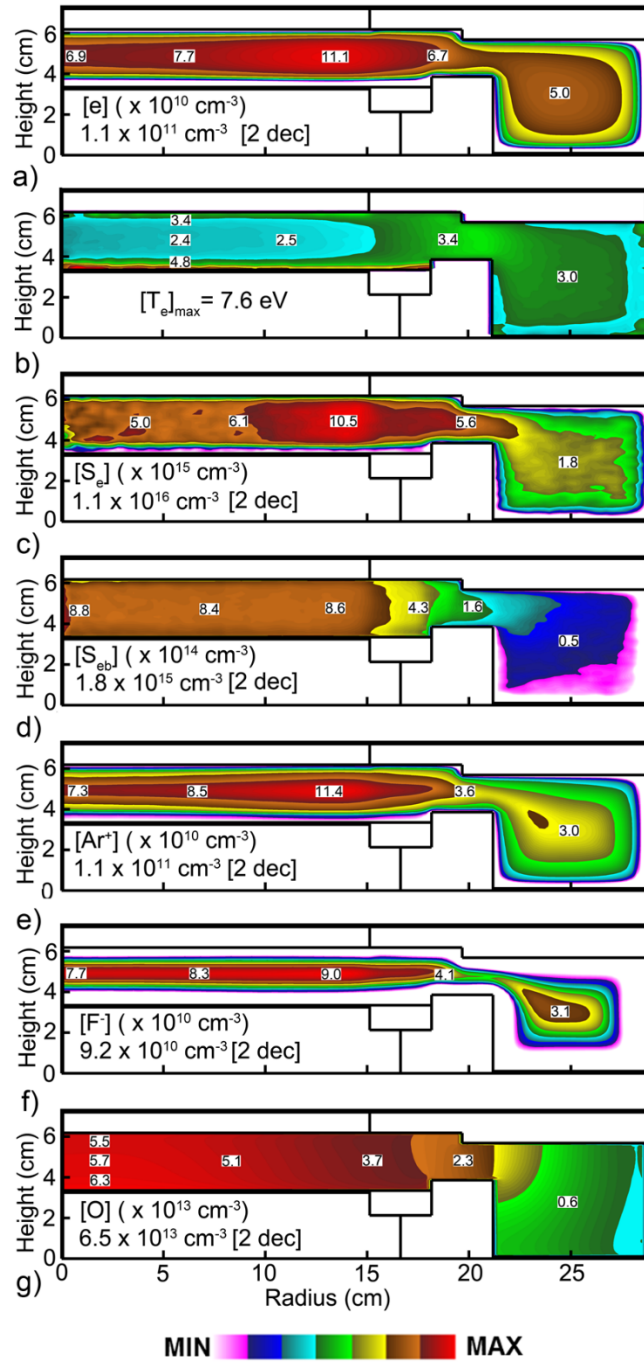
Fig. 6.3 2D profile of a) electron density, b) electron temperature, c) ionization source by bulk electrons, d) ionization source by beam electrons, e) Ar$^+$ density, f) F$^-$ density and g) O density in base case. Ar/CF$_4$/O$_2$ (75/15/10), 25 mTorr, top electrode: 500 W (80 MHz), substrate: 400 W (5 MHz), 400 W (10 MHz).
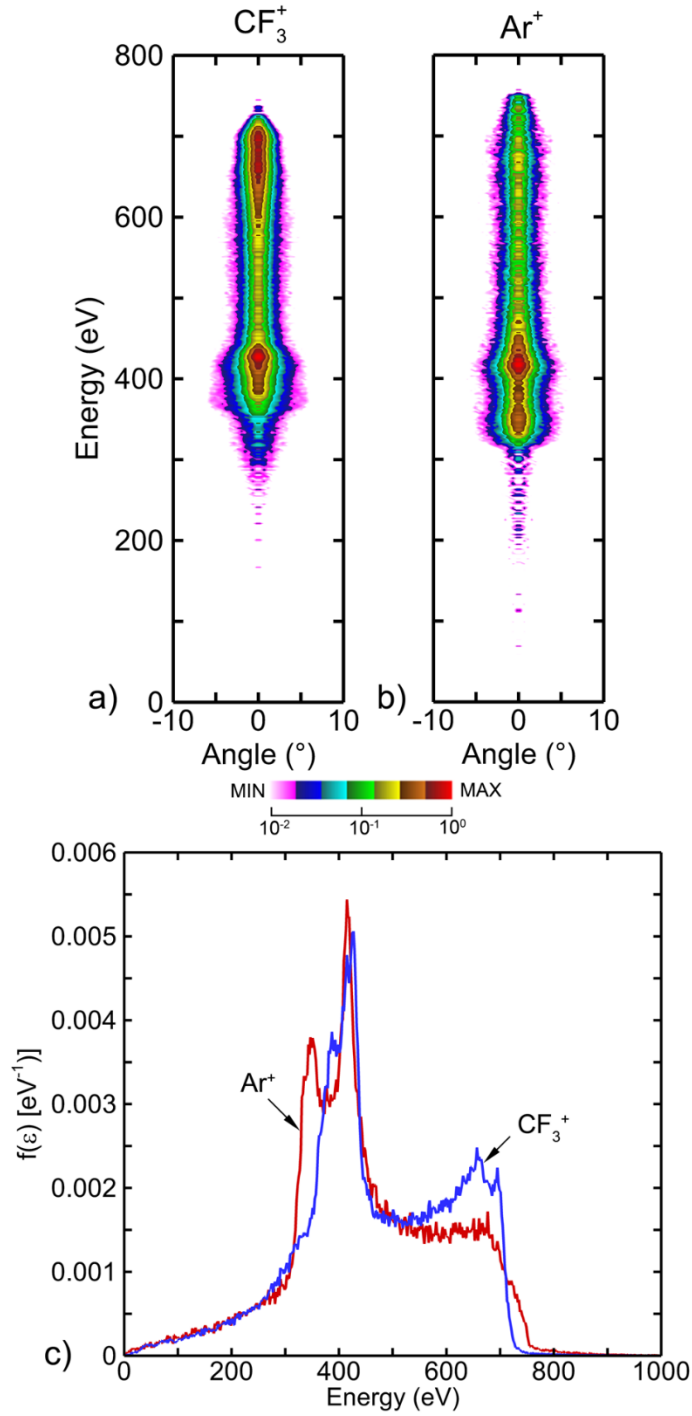
Fig. 6.4 The a) IEADs averaged over 0° and b) normalized IEDs of CF_3^+ and Ar^+ at mid-radius of the wafer (r = 7.5 cm). Ar/CF$_4$/O$_2$ (75/15/10), 25 mTorr, top electrode: 500 W (80 MHz), substrate: 400 W (5 MHz), 400 W (10 MHz).
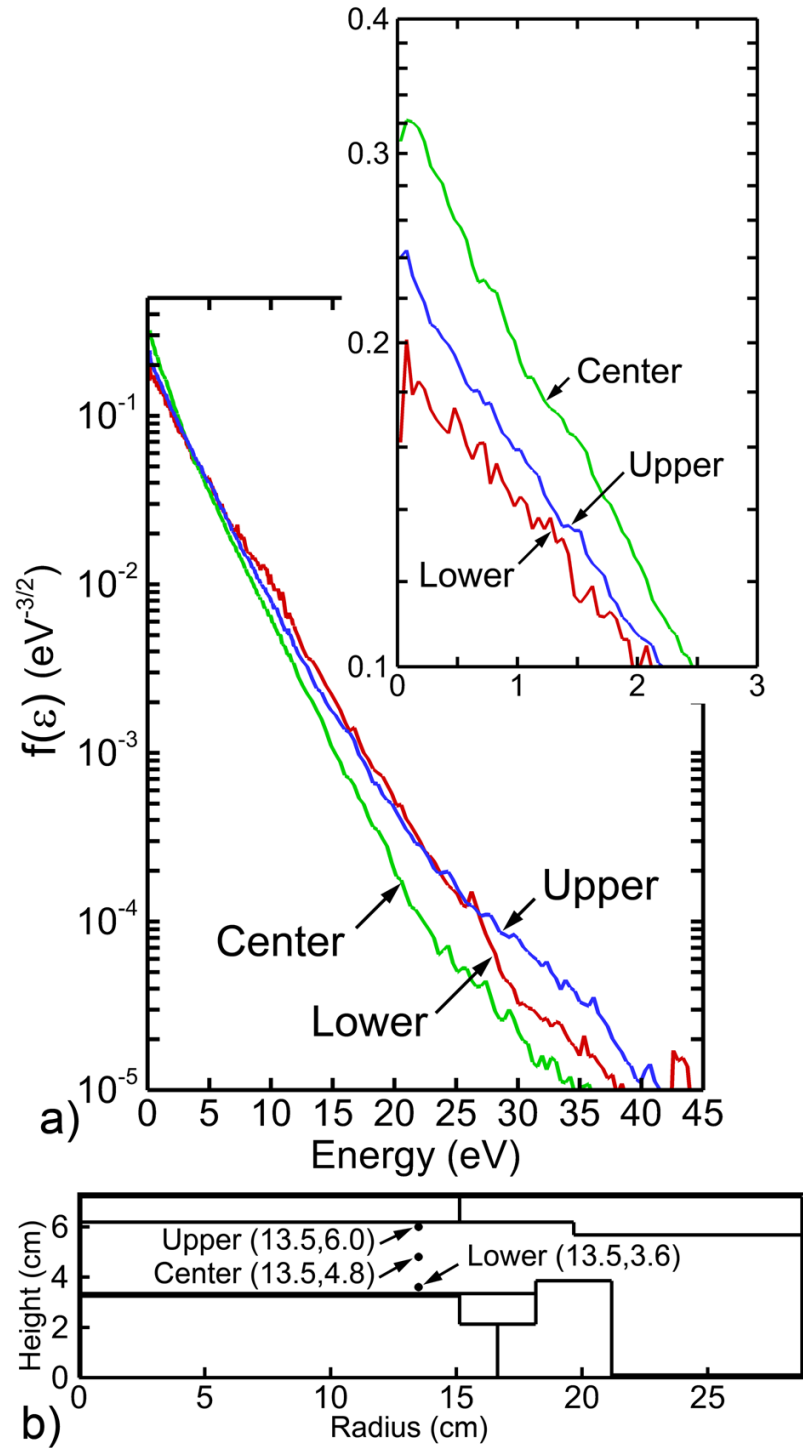
Fig. 6.5 a) EEDFs from different axial locations and b) the locations from where the EEDFs are recorded. Ar/CF$_4$/O$_2$ (75/15/10), 25 mTorr, top electrode: 500 W (80 MHz), substrate: 400 W (5 MHz), 400 W (10 MHz).

197
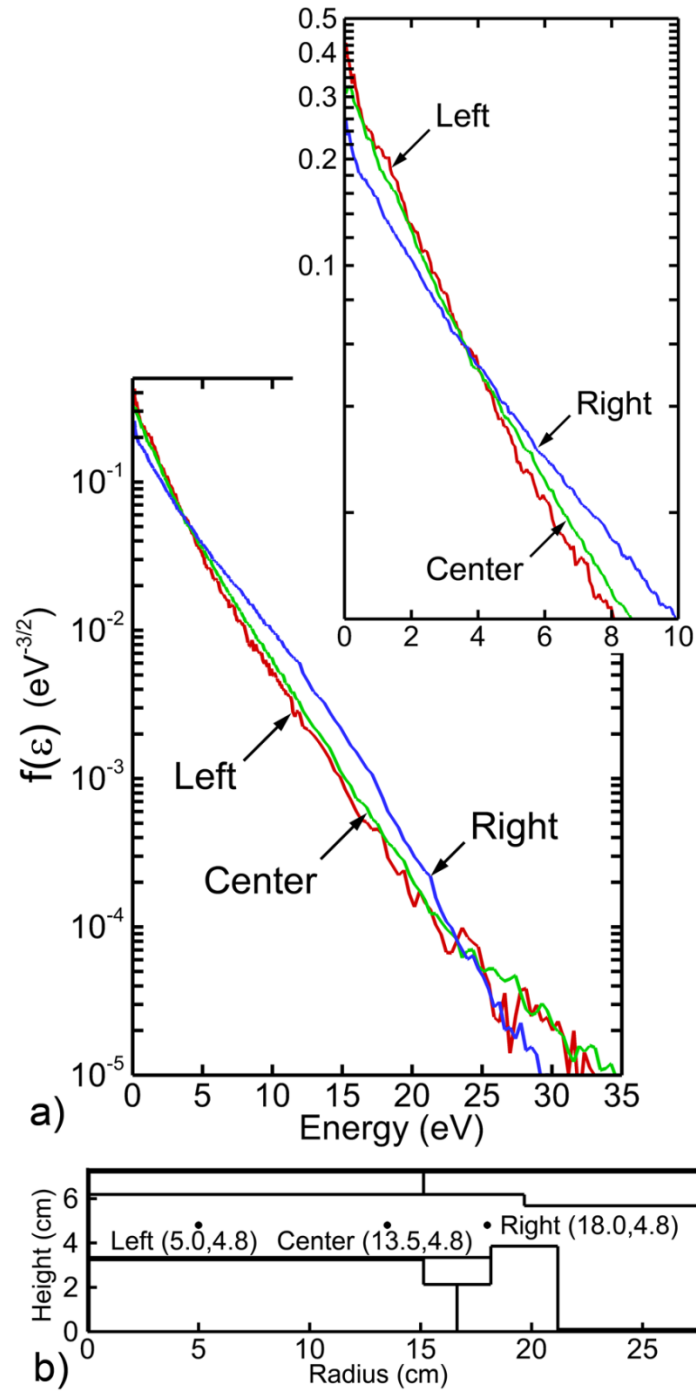
Fig. 6.6 a) EEDFs from different radial locations and b) the locations from where the EEDFs are recorded at $z = 4.8$ cm. Ar/CF$_4$/O$_2$ (75/15/10), 25 mTorr, top electrode: 500 W (80 MHz), substrate: 400 W (5 MHz), 400 W (10 MHz).
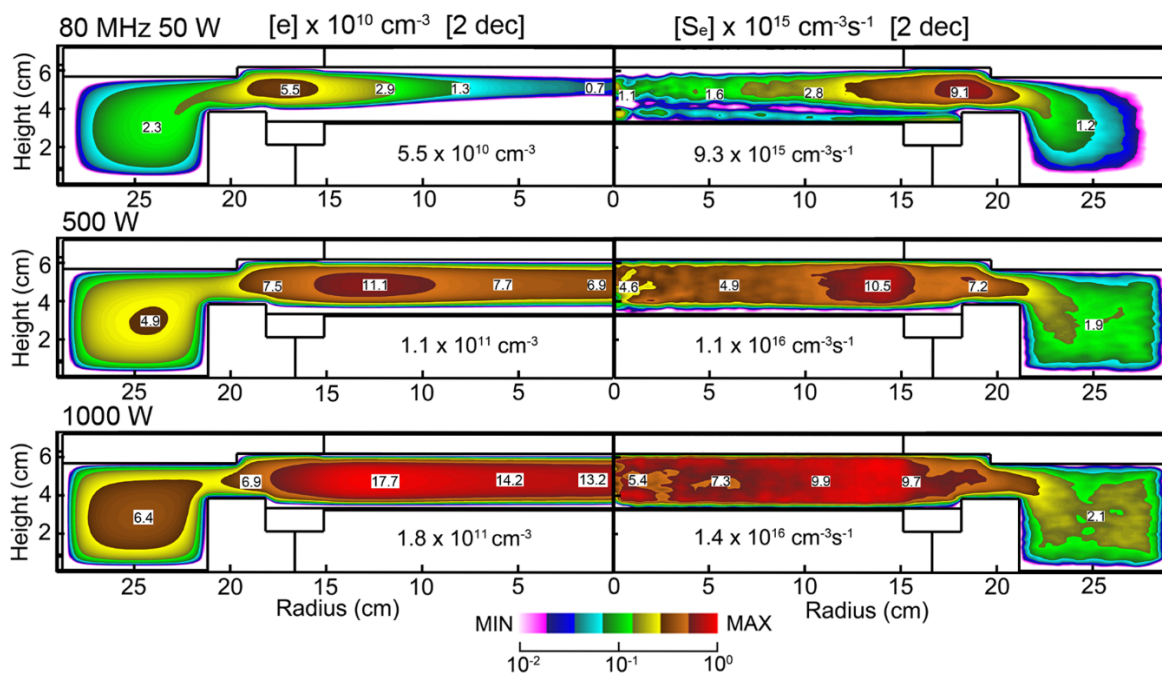
Fig. 6.7 2D profiles of the electron density and ionization source by bulk electrons when the power from 80 MHz power source is 50, 500 and 1000 W. Ar/CF$_4$/O$_2$ (75/15/10), 25 mTorr, top electrode: varied power (80 MHz), substrate: 400 W (5 MHz), 400 W (10 MHz).
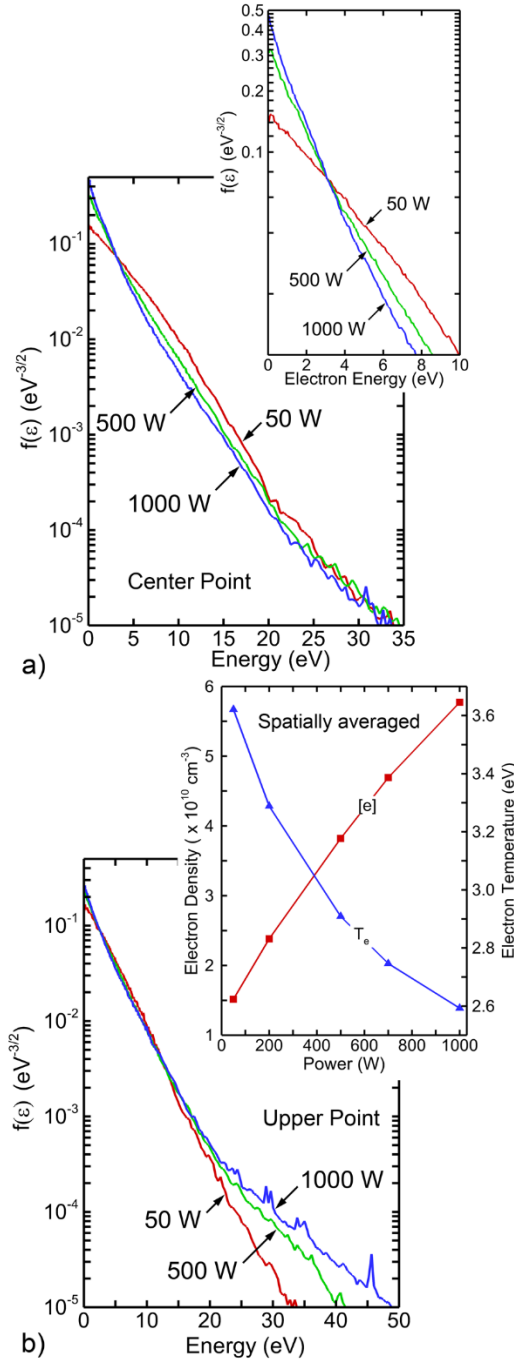
Fig. 6.8 The EEDFs from a) center ($r = 13.5$ cm, $z = 4.8$ cm) and b) upper ($r = 13.5$ cm, $z = 6.0$ cm) point when the power from 80 MHz power source is 50, 500 and 1000 W. Inset of a) is the zoom-in on the low energy component of EEDFs at center point and the inset of b) is the spatially averaged electron density and electron temperature with increasing HF power. Ar/CF$_4$/O$_2$ (75/15/10), 25 mTorr, top electrode: varied power (80 MHz), substrate: 400 W (5 MHz), 400 W (10 MHz).
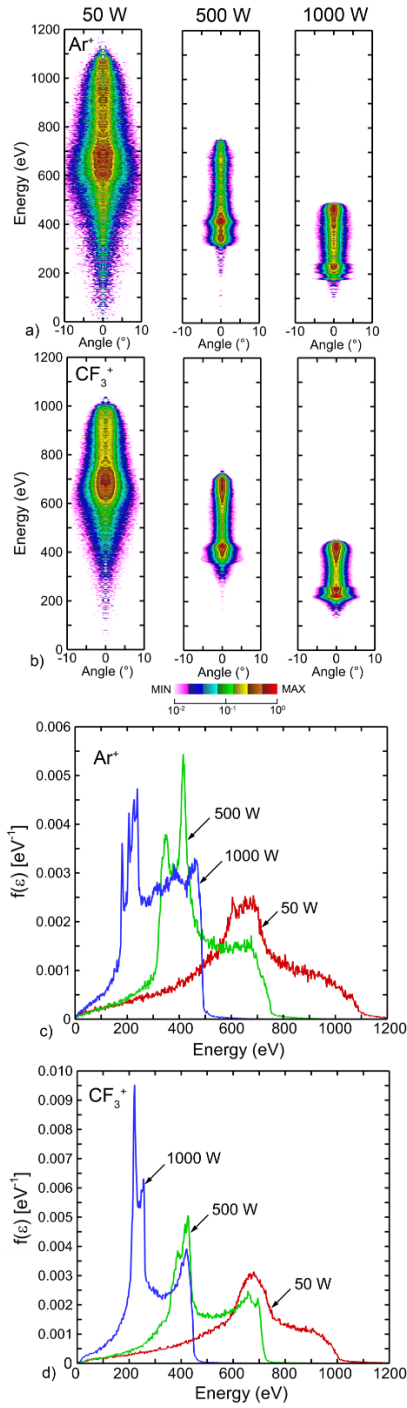
Fig. 6.9 IEADs of a) Ar^+ and b) CF_3^+ and the normalized IEDs of c) Ar^+ and d) CF_3^+ when the power from 80 MHz power source is 50, 500 and 1000 W. $Ar/CF_4/O_2$ (75/15/10), 25 mTorr, top electrode: varied power (80 MHz), substrate: 400 W (5 MHz), 400 W (10 MHz).
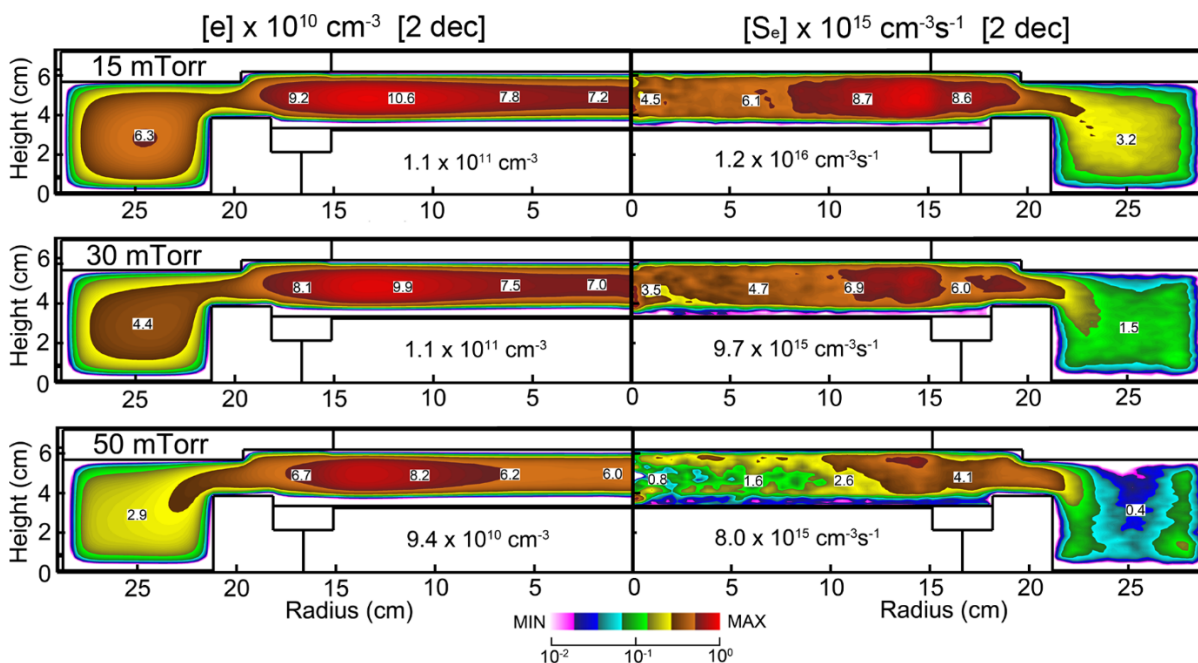
Fig. 6.10 2D profiles of the electron density and ionization source by bulk electrons when the pressure is 15, 30 and 50 mTorr. Ar/CF$_4$/O$_2$ (75/15/10), varied pressure, top electrode: 500 W (80 MHz), substrate: 400 W (5 MHz), 400 W (10 MHz).

202
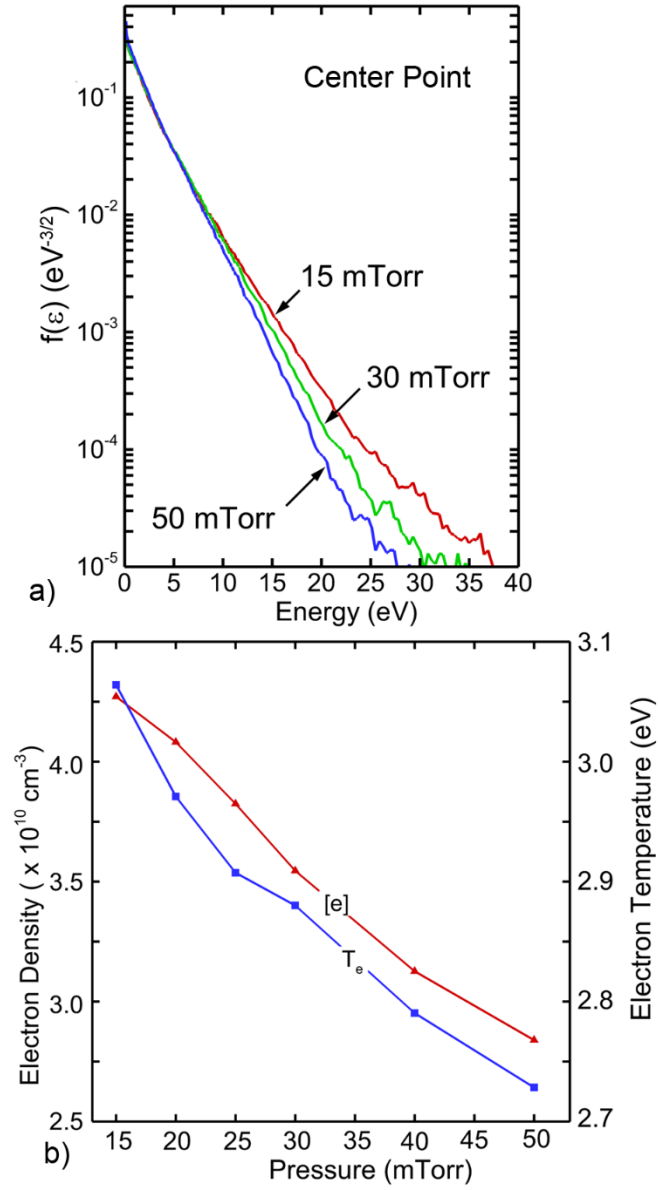
Fig. 6.11 a) EEDFs from the center point (r = 13.5 cm, z = 4.8 cm) when the pressure is 15, 30 and 50 mTorr. And the b) spatially averaged electron density and electron temperature. Ar/CF$_4$/O$_2$ (75/15/10), varied pressure, top electrode: 500 W (80 MHz), substrate: 400 W (5 MHz), 400 W (10 MHz).
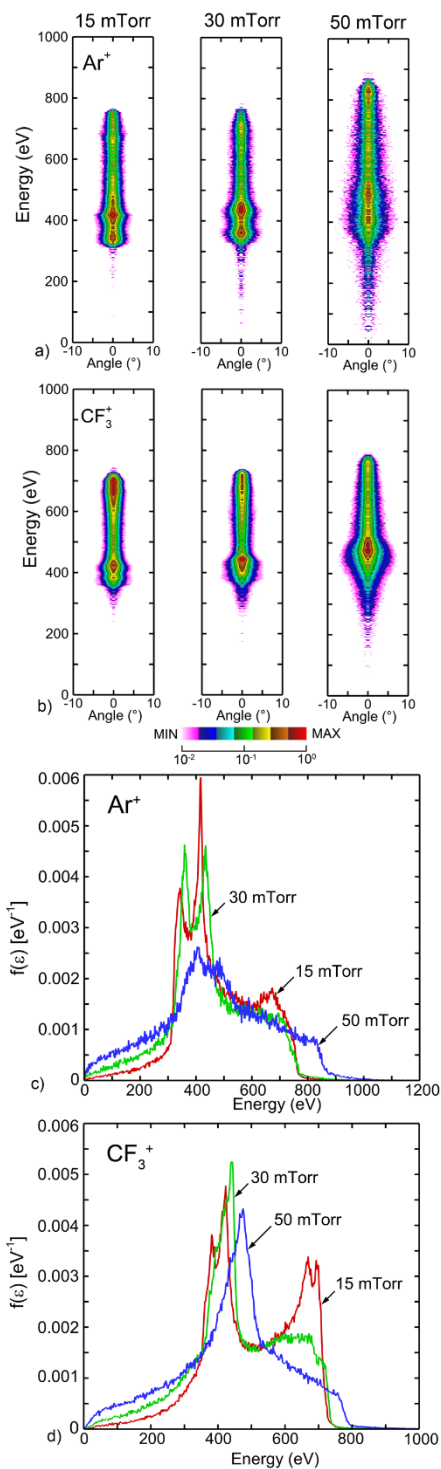
Fig. 6.12 The IEADs of a) Ar^+ and b) CF_3^+ and the normalized IEDs of c) Ar^+ and d) CF_3^+ when the pressure is 15, 30 and 50 mTorr. Ar/CF$_4$/O$_2$ (75/15/10), varied pressure, top electrode: 500 W (80 MHz), substrate: 400 W (5 MHz), 400 W (10 MHz).
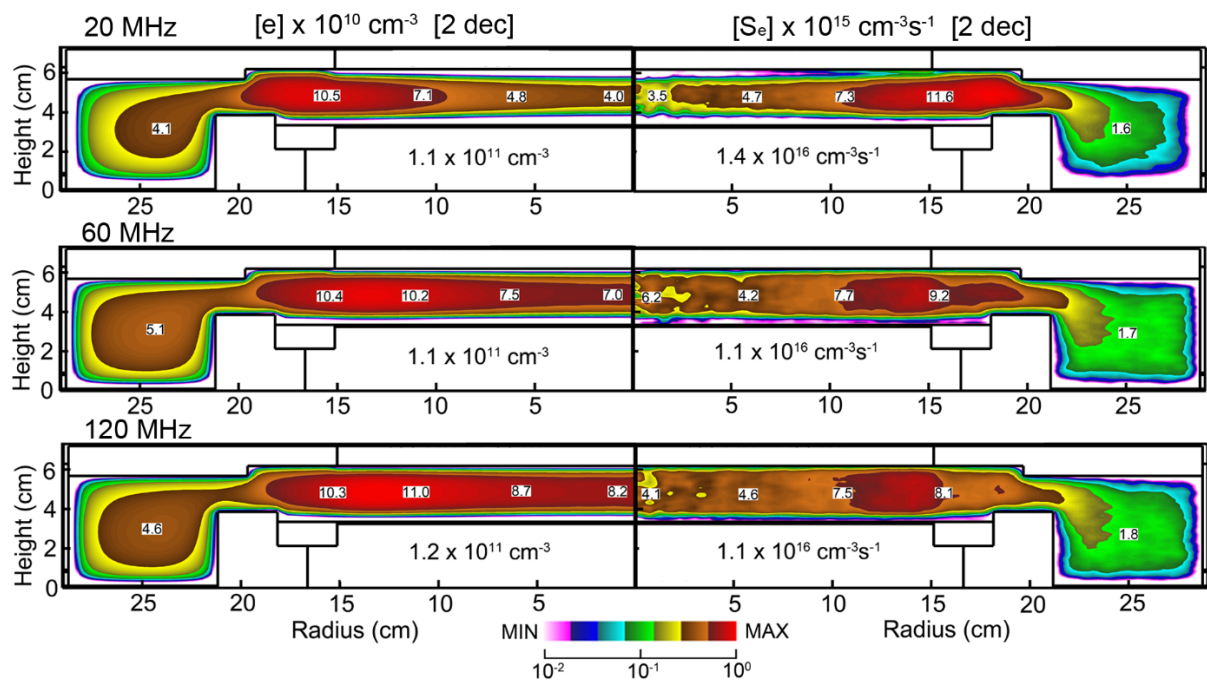
Fig. 6.13 2D profiles of the electron density and ionization source by bulk electrons when the frequency from the HF power source is 20, 60 and 120 MHz. Ar/CF$_4$/O$_2$ (75/15/10), 25 mTorr, top electrode: 500 W (varied frequency), substrate: 400 W (5 MHz), 400 W (10 MHz).
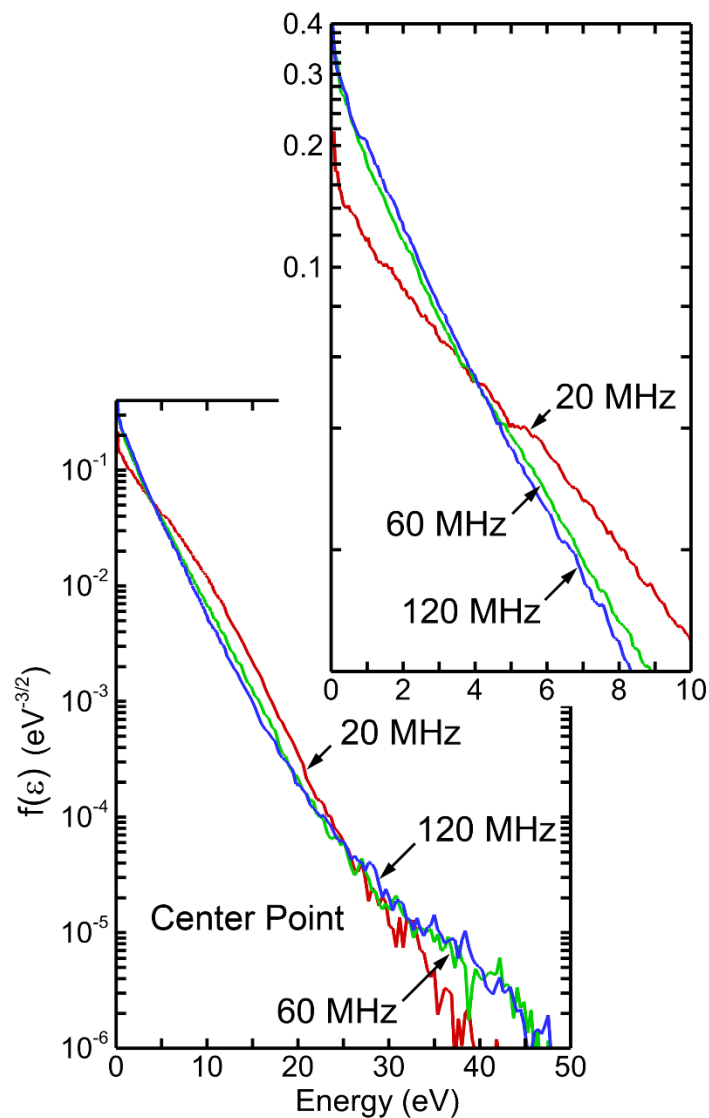
Fig. 6.14 EEDFs at the center point (r = 13.5 cm, z = 4.8 cm) when the frequency from the HF power source is 20, 60 and 120 MHz. Ar/CF$_4$/O$_2$ (75/15/10), 25 mTorr, top electrode: 500 W (varied frequency), substrate: 400 W (5 MHz), 400 W (10 MHz).
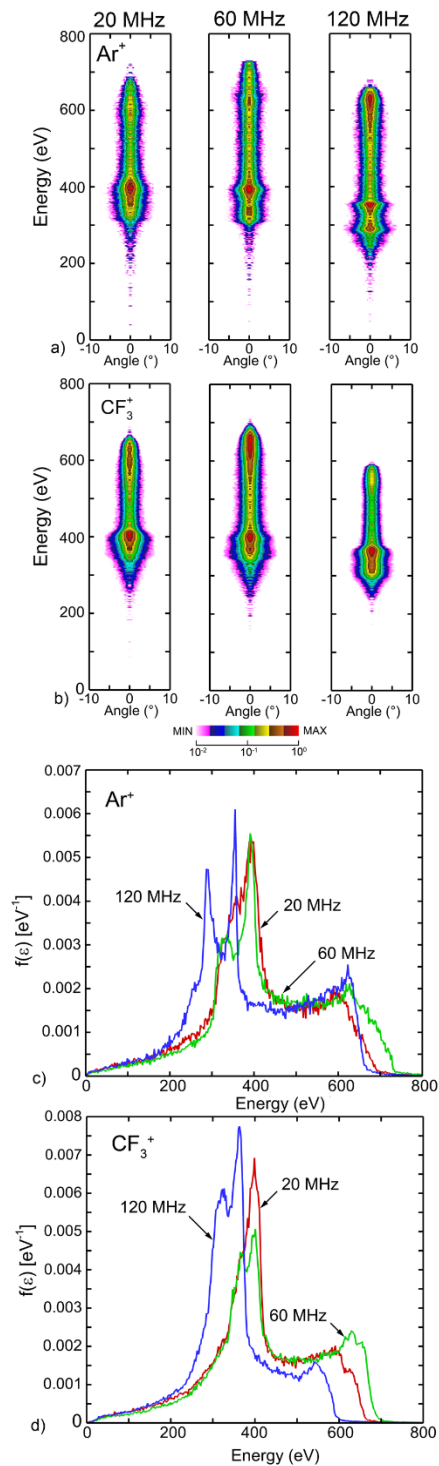
Fig. 6.15 IEADs of a) Ar^+ and b) CF_3^+ and the normalized IEDs of c) Ar^+ and d) CF_3^+ when the frequency from the HF power source is 20, 60 and 120 MHz. $Ar/CF_4/O_2$ (75/15/10), 25 mTorr, top electrode: 500 W (varied frequency), substrate: 400 W (5 MHz), 400 W (10 MHz).

207
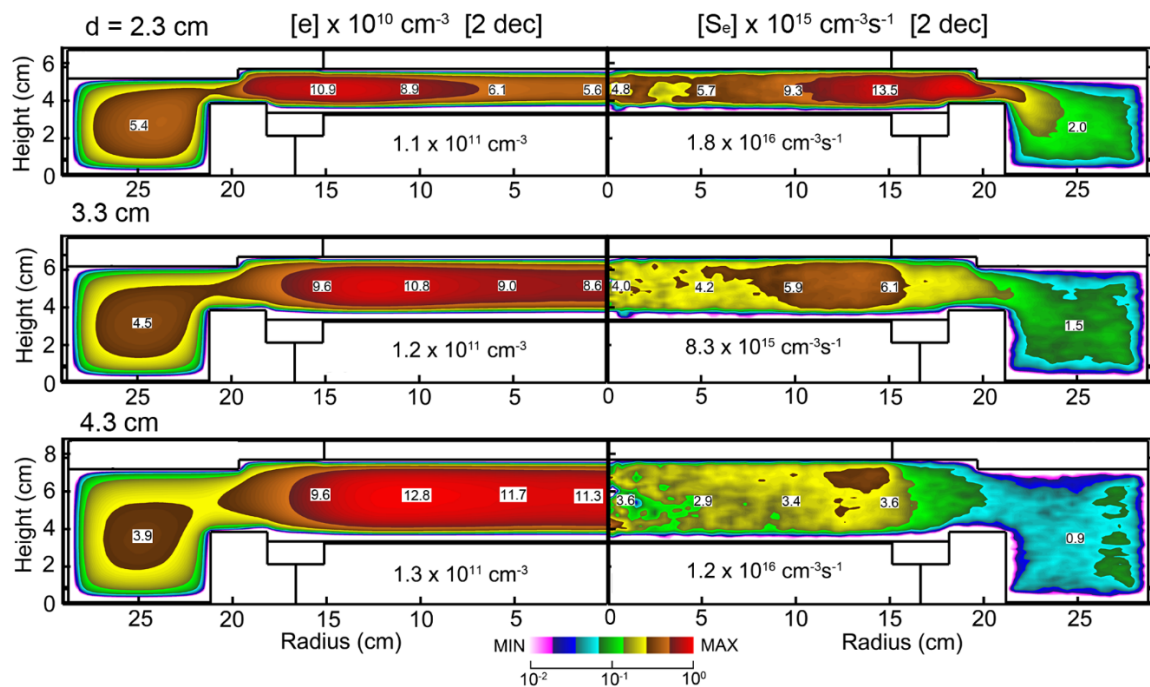
Fig. 6.16 2D profiles of the electron density and ionization source by bulk electrons when the gap length is 2.3, 3.3 and 4.3 cm. Ar/CF$_4$/O$_2$ (75/15/10), 25 mTorr, top electrode: 500 W (80 MHz), substrate: 400 W (5 MHz), 400 W (10 MHz).
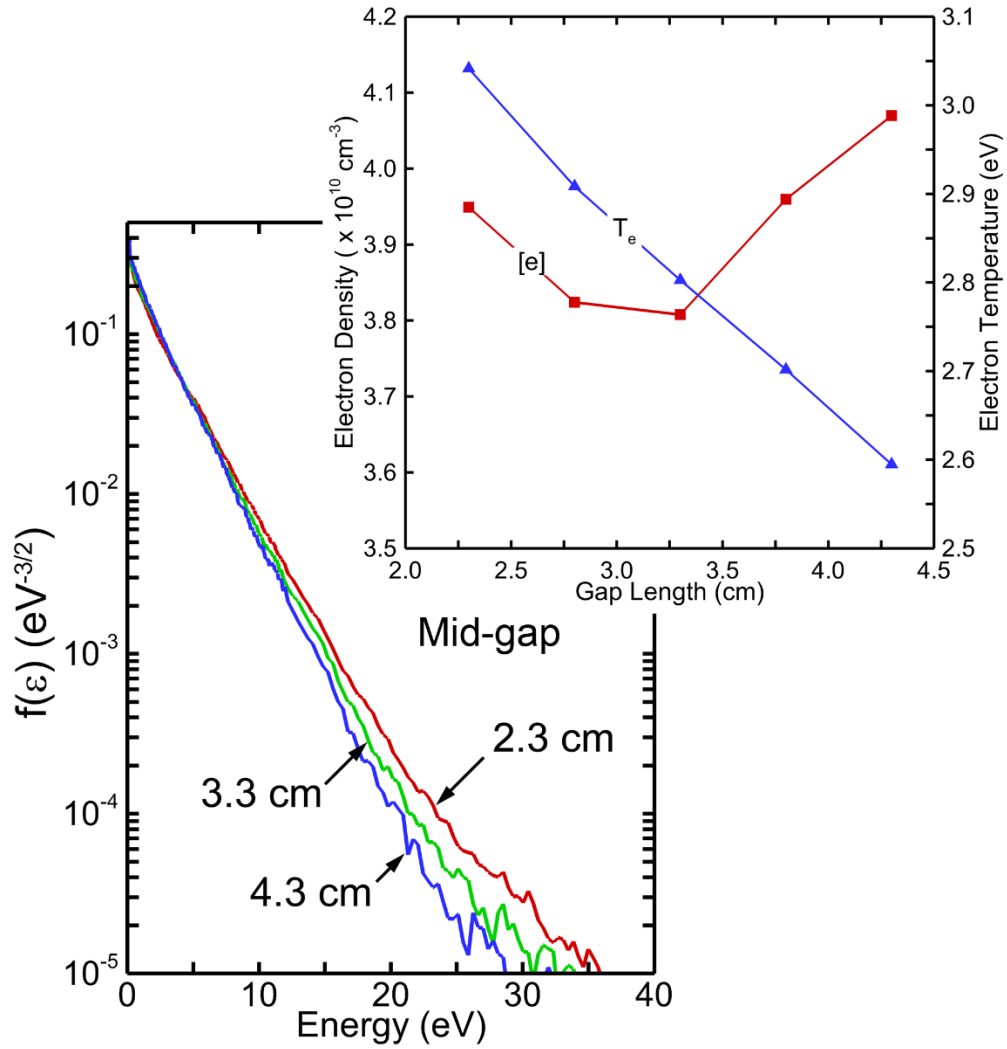
Fig. 6.17 EEDFs from the center point (r = 13.5 cm, z = 4.8 cm) when the gap length is 2.3, 3.3 and 4.3 cm. The inset is the spatially averaged electron density and electron temperature with increasing gap length. Ar/CF$_4$/O$_2$ (75/15/10), 25 mTorr, top electrode: 500 W (80 MHz), substrate: 400 W (5 MHz), 400 W (10 MHz).
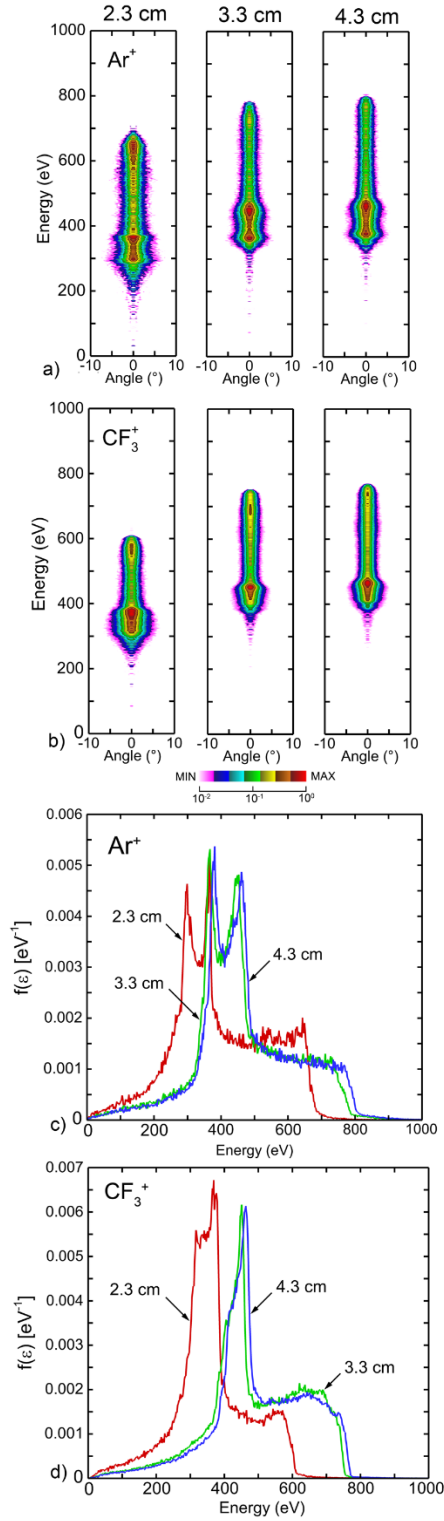
Fig. 6.18 IEADs of a) Ar^+ and b) CF_3^+ and the normalized IEDs of c) Ar^+ and d) CF_3^+ when the gap length is 2.3, 3.3 and 4.3 cm. $Ar/CF_4/O_2$ (75/15/10), 25 mTorr, top electrode: 500 W (80 MHz), substrate: 400 W (5 MHz), 400 W (10 MHz).

6.6 References

1. W. M. Greene, M. A. Hartney, W. G. Oldham, and D. W. Hess, J. Appl. Phys. **63**, 1367 (1988).

2. E. Kawamura, V. Vahedi, M. A. Lieberman, and C. K. Birdsall, Plasma Sources Sci. Technol. **8**, R45 (1999).

3. F. R. Myers, M. Ramaswami, and T. S. Cale, J. Electrochem Soc. **141**, 1313 (1994).

4. X. Li, Z. Bi, D. Chang, Z. Li, S. Wang, X. Xu, Y. Xu, W. Lu, A. Zhu, and Y. Wang, Appl. Phys. Lett. **93**, 031504 (2008).

5. M. A. Lieberman and A. J. Lichtenberg, Principles of Plasma Discharges and Materials Processing (Wiley, New Jersey, 2005).

6. J. Yeom, Y. Wu, J. C. Selby, and M. A. Shannon, J. Vac. Sci. Technol., B **23**, 2319 (2005).

7. G. Kokkoris, A. G. Boudouvis, and E. Gogolides, J. Vac. Sci. Technol., A **24**, 2008 (2006).

8. B. Wu, A. Kumar, and S. Pamarthy, J. Appl. Phys. **108**, 051101 (2010).

9. T. Ohchi, S. Kobayashi, M. Fukasawa, K. Kugimiya, T. Harano, A. Ando, T. Kawase, S. Hamaguchi, and S. Iseda, Jpn. J. Appl. Phys. **47** 5324 (2008).

10. A. Matsuda, Y. Nakakubo, Y. Takao, K. Eriguchi, and K. Ono, Thin Solid Films **518**, 3481 (2010).

11. U. Czarnetzki, J. Schulze, E. Schüngel, and Z. Donkó, Plasma Sources Sci. Technol. **20**, 024010 (2011).

12. S. Wang, H. Long, Z. Bi, W. Jiang, X. Xu, and Y. Wang, Chinese Phys. B, **25** 115202 (2016).

13. J. Schulze, E. Schüngel, Z. Donkó, and U. Czarnetzki, Plasma Sources Sci. Technol. **20** 015017 (2011).

14. Y. Zhang, Y. Hu, F. Gao, Y. Song, and Y. Wang, Plasma Sources Sci. Technol. **27** 055003 (2018).

15. I. Korolov, Z. Donkó, U. Czarnetzki, and J. Schulze, J. Phys. D: Appl. Phys. **45** 465205 (2012).

16. D. O'Connell, T. Gans, E. Semmler, and P. Awakowicz, Applied Physics Letters, **93**(8) 081502 (2008).

17. P C Boyle, A R Ellingboe, and M M Turner, J. Phys. D: Appl. Phys. **37** 697 (2004).

18. K. Denpoh, Jpn. J. Appl. Phys. **53**, 080304 (2014).

19. V. Georgieva, A. Bogaerts, and R. Gijbels, Physical Review E **69**, 026406 (2004).

20. B. G. Heil, U. Czarnetzki, R. P. Brinkmann, and T Mussenbrock, J. Phys. D: Appl. Phys. **41**, 165202 (2008).

21. B. B. Sahu, and J. G. Han, Physics of Plasmas **23**, 053514 (2016).

22. P. Diomede, D. J. Economou, T. Lafleur, J. P. Booth, and S. Longo, Plasma Sources Sci. Technol. **23**, 065049 (2014).

23. S. H. Lee, P. K. Tiwari, and J. K. Lee, Plasma Sources Sci. Technol. **18**, 025024 (2009).

24. E. Kawamura, M. A. Lieberman, and D. B. Graves, Plasma Sources Sci. Technol. **23**, 064003 (2014).

25. M. J. Kushner, J. Phys. D **42**, 194013 (2009).

26. S. Song, and M. J. Kushner, Plasma Sources Sci. Technol. **21**, 055028 (2012).

27. C. Bohm, and J. Perrin, Rev. Sci. Instrum. **64,** 31 (1993).

Chapter 7: Computational Investigation of Plasma Enhanced Atomic Layer Deposition of SiO$_2$ Film Using Capacitively Coupled Ar/O$_2$ Plasmas

7.1 Introduction

Atomic layer deposition (ALD) is a material deposition technology that enables minutely delicate control over film quality at the angstrom-scale. An ideal ALD process is self-limiting, meaning that the kinetics of the film growth saturates, resulting in a maximum of only one monolayer of deposition per cycle. The deposited films often yield high conformality and uniformity, which is necessary for applications ranging from conventional semiconductor manufacturing and solar panel fabrication, to novel applications such as energy storage fuel cell manufacturing [1-5]. For semiconductor manufacturing, deposition of silicon-based dielectrics is still one of the most targets for refinement of ALD technologies [6-12].

Thin SiO$_2$ film is widely used as an isolation liner and sidewall spacer in microelectronics devices [13-15]. Even though some relatively sophisticated film deposition approaches are available, the current technology nodes at the less than 10 nm scale, having more challenging demands for high-conformality film deposition. More severe operating conditions require highly uniform thin dielectric films, to deliver consistent performance. For example, one of the most pressing issues challenging the dependability of SiO$_2$ films is electrical breakdown [16-17]. This is more likely to happen if the SiO$_2$ film contains defects in the film. Stathis reported that in films thinner than 2 nm, a single defect is enough to cause a breakdown and inconsistent performance [17].

Thermal ALD is one of the more well established SiO_2 film deposition techniques. Typically, in a thermal ALD process, the target surface is sequentially treated with inorganic silicon precursor (e.g., $SiCl_4$, $SiCl_3H$) and oxidant (e.g., H_2O, O_3). Each cycle produces a fraction of a monolayer of film. Repeating the 2-steps builds the film layer by layer. To activate these processes the substrate is usually heated to > 300 ˚C. Using a $SiCl_4$ and H_2O binary reaction sequence, Sneh et al. achieved controlled SiO_2 film deposition at temperatures of 330-410 °C at a growth rate of 1.1 Å/cycle in 1995 [18]. In a later work, Lee et al. proposed a SiO_2 ALD mechanism having cycles of alternating Si_2Cl_6 and O_3 with a substrate temperature of 403-453 °C [19]. A temperature of 471 °C or higher was needed for a deposition rate higher than 0.32 nm/cycle. Even though this temperature is already lower than that used in many other SiO_2 deposition techniques, such as low-pressure chemical vapor deposition, it is still high enough to tax the allowed thermal budget of the manufacturing process. This higher temperature also limits the use of temperature-sensitive materials such as those used for flexible electronics.

One way to decrease the temperature of ALD of SiO_2 deposition is to use plasma-enhanced ALD (PE-ALD). In a typical SiO_2 PE-ALD process, the target surface is first treated with the silicon precursor and then oxidized in an oxygen plasma. The process is repeated itself, and the SiO_2 is thus grown layer-by-layer. Unlike thermal ALD, in a PE-ALD, oxidation reactions are enabled by reactive species in the plasma. Fang et al. reported that $O_2(^1\Delta)$, O_3 and $O(^1D)$ are the primary reactants that oxidize a precursor-dosed surface during plasma exposures in SiO_2 PE-ALD, and this enables the low-temperature deposition [20]. Choi et al. also reported the deposition of SiO_2 films of 10s nm using PE-ALD with a temperature of less than 200 °C [21]. Jeon et al. used plasma-activated triisopropylsilane [TIPS, ((iPr)3SiH)] as a silicon precursor during dosing in a PE-ALD process [11]. They found that the deposition temperature

can be decreased to as low as 50 °C, and these SiO_2 films have no detectable impurities.

In side-by-side comparison of SiO_2 films deposited using PE-ALD and plasma-enhanced chemical vapor deposition (PECVD), Jung et al. found that the PE-ALD prepared film had higher purity, more proper stoichiometry, and lower leakage current [12]. When tested as the gate insulator in a thin film transistor, PE-ALD SiO_2 film appeared to be less susceptible to the negative threshold voltage shift than PECVD SiO_2 film due to a smoother insulator/channel contact interface. Civale et al. studied 200 nm-thick SiO_2 liners for a high aspect ratio (25:1) through silicon via (TSV) as used in 3D interconnections, prepared using PE-ALD [13]. They reported near-ideal film conformality and electrical properties, suggesting a role of PE-ALD grown SiO_2 films in high aspect ratio applications. However, the quality of SiO_2 films grown using PE-ALD is sensitive to the scale of the feature. For example, growing a SiO_2 film in a high aspect ratio feature having a critical dimension of less than 20 nm can be more challenging than depositing this film in a feature with a critical dimension of 10s to 100s nm and the same aspect ratio.

Similar to other thin film deposition techniques, many parameters can affect the quality of a PE-ALD process. Shin et al. found that for SiO_2 PE-ALD, the deposition rate measured as growth-per-cycle (GPC) depends on the plasma exposure time [8]. The GPC decreased from 2.0 to 1.6 Å/cycle as O_2 plasma exposure time increased from 0.5 to 5.0 s, which was thought to be the result of surface heating and film densification. Kobayashi et al. found that the deposition temperature can also affect PE-ALD [6]. A higher GPC was achieved with lower deposition temperature. Using BDEAS (Bis(diethylamino)silane, $SiH_2[N(CH_2CH_3)_2]_2$) as the silicon precursor, they found that the saturated GPC increases from 0.10 to 0.15 nm/cycle as the deposition temperature decreases from 300 to 50 °C. They concluded that as the substrate

215

temperature increases, desorption reactions decrease the GPC.

Other than the external operating conditions, the chemical properties of silicon precursors have a significant impact on the PE-ALD process [22-23]. In work comparing SiO_2 PE-ALD by silicon precursors: BTBAS (bis(tertiary-butylamino)silane, $SiH_2[NH(C_4H_9)]_2$), BDEAS, and DSBAS (di-sec-butylaminosilane, $SiH_3[N(C_4H_9)_2]$), Mallikarjunan et al. concluded that because DSBAS is a monoaminosilane precursor, it has fewer organic substitutions than BTBAS and BDEAS [23]. Therefore, the surface packing density of silicon-containing components after the precursor dosing is higher when using DSBAS, and so is the growth rate. From this work, it is clear that the structure of the precursor can affect PE-ALD through steric hindrance.

Steric hindrance occurs when the ligand group from the silicon precursor remains on the target surface and blocks the otherwise exposed neighboring surfaces. The blockage reduces the surface coverage of the desired species and hinders the growth of the film. Using density functional theory (DFT) to study the steric effect in an ALD process, Murray et al. concluded that a sizeable steric bulk of alkyl ligand groups is less likely to form bound reactant structures with the surface, resulting in reduced adsorption probability [7]. Once deposited, these large ligand groups can cause significant steric hindrance and impede further deposition.

In this chapter, we discuss results from computational investigations of PE-ALD of SiO_2 films for blanket deposition, and in trench and via structures. We performed a parametric study on the input power of the oxidizing plasma from 400 to 1000 W, and the pressure from 0.5 to 2 Torr. We have found that changing power has a small effect on film quality, but decreasing pressure promotes ion bombardment, and produces a more porous film. The deposition probability of ligand groups with precursors was varied from 0.001 to 0.5. Both film growth rate, and film density, decrease with an increase of the ligand group co-deposition probability.

The model used in this investigation is briefly discussed in Sec. 7.2. Plasma and film properties as a function of power, pressure, and ligand group co-deposition probability are discussed in Sec. 7.3. Concluding remarks are in Sec. 7.4.

7.2 Description of the Model

The computational investigation platforms used in this work are the Hybrid Plasma Equipment Model (HPEM) and the Monte Carlo Feature Profile Model (MCFPM). The details of the models are discussed in Chapter 2, Ref [24] and Ref [25]. Only a brief description of these is provided here.

The modules from the HPEM that are used in this work are the Fluid Kinetics Poisson Module (FKPM), the Electron Energy Transport Module (EETM), and the Plasma Chemistry Monte Carlo Module (PCMCM). In the FKPM, the continuity, momentum, and energy equations of the heavy particles are solved coincidently with Poisson's equation to provide heavy particle densities and electrostatic potential. The Boltzmann equation is solved in the EETM for the electron energy distribution function (EEDF), from which electron transport and rate coefficients are obtained. The PCMCM is used when the plasma reaches the quasi-steady state to calculate energy and angular distributions (EADs) of ions and reactive neutrals onto the wafer.

In the MCFPM, gas-phase pseudoparticles with EADs providing by the HPEM are launched on at the top of the target feature and tracked using Monte Carlo technique. Elastic collision of gas-phase particles is included with isotropic scattering. The steric hindrance of large ligand groups in the Si precursor is addressed by "co-depositing" a ligand-representing cell in the neighbor cells of the primarily deposited silicon cell.

The following process is used to co-deposit the ligands. The Si precursor is specified to have N ligand groups. Upon deposition of the Si precursor, a random number $r=(0,1)$ is selected.

If $r \leq p_R$, then a co-deposition of the first ligand is attempted. A search is made of the sites surrounding the deposition site for an empty voxel to co-deposit the ligand. The search order is randomized. For a 2D simulation, there are 8 possible sites. For a 3D simulation, there are 26 possible sites. When an empty site is found, a ligand is placed in that voxel. The process is then repeated for the N ligand groups.

The species included in the reactor scale simulation are Ar, Ar($1s_5$), Ar($1s_4$), Ar($1s_3$), Ar($1s_2$), Ar($4p$), Ar($4d$), Ar_2^*, Ar^+, Ar_2^+, O_2, $O_2(v)$, $O_2(a^1\Delta_g)$, $O_2(b^1\Sigma_g^+)$, O_2^+, O_2^-, $O(^1D)$, $O(3s\ ^5S^0)$, $O(3s\ ^3S^0)$, $O(3p\ ^5P)$, $O(^1S)$, O^+, O^-, O_3, O_3^- and electrons.

7.3 Surface Reaction Mechanism for SiO$_2$ PE-ALD Using Ar/O$_2$ Plasma

The gas-phase species, surface sites, and surface reaction mechanism of SiO2 PE-ALD using a silicon precursor with two ligand groups (such as BTBAS) and Ar/O2 plasma as oxidation agent are shown in Table II.

The gas-phase species included the feature scale simulation can be classified as follows. a) Ions bring high energy to the feature due to acceleration in the sheath. b) Hot neutrals have similar energy as ions. They are produced when ions hit a surface, lose their charge, and are reflected from the wall. c) Thermal neutrals have energy less than 0.1 eV. Many thermal neutrals, such as O and O$_3$, are the primary species for surface oxidation. d) Reaction products are gas phase particles removed from the surface by ions and hot neutrals or chemical reactions. Many reaction products can be re-deposited on the surface.

Surface sites are classified by the layer they belong to. A silicon layer contains sites that are produced from precursor dosing, and an oxygen layer contains sites that are produced during plasma exposure. Each voxel in the MCFPM represents a site in the oxygen layer containing

two physical bonds due to Si/O = 1:2 in SiO_2 film. For example, x-Si-y(s) denotes x and y sites connected to a shared silicon atom, although this silicon atom is not included in that voxel.

The PE-ALD process starts with precursor dosing on a surface covered with hydroxyl sites. The ligand group R from the precursor SiH_2R_2 combines with the hydrogen from hydroxyl sites and forms a volatile species HR. The remaining precursor SiH_2 is then bonded to the oxygen, and deposited on the surface as SiH_2(s). In a process that completely eliminates the ligands:

$$OH\text{-}Si\text{-}OH(s) + SiH_2R_2 \rightarrow O_2(s) + SiH_2(s) + 2HR \qquad (7.1a)$$

However, there are cases where deposition of SiH_2(s) can occur on some surface sites with insufficient hydroxyls.

$$OH\text{-}Si\text{-}H(s) + SiH_2R_2 \rightarrow O(s) + SiH_2(s) + 2HR \qquad (7.1b)$$

$$OH\text{-}Si(s) + SiH_2R_2 \rightarrow O(s) + SiH_2(s) + p_RR(s) + (1\text{-}p_R)HR + HR \qquad (7.1c)$$

$$O\text{-}Si\text{-}H(s) + SiH_2R_2 \rightarrow O(s) + SiH_2(s) + p_RR(s) + (1\text{-}p_R)HR + HR \qquad (7.1d)$$

$$OH\text{-}Si\text{-}O(s) + SiH_2R_2 \rightarrow O(s) + SiH_2(s) + p_RR(s) + (1\text{-}p_R)HR + HR \qquad (7.1e)$$
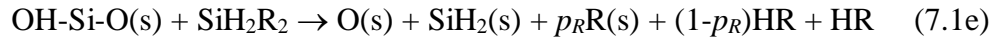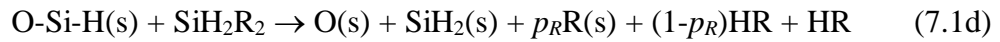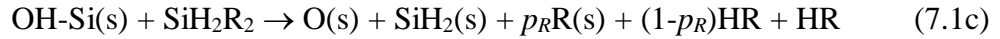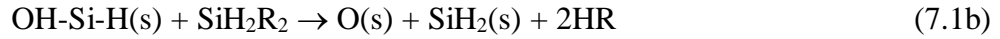
In reactions 7.1b, 7.1c, and 7.1d, O(s) instead of O_2(s) is deposited. If this happens too often, the O/Si ratio will decrease, leading to an disordered film structure. Note that ligand groups R(s) are not co-deposited with SiH_2(s) even when the direct surface reactant has insufficient hydroxyl sites, such as in reaction 7.1c, 7.1d, and 7.1e. This is because, if any of the nearest neighbors of the direct surface reactant can provide hydrogen atoms, the ligand from the silicon precursor can combine with them and form volatile HR. That said, it would be very computationally expensive to check the nearby neighbors of a direct surface reactant wherever a deposition occurs. Therefore, we rely on the co-deposition probability p_R for the deposition of ligand remnants R(s). For example, if a SiH_2(s) is deposited on a surface with SiH_2R_2 as a reactant, an R(s) site is co-deposited with the probability p_R.

During plasma exposure, the surface is oxidized by ROS (reactive oxygen species) from the plasma. The oxidation can be a multi-step process.

$$SiH_2(s) + O \rightarrow Si(s) + OH\text{-}Si\text{-}H(s) \tag{7.2a}$$

$$OH\text{-}Si\text{-}H(s) + O \rightarrow OH\text{-}Si\text{-}OH(s) \tag{7.2b}$$

Both the excited state oxygen radical (such as $O(^1D)$) and O^+ can have the same reactions with higher probability. The oxidation can also become a one-step process by excited state oxygen molecules.

$$SiH_2(s) + O_2(^1\Delta) \rightarrow Si(s) + OH\text{-}Si\text{-}OH(s) \tag{7.2c}$$
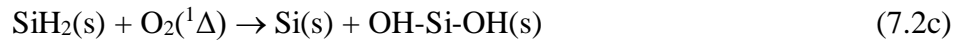
The goal of plasma exposure is to deposit the oxygen layer on the film and populate the surface with hydroxyl sites.

Despite a high pressure of up to a few Torr, some ions reach the surface with energy exceeding 30 eV can produce damage by sputtering.

$$OH\text{-}Si\text{-}OH(s) + I^+ \rightarrow OH\text{-}Si(s) + OH + I(h) \tag{7.3a}$$

$$SiH_2(s) + I^+ \rightarrow SiH_2 + I(h) \tag{7.3b}$$

$$R(s) + I^+ \rightarrow R + I(h) \tag{7.3c}$$
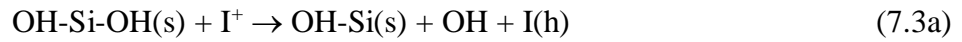
The sputtering thresholds for oxygen and hydroxyl are 30 eV, and for silicon, $SiH_2(s)$, and $SiH(s)$ are 35 eV. The sputtered particles can be re-deposited on the surface when they have collided with sites having dangling bonds. Gas-phase OH and R particles can combine with hydrogen and create a dangling bond on the surface.

$$SiH_2(s) + OH \rightarrow SiH(s) + H_2O \tag{7.4a}$$

$$OH\text{-}Si\text{-}OH(s) + OH \rightarrow OH\text{-}Si\text{-}O(s) + H_2O \tag{7.4b}$$

$$SiH_2(s) + R \rightarrow SiH(s) + HR \tag{7.4c}$$

$$OH\text{-}Si\text{-}OH(s) + R \rightarrow OH\text{-}Si\text{-}O(s) + HR \tag{7.4d}$$
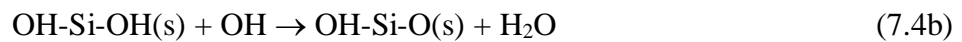
Hydrogen is typically bonded to Si or O. No hydrogen-only sputtering is included due to the low kinetic energy transfer efficiency between a light hydrogen atom and a heavy incident particle.

Besides sputtering, the recombination reactions of oxygen radicals and O_3 can also reduce the oxygen contents of SiO_2 film.

$$O(s) + O \rightarrow O_2 \qquad (7.5a)$$

$$O_2(s) + O \rightarrow O(s) + O_2 \qquad (7.5b)$$

$$O_2(s) + O_3 \rightarrow O_2 + O_2 \qquad (7.5c)$$

Despite low reaction rates ($p_0 = 6 \times 10^{-5}$), the high O density in the plasma makes these reactions common.

Removal of the R(s) ligands can occur through 2 processes. The first is removal process is sputtering by ions and hot neutrals. R(s) This can also be removed through replacement reactions with reactive oxygen species (ROS) where O inserts into the Si-R(s) bond and displaces the R.

$$R(s) + O \rightarrow O(s) + R \qquad (7.6a)$$

$$R(s) + O^* \rightarrow O(s) + R \qquad (7.6b)$$

$$R(s) + O_3 \rightarrow O(s) + R + O_2 \qquad (7.6c)$$

At low substrate temperatures, these reactions have low reaction probabilities. In experiments by Lu et al., the oxygen plasma exposure time to remove the ligands was up to several minutes, which is much longer than the exposure time for of any given cycle (1 s) addressed here [26].

7.4 Plasma Characteristics and Film Deposition Profile

The reactor used in this work is shown in Fig. 7.1. It is a cylindrically symmetric capacitively coupled plasma (CCP) reactor maintained at a pressure of 2 Torr. The reactor is designed to process a wafer with a 30 cm diameter that is on a grounded substrate with a 4 cm quartz (relative permittivity $\varepsilon_r = 4.0$) focus ring. 500 W (10 MHz) radiofrequency (RF) power is applied to the top electrode 1.5 cm above the substrate. Two gas inlets are used in this reactor. The primary showerhead overlaps with the top electrode and injects an Ar/O_2 (80/20) mixture at

5 standard liters per minute (slm). The secondary inlet is located at the top of the reactor at $r >$ 20 cm, from which pure O_2 is flowed at 6 slm. The purpose of the secondary inlet is to entrain flow from the primary showerhead towards the pump, which is located at the bottom of the reactor surrounding the substrate. The secondary electron emission coefficient for ions is 0.05 for all the surfaces exposed to the plasma.

The base case conditions produce a time averaged plasma potential of 137 V. A DC bias of -30 V is generated on the blocking capacitor connected to the top electrode. The dominant cations and anions are O_2^+ and O^-. The O_2 flow, electron density (n_e), O_2^+ density, and O^- density are shown in Fig. 7.2. The flow of O_2 demonstrates that the gas from the secondary inlet has little impact on the plasma between the electrode and substrate. The plasma properties are predominantly determined by the gas mixture from the primary showerhead. The electron density n_e peaks at $r = 19$ cm at 2.3×10^{10} cm^{-3} due to electric field (E-field) enhancement at the edge of the top electrode, and is otherwise uniform in the radial direction across the wafer. The wafer has a fairly high conductivity (σ) of 0.05 Ω^{-1}cm^{-1}, while the quartz focus ring is an ideal dielectric. When solving Poisson's equation using the substrate as a ground, the E-field is negligible in the wafer but relatively high in the focus ring (150 V/cm). The end result is a higher potential on the surface of the focus ring (50 V) than on the wafer (4 V), which perturbs the sheath on the wafer-quartz interface and causes a non-uniform plasma distribution above the focus ring. However, both the hot spot of n_e and this perturbation of the plasma distribution occur downstream of the gas flow. Therefore, their impact on the bulk plasma is insignificant.

In a high pressure CCP, ionization can be sustained by bulk electrons, which are mostly resistively heated, and beam electrons that are from secondary electron emission. At 2 Torr, the electron mean free path is much smaller than the gap length. Therefore, it is difficult for bulk

electrons heated at the edge of the sheath to transport to mid-gap with enough energy to enable further ionization. However, when accelerated by the sheath, beam electrons can have energy up to 10s to more than 100 eV, enabling them to travel further into the bulk plasma.

The ionization source for bulk electrons (S_e) near the sheath is comparable with that for beam electrons (S_{eb}), with $S_e = 6.7 \times 10^{15}$ cm^{-3}s^{-1} and $S_{eb} = 4.4 \times 10^{15}$ cm^{-3}s^{-1}. However, at 0.3 cm below the top electrode, S_e drops to zero, and the ionization is maintained only by beam electrons ($S_{eb} = 2.7 \times 10^{15}$ cm^{-3}s^{-1}). Because the plasma is mainly sustained by beam electrons, the plasma is thereby operated in the γ-mode.

The dominant cation O_2^+ shares the same uniform radial distribution with electrons, and peaks at 6.2×10^{10} cm^{-3} at the corner of the top electrode. In the axial direction, O_2^+ density decreases from 2.4×10^{10} cm^{-3} near the sheath adjacent to the top electrode to 1.9×10^{10} cm^{-3} at the mid-gap. O_2 undergoes dissociative attachment producing O$^-$ which has a relatively high density. The O$^-$ density is nearly 70% of n_e in the bulk plasma. However, because of its low temperature, O$^-$ is confined in the bulk plasma and has a negligible flux to the wafer.

The energy and angular distributions (EADs) of Ar$^+$, O_2^+, and O are shown in Fig. 7.3a. These data are averaged over the wafer and averaged in angle across the normal. Both Ar$^+$ and O_2^+ have relatively narrow angular distributions with an incident angle of less than 20˚. The sheath by the wafer accelerates ions up to 45 eV. However, the plasma potential is 137 V, almost three times the peak ion energy, indicating that the sheath is highly collisional such that ions dissipate their energy through multiple collisions as they travel across the sheath. Because the majority of ions have energy less than 20 eV, smaller than the sputtering threshold of SiO$_2$ (30 eV), only minor ion bombardment damage to the film is expected. Unlike ions, neutral species have close to thermal energy and wide angular distribution. The peak O energy reaches

0.3 eV, which is likely caused by charge exchange reactions near the wafer. When hot O^+ atoms collide with O, they exchange the charge but preserve their initial kinetic energy and form a hot O and a cold O^+. The hot neutral will no longer gain energy from E-field but will lose its energy through collisions with other particles as it moves toward the wafer. Consequently, when it hits the surface, its energy is much lower than the energy of most ions but is still higher than the thermal energy of many neutral species. This slightly higher energy of 0.2 eV is unlikely to cause any significant difference regarding the surface reaction rates.

The fluxes of some major species as a function of radius are shown in Fig. 7.3b. Most species have a fairly uniform flux across the wafer. For example, the O flux remains at 1.6×10^{18} $cm^{-2}s^{-1}$ at $r < 12$ cm with only minor fluctuation ($\pm 1.0 \times 10^{16}$ $cm^{-2}s^{-1}$). However, it increases to 1.7×10^{18} $cm^{-2}s^{-1}$ at $r = 15$ cm due to a slight increase of O density near the edge of the top electrode. Note that the high pressure produces a reasonably high O_3 density (3.6×10^{11} cm^{-3} at mid-gap), which produces a O_3 flux of $\approx 3 \times 10^{15}$ $cm^{-3}s^{-1}$. Even though it is three orders of magnitudes smaller than the O flux, O_3 is an important oxidant that is commonly used in the deposition of oxides due to its highly reactive nature. The dominant cations Ar^+ and O_2^+ also have fluxes of $\sim10^{15}$ $cm^{-2}s^{-1}$. Even though the resulting ion bombardment sputtering is not expected to be severe with the default setup, changing the operating conditions such as decreasing the pressure can increase ion energy and produce damage.

A deposition schematic of PE-ALD of SiO_2 film is shown in Fig. 7.4. The wafer is repeatedly exposed to the silicon precursor and Ar/O_2 plasma. Gas purge is not included in the simulation and we assume that no gas remains from the previous steps. The cubic voxels used in the MCFPM are 0.5^3 nm^3. Each cycle deposits 2 layers of voxels representing a monolayer of silicon dioxide. Si voxels are displayed in two colors to help distinguish deposition from other

224

steps. In the base case, the precursor dosing time is 0.8 s, and the plasma exposure time is 1.0 s. During precursor dosing, precursor flux of 1×10^{20} cm^{-2}s^{-1} is launched from the top of the feature; while during plasma exposure, the fluxes are obtained from the HPEM results. Unless otherwise specified, the ligand group co-deposition probability $p_R = 0.005$. As shown in Fig. 7.4b, the impact of a buried ligand group increases as the film grows thicker. The initial disruption of the layered structure caused by the embedded ligand group escalates to misalign in the upper layers and produces an increasingly coarse surface. Some unoccupied gas voxels appear in the film as vacancies. A vacancy occurs when the fast-growing neighbors of a gas voxel bridge over an unoccupied site. A vacancy is defined as a gas phase voxel with less than two consecutive gas voxel neighbors in any direction. The vacancy density reduces the quality of a film. Generally, a high vacancy density translates to a high wet etch rate (WER).

Blanket film deposition was first performed on a 65 nm (L) $\times$ 10 nm (W) area and meshed with 130×20 computational voxels. A reflective boundary condition was used on all the boundaries. A gas phase particle crossing the boundary is specularly reflected back. For these results, R(s) ligands are only removed by sputtering. The SiO$_2$ film deposited in 10 cycles is shown in Fig. 7.5. Note that every two colored layers represent one monolayer of SiO$_2$. The film is fairly dense and uniform in the first 5 cycles but becomes less ordered later in the process. Early in the deposition, misalignments that are partly caused by the ligand remnants affect only their direct neighbors. For a single ligand site, the immediate next layer will have only local imperfections, and with a low co-deposition probability ($p_R = 0.005$), the impact of these imperfections is reasonably small. By the end of the 5th cycle, irregularities are only sparsely distributed on the surface such that the film can still be considered smooth. However, imperfections that occur in the early stages affect a larger area as the film grows.

The exposure of the side of a site enables non-epitaxial deposition. For example, if the side of an OH-Si-OH(s) site is left open after the plasma exposure, in the following precursor dosing, a $SiH_2(s)$ site can deposit next to it instead of above it, causing a silicon atom to be embedded in an oxygen layer. The OH-Si-OH(s) site this $SiH_2(s)$ is attached to (its neighbor) will be redefined as $O_2(s)$ and be exposed to the plasma. An $O_2(s)$ cannot be easily deposited on by a silicon precursor because it cannot provide a hydrogen atom to combine with the ligand group from the precursor SiH_2R_2. In this case an exposed $O_2(s)$ often produces a halt to the local deposition. As a result, a single missing OH-Si-OH(s) induces two potential defects: a $SiH_2(s)$ embedded in an oxygen layer, and an exposed $O_2(s)$. Both lead to staggered depositions in the layers above, and the following deposition on these misaligned sites occur in different steps as their neighbors.

For example, when the $SiH_2(s)$ is deposited with O(s) during plasma exposure, most of its neighboring OH-Si-OH(s) are deposited upon in precursor dosing. This staggered deposition may expose more sites with open sides and consequently enlarge the misaligned areas and eventually lead to non-ordered layers. Because sparsely distributed defects and imperfections in the early stage can make the film highly disordered and rough later in the deposition, it is vital to perform quality control from the beginning of PE-ALD.

$O_2(s)$ cannot be directly deposited on with a silicon precursor. Therefore, the $O_2(s)$ surface coverage ratio increases through the deposition process, as shown in Fig. 7.6a. The surface coverage ratio of $O_2(s)$ is the fraction of surface sites that are occupied by $O_2(s)$. The sampled area occupies the center of the feature in a 10 nm $\times$ 10 nm square. In this work, the surface coverage ratio of $O_2(s)$ does not reach saturation in 10 cycles. However, it eventually saturates $\approx 50\%$ as the exposure of $O_2(s)$ is balanced through recombination reactions with other

gas phase species such as O and O_3.

The accumulation of $O_2(s)$ on the surface is part of the reason for the decreasing film growth rate. The concentration of O (η_O), Si (η_{Si}), vacancy (η_{Vac}), and ligand groups (η_R) in the entire film is shown in Fig. 7.6b. Note that hydrogen is not counted, so that $\eta_{Si} + \eta_O + \eta_{Vac} + \eta_R = 1$. In the first 10 cycle (18 s), both η_{Si} and η_O are relatively stable, with $\eta_O/\eta_{Si} \approx 2.0$. Excessive O(s) deposition occurs when an already saturated Si(s) (silicon with four bonds occupied) is exposed to the plasma. This is not a physical process. To reduce its impact, the oxygen deposition probability on Si(s) was decreased to a smaller value (1×10^{-4}), which is not expected to artificially decrease the O content. With minor sputtering in a PE-ALD, the exposed Si(s) are often saturated with all of its bonds occupied and are exposed because of the slow growth of its neighbors. It is unlikely for O to deposit on these silicon sites. Ideally, the end surface after the precursor dosing is $SiH_2(s)$, which will be oxidized to OH-Si-OH(s). Therefore, the film growth does not rely on the oxidation of Si(s) using this mechanism.

The ligand group co-deposition probability, $p_R = 0.005$, is constant through the ALD process, thereby η_R is constant $\approx 0.2\%$. The film becomes coarser and more disordered as it thickens. The vacancy density increases and peaks at 1% by the end of the 10th cycle. The complicated surface concentration causes uneven growth on different parts of the surface and this ultimately results in more bridging and therefore more vacancies.

The average (ξ_{avg}) and instantaneous (ξ_{ins}) growth rate are shown in Fig. 7.6c. A 1-layer/cycle refers to ideal PE-ALD of a monolayer SiO_2 deposition in each cycle, which is represented by 2 computational layers. ξ_{avg} is calculated by dividing the spatially averaged film thickness with the number of cycles, while ξ_{ins} is the increase of the film thickness from the last cycle. The film thickness is also averaged in the center of the blanket deposition in a 10 nm $\times$ 10

nm square. Both ξ_{avg}, and ξ_{ins} decrease with time, partly because of the growing complexity of the surface contents as the film becomes more disordered later in the process. Compared to ξ_{avg}, ξ_{ins} decreases much faster, from 1 to 0.7 layer/cycle in 10 cycles. In practice, ξ_{ins} is often < 1 layer/cycle.

The deposition of SiO_2 film was also investigated in a trench structure, shown in Fig. 7.7. The process flow and reaction mechanisms are identical to the blanket deposition. The precursor dosing is 0.8 s and the plasma exposure is 1.0 s. The width of the trench is 30 nm and the height is 120 nm, the depth of the simulation domain is 10 nm with reflective boundary conditions. The voxels are 0.5^3 nm^3 cubes. The size of the computational geometry, including the walls is 70 (W) $\times$ 243 (H) $\times$ 20 (D) voxels. The film deposited in a trench, similar to the blanket deposition, has a relatively uniform structure early in the process that becomes coarse and disordered as it grows thicker.

Deposition into a trench is also subject to conduction limits, which does not apply to a blanket deposition. A conduction limit is basically a limitation of the distance a neutral particle can travel into a 3-dimensional feature. For thermal neutrals hitting the surface without a surface reaction, they are diffusively reflected back to the plasma. There is a 50% probability that these neutral particles come off a surface with a velocity component pointing upwards toward the opening of the feature. This leads them to transporting out of the feature instead of deeper inside. Due to the conduction limit, the neutral fluxes in the bottom of the feature are often smaller than those in the top. For example, an O flux logged at the bottom center is 9.7×10^{17} $cm^{-2}s^{-1}$ during plasma exposure in the first cycle. That is reduced by almost 40% compared to the O flux at the top (1.6×10^{18} $cm^{-2}s^{-1}$). As the film thickens, the aspect ratio increases and conduction limits increase. The oxidant fluxes are high enough that even at the bottom of the

feature, an epitaxial deposition with a clear, layered structure is obtained in the first several cycles. However, the conduction limit still affects the film deposition, especially for the oxidation process by reducing the excited state O_2^* flux deep into the trench.

Concentrations of the solid materials and vacancy, η_O/η_{Si} and average and instantaneous growth rate of the film at the bottom of the trench are shown in Fig. 7.8. Similar to blanket deposition, when depositing a SiO_2 film in the trench, concentrations of Si and O are relatively stable in the first 10 cycles, providing $\eta_O/\eta_{Si} \approx 1.9$. A $\eta_O/\eta_{Si} < 2$ suggests insufficient oxidation. This is partly caused by lack of oxidant in the lower trench due to conduction limits. This could be addressed by longer plasma exposure. At the end of the 10th cycle, η_O/η_{Si} is 1.95 in the top half of the trench and 1.88 in the bottom half, indicating a significant non-stoichiometric growth at the bottom. In an oxygen plasma, O and O_2^* are the main oxidants. Their fluxes decrease by factors of 1.6 and 9.6, respectively at the bottom of the trench. The O_2^* flux has a much faster fractional decrease than O flux because, when hitting a surface, O_2^* loses its energy and becomes a ground state inactive O_2 molecule, while O retains its highly reactive nature. Therefore, the O_2^* reaching the bottom of the trench have zero contact with any surface.

As the film grows thicker, the aspect ratio of the feature increases, from 4 to 4.8 in 10 cycles, which further exacerbates the conduction limit, and significantly affects the O_2^* flux. Compared to the flux at the bottom of the feature in the first cycle, by the end of the 10th cycle, O_2^* flux has further decreased by a factor of 4, but the O flux remains almost the same. These results demonstrate that unlike blanket deposition, when depositing in a 3-dimenstional structure such as a trench, the main oxidant is O rather than a combination of O and O_2^*. This is especially true at the bottom of a high aspect ratio feature. Because the oxidation by O is a multi-step process, insufficient oxidation is all the more common in a film deposited in a trench

than blanket deposition, which explains the lower η_O/η_{Si}. With the decrease of O_2^* flux during plasma exposure as the film grows, the film growth rate decreases faster in a trench. The deposition drops from 1 layer/cycle to 0.5 layer/cycle in 10 cycles as opposed to from 1 layer/cycle to 0.7 layer/cycle for a blanket deposition.

7.4.1 Power

The CCP power was varied from 400 W to 1 kW. Its impact on the SiO_2 PE-ALD process is discussed.

The EADs of Ar^+ and O when the power is 400 W, and 1 kW are shown in Fig. 7.9a. Neither the ion energy and angular distribution (IEAD) nor the neutral energy and angular distribution (NEAD) experience significant changes based on power. For this reactor, the blocking capacitor is connected to the top electrode. This means that the DC bias is not on the substrate, and ion energy distribution (IED) is only affected by the oscillation of the plasma potential. From 400 W to 1 kW, the bulk plasma density increases from 4.3×10^9 cm^{-3} to 1.2×10^{11} cm^{-3}, while the plasma potential increases from 127 to 137 V. As shown in Fig. 7.9a, with the increase of power the peak Ar^+ energy is increased by ≈ 5 eV from 40 to 45 eV, but the majority of the ions have lower energy, less than 5 eV, due to the highly collisional sheath. The almost identical IEADs and ion fluxes (Fig. 7.9b) suggest minimal changes in the sputtering with varying power. The NEAD also stays nearly the same when changing power.

The fluxes of some main oxidants have notable variations with power that can potentially affect SiO_2 film deposition. As the power increases from 400 W to 1 kW, O_3 flux decreases by a factor of 10, from 6.5×10^{15} cm^{-2}s^{-1} to 7.5×10^{14} cm^{-2}s^{-1} owing to the decreased O_3 density caused by additional dissociative reactions. At the same time, the excited state O_2^* density increases with the power from 1.9×10^{18} cm^{-2}s^{-1} at 400 W, to 5.6×10^{18} cm^{-2}s^{-1} at 1 kW, which

may lead to a higher growth rate especially when in blanket deposition. However, with a plasma exposure time of 1 s, the deposition is already self-limiting during plasma exposure when the input power is 500 W. Therefore, any increase of the film growth rate with power is not large.

The SiO_2 film was deposited on a blanket feature while varying power. The film concentrations and growth rate are shown in Fig. 7.10. The data are gathered at the end of the 5th cycle. As expected, with a long enough plasma exposure time, changing the power has a limited effect on the film quality. Both oxygen and silicon have almost the same constant concentrations in the film. Because the minimum sputtering threshold on SiO_2 film is 30 eV, which is much higher than the energy of most ions (1-5 eV), the ion bombardment damage to the film is negligible. In this example, ordered growth of oxygen and silicon layers occurs in the first 5 cycles, as shown in the 2D film profile at the top of Fig. 7.10. However, the increased O_2^* flux indeed promotes the oxidation process. Therefore, the η_O/η_{Si} has a slight increase as power increases from 400 W to 1 kW. Both the average and instantaneous growth rates are close to 1 layer/cycle with varying power. The lower than average instantaneous growth rate suggests some presence of surface coarseness and the occurrence of slowly growing sites. Even though input power has little effect on film deposition in this setup, it is expected to have a more significant impact on film deposition when the plasma exposure time is shorter. By increasing power from 400 W to 1 kW, the O_2^* flux is tripled, which will significantly increase the oxidation rate to the level of self-limiting during plasma exposure.

Deposition in the trench with varying power was also studied. Varying power had a more significant impact when depositing a film in a trench than blanket deposition. As the power increases from 400 to 700 W, the η_O/η_{Si} ratio decreases from 1.94 to 1.85, and then rises up to 1.90 as the power keeps increasing to 1 kW. This non-monotonic of η_O/η_{Si} is mainly caused by

231

the change of η_O owing to the variation of O flux with power. Film oxidation in a trench heavily relies on O instead of O_2^*. Therefore, even though the flux of O_2^* is tripled as the input power increases from 400 W to 1 kW, it has little effect on film deposition deep in a trench. Even with 1 kW, by the end of the 5th cycle, the O_2^* flux is 2.8×10^{17} $cm^{-2}s^{-1}$ at the bottom of the trench, as opposed to 6.9×10^{17} $cm^{-2}s^{-1}$ for O flux, which is more than twice of the O_2^* flux. As a result, when depositing in the trench, the film quality is directly affected by the magnitude of O flux, such that a lower O flux leads to less oxidation, hence more imperfections and misalignments in the film, more vacancies and a slower film growth rate.

7.4.2 Pressure

The IEAD is affected by sheath collisionality and thus the plasma pressure. Increasing pressure makes a sheath more collisional, which broadens the ion angular distribution (IAD) and reduces the overall ion energy. At the same time, with decreasing pressure, ions travel across a sheath with fewer or no collisions, resulting in a higher ion energy up to the maximum of sheath potential. The pressure was varied from 0.5 to 2 Torr, and its effect on SiO_2 film deposition was studied. Power is 500 W, the same as the base case.

The EADs of Ar^+ and O when pressure is 0.5, and 2 Torr are shown in Fig. 7.12a. The maximum ion energy reaches 50 eV at 0.5 Torr, and 40 eV at 2 Torr. Even though the maximum ion energy only differs by 10 eV, there is a much higher fraction of ions with energy higher than 30 eV when the pressure is 0.5 Torr than 2 Torr. The higher ion energy at low pressure is collectively caused by the higher plasma potential and low collision frequency. At 0.5 Torr, the plasma potential is 170 V, which decreases to 138 V at 2 Torr. As pressure increases from 0.5 to 2 Torr, the mean free path of Ar^+ shortens from 0.1 mm to 0.02 mm, suggesting more collisions as ions are accelerated towards the wafer, which helps dissipate the ion energy.

Again, the EAD of neutral species is not significantly affected by changes of pressure. O

has almost identical thermal EADs when the pressure is both 0.5 and 2 Torr. The fluxes of some major species are shown in Fig. 7.12c. For most of these species, increasing pressure causes an increase in their fluxes as high pressure leads to higher ionization and excitation reaction rates. However, at high pressure, even though the ion fluxes are high, most of these ions have low energy. Therefore, their effect on the SiO_2 film deposition process is minor. The O_3 flux decreases with an increasing pressure O_3 due to increased rates of electron collision quenching.

Film concentrations and growth rates with varying pressure for blanket deposition are shown in Fig. 7.13. The film properties show only minor changes when the pressure is higher than 1 Torr. However, at 0.5 Torr, because of increased ion bombardment damage to the film, there are higher vacancy concentration and lower η_O/η_{Si} ratio. As pressure increases from 0.5 to 1 Torr, vacancy concentrations decrease by a factor of 3 from 1.5% to 0.5%. In spite of a higher rate of sputtering at 0.5 Torr the ion flux is orders of magnitude smaller than that of the neutral species. Therefore, any vacant sites caused by sputtering during plasma exposure are likely to be "repaired" by the reactive oxidants. If a thicker film is being deposited, this slight increase of η_{Vac} in the early stage can cause much coarser and disordered structure in the top layers of the film.

Similar to film concentration, the growth rate is lower when pressure is 0.5 Torr. This is, again, caused by ion bombardment sputtering. Sputtering of the film compromises the continuous structure of the layers, which complicates surface structure and causes a low deposition rate. For example, if a $SiH_2(s)$ site is sputtered from the surface at the beginning of a plasma exposure step, the exposed $O_2(s)$ below it cannot be deposited upon with more oxygen until it is covered with another $SiH_2(s)$ in the following precursor dosing. The end result is that it takes two instead of one cycle to deposit a monolayer of SiO_2 at that position. The spatially

averaged layer thickness is then thinner, and the film growth rate will be slower.

The results of film deposition with varying pressure in a trench are given in Fig. 7.14. Generally, increasing pressure has the same effect on film deposited in a trench as for blanket deposition. Increasing the pressure results in less ion bombardment damage, thereby a higher η_O/η_{Si} ratio, lower vacancy concentrations, and higher film growth rates. When deposited in a trench, by the end of the 5th cycle, as pressure increases from 0.5 to 2 Torr, the vacancy concentration halves from 2.1% to 1.1%. However, for blanket deposition, it decreases by a factor of 5, from 1.5% to 0.3%. The vacancy concentration is less sensitive to pressure in a trench because ion bombardment damage to the film is not as significant in a trench for blanket deposition. Note that sputtering is angularly dependent, and the sputtering yield is close to 0 when the incident angle of the particle is grazing near 90°. Therefore, in a trench, ions lose some energy by grazing the vertical walls but cause little sputtering. Once contacted with a surface, ions lose their charge and become hot neutrals. By continually colliding on the walls, hot neutrals loss more energy and become thermal neutrals. Neutrals are also subject to the conduction limit such that their fluxes decrease from the top to bottom of a trench. When the pressure is 0.5 Torr, in the 5th cycle, the total flux of ions and hot neutrals in the bottom of the trench is 2.8×10^{14} cm^{-2}s^{-1}, which is smaller by a factor of 7 comparing to the summation of ion fluxes from the top (2.0×10^{15} cm^{-2}s^{-1}). Therefore, the ion bombardment damage is weak at the bottom; even though it is in that position that the incident angle of ions and hot neutrals is small enough to most likely cause sputtering.

Changing the pressure has the same impact for films in a trench as for blanket deposition. However, the film in a trench is less sensitive to the pressure changes due to conduction limits.

7.4.3 Co-deposition Probability

Steric hindrance occurs when ligands from the precursor fail to react with hydrogen

atoms from the surface and thus remain bonded with the silicon that is deposited on the surface. Ligands may block nearby sites from reacting with the gas phase particles and hinder the deposition process. In the current mechanism, steric hindrance is addressed by co-depositing a ligand group R(s) along with the precursor at probability p_R with a default value of 0.005. In this section, p_R is varied from 0.001 to 0.5, and its impact on the SiO_2 film quality is studied.

The resulting film concentrations and growth rates with varying p_R for blanket deposition are shown in Fig. 7.15. The effect of p_R becomes noticeable only when $p_R \geqslant 0.01$. As p_R increases, both oxygen and silicon concentrations decrease. Also, the R(s) deposition directly affects the η_{Si} since co-deposition occurs during precursor dosing, such that when an R(s) is co-deposited next to a $SiH_2(s)$, it occupies a space that otherwise should be taken by another $SiH_2(s)$ site. Therefore, with a high p_R, it is unlikely to attain 100% $SiH_2(s)$ surface coverage at the end of precursor dosing, which then leads to a lower η_{Si}. However, it is also possible for R(s) to be co-deposited above the primarily deposited $SiH_2(s)$ and occupy voxels in the oxygen layer. With the same SiH_2R_2 flux and the deposition probability of $SiH_2(s)$, higher p_R results in more R(s) in the oxygen layer, thus less OH-Si-OH(s) formation during the plasma exposure.

When $p_R > 0.01$, η_O starts to decrease faster than η_{Si}, leading to an abrupt drop of the η_O/η_{Si} ratio from 1.98 at $p_R = 0.01$ to 1.78 at $p_R = 0.5$. The increase of R(s) concentration also complicates the affected surface components as the film growth becomes highly uneven, which encourages bridging and prompts the formation of vacancies. As p_R increases from 0.05 to 0.5, vacancies increase from 1% to 3%. Note that in many applications, after deposition, the ligand remnants are removed through annealing, such that the final vacancy concentration in the film is $\eta_{Vac}+\eta_R$. In that scenario, the vacancy concentration reaches 2.5% even when $p_R = 0.05$. As described earlier, the growth rate of a film decreases as the surface becomes rougher. Decreases

in both average and instantaneous growth rates occur when p_R increases from 0.001. When $p_R =$ 0.001, the deposition process is almost ideal, with a growth rate of 1 monolayer per cycle. At p_R = 0.5, the instantaneous growth rate decreases to almost 0.4 layer/cycle.

The results of film deposition with a varying p_R in the trench are shown in Fig. 7.16. The result is similar to that for blanket deposition. With an increasing p_R from 0.001 to 0.5, by the end of the 5th cycle, η_O/η_{Si} decreases from 1.88 to 1.68, and η_{Vac} increases from 1% to 3%. Film quality is notably affected by conduction limits in the trench. When p_R is small, insufficient oxidation caused by a low oxidant flux already produces a η_{Vac} = 1%. This high vacancy concentration overshadows the impact of the increasing p_R until it is $\geqslant$ 0.05. The same occurs to the instantaneous film growth rate. Owing to conduction limits, the film growth rate is only 0.8 layer/cycle at the bottom of the trench even with small p_R. A clear decrease of ξ_{ins} occurs only when $p_R \geqslant$ 0.01. Before that, the impact of p_R on growth rate is outweighed by the effects of conduction limits.

Varying p_R affects precursor dosing, which is a thermal process that is not significantly affected by the target feature. Therefore, other than the high vacancy concentration and low instantaneous deposition rate when $p_R < 0.05$, changes of the film properties with a varying p_R when depositing in a trench are quantitatively similar to that for blanket deposition.

Reaction probabilities are not known for these reactions of ROS with co-deposited R(s). Based on analogies to gas phase processes and reaction probabilities for removal of R(s) by O, O(^{1}D) and O$_3$ (reactions 7.6a, b and c) were estimated as 1×10^{-4}, 1×10^{-3}, and 1×10^{-5}. Film concentrations of R(s), vacancies and η_O/η_{Si} with and without oxygen replacement reactions as a function of p_R are shown in Fig. 7.17. These properties do not significantly change with oxygen replacement reactions until $p_R > 0.1$. The oxygen replacement reactions enable more complete

oxidation during plasma exposure, thereby resulting in higher oxygen concentration and higher η_O/η_{Si}. With $p_R = 0.5$, reactions of R(s) with ROS decrease η_R by 2% from 15% to 13%, and η_O/η_{Si} increases from 1.79 to 1.86. With $p_R < 0.1$, there are not enough R(s) deposition on the film to make oxygen replacement reactions important when the plasma exposure time is only 1 s. The average and instantaneous film growth rates with and without the oxygen replacement reactions with varying p_R are shown in Fig. 7.17b. Almost identical film growth rates are obtained.

For small p_R and short plasma exposure time, oxygen replacement reactions with R(s) do not significantly affect the SiO_2 PE-ALD discussed in this chapter. However, these conclusions could certainly change if the reaction probabilities for ROS at low substrate temperature are significantly higher than estimated here.

7.4.4   Aspect Ratio

Conduction limits predominantly affects film deposition in high aspect ratio features. Because conduction limits are significantly affected by the aspect ratio (AR) of the feature, in this section, the AR of a 3D feature is varied, and its impact on film deposition is discussed.

SiO_2 film deposition was first performed in a trench. The width of the trench is 30 nm, the same as that used for the previous investigations. The AR was varied by changing the height of the trench. AR was varied from 2 to 8, meaning the height of the trench was varied from 60 to 240 nm. The concentrations of solid materials in the entire film, as well as the η_O/η_{Si} ratio are shown in Fig. 7.18a. The instantaneous and average film growth rates logged in the bottom of the trench are shown in Fig. 7.18b. Increasing AR increases conduction limits as particles encounter more collisions with walls before reaching the bottom of the feature. This has the most impact on the unstable or excited state reactive species. For example, as recorded in the bottom of a trench, when the aspect ratio increases from 2 to 8, O_2^* flux decreases by a factor of

4.4, from 5.7-1.3 $\times 10^{17}$ cm^{-2}s^{-1} in the first plasma exposure. This reduction of oxidant results in insufficient film oxidation, which then causes a slow film growth rate. In the 5th cycle, the instantaneous growth rate in the bottom of the trench when AR = 8, is 0.69 layers/cycle, only 83% of that when AR = 2 (0.83 layers/cycle). Note that conduction limits only affect film quality in the bottom of the trench. For example, there is a slight decrease instead of an increase of η_{Vac} as AR increases when sampling the entire film, owing to the film deposition in the top of the trench outweighing the effect of film deposition in the bottom. If sampled using the film deposited at the bottom 30 nm of the trench, η_{Vac} increases from 1.3% to 1.5% as the AR increases from 2 to 8.

To further study the impact of aspect ratio on film deposition, a SiO$_2$ film was deposited in a via. A via is a cylindrical connection between two devices located in different layers of an integrated structure. A thin layer of dielectric material is often deposited on the wall of a via as an electrical insulator. The diameter of the via is 30 nm and the height was between 60 to 240 nm, providing an AR between 2 to 8. Because a via is a symmetrical structure, only a quarter of a via was used for the simulation (Fig. 7.19a) in deference to being computationally efficient. A reflective boundary condition was applied to all vertical boundaries. The process flow is the same as depositing in a trench: 0.8 s precursor dosing and 1 s plasma exposure.

The film deposited in a via is reasonably conformal, the structure of a via can still be seen after 5 cycles of deposition. Similar to the deposition in a trench or blanket deposition, in a via, layers deposited in the first several cycles are more uniform, having only sparsely distributed imperfections and misalignments that would affect the deposition of upper layers.

The concentrations of materials and the elementary ratio η_O/η_{Si} at the end of the 5th cycle are shown in Fig. 7.19b. Note that compared to the film deposited in a trench, the film deposited

in a via has a lower η_O/η_{Si} ratio and higher vacancy concentration, indicating a an even more insufficient oxidation process and more porous film structure. This occurs because a via has a higher surface to volume ratio than a trench when their AR is the same. With unbounded front and back sides, a trench of 30 nm (W) $\times$ 120 nm (H) $\times$ 10 nm (D) has a surface to volume ratio of 0.075, while a via with a 30 nm diameter and 120 nm height has a surface to volume ratio of 0.142. Doubling the surface to volume ratio produces more severe conduction limits that restrain the fluxes to the bottom of the feature. For example, with AR = 8, in the first plasma exposure, the O flux at the bottom center of the trench is 9.0×10^{17} cm^{-2}s^{-1}, as opposed to 2.0×10^{17} cm^{-2}s^{-1} in the via. The decrease of flux in the via is even more significant for unstable species such as O$_2^*$, which is 2.0×10^{15} cm^{-2}s^{-1} in the bottom of a via, but 1.1×10^{17} cm^{-2}s^{-1} in the bottom of a trench. Remember that low oxidant fluxes result in insufficient oxidation. At the end of the 5th cycle, at the bottom 30 nm of the feature, a SiO$_2$ film deposited in a trench has a η_O/η_{Si} ratio of 1.79, but the film deposited in a via only has a η_O/η_{Si} ratio of 1.61. The vacancy concentration almost doubles when depositing in a via compared to a trench.

7.5 Concluding Remarks

Plasma enhanced atomic layer deposition (PE-ALD) of SiO$_2$ film on a nm-scale blanket target was investigated using 3-dimensional voxel-based simulation, the MCFPM. The computational investigation was performed at the reactor scale for an Ar/O$_2$ (80/20) capacitively coupled plasma (CCP) using the 2-dimensional hybrid plasma simulator, the HPEM. Fluxes on the wafer, and energy and angular distributions (EADs) of major species obtained from the HPEM were transferred to the MCFPM for feature-scale investigation.

In the base case, 500 W power was applied to the top electrode of the CCP reactor to sustain an Ar/O$_2$ plasma at 2 Torr. The dominant neutrals were O$_2$(a$^1\Delta_g$), O, and O$_2$(b$^1\Sigma_g^+$), all

with close to thermal EADs. The dominant ions, Ar^+ and O_2^+, had incident angle less than 20˚ and peak energy up to 40 eV. Due to the high pressure and highly collisional sheath, most ions had energy less than 20 eV, which is smaller than the sputtering threshold of SiO_2 (30 eV). These, as well as low ion fluxes suggest insignificant impact of ion bombardment damage to the film.

A deposition mechanism of SiO_2 using silicon precursors with two ligand groups and Ar/O_2 plasma was developed. The PE-ALD process consisted of repeated precursor dosing (0.8 s) and plasma exposure (1.0 s). Steric hindrance was addressed by co-depositing a ligand site along with the silicon during precursor dosing at a co-deposition probability p_R. The impact of the insertion of ligand remnants at the early stage of deposition were shown to increase as the film grows thicker. The end result is a disordered film structure and large areas of roughness on the surface above the initial ligand remnant. The roughness on the surface exposes both silicon and oxygen layers to the plasma. Because the silicon precursor cannot directly be deposited on the oxygen sites $O_2(s)$, and because of the low sputtering rate, the surface coverage ratio of $O_2(s)$ increases with time and causes the decrease of the instantaneous film growth rate. Film deposition in a trench follows many of the same trends as blanket deposition. Vacancy concentrations increase while the film growth rate decreases. Due to conduction limits, the film growth rate at the bottom of a trench decreases faster than that for blanket deposition.

The impact of power, pressure and the co-deposition probability of the ligand remnant p_R on the SiO_2 film blanket deposition and a trench were investigated. Varying the power from 400 W to 1 kW, showed no obvious changes of IEADs and NEADs due to the highly collisional sheath at 2 Torr. With a plasma exposure time of 1.0 s, the film growth is found to be almost self-limiting. Therefore, neither the film concentration nor the growth rate was significantly

sensitive to variations of input power for blanket deposition. However, conduction limits do restrain the O_2^* flux in a trench, making the growth rate and elementary ratio η_O/η_{Si} sensitive to the change of O flux.

Varying pressure was found to significantly affect film quality for blanket deposition. Decreasing pressure resulted in a less collisional sheath and a longer ion mean free path. As a result, when the pressure is 0.5 Torr, the peak ion energy reaches 50 eV and sputtering rates increase. Consequently, using lower pressure during plasma exposure promotes the production of vacancies and slows film growth. However, when depositing in a trench, conduction limits buffer the impact of a varying of pressure. Both the material concentration and growth rate experience smaller variation with pressure compared to blanket deposition.

Varying the co-deposition probability of a ligand group has similar effect to blanket deposition as in a trench, due to the fact that it affects the film deposition through precursor dosing, which is a thermal process. The co-deposition of ligand group probability p_R was increased from 0.001 to 0.5. At low $p_R < 0.05$ the film is uniform and conformal. A high $p_R \geq$ 0.05 produces disordered and rough films. If annealing is used to remove ligand remnants after film deposition, the sum of vacancy and ligand concentrations translate to the vacancy concentration in the final product. When $p_R = 0.05$, at the end of the 5th cycle, this value reaches 2.5% for blanket deposition and 3.2% when depositing in a trench.

Finally, the effect of aspect ratio (AR) on film deposition when depositing in a trench and a via was discussed. For both cases, increasing AR leads to a decrease of oxidant fluxes in the bottom of the feature, which lowers film growth rate and causes porous film structure. However, for the same AR, a via has a bigger surface to volume ratio when the diameter of a via equals the width of a trench. Therefore, conduction limits are more significant in a via, which suggests a

241

longer period for self-limited deposition in a via.

To conclude, due to conduction limits, deposition in different structures depend on different species. The O radical is the dominant oxidant in a 3-dimensional feature such as a trench or a via, while both O and O_2^* are important for blanket deposition. The effect of power on PE-ALD is insignificant with a sufficiently long plasma exposure time. Sputtering can still be a major concern when the pressure is lower than 2.0 Torr. Ligand remnants in the film can greatly affect the film quality. With a co-deposition probability >5%, the vacancy concentration of the final product can reach more than 2% for blanket deposition and more than 3% in a trench. In summary, high pressure (> 1.0 Torr) and low p_R (< 0.05) are desired for the PE-ALD of SiO_2 films.

The results discussed in this chapter should help guide the design of SiO_2 PE-ALD processes. These results suggest that it is important to reduce ligand remnants on the surface after precursor dosing, especially in the early stage of the deposition. The roughness that remnant ligand groups produce starting in the first several layers enlarges as the film grows. To deposit a uniform and dense film, surface reactions during each step (precursor dosing and plasma exposure) should reach the stage of being self-limiting, which is achieved by employing long cycles and high reactants fluxes. Longer cycles are not necessarily desirable in high volume manufacturing.

In practice, the quality of films is gauged by the wet etch rate (WER). A high WER infers a less dense film, a high vacancy concentration and thus a poor film quality. Based on the simulation results, the WER is expected to increase with decreasing pressure (from 2 Torr), increasing ligand remnant density, and increasing aspect ratio.

Table II. **Surface Reaction Mechanism for PE-ALD of SiO₂ Using Ar/O₂ Plasma as Oxidation Agent and BTBAS as Si Precursor**

Gas Phase Species		Notes
Ions or excited states, hot neutrals, and neutral partners	Ar^+, Ar_2^+, $Ar(h)$, Ar O_2^+, $O_2(h)$, O_2 O^+, $O(h)$, O O_2^*, O_2 O^*, O O_3	a)
Precursor	SiH_2R_2	b)
Sputtered materials and deposition by-products	SiH_2, SiH, Si, OH, R, HR, H_2O	
Surface Sites		
Silicon layer	$SiH_2(s)$, $SiH(s)$, $Si(s)$	c)
Oxygen layer	$O_2(s)$, $O(s)$, $OH-Si-OH(s)$, $OH-Si-H(s)$, $OH-Si(s)$, $O-Si-H(s)$	c)

a) O_2^* denotes $O_2(a^1\Delta_g)$ and $O_2(b^1\Sigma_g^+)$. O^* denotes $O(^1D)$ and $O(^1S)$.

b) R represents ligand group from silicon precursor, in the case of BTBAS, R denotes $[NH(C_4H_9)]$- group.

c) SiO_2 is represented by a $Si(s)$ voxel connected to two $O_2(s)$ voxels. Ideally, SiO_2 film consists of staggered layers of $Si(s)$ (silicon layer) and $O_2(s)$ (oxygen layer). x-Si-y(s) represents two sites connected to $Si(s)$ with this $Si(s)$ not included in this voxel.

Reactions[a]	po[b]	$E_{th}(eV)$[b]	$E_r(eV)$[b]	Notes
Initial deposition of SiH₂R₂				
$W(s) + SiH_2R_2 \rightarrow W(s) + SiH_2(s) + 2HR$	0.01			c)
SiH₂R₂ deposition on hydroxyl-rich surface				
$OH-Si-OH(s) + SiH_2R_2 \rightarrow O_2(s) + SiH_2(s) + 2HR$	0.01			
$OH-Si-H(s) + SiH_2R_2 \rightarrow O(s) + SiH_2(s) + 2HR$	0.01			
$OH-Si(s) + SiH_2R_2 \rightarrow O(s) + SiH_2(s) + HR$	0.005			d)
$O-Si-H(s) + SiH_2R_2 \rightarrow O(s) + SiH_2(s) + HR$	0.005			d)
$OH-Si-O(s) + SiH_2R_2 \rightarrow O_2(s) + SiH_2(s) + HR$	0.005			d)
Oxidation of surface sites				
$SiH_2(s) + O \rightarrow Si(s) + OH-Si-H(s)$	0.01			
$SiH_2(s) + O^* \rightarrow Si(s) + OH-Si-H(s)$	0.015			
$SiH_2(s) + O_3 \rightarrow Si(s) + OH-Si-H(s) + O_2$	0.015			
$SiH_2(s) + O^+ \rightarrow Si(s) + OH-Si-H(s)$	0.015			
$SiH_2(s) + O_2^* \rightarrow Si(s) + OH-Si-OH(s)$	0.015			

$SiH_2(s) + O_2^+ \rightarrow Si(s) + OH\text{-}Si\text{-}OH(s)$	0.015			
$SiH(s) + O \rightarrow Si(s) + O\text{-}Si\text{-}H(s)$	0.015			
$SiH(s) + O \rightarrow Si(s) + OH\text{-}Si(s)$	0.01			
$SiH(s) + O^* \rightarrow Si(s) + O\text{-}Si\text{-}H(s)$	0.02			
$SiH(s) + O^* \rightarrow Si(s) + OH\text{-}Si(s)$	0.015			
$SiH(s) + O_3 \rightarrow Si(s) + O\text{-}Si\text{-}H(s) + O_2$	0.002			
$SiH(s) + O_3 \rightarrow Si(s) + OH\text{-}Si(s) + O_2$	0.015			
$SiH(s) + O^+ \rightarrow Si(s) + O\text{-}Si\text{-}H(s)$	0.02			
$SiH(s) + O^+ \rightarrow Si(s) + OH\text{-}Si(s)$	0.015			
$SiH(s) + O_2^* \rightarrow Si(s) + OH\text{-}Si\text{-}O(s)$	0.02			
$SiH(s) + O_2^+ \rightarrow Si(s) + OH\text{-}Si\text{-}O(s)$	0.02			
$SiH(s) + OH \rightarrow Si(s) + OH\text{-}Si\text{-}H(s)$	0.02			
$OH\text{-}Si\text{-}H(s) + O \rightarrow OH\text{-}Si\text{-}OH(s)$	0.01			
$OH\text{-}Si\text{-}H(s) + O^* \rightarrow OH\text{-}Si\text{-}OH(s)$	0.015			
$OH\text{-}Si\text{-}H(s) + O_3 \rightarrow OH\text{-}Si\text{-}OH(s) + O_2$	0.015			
$OH\text{-}Si\text{-}H(s) + O^+ \rightarrow OH\text{-}Si\text{-}OH(s)$	0.02			
$Si(s) + O \rightarrow Si(s) + O(s)$	10^{-4}			e)
$Si(s) + O^* \rightarrow Si(s) + O(s)$	2×10^{-4}			e)
$Si(s) + O^* \rightarrow Si(s) + O(s) + O_2$	2×10^{-4}			e)
$Si(s) + O^+ \rightarrow Si(s) + O(s)$	2×10^{-4}			e)
$Si(s) + O_2^* \rightarrow Si(s) + O_2(s)$	2×10^{-4}			e)
$Si(s) + O_2^+ \rightarrow Si(s) + O_2(s)$	2×10^{-4}			e)
$Si(s) + OH \rightarrow Si(s) + OH\text{-}Si(s)$	0.001			
$O(s) + O \rightarrow O_2(s)$	0.01			
$O(s) + O^* \rightarrow O_2(s)$	0.015			
$O(s) + O_3 \rightarrow O_2(s) + O_2$	0.015			
$O(s) + O^+ \rightarrow O_2(s)$	0.015			
$O(s) + O_2^* \rightarrow O_2(s) + O$	0.001			
$O(s) + O_2^+ \rightarrow O_2(s) + O(h)$	0.005			
$O(s) + OH \rightarrow OH\text{-}Si\text{-}O(s)$	0.03			
$OH\text{-}Si(s) + O \rightarrow OH\text{-}Si\text{-}O(s)$	0.015			
$OH\text{-}Si(s) + O^* \rightarrow OH\text{-}Si\text{-}O(s)$	0.02			
$OH\text{-}Si(s) + O_3 \rightarrow OH\text{-}Si\text{-}O(s) + O_2$	0.02			
$OH\text{-}Si(s) + O^+ \rightarrow OH\text{-}Si\text{-}O(s)$	0.02			
$OH\text{-}Si(s) + O_2^* \rightarrow OH\text{-}Si\text{-}O(s) + O$	0.001			
$OH\text{-}Si(s) + O_2^+ \rightarrow OH\text{-}Si\text{-}O(s) + O(h)$	0.005			
$OH\text{-}Si(s) + OH \rightarrow OH\text{-}Si\text{-}OH(s)$	0.03			
$O\text{-}Si\text{-}H(s) + O \rightarrow OH\text{-}Si\text{-}O(s)$	0.01			
$O\text{-}Si\text{-}H(s) + O^* \rightarrow OH\text{-}Si\text{-}O(s)$	0.015			
$O\text{-}Si\text{-}H(s) + O_3 \rightarrow OH\text{-}Si\text{-}O(s) + O_2$	0.015			
$O\text{-}Si\text{-}H(s) + O^+ \rightarrow OH\text{-}Si\text{-}O(s)$	0.015			
Sputtering by ion and hot neutrals				

$SiH_2(s) + I^+ \rightarrow SiH_2 + I(h)$	0.9	35	140	g)
$SiH(s) + I^+ \rightarrow SiH + I(h)$	0.9	35	140	g)
$Si(s) + I^+ \rightarrow Si + I(h)$	0.9	35	140	g)
$OH\text{-}Si\text{-}OH(s) + I^+ \rightarrow OH\text{-}Si(s) + OH + I(h)$	0.9	30	120	g)
$OH\text{-}Si\text{-}H(s) + I^+ \rightarrow OH + H + I(h)$	0.9	30	120	f), g)
$O\text{-}Si\text{-}H(s) + I^+ \rightarrow O + H + I(h)$	0.9	30	120	f), g)
$OH\text{-}Si(s) + I^+ \rightarrow OH + I(h)$	0.9	30	120	g)
$OH\text{-}Si\text{-}O(s) + I^+ \rightarrow OH\text{-}Si(s) + O + I(h)$	0.45	30	120	g)
$OH\text{-}Si\text{-}O(s) + I^+ \rightarrow O(s) + OH + I(h)$	0.45	30	120	g)
$O(s) + I^+ \rightarrow O + I(h)$	0.9	30	120	g)
$O_2(s) + I^+ \rightarrow O(s) + O + I(h)$	0.9	30	120	g)
$R(s) + I^+ \rightarrow R + I(h)$	0.9	40	160	g)
R(s) removal by reactive oxygen species				
$R(s) + O \rightarrow O(s) + R$	10^{-4}			
$R(s) + O^* \rightarrow O(s) + R$	10^{-3}			
$R(s) + O_3 \rightarrow O(s) + R + O_2$	10^{-5}			
Redeposition of sputtered species				
$SiH(s) + SiH_2 \rightarrow SiH(s) + SiH_2$	0.03			
$SiH(s) + SiH \rightarrow SiH(s) + SiH(s)$	0.03			
$SiH(s) + Si \rightarrow SiH(s) + Si(s)$	0.03			
$SiH(s) + R \rightarrow SiH(s) + R(s)$	0.01			
$Si(s) + SiH_2 \rightarrow Si(s) + SiH_2(s)$	0.001			e)
$Si(s) + SiH \rightarrow Si(s) + SiH(s)$	0.001			e)
$Si(s) + Si \rightarrow Si(s) + Si(s)$	0.001			e)
$Si(s) + R \rightarrow Si(s) + R(s)$	0.001			e)
$O(s) + SiH_2 \rightarrow O(s) + SiH_2(s)$	0.03			
$O(s) + SiH \rightarrow O(s) + SiH(s)$	0.03			
$O(s) + Si \rightarrow O(s) + Si(s)$	0.03			
$O(s) + R \rightarrow O(s) + R(s)$	0.01			
$O_2(s) + SiH_2 \rightarrow O_2(s) + SiH_2(s)$	0.03			
$O_2(s) + SiH \rightarrow O_2(s) + SiH(s)$	0.03			
$O_2(s) + Si \rightarrow O_2(s) + Si(s)$	0.03			
$O_2(s) + R \rightarrow O_2(s) + R(s)$	0.01			
$OH\text{-}Si(s) + SiH_2 \rightarrow OH\text{-}Si(s) + SiH_2(s)$	0.03			
$OH\text{-}Si(s) + SiH \rightarrow OH\text{-}Si(s) + SiH(s)$	0.03			
$OH\text{-}Si(s) + Si \rightarrow OH\text{-}Si(s) + Si(s)$	0.03			
$O\text{-}Si\text{-}H(s) + SiH_2 \rightarrow O\text{-}Si\text{-}H(s) + SiH_2(s)$	0.03			
$O\text{-}Si\text{-}H(s) + SiH \rightarrow O\text{-}Si\text{-}H(s) + SiH(s)$	0.03			
$O\text{-}Si\text{-}H(s) + Si \rightarrow O\text{-}Si\text{-}H(s) + Si(s)$	0.03			
$OH\text{-}Si\text{-}O(s) + SiH_2 \rightarrow OH\text{-}Si\text{-}O(s) + SiH_2(s)$	0.03			
$OH\text{-}Si\text{-}O(s) + SiH \rightarrow OH\text{-}Si\text{-}O(s) + SiH(s)$	0.03			
$OH\text{-}Si\text{-}O(s) + Si \rightarrow OH\text{-}Si\text{-}O(s) + Si(s)$	0.03			

Reaction				
OH-Si-O(s) + R → OH-Si-O(s) + R(s)	0.01			
Oxidation by hydroxyl radical				
$SiH_2(s)$ + OH → SiH(s) + H_2O	0.01			
SiH(s) + OH → Si(s) + H_2O	0.01			
OH-Si-OH(s) + OH → OH-Si-O(s) + H_2O	0.01			
OH-Si-H(s) + OH → O-Si-H(s) + H_2O	0.01			
OH-Si-H(s) + OH → OH-Si(s) + H_2O	0.01			
O-Si-H(s) + OH → O(s) + H_2O	0.01			
OH-Si-O(s) + OH → O_2(s) + H_2O	0.01			
Recombination by sputtered ligand group				
$SiH_2(s)$ + R → SiH(s) + HR	0.01			
SiH(s) + R → Si(s) + HR	0.01			
OH-Si-OH(s) + R → OH-Si-O(s) + HR	0.01			
OH-Si-H(s) + R → O-Si-H(s) + HR	0.01			
OH-Si-H(s) + R → OH-Si(s) + HR	0.01			
O-Si-H(s) + R → O(s) + HR	0.01			
Oxygen Recombination				
O(s) + O → O_2	6×10^{-5}			
O(s) + O^* → O_2	10^{-4}			
O(s) + O_3 → O_2 + O_2	10^{-4}			
O(s) + O^+ → O_2	10^{-4}			
O_2(s) + O → O(s) + O_2	6×10^{-5}			
O_2(s) + O^* → O(s) + O_2	10^{-4}			
O_2(s) + O_3 → O(s) + O_2 + O_2	10^{-4}			
O_2(s) + O^+ → O(s) + O_2	10^{-4}			
O-Si-H(s) + O → O_2 + H	6×10^{-5}			f)
O-Si-H(s) + O^* → O_2 + H	10^{-4}			f)
O-Si-H(s) + O_3 → O_2 + O_2 + H	10^{-4}			f)
O-Si-H(s) + O^+ → O_2 + H	10^{-4}			f)
OH-Si-O(s) + O → OH-Si(s) + O_2	6×10^{-5}			
OH-Si-O(s) + O^* → OH-Si(s) + O_2	10^{-4}			
OH-Si-O(s) + O_3 → OH-Si(s) + O_2 + O_2	10^{-4}			
OH-Si-O(s) + O^+ → OH-Si(s) + O_2	10^{-4}			
Dissociation of O_3				
Surface(s) + O_3 → Surface(s) + O + O_2	0.05			h)

a)   All ions neutralize on surfaces, returning to gas phase as their hot neutral partner. Ions and their hot neutral partners have the same surface reactions with the same probability. Only surface reactions for ions are shown in the table. All such reactions (with the exception of neutralization) should be duplicated for the ion's hot neutral partner. Ar_2^+ is reflected from the surface as two Ar hot neutrals.

b)   If E_{th} and E_r are blank, the reaction has no energy dependence and the probability of the reaction is a constant, p_0. If E_{th} and E_r have non-zero values, the reaction has an energy

dependent probability. When the probability of reaction is less than unity, the remaining probability is allocated to no energy-dependent reactions.

c) W(s) is the ideal surface upon which the SiO_2 PE-ALD is performed, it provides sufficient hydroxyl sites for the first-step silicon precursor dosing.

d) The ligand group remnants R(s) during precursor dosing is addressed using co-deposition probability. Extra n_R voxel is deposited with the silicon, at a deposition probability p_R.

e) Oxidation probability of Si(s) is reduced to avoid the excessive oxidation when more than one surfaces of the Si(s) voxel is exposed to the plasma. The adjustment is only made for Si(s) as it is the final product upon which a high-density reactant (O) can be deposited.

f) The hydrogen site is removed along with the oxygen or hydroxyl sites in an sputtering and oxygen recombination process due to the lack of information of the neighbors of the direct surface reactant. This has minor effect in the current work due to the low concentrations of OH-Si-H(s) and O-Si-H(s) (< 1%), and low etching probability. One method to improve the accuracy of the regarding surface reactions is to check the immediate neighbors of the surface reactant and transfer hydrogen reminant to the nearby Si(s) or SiH(s) to form SiH(s) or SiH_2(s) accordingly.

g) Reaction with physical sputtering angular dependence.

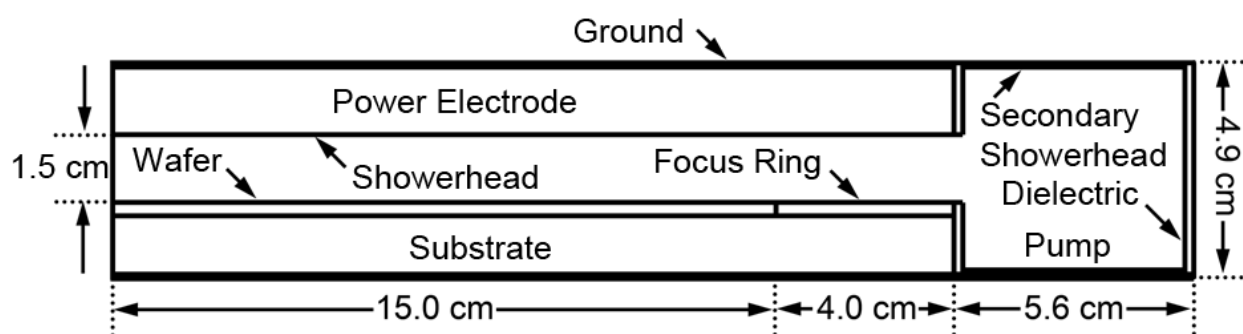h) Surface(s) represents any solid-state surface site.

7.6 Figures

Fig. 7.1 Geometry of the reactor. 500 W (10 MHz), 2 Torr, primary gas inlet: Ar/O$_2$ (4/1), 5 slm; secondary gas inlet: O$_2$, 6 slm.
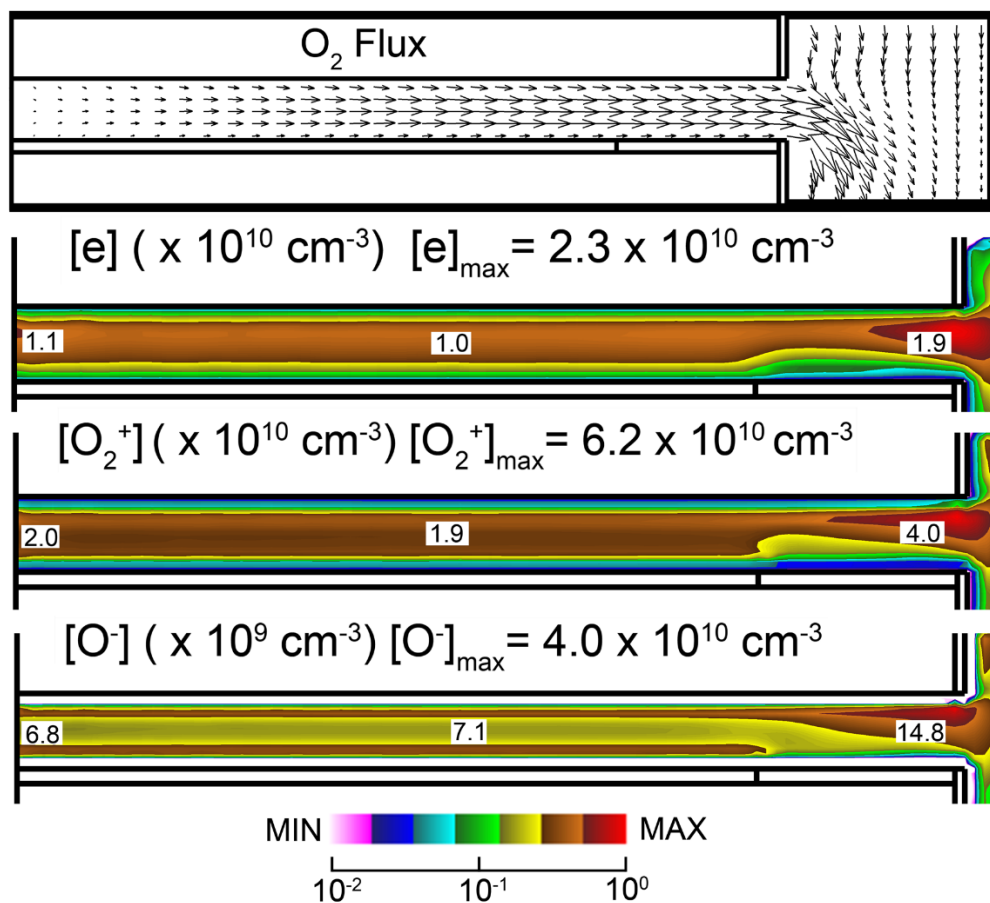
Fig. 7.2 O$_2$ flux, 2-dimensional distribution of electron density, O$_2^+$ density and O$^-$ density. 500 W (10 MHz), 2 Torr, primary gas inlet: Ar/O$_2$ (4/1), 5 slm; secondary gas inlet: O$_2$, 6 slm.
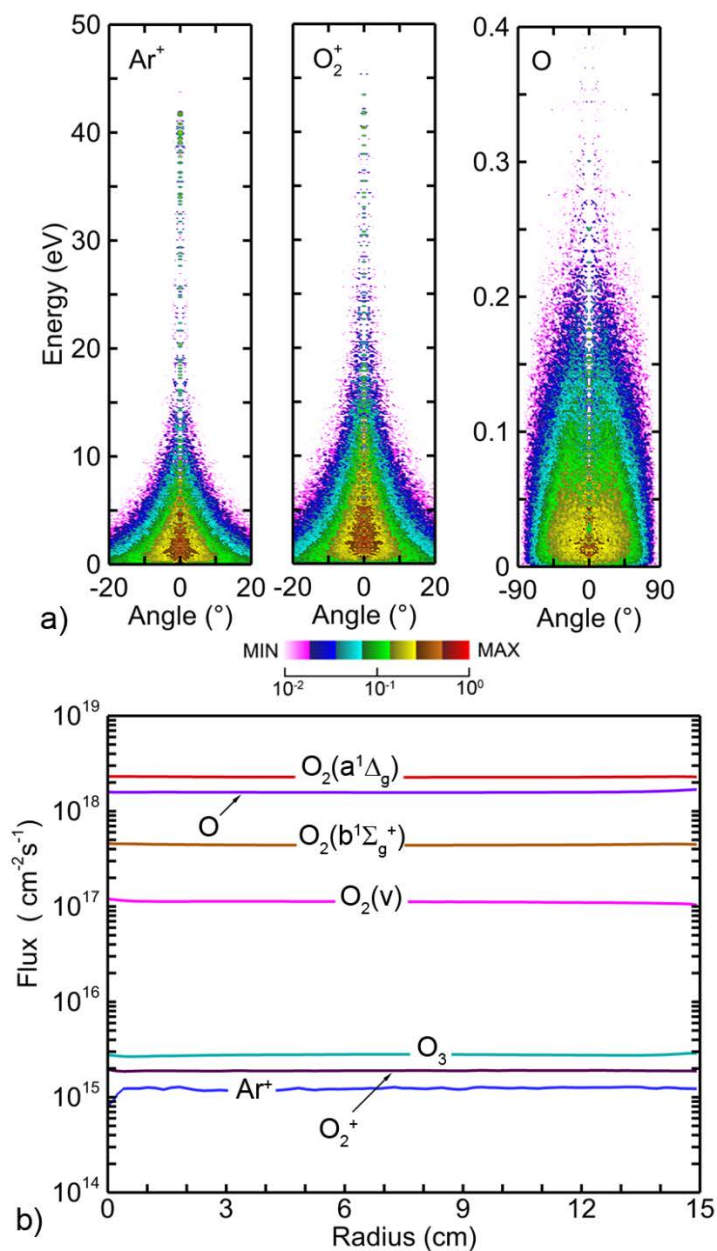
Fig. 7.3 a) Energy and angular distributions (EADs) of dominant cations Ar^+ and O_2^+, and radical O. b) Fluxes of major species across half-wafer. 500 W (10 MHz), 2 Torr, primary gas inlet: Ar/O_2 (4/1), 5 slm; secondary gas inlet: O_2, 6 slm.
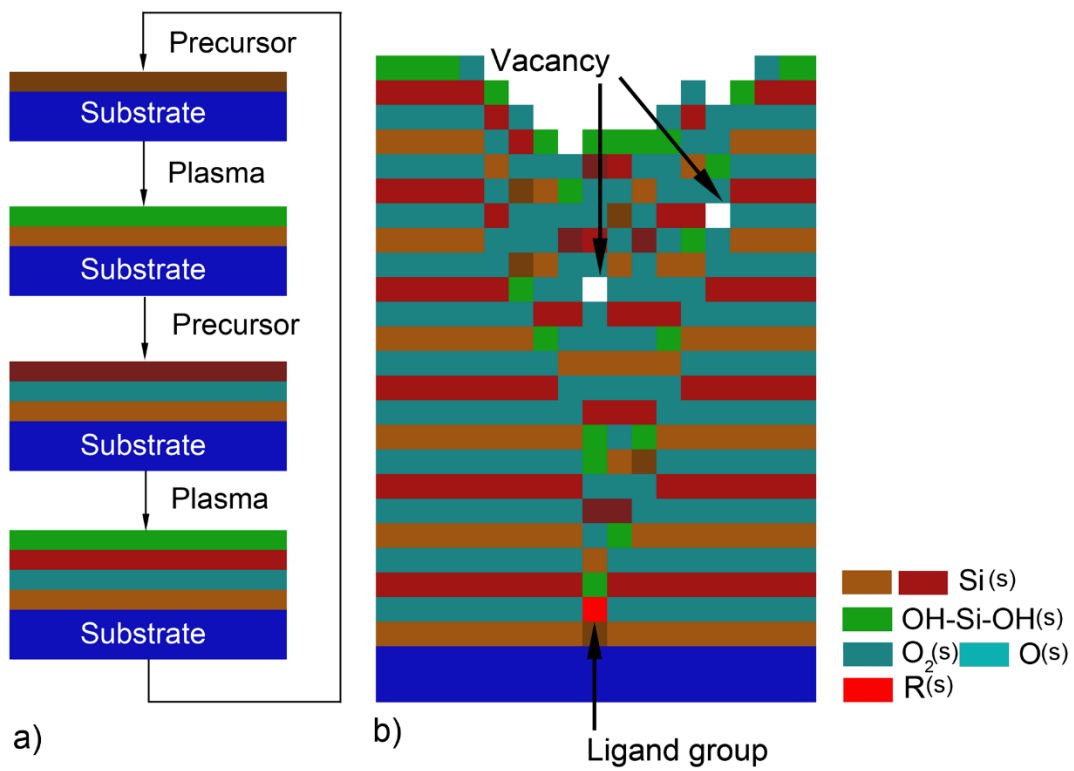
Fig. 7.4 a) Flowchart of SiO$_2$ PE-ALD process and b) impact of ligand remnant on the upper layer of SiO$_2$ film deposition.
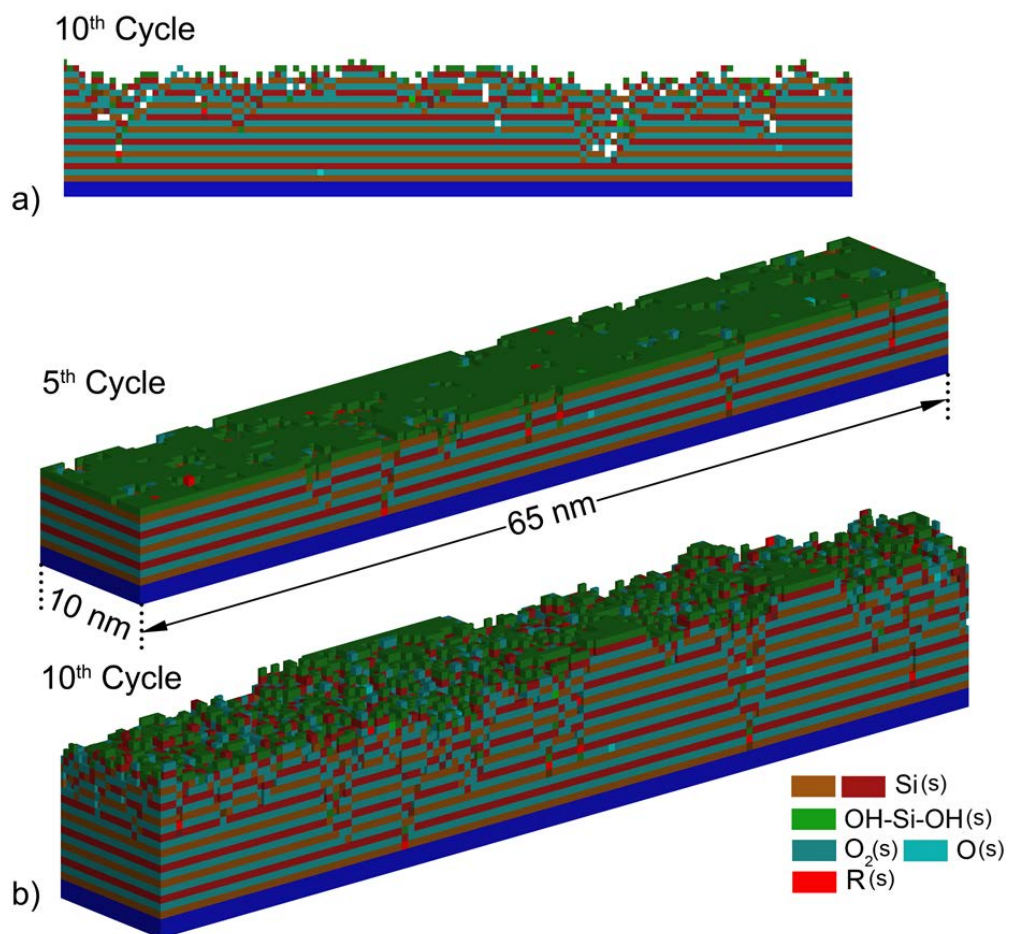
Fig. 7.5 a) 2-dimensional film profile of the middle slice at $y = 5$ nm and b) 3-dimensional profile of the SiO$_2$ film at the end of 5th and 10th cycle.
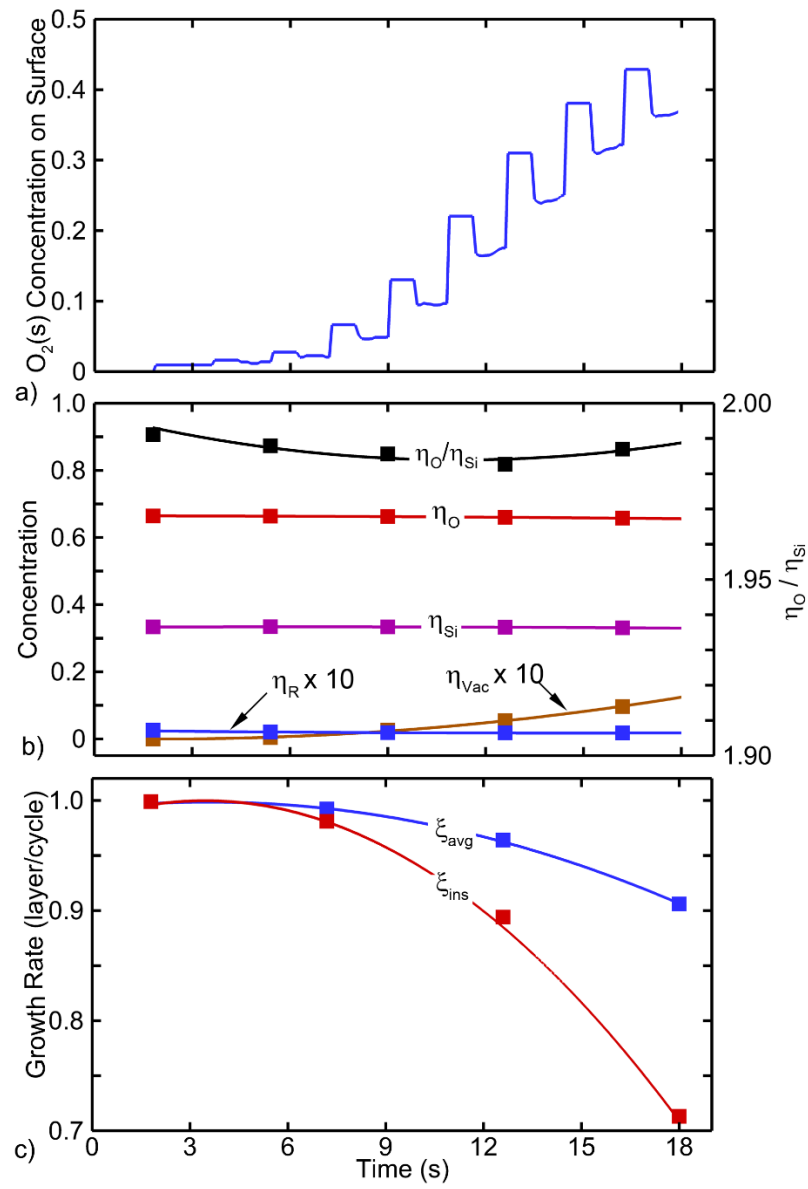
Fig. 7.6 a) $O_2(s)$ sites surface coverage ratio, b) concentrations of oxygen, silicon, vacancy and ligand group in entire film and oxygen to silicon ratio and c) time-averaged and instantaneous film growth rate using the default setup. 0.5 nm/cell, 1 nm per SiO_2 layer, blanket deposition.
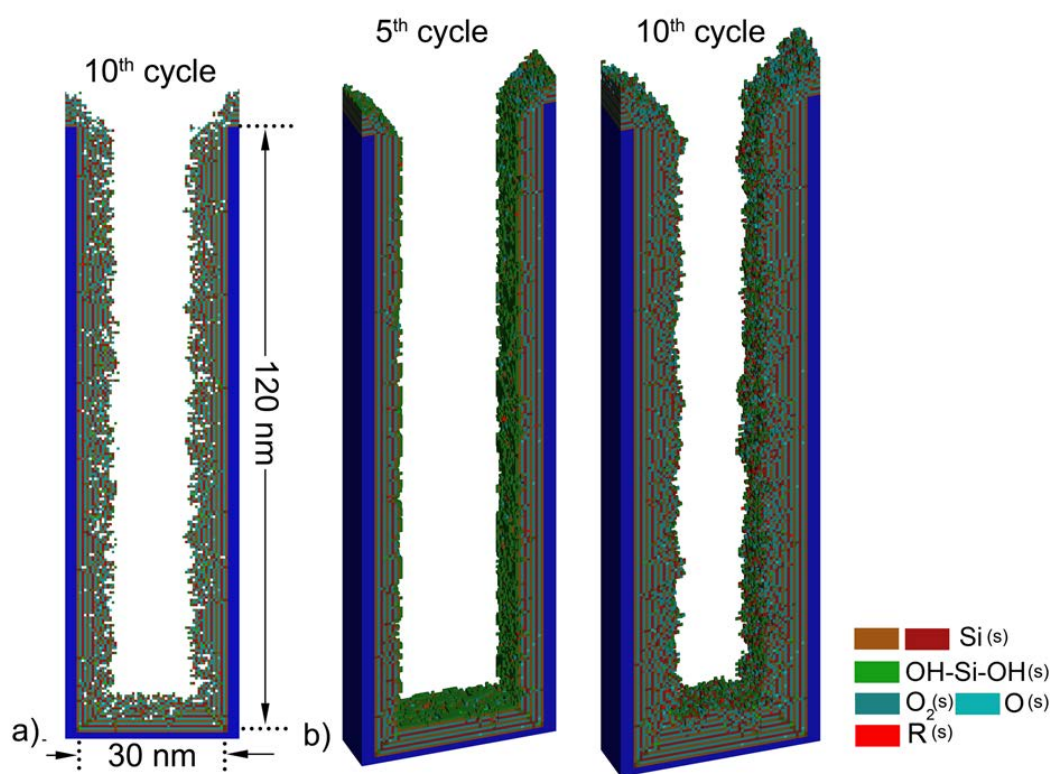
Fig. 7.7 a) 2D film profile at the end of the 10th cycle and b) 3D film profiles at the end of the 5th and 10th cycle when depositing in a trench of 30 nm (W) $\times$ 120 nm (H) $\times$ 10 nm (D).

Fig. 7.8 a) Concentrations of oxygen, silicon, vacancy and ligand group in entire film and oxygen to silicon ratio and c) time-averaged and instantaneous film growth rate at the bottom of the trench. 0.5 nm/cell, 1 nm per SiO_2 layer, trench deposition.
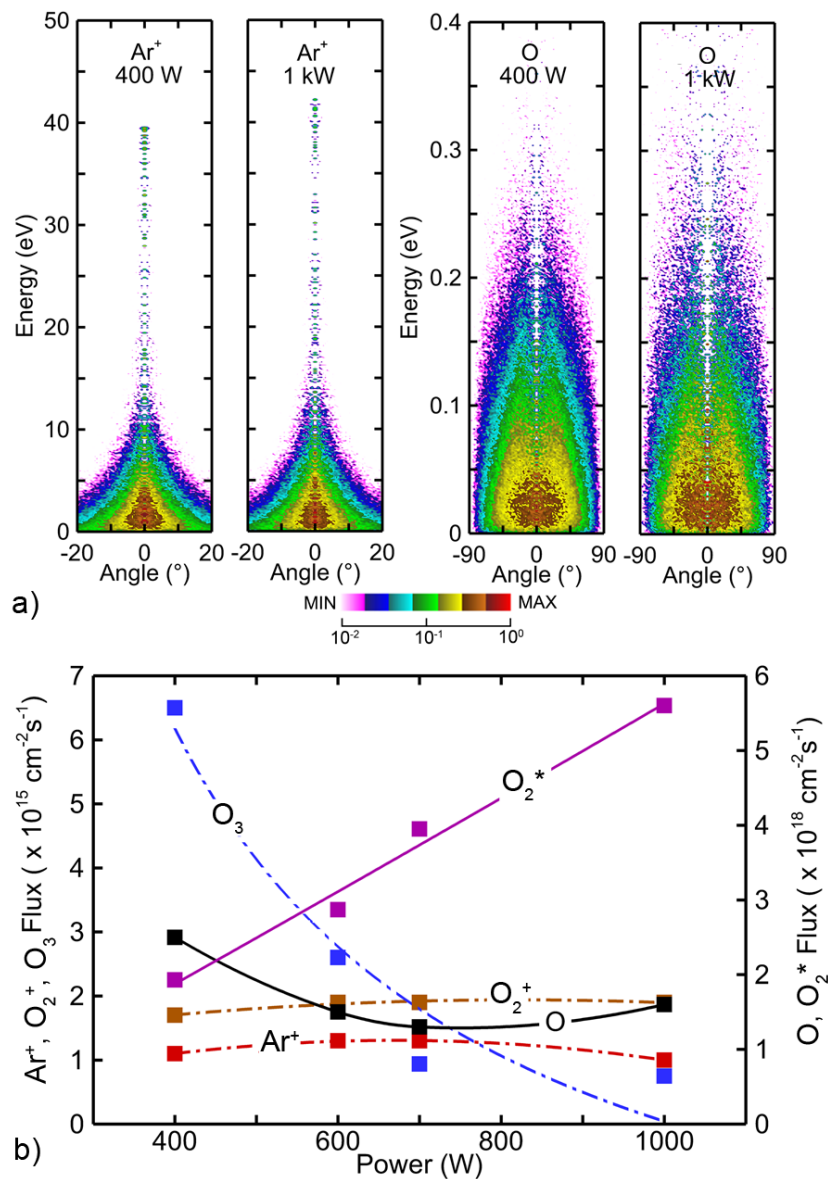
Fig. 7.9 a) Energy and angular distributions (EADs) of Ar⁺ and O when power is 400 W and 1 kW and b) fluxes of major species at mid-radius of wafer. 10 MHz, 2 Torr, primary gas inlet: Ar/O_2 (4/1), 5 slm; secondary gas inlet: O_2, 6 slm.

Fig. 7.10 a) Concentrations of oxygen, silicon, vacancy, and ligand groups in the entire film and oxygen to silicon ratio, and b) time-averaged and instantaneous film growth rate with varying power. Data are from 5th cycle. 10 MHz, 2 Torr, primary gas inlet: Ar/O$_2$ (4/1), 5 slm; secondary gas inlet: O$_2$, 6 slm. 0.5 nm/cell, 1 nm per SiO$_2$ layer.
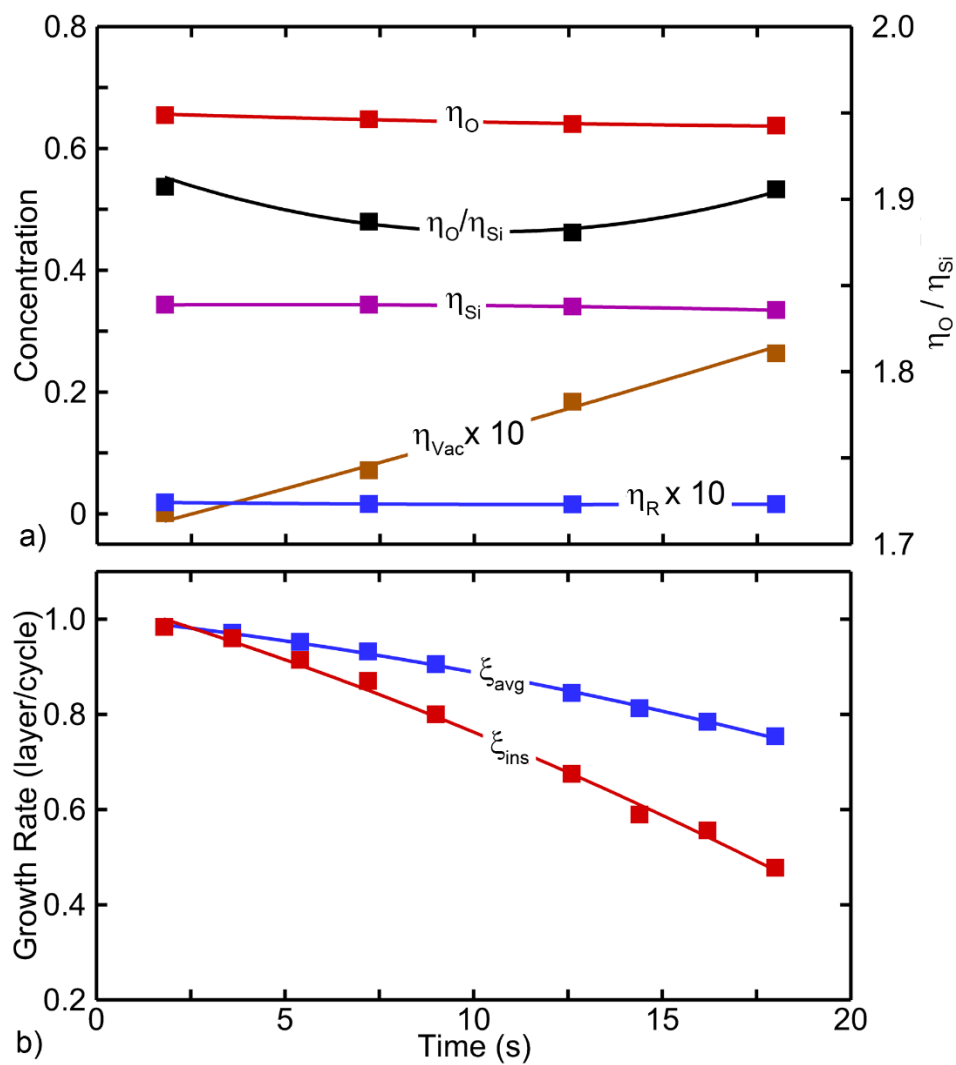
Fig. 7.11 a) Concentrations of oxygen, silicon, vacancy, and ligand groups in the entire film and oxygen to silicon ratio, and b) time-averaged and instantaneous film growth rate at the bottom of a trench with varying power. Data are from 5th cycle. 10 MHz, 2 Torr, primary gas inlet: Ar/O_2 (4/1), 5 slm; secondary gas inlet: O_2, 6 slm. 0.5 nm/cell, 1 nm per SiO_2 layer.

Fig. 7.12 a) Energy and angular distributions (EADs) of Ar^+ and O when pressure is 0.5 and 2 Torr, b) energy distribution function of all cations and c) fluxes of major species at mid-radius of wafer. 500 W, 10 MHz, primary gas inlet: Ar/O_2 (4/1), 5 slm; secondary gas inlet: O_2, 6 slm.

Fig. 7.13 a) Concentrations of oxygen, silicon, vacancy, and ligand groups in the entire film and oxygen to silicon ratio, and b) time-averaged and instantaneous film growth rate with varying pressure. Data are from 5th cycle. 10 MHz, primary gas inlet: Ar/O_2 (4/1), 5 slm; secondary gas inlet: O_2, 6 slm. 0.5 nm/cell, 1 nm per SiO_2 layer.
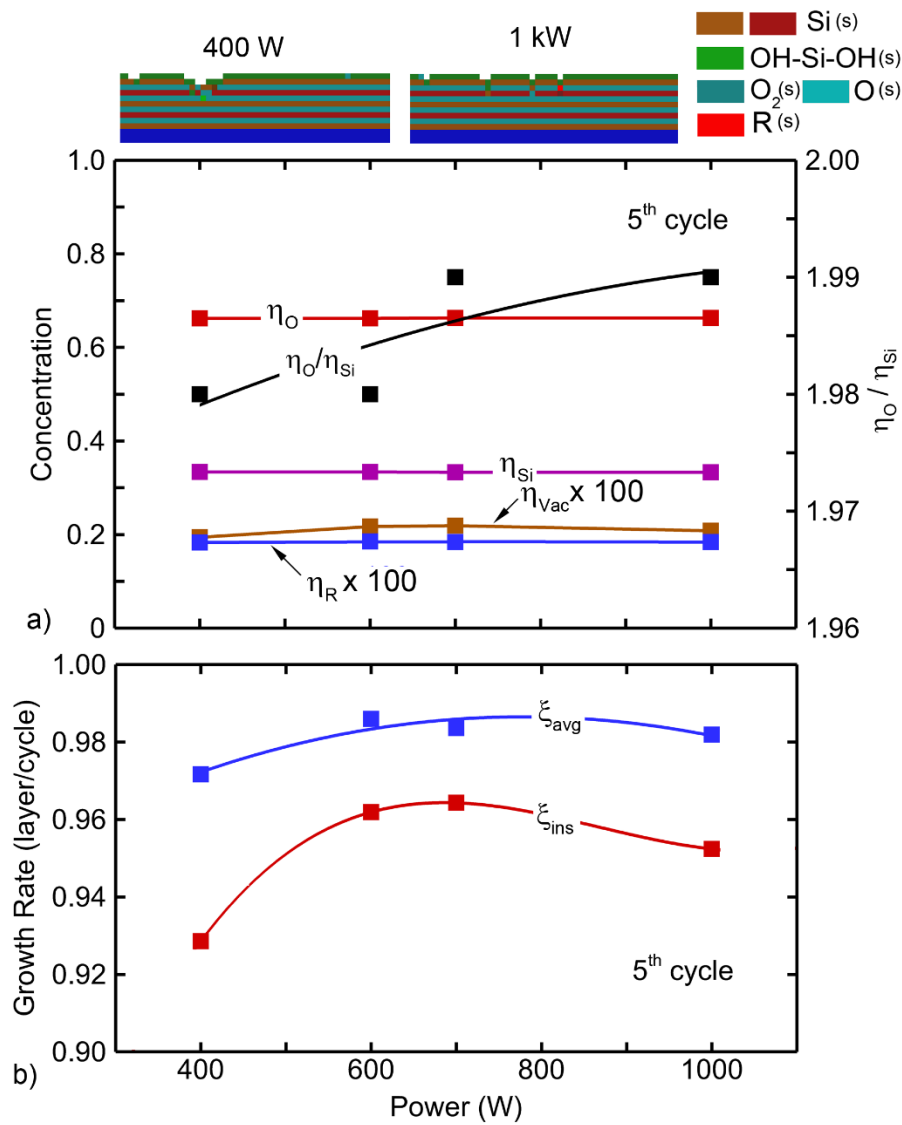
Fig. 7.14 a) Concentrations of oxygen, silicon, vacancy, and ligand groups in the entire film and oxygen to silicon ratio, and b) time-averaged and instantaneous film growth rate at the bottom of a trench with varying pressure. Data are from 5th cycle. 10 MHz, primary gas inlet: Ar/O$_2$ (4/1), 5 slm; secondary gas inlet: O$_2$, 6 slm. 0.5 nm/cell, 1 nm per SiO$_2$ layer.
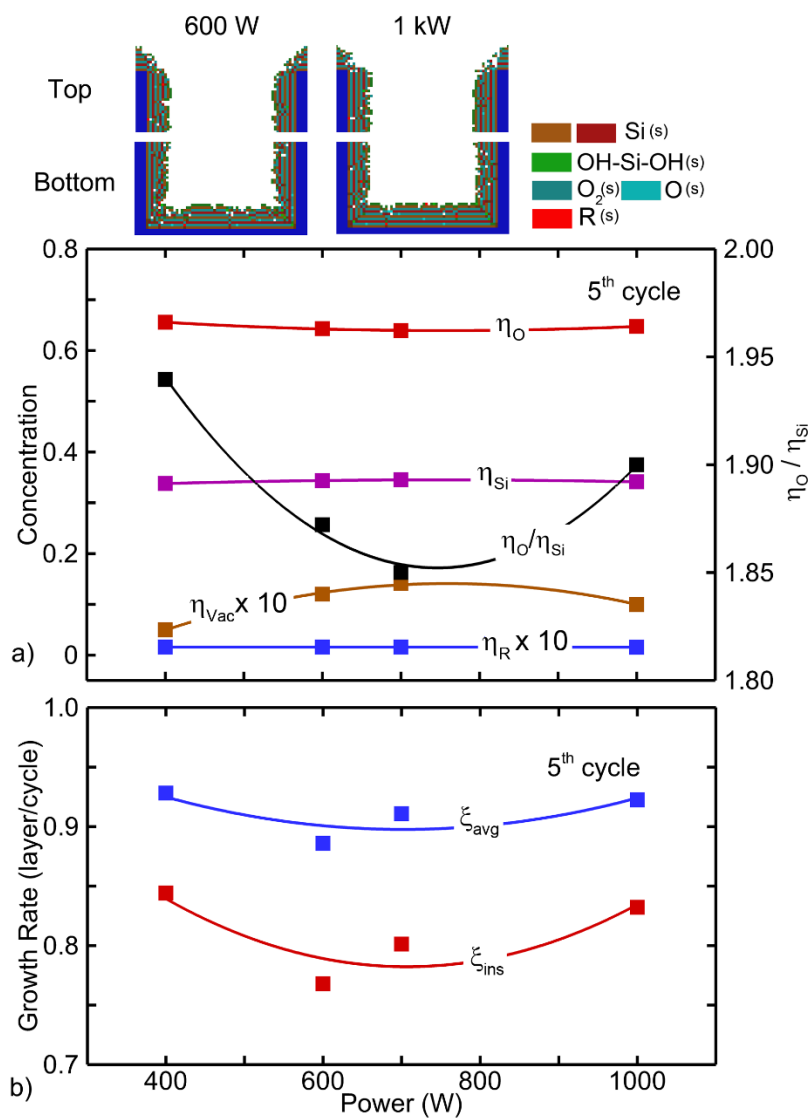
Fig. 7.15 a) Concentrations of oxygen, silicon, vacancy, and ligand groups in the entire film and oxygen to silicon ratio, and b) time-averaged and instantaneous film growth rate with varying co-deposition probability p_R. Data are from 5th cycle. 500 W, 10 MHz, 2 Torr, primary gas inlet: Ar/O$_2$ (4/1), 5 slm; secondary gas inlet: O$_2$, 6 slm. 0.5 nm/cell, 1 nm per SiO$_2$ layer.

Fig. 7.16 a) Concentrations of oxygen, silicon, vacancy, and ligand groups in the entire film and oxygen to silicon ratio, and b) time-averaged and instantaneous film growth rate at the bottom of a trench with varying co-deposition probability p_R. Data are from 5th cycle. 500 W, 10 MHz, 2 Torr, primary gas inlet: Ar/O_2 (4/1), 5 slm; secondary gas inlet: O_2, 6 slm. 0.5 nm/cell, 1 nm per SiO_2 layer.
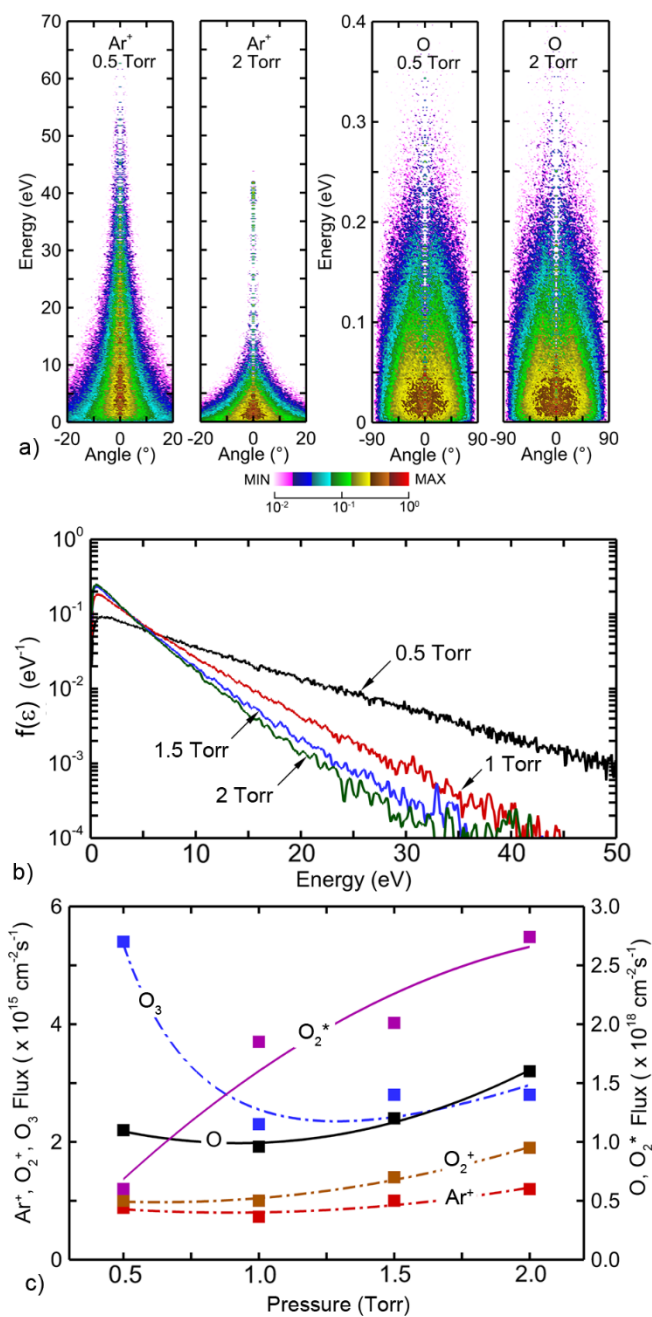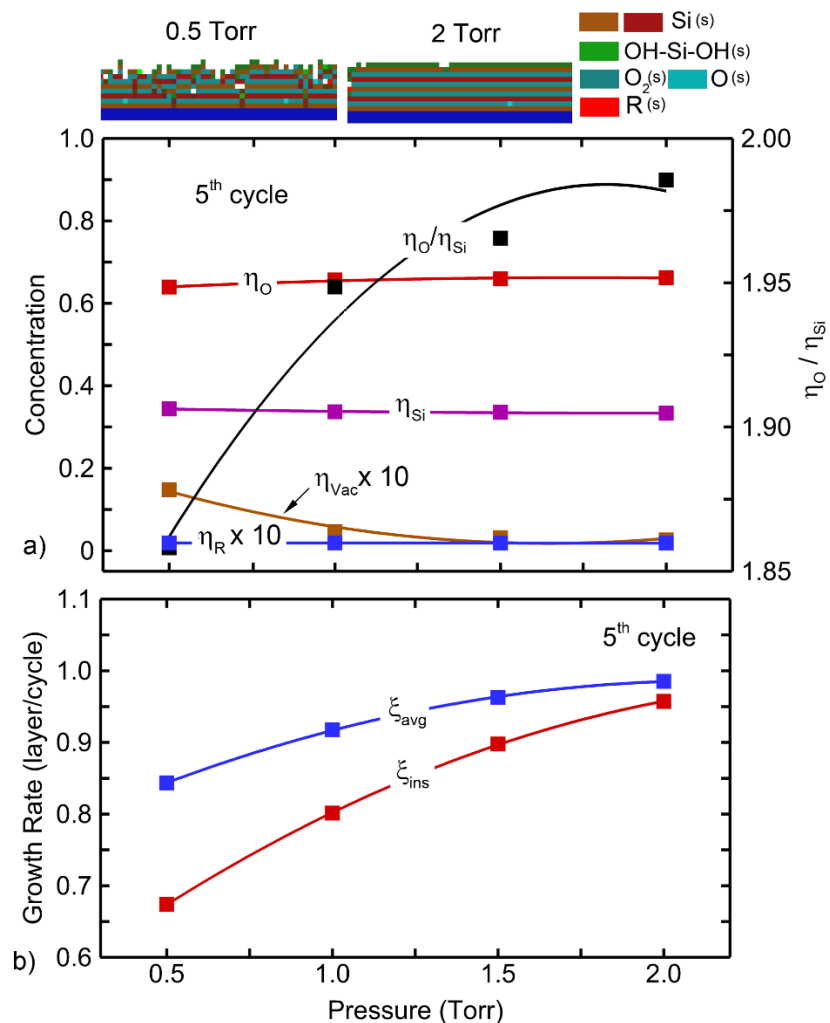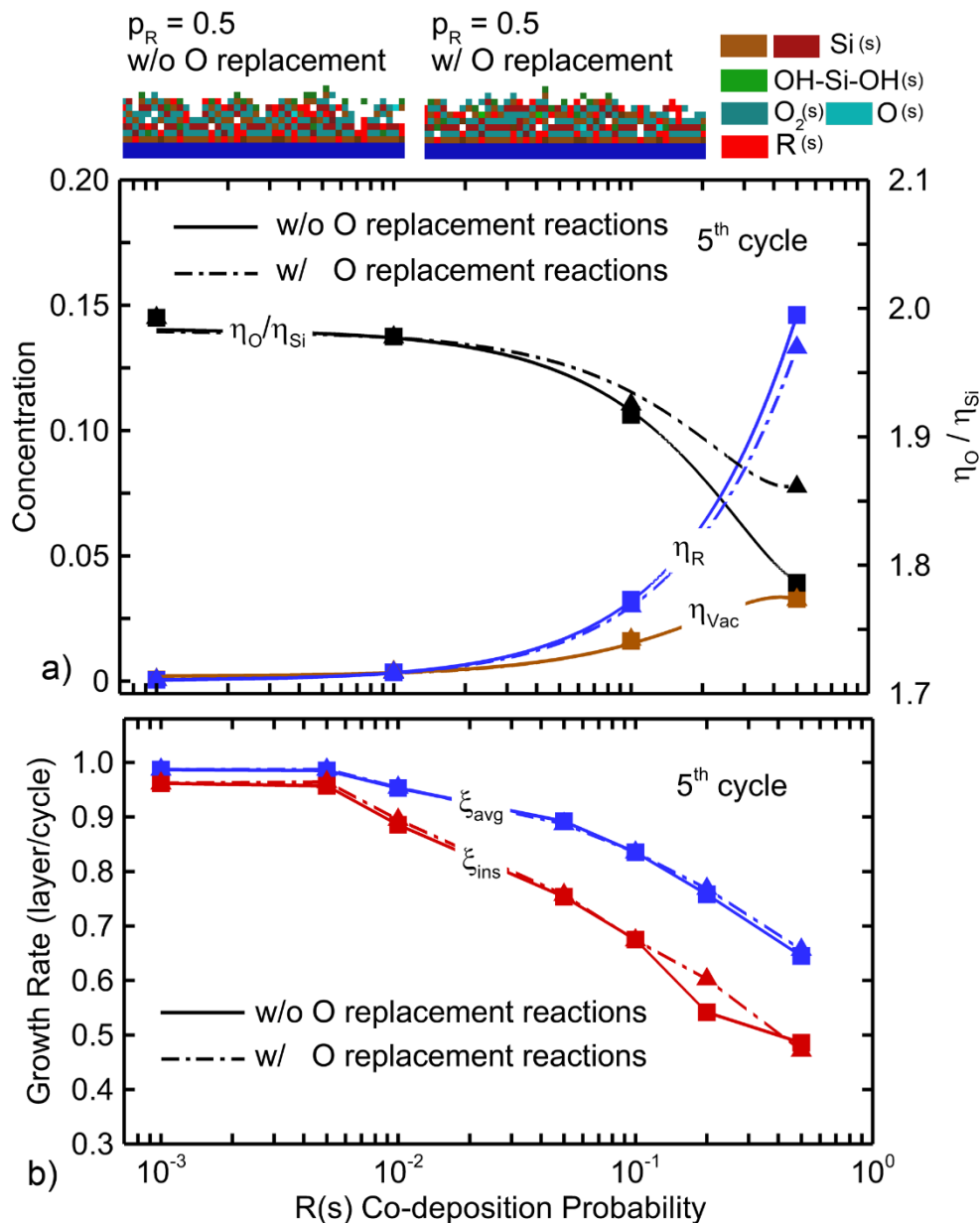
Fig. 7.17 a) Concentrations of oxygen, silicon, vacancy, and ligand groups in the entire film and oxygen to silicon ratio, and b) time-averaged and instantaneous film growth rate for blanket deposition with and without oxygen replacement reactions. Data are from 5th cycle. 500 W, 10 MHz, 2 Torr, primary gas inlet: Ar/O_2 (4/1), 5 slm; secondary gas inlet: O_2, 6 slm. 0.5 nm/cell, 1 nm per SiO_2 layer.
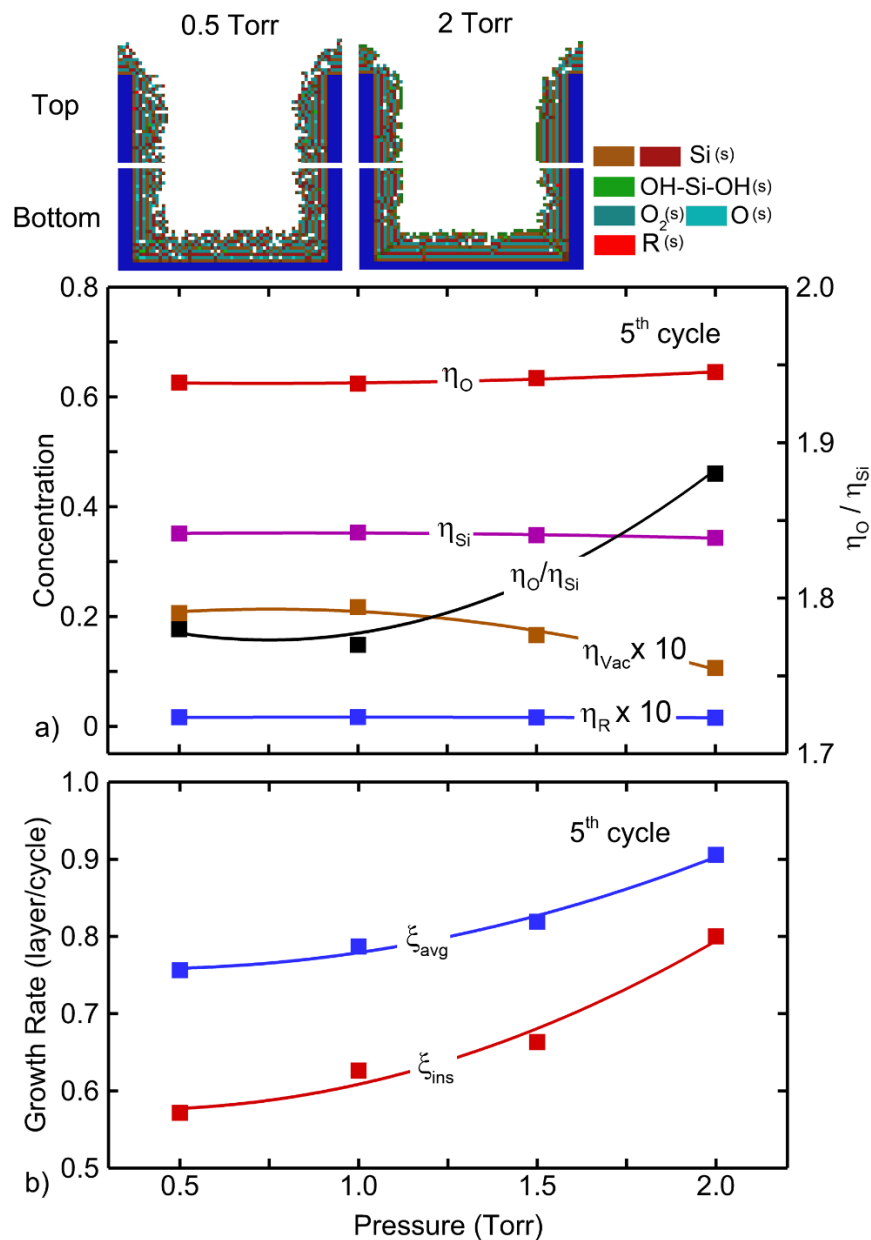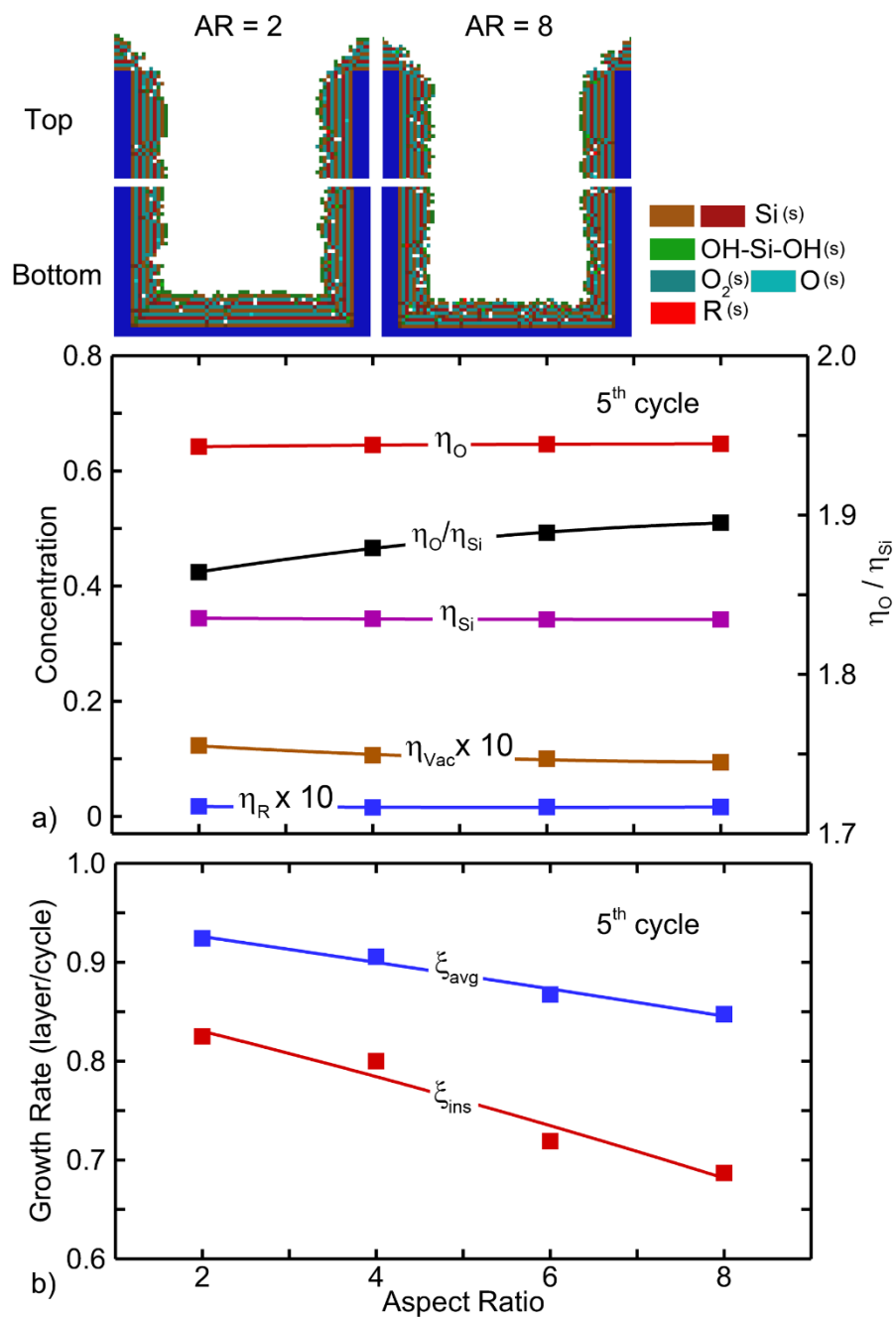
Fig. 7.18 a) Concentrations of oxygen, silicon, vacancy, and ligand groups in the entire film and oxygen to silicon ratio, and b) time-averaged and instantaneous film growth rate in the bottom of a trench with varying aspect ratio from 2-8. Data are from 5th cycle. 500 W, 10 MHz, 2 Torr, primary gas inlet: Ar/O_2 (4/1), 5 slm; secondary gas inlet: O_2, 6 slm. 0.5 nm/cell, 1 nm per SiO_2 layer.

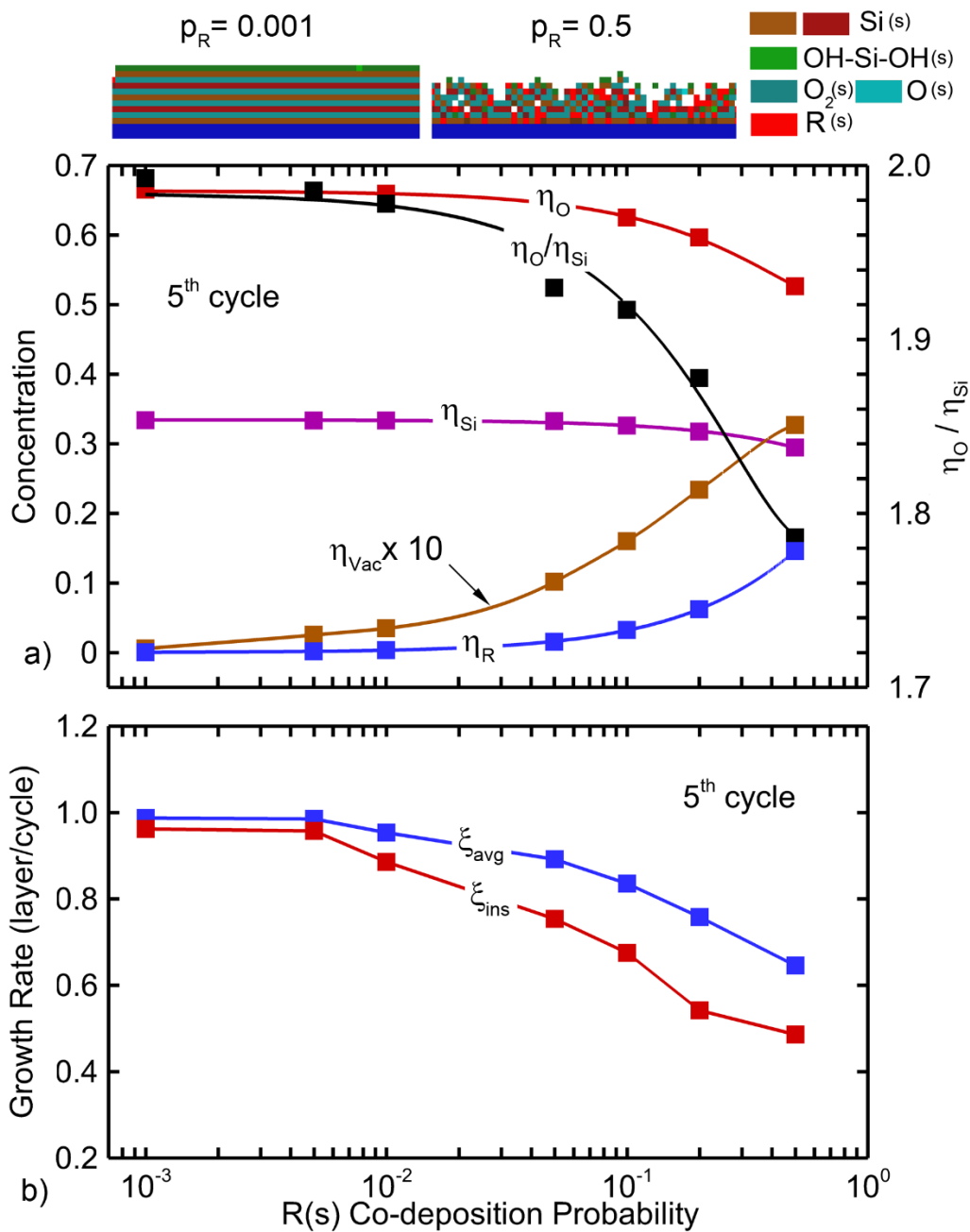Fig. 7.19 a) Geometry of the via and film profile at the end of the 5th cycle and b) concentrations of oxygen, silicon, vacancy, and ligand groups in the entire film and oxygen to silicon ratio, and c) time-averaged and instantaneous film growth rate in the bottom of this via with varying aspect ratio from 2-8. Data are from 5th cycle. 500 W, 10 MHz, 2 Torr, primary gas inlet: Ar/O₂ (4/1), 5 slm; secondary gas inlet: O₂, 6 slm. 0.5 nm/cell, 1 nm per SiO₂ layer.
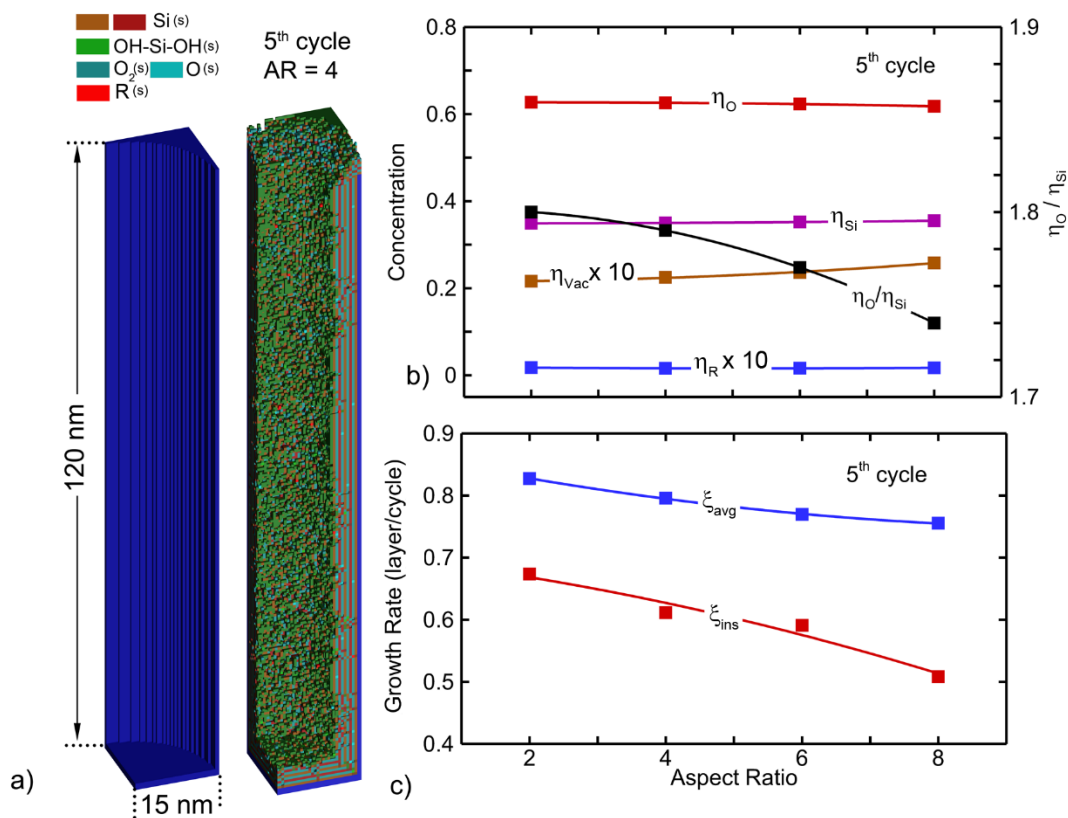
7.7 References

1. R. W. Johnson, A. Hultqvist, and S. F. Bent, Mater. Today 17, 236-246 (2014).

2. R. A. Ovanesyan, E. A. Filatova, S. D. Elliott, D. M. Hausmann, D. C. Smith, and S. Agarwal, J. Vac. Sci. Technol. A **37**, 060904 (2019).

3. H. B. Profijt, S. E. Potts, M. C. M. van de Sanden, and W. M. M. Kessels, J. Vac. Sci. Technol. A **29**, 050801 (2011).

4. J. R. Bakke, K. L. Pickrahn, T. P. Brennan, and S. F. Bent, Nanoscale **3**, 3482 (2011).

5. C.-C. Chao, J. S. Park, X. Tian, J. H. Shim, T. M. Gür, and F. B. Prinz, ACS Nano **7**, 2186-2191 (2013).

6. A. Kobayashi, N. Tsuji, A. Fukazawa, and N. Kobayashi, Thin Solid Films **520**, 3994-3998 (2012).

7. C. A. Murray, S. D. Elliott, D. Hausmann, J. Henri, and A. LaVoie, ACS Appl. Mater. Interfaces **6**, 10534-10541 (2014).

8. D. Shin, H. Song, M. Lee, H. Park, and D.-H. Ko, Thin Solid Films **660**, 572-577 (2018).

9. F. Koehler, D. H. Triyoso, I. Hussain, B. Antonioli, and K. Hempel, Phys. Status Solidi C **11**, No. 1, 73-76 (2014).

10. T. Usui, C. A. Donnelly, M. Logar, R. Sinclair, J. Schoonman, and F. B. Prinz, Acta Materialia **61**, 7660-7670 (2013).

11. K.-M. Jeon, J.-S. Shin, J.-Y. Yun, S. J. Lee, and S.-W. Kang, J. Vac. Sci. Technol. A **32**, 031511 (2014).

12. H. Jung, W.-H. Kim, I.-K. Oh, C.-W. Lee, C. Lansalot-Matras, S. J. Lee, J.-M. Myoung, H.-B.-R. Lee, and H. Kim, J. Mater. Sci. **51**, 5082-5091 (2016).

13. Y. Civale, A. Redolfi, D. Velenis, N. Heylen, J. Beynet, I. Jung, J.-J. Woo, B. Swinnen, G. Beyer, and E. Beyne, Proc. 4th Electron. Sys.-Integr. Technol. Conf. (ESTC), Amsterdam, The Netherlands, pp. 1-4, Sep. 2012.

14. J. M. Chan, C. S. Tan, and K. C. Lee, IEEE EPTC, Nov. 2016.

15. K. Endo, Y. Ishikawa, T. Matsukawa, Y. Liu, S.-i. O'uchi, K. Sakamoto, J. Tsukada, H. Yamauchi, and M. Masahara, Solid State Electronics **74**, 13-18 (2012).

16. F. Palumbo, C. Wen, S. Lombardo, S. Pazos, F. Aguirre, M. Eizenberg, F. Hui, and M. Lanza, Adv. Func. Mater. 1900657 (2019).

17. J. H. Stathis, IBM Journal of R&D **46**, No. 2/3 (2002).

18. O. Sneh, M. L. Wise, A. W. Ott, L. A. Okada, and S. M. George, Surf. Sci. **334**, 135-152 (1995).

19. S.-W. Lee, K. Park, B. Han, S.-H. Son, S.-K. Rha, C.-O. Park, and W.-J. Lee, Electrochem. Solid-State Lett. **11** (7), G23-G26 (2008).

20. G.-Y. Fang, L.-N. Xu, Y.-Q. Cao, L.-G. Wang, D. Wu, and A.-D. Li, Chem. Commun. **51**, 1341 (2015).

21. Y.-J. Choi, S.-M. Bae, J.-H. Kim, E.-H. Kim, H.-S. Hwang, J.-W. Park, H. Yang, E. Choi, and J.-H. Hwang, Ceram. Int. **44**, 1556-1565 (2018).

22. M Putkonen et. al., Thin Solid Films **558**, 93-98 (2014).

23. A. Mallikarjunan, H. Chandra, M. Xiao, X. Lei, R. M. Pearlstein, H. R. Bowen, M. L. O'Neill, A. Derecskei-Kovacs, and B. Han, J. Vac. Sci. Technol. A **33**, 01A137 (2015).

24. M. J. Kushner, J. Phys. D: Appl. Phys. **42**, 194013 (2009).

25. Y. Zhang, C. Huard, S. Sriraman, J. Belen, A. Peterson, and M. J. Kushner, J. Vac. Sci. Technol. A **35**, 021303 (2017).

26. Y. Lu, A. Kobayashi, H. Kondo, K. Ishikawa, M. Sekine, and M. Hori, Jpn. J. Appl. Phys. **53**, 010305 (2014).

Chapter 8: Conclusions and Future Work

Some of the most critical challenges in semiconductor fabrication processes involving low-temperature plasma are maintaining a high stability and uniformity of the plasma, increasing the power deposition efficiency, as well as accomplishing independent control of the plasma density and ion energy on the wafer. In addition, approaches that help us to understand the physics in an nm-scale feature within a plasma-enhanced atomic layer deposition (PE-ALD) process are highly desirable in order to improve the current technology. In this dissertation, a 2-dimensional reactor-scale hybrid hydrodynamic simulation platform (the HPEM) and a 3-dimensional feature-scale voxel-based model (the MCFPM) were utilized to study these challenges. The insights provided in this dissertation can help further optimize the design of low-temperature plasma (LTP) reactors for industrial applications, and help us to understand the SiO$_2$ PE-ALD process. Summaries of each chapter are presented in Sec. 8.1. Contributions of this work are described in Sec. 8.2. Future work is discussed in Sec. 8.3.

8.1 Summary

In Chapter 1, the fundamental properties and equations governing low temperature plasma are introduced. Two types of plasma source—inductively coupled plasma (ICP) and capacitively coupled plasma (CCP)—were reviewed. The fabrication process of using a plasma-enhanced atomic layer deposition (PE-ALD) technique in order to grow a thin silicon dioxide

(SiO_2) film was reviewed. A review and comparison of both reactor- and feature-scale plasma models were then presented.

In Chapter 2, the models used in this thesis were discussed in detail. The 2-dimensional reactor-scale hybrid hydrodynamic model, the HPEM, was updated and equipped with a circuit model to address the impedance matching network (IMN) and frequency tuning. The eMCS module in the HPEM was updated with parallel computation enabled, utilizing an application programming interface, OpenMP, to be more computationally efficient. The 3-dimensional feature scale model, the MCFPM, was updated to address steric hindrance caused by the ligand group remnants on a surface in the PE-ALD process.

In Chapter 3, the uniformity of an inductively coupled plasma (ICP) powered with a high-low pulsed power while being sustained in an Ar/Cl_2 gas mixture was investigated. An upward spike of electron temperature (T_e) was observed at the leading edge of the pulse; likewise, a downward spike was observed during power transition from high-to-low. The instabilities of T_e, electron density, and ion densities caused by the pulse diminish toward the bottom of the reactor as distance from the power source increases, due to the long transportation time and low power density. This work demonstrates that a pulsed plasma is a highly dynamic system with strong time- and spatial-dependency.

In Chapter 4, power deposition to an Ar/Cl_2 ICP was investigated with both inductive and capacitive power coupling included. The set-point impedance matching technique was then applied. In an ICP, when power is mainly transferred to the plasma through electromagnetic fields (EM-fields) with a solenoidal electric field (E-field), plasma is in H-mode. When the power is predominantly coupled to the electrons and ions near the coils through an electrostatic E-field, the plasma is in E-mode. Choosing the IMN to match the early pulse promotes E-mode,

which assists in plasma ignition, but the tradeoff is a high reflection coefficient through the pulse. In contrast, matching to the late pulse encourages H-mode and reduces the power reflection coefficient for the majority of a pulse, but delays the onset of the H-mode. This elongates the time plasma operates in E-mode. A severe E-mode was found to launch electrostatic waves to the plasma in the leading RF cycles during pulsed-on due to the oscillation of the sheath produced by the electrostatic field from the coil. The implications of duty cycle and geometry on the impedance match were also studied. Short duty cycle promotes the E-mode at the beginning of a pulse owing to the low electron density caused by the sufficient loss during inter-pulse period. A big gap between coil and dielectric window produces low capacitance that constrains capacitive power coupling, which then weakens the E-mode and delays the onset of the H-mode.

In Chapter 5, utilizing a pure Ar ICP sustained in pulsed power, two impedance matching techniques were investigated: the first used only a fixed impedance matching network (IMN), referred to as set-point matching, and the second utilized a combination of set-point matching with a real-time impedance matching approach (frequency tuning). When only the IMN was used to match impedance, it created an impedance mismatch during other times within the pulse, resulting in a high power reflection coefficient and low power transition efficiency. This impedance mismatch can be minimized by frequency tuning. Matching impedance in the early pulse was found to be vital for plasma ignition. An impedance matching procedure that utililizes set-point matching for a coarse match and then refines it using frequency tuning was proposed.

In Chapter 6, reactor-scale modeling was used to investigate the triple-frequency, capacitively coupled plasma (TF-CCP) sustained in Ar/CF$_4$/O$_2$ mixtures. A high frequency (HF) 80 MHz continuous wave (CW) power was applied to the top electrode, while lower frequency

powers (5, and 10 MHz) were applied to the substrate. The high frequency was found to be more efficient in heating electrons, due to the fact that stochastic heating is propotional to the frequency. Ion energy on the substrate decreases with the increase of HF power, due to the less negative DC bias (-660 to -121V as power increases from 50 to 1000 W). Increasing pressure results in a more collisional sheath above the substrate, which broadens the ion angular distribution (IAD). Increasing HF promotes stochastic heating, which in turn causes the increase of plasma density in the center of the reactor. Increasing the gap length between electrodes leads to a more uniform plasma distribution in the plasma bulk and a more negative DC bias.

In Chapter 7, using integrated reactor- and feature-scale models, we examined plasma-enhanced atomic layer deposition (PE-ALD) of a thin SiO_2 film deposited on blanket, trench and via structures using Ar/O_2 plasma as oxidation agents. A SiO_2 deposition mechanism was developed for the feature scale simulation. The steric hindrance was included by depositing the ligand group along with the primary silicon sites at a probability p_R. Sparsely distributed imperfections and misalignments in the layers deposited in the early stages affected film deposited later in upper layers, resulting in disordered film structure. The growth rate of the film decreases as it thickenes due to the increased complexity of the surface components. Both oxygen radical O and excited state oxygen molecule O_2^* affect film deposition on a blanket, but O was found to be the dominant oxidant when depositing in a trench or a via due to the significant impact of the conduction limit on the O_2^* flux. Varying power affects the SiO_2 film deposition differently when the film is on a blanket, compared to in a trench, because O_2^* and O fluxes follow different paths as the power varies. Increasing pressure results in a more collisional sheath, which reduces the ion energy and consequently reduces the ion bombardment damages to the film. Changing the co-deposition probability of ligand group has a similar effect

272

on the film deposition, regardless of the structure of the target feature. Higher p_R leads to lower film growth rate and higher vacancy concentration in the film. Because a via has higher surface to volume ratio than a trench when their aspect ratio is the same, conduction limit has a more significant effect in a via than in a trench.

8.2 Contributions

The work in this dissertation helps us to understand the fundamental physcis in low temperature plasmas within industrial applications, and provides information needed to optimize the design of a LTP reactor and operating conditions.

1. IMN circuit components are analytically solved for the perfect matching condition. Frequency tuning is implemented for real-time impedance matching.

A new method of analyticlally solving the values of circuit components used in the IMN in order to create perfect matching was added to the HPEM in order to provide more accurate results with less time consumption. Frequency tuning was also implemented in the HPEM to enable a real-time impedance matching. Using these updates, plasma behaviors were investigated using different impedance matching approaches. The results can be used to guide the selection of IMN to maximize power deposition efficiency while minimizing plasma instability. Results that utilize frequency tuning can help with choosing frequencies to match the impedance at various transients during processing. Applications using a continuously changing power profile, such as a sawtooth waveform, will especially benefit from real-time impedance matching like frequency tuning.

2. Implementation of parallel computation in electron Monte Carlo Simulation module.

A parallel computing technique using the application programming interface OpenMP was implemented into the HPEM to enable efficient modeling in electron Monte Carlo

273

Simulation module (eMCS). In order to prevent the cross-talks between variables during parallel computing, variables are made thread-aware at the beginning of the eMCS. That is, parts of each variable are distributed to individual threads with the thread number logged. These threads perform the computation independently through the eMCS and then merge the variables back into their initial form at the end of executing the eMCS. This technique prevents cross-talks between the parts of variables and enables independent calculations on pseudoparticles. The most conspicuous acceleration was achieved when a large amout of pseudoparticles was launched.

3. *Integrated investigation of plasma enhance atomic layer deposition system of SiO₂ film deposition on blanket, trench and via features.*

The reactor-scale plasma properties (e.g., electron density, ion fluxes to the wafer, ion energy and angular distributions, etc.) of an Ar/O$_2$ capacitively-coupled plasma (CCP) were studied using a 2-dimensional hybrid hydrodynamic model (the HPEM). The surface reaction mechanism of plasma-enhanced atomic layer deposition (PE-ALD) of SiO$_2$ film was developed for the feature-scale investigations. Steric hindrance was addressed by depositing the ligand sites along with the primary deposited silicon sites at a co-deposition probability p_R. The impact of microscopic parameters on film quality was investigated using the feature-scale model (the MCFPM). These microscopic parameters could be controlled through varying macroscopic parameters, such as the input power to the plasma, pressure in the reactor, and the choice of silicon precursor. Results from this work provide guidance for SiO$_2$ PE-ALD fabrication process optimization and for reactor design. Parametric studies of power, pressure, and the ligand group remnant co-deposition probability were performed on blanket deposition and film deposition in a

trench. Impact of aspect ratio on the SiO_2 film quality was explored when depositing the film in a trench and in a via structure.

8.3 Future Work

Reactor- and feature-scale models were updated and executed to simulate low temperature plasmas involved in industrial applications. Future work that will improve the performance of the plasma modeling is proposed as follows:

1. Enable neighbor checks in the MCFPM for specified reactions.

In the current version of the surface reaction mechanism of PE-ALD for an SiO_2 film, the deposition probability of gas-phase oxygen radical O on the silicon site Si (s) is reduced to 10^{-4}, to accommodate the exposure of saturated silicons, with all of their bonds occupied. This reduction of deposition probability of O on Si (s) was empirically derived and is somewhat arbitrary; this can be avoided if the neighbor of the surface reactant is checked to determine if that surface reactant is in a saturated state. Considering that performing this check will be highly time consuming if it is executed every time a surface reaction occurs, some form of tag —such as a special number— should be given to specified reactions so that if a tagged reaction occurs, a neighbor check is conducted.

2. Parallel calculation in module PCMCM.

Like eMCS, PCMCM tracks particles (charged and neutral) using a Monte Carlo approach. Because pseudoparticles are moved and tracked independently, PCMCM is also suitable for parallel computation. Similar to the eMCS, parameters of pseudoparticles should be distributed to a number of threads and become thread-aware at the beginning of the PCMCM; each thread then independently moves and tracks the pseudoparticles assigned to it and returns the information back to the master thread at the end of the PCMCM. Using parallel computing

for the PCMCM should greatly reduce the time spent in the module especially when a large amount of the pseudoparticles are used, for instance, when neutral energy and angular distribution (NEAD) are to be recorded.

3. Implement IMN and frequency tuning for CCP reactor.

In the current version of the HPEM, the IMN and frequency tuning are only implemented for the calculation in an ICP reactor. These should also be enabled in a CCP reactor so that the simulation can have better agreement with the experimental results.

4. Apply machine learning to determine optimal operating conditions for fabrication processes.

Machine learning (ML) can be employed to help choose the optimal operating conditions and reduce the number of test wafers to run during process development. Simulation results from models such as the HPEM and MCFPM could be used for preliminary training datasets to reduce the number of wafers that need to be run. Quantifiable physics parameters such as the reaction probabilities for ion and radical fluxes to the wafer should be a desired outcome of the ML so that the results can be transferred to other system. ML algorithm are typically based on describing the flux to the wafer as a function of operating conditions (power, pressure, etc.) when the plasma is sustained in a certain gas mixture and certain reactor. These outcomes do not necessarily transfer to other systems (different gas mixture, different method of excitation). Building the ML algorithm to isolate physical parameters that are not functions of operating conditions should make the outcome of ML more broadly applicable, for example, applying to both ICP and CCP.

Appendix: Analytical Solution of Components in Impedance Matching Networks

    The components used in the impedance matching network (IMN) is analytically solved in the HPEM to provide perfect impedance matching. The solutions of theses components are subjected to the choice of IMN schematic. In the HPEM, three types of the IMNs can be used. The schematics of these IMNs and solutions of the components in the IMN that can produce perfect impedance matching are provided in this Appendix.

A.1 IMN Type 1

    The schematic of type 1 IMN is
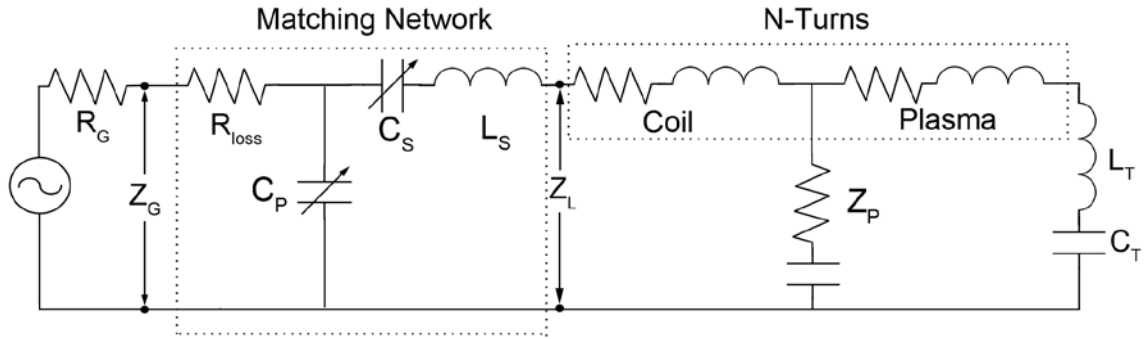
where R_G is the resistance of the power supply, R_{loss} is the resistance in the IMN, C_P and C_S are capacitors that are tuned to produce perfect impedanc1e matching, L_S is an inductor with fixed user-defined inductance, Z_L is the impedance of the load consisting of plasma and reactor, Z_P is the impedance of the plasma, L_T and C_T are the termination components connected to ground.

    The total impedance including match box components, plasma and termination components is

$$Z = R_{loss} + \cfrac{1}{j\omega C_P + \cfrac{1}{\cfrac{1}{j\omega C_S} + j\omega L_s + \mathrm{Re}(Z_L) + j\,\mathrm{Im}(Z_L)}} \tag{A.1}$$

where $\mathrm{Re}(Z_L)$ denotes the real component of Z_L and $\mathrm{Im}(Z_L)$ is the imaginary component of Z_L, ω is the radian frequency of the power supply, and j is the imaginary unit. For a perfect matching, $Z = Z_G$, utilizing $\mathrm{Im}(Z) = \mathrm{Im}(Z_G)$ provides:

$$C_S = \frac{C_S\left\{\left[\omega L_S + \mathrm{Im}(Z_L)\right]\omega C_S - 1\right\}}{A_1 C_S^2 + B_1 C_S + 1} \tag{A.2}$$

where

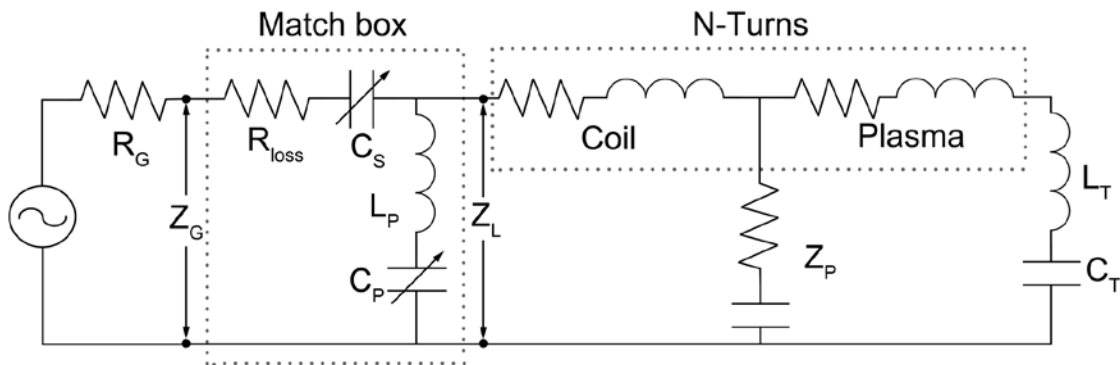$$A_1 = \omega^2\left|Z_L\right|^2 + \omega^4 L_S^2 + 2\omega^3 L_S\,\mathrm{Im}(Z_L) \tag{A.3}$$

$$B_1 = -2\omega^2 L_S - 2\omega\,\mathrm{Im}(Z_L) \tag{A.4}$$

where $|Z_L|$ is the modulus of Z_L. Then by requiring $\mathrm{Re}(Z) = \mathrm{Re}(Z_G)$,

$$C_S = \frac{-B_1 \pm \sqrt{B_1^2 - 4\left\{A_1 - \omega^2\,\mathrm{Re}(Z_L)\left[\mathrm{Re}(Z_G) - R_{loss}\right]\right\}}}{2\left\{A_1 - \omega^2\,\mathrm{Re}(Z_L)\left[\mathrm{Re}(Z_G) - R_{loss}\right]\right\}} \tag{A.5}$$

A.2 IMN Type 2

The schematic of type 2 IMN is

The denotations are the same as type 1 IMN other than instead of utilizing a series inductor L_S, a parallel inductor L_P is used in the IMN. In a type 2 IMN, the total impedance of the match box components, plasma and termination components is

$$Z = R_{loss} + \frac{1}{j\omega C_s} + \cfrac{1}{\cfrac{1}{j\omega L_p + \cfrac{1}{j\omega C_p}} + \cfrac{1}{\text{Re}(Z_L) + j\,\text{Im}(Z_L)}} \tag{A.6}$$

Matching $\text{Re}(Z) = \text{Re}(Z_G)$, we obtain

$$C_P = \frac{-B_2 \pm \sqrt{B_2^{\,2} - 4A_2 C_2}}{2A_2} \tag{A.7}$$

where

$$A_2 = [\text{Re}(Z_G) - R_{loss}]\left\{|Z_L|^2\,\omega^4 L_P^2 + \omega^2 |Z_L|^4 + 2\omega^3 L_P\,\text{Im}(Z_L)|Z_L|^2\right\} - \text{Re}(Z_L)\omega^4 L_P^2 |Z_L|^2 \tag{A.8}$$

$$B_2 = 2\omega^2 L_P\,\text{Re}(Z_L)|Z_L|^2 - 2\omega|Z_L|^2\Big[\text{Re}(Z_G) - R_{loss}\Big]\Big[\omega L_P + \text{Im}(Z_L)\Big] \tag{A.9}$$
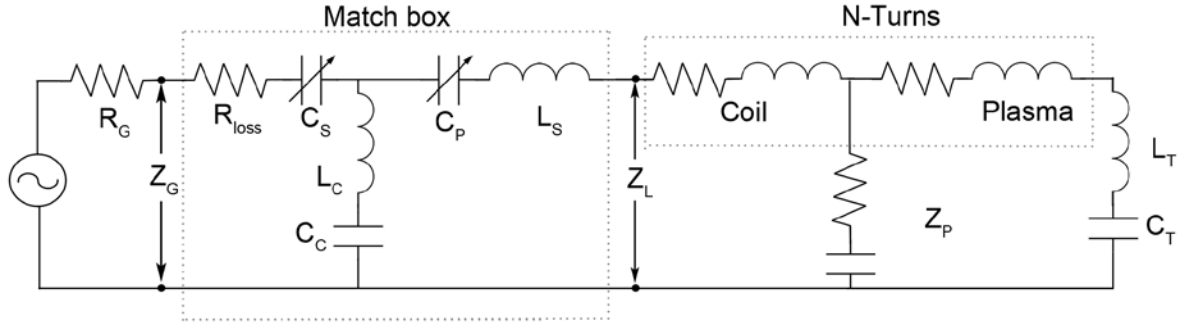
$$C_2 = \left\{\Big[\text{Re}(Z_G) - R_{loss}\Big] - \text{Re}(Z_L)\right\}|Z_L|^2 \tag{A.10}$$

Then C_S is solved by matching the imaginary part of the impedance $\text{Im}(Z) = \text{Im}(Z_G)$:

$$C_S = -\frac{\text{Re}^2(Z_L)\left(1 - \omega^2 L_P C_P\right)^2 + \left[\omega C_P |Z_L|^2 - \text{Im}(Z_L)\left(1 - \omega^2 L_P C_P\right)\right]^2}{\omega\left(1 - \omega^2 L_P C_P\right)|Z_L|^2\left[\omega C_P |Z_L|^2 - \text{Im}(Z_L)(1 - \omega^2 L_P C_P)\right]} \tag{A.11}$$

A.3 IMN Type 3

The schematic of type 3 IMN is

The denotations are the same as those used in type 1 and 2 IMNs. However, C_P and C_S are in series in the circuit. Constant inductor and capacitor L_C and C_C are added in the IMN. In a type 3 IMN, the total impedance of the match box components, plasma and termination components is

$$Z = R_{loss} + \frac{1}{j\omega C_S} + \cfrac{1}{\cfrac{1}{j\omega L_C + \cfrac{1}{j\omega C_C}} + \cfrac{1}{j\omega L_S + \cfrac{1}{j\omega C_P} + \mathrm{Re}(Z_L) + j\,\mathrm{Im}(Z_L)}} \tag{A.12}$$

Matching $\mathrm{Re}(Z) = \mathrm{Re}(Z_G)$, we obtain

$$C_P = \frac{-B_3 \pm \sqrt{B_3^{\,2} - 4A_3 C_3}}{2A_3} \tag{A.13}$$

where

$$A_3 = \alpha^2 \mathrm{Re}(Z_L) - [\mathrm{Re}(Z_G) - R_{loss}]\mathrm{Re}^2(Z_L) - [\mathrm{Re}(Z_G) - R_{loss}]\beta^2 \tag{A.14}$$

$$B_3 = \frac{2\beta[\mathrm{Re}(Z_G) - R_{loss}]}{\omega} \tag{A.15}$$

$$C_3 = \frac{\mathrm{Re}(Z_G) - R_{loss}}{\omega^2} \tag{A.16}$$

$$\alpha = \omega L_C - \frac{1}{\omega C_C} \tag{A.17}$$

$$\beta = \alpha + \mathrm{Im}(Z_L) + \omega L_S \tag{A.18}$$

Then C_S is solved by matching the imaginary components of the impedances

$$C_S = \frac{\mathrm{Re}^2(Z_L) + (\alpha + \gamma)^2}{\omega\alpha\left\{\gamma(\alpha + \gamma) + \mathrm{Re}^2(Z_L)\right\}} \qquad \text{(A.19)}$$

where

$$\gamma = \mathrm{Im}(Z_L) + \omega L_S - \frac{1}{\omega C_P} \qquad \text{(A.20)}$$